Lagrangian connectivity of the upper limb of the overturning circulation studied with high-resolution ocean models

Dissertation
for the degree Doctor of Natural Sciences
at the Faculty of Mathematics and Natural Sciences
of the Christian-Albrechts-Universität zu Kiel

submitted by

Siren Rühs

Kiel, 2018

Siren Rühs (2018): *Lagrangian connectivity of the upper limb of the overturning circulation studied with high-resolution ocean models*. Dissertation at the Faculty of Mathematics and Natural Sciences of the Christian-Albrechts-Universität zu Kiel.

Reviewer1 : Prof. Dr. Arne Biastoch
Reviewer2 : Prof. Dr. Peter Brandt
Date of oral examination : September 11th, 2018
Approved for publication : September 11th, 2018

Prof. Dr. Frank Kempten, Dean

Declaration

Hiermit erkläre ich, dass ich diese Arbeit selbstständig gemäß den Regeln zur guten wissenschaftlichen Praxis der Deutschen Forschungsgemeinschaftangefertigt angefertigt und keine anderen als die angegebenen Hilfsmittel verwendet habe, nicht mit demselben Thema zeitgleich an einer anderen Fakultät im In- oder Ausland die Zulassung zur Promotion beantragt habe oder beantragen werde, noch an keiner anderen Hochschule oder an keiner anderen Fakultät dieser Hochschule ein Promotionsvorhaben endgültig nicht bestanden habe und mir noch kein akademischer Grad entzogen wurde.

Kiel, July 9th, 2018

Siren Rühs

Publications

This thesis is based on the following manuscripts, which are listed below according to their order of appearance:

Van Sebille, E., Griffies, S. M., Abernathey, R., Adams, T. P., Berlof, P., Biastoch, A., Blanke, B., Chassignet, E. P., Cheng, Y., Cotter, C. J., Deleersnijder, E., Döös, K., Drake, H. F., Drijfhout, S., Gary, S. F., Heemink, A. W., Kjellsson, J., Koszalka, I. M., Lange, M., Lique, C., MacGilchrist, G. A., Marsh, R., Adame, C. G. M., McAdam, R., Nencioli, F., Paris, C. B., Piggott, M. D., Polton, J. F., **Rühs, S.**, Shah, S. H. A. M., Thomas, M. D., Wang, J., Wolfram, P. J., Zanna, L. & J. D. Zika (2018): *Lagrangian ocean analysis: fundamentals and practices*. Ocean Modelling, 121, 49–75, doi:10.1016/j.ocemod.2017.11.008.

(chapter 2; candidate contributions: assisting with structuring the paper, performing exemplary Lagrangian analysis and producing original Fig. 4-6, co-writing original sections 2.4, 3.2.3, 3.3.3, 4.1, 4.3-4.5, A.1.1, contributing with ideas, discussion and comments to the other sections)

Rühs, S., Schwarzkopf, F., and A. Biastoch (manuscript in preparation for submission to Ocean Science): *Cold vs. warm water route — sources for the upper limb of the AMOC revisited in a high-resolution ocean model*.

(chapter 3; candidate contributions: defining the research problem and methodology, performing Lagrangian trajectory calculations, analyzing simulated Lagrangian trajectory data sets, producing all figures, writing the paper)

Durgadoo, J. V., **Rühs, S.**, Biastoch, A., and C. W. Böning (2017): *Indian Ocean sources of Agulhas leakage*. Journal of Geophysical Research: Oceans, 122(4), 3481–3499, doi:10.1002/2016JC012676.

(chapter 4; candidate contributions: assisting with Lagrangian trajectory calculations, suggesting to include water mass transformation analysis, refining methodology of pathway analysis by means of Lagrangian streamfunctions, writing the respective parts of method section, contributing to overall writing process from the first draft to the final version of the paper)

Rühs, S., Zhurbas, V., Koszalka, I. M., Durgadoo, J. V., and A. Biastoch (2018): *Eddy diffusivity estimates from Lagrangian trajectories simulated with ocean models and surface drifter data — a case study for the greater Agulhas system*. Journal of Physical Oceanography, 48(1), 175–196, doi:10.1175/JPO-D-17-0048.1.

(chapter 5; candidate contributions: defining the research problem and methodology, performing Lagrangian trajectory calculations, performing and analyzing diffusivity calculations from simulated trajectories, comparing diffusivity estimates from simulated and observed particle dispersal, producing all figures, writing the paper)

Related manuscripts including candidate contributions:

Tim, N., Zorita, E., Schwarzkopf, F. U., **Rühs, S.**, Emeis, K.-C., and A. Biastoch (submitted to Journal of Geophysical Research: Oceans): *The impact of Agulhas leakage on the central water masses in the Benguela upwelling system from a high-resolution ocean simulation*.

(candidate contributions: assisting with Lagrangian trajectory calculations and evaluation, co-writing sections 2.3 and 3.3, contributing to overall writing process)

Wagner, P., **Rühs, S.**, Schwarzkopf, F., Koszalka, I. M., and A. Biastoch (in preparation for submission to Journal of Physical Oceanography): *Can Lagrangian tracking simulate tracer spreading in a high-resolution Ocean General Circulation Model?*

(candidate contributions: co-defining research problem, assisting with Lagrangian diffusivity calculation and evaluation, contributing to overall writing process)

Abstract

Lagrangian connectivity studies with ocean models comprise the analysis of sets of virtual fluid particle trajectories to identify connecting pathways, as well as associated timescales and transports between distinct oceanic regions. They constitute a powerful tool in physical oceanography and a unique means to coherently study seawater pathways associated with the global overturning circulation (GOC). However, there are several open questions related to the (partially unresolved) impact of small-scale flow variability on large-scale Lagrangian connectivity measures. This doctoral dissertation addresses different aspects of the question how high-resolution ocean models can help improving our understanding of the spreading of water masses associated with the global overturning circulation, by: (i) reviewing the theoretical background of Lagrangian connectivity studies with ocean models, thereby highlighting the importance to distinguish Lagrangian analyzes of simulated purely advective volume transport trajectories from Lagrangian modeling approaches to estimate advective-diffusive tracer trajectories; (ii) investigating Lagrangian volume transport pathways and along-track tracer changes of the GOC's upper limb in the South Atlantic (study 1) and Indian Ocean (study 2) with high-resolution models; and (iii) assessing the performance of near-surface particle dispersal simulations in the extended Agulhas Current system by means of lateral eddy diffusivity estimates (study 3).

The major aim of study 1 was to revisit the relative importance of the different sources for the GOC's upper limb in the South Atlantic, that are, waters entering from the Indian Ocean through the Agulhas Current system versus waters entering from the Pacific through Drake Passage. To do so, backward trajectory calculations from the North Brazil Current have been employed. They revealed a substantially higher volumetric contribution of waters originating at Drake Passage than estimated by previous Lagrangian studies with coarser resolution models. Moreover, the majority of waters with Drake Passage and Agulhas origin experiences substantial water property modifications along their transit through the South Atlantic. A first analysis of temporal changes in the ratio of the two contributions further indicates that an ongoing increase in Agulhas leakage may evoke an increase in the Agulhas contribution to the upper limb of the Atlantic part of the GOC, while the Drake

Passage contribution decreases.

In study 2 the Agulhas Current contribution to the GOC's upper limb was further decomposed into its different sources from the Indian Ocean. It constitutes the first coherent Lagrangian analysis of large-scale connectivity associated with the upper limb return flow from the Pacific via the Indian Ocean into the Atlantic. The analysis highlights the dominant contribution of surface-bound Indonesian Throughflow waters that salinify and cool during their transit through the South Atlantic. Additionally, it reports a relative high contribution of intermediate water with origin South of Australia, which largely maintain their properties during transit.

Study 3 presents an analysis of near-surface lateral eddy diffusivity estimates obtained from Lagrangian trajectories simulated with a high resolution model for the greater Agulhas system. It further includes the first comparison of eddy diffusivity estimates from simulated Lagrangian trajectories and observed drifter trajectories for that region. Notably, eddy diffusivity estimates from the high-resolution model are consistent with the spatial pattern and magnitude of drifter-based eddy diffusivity estimates — without the need for an additional diffusion parametrization in the trajectory calculation.

Overall, these studies contributed to a revised picture of large-scale connectivity associated with the GOC and yielded new insights regarding the suitability of Lagrangian analyzes for assessing large-scale spreading of water masses. In particular, the presented studies highlight the benefits of Lagrangian analyzes to investigate the simulated flow field of ocean models in terms of volume transport pathways and timescales, as well as net water mass transformations. At the same time they indicate that Lagrangian analyzes are of limited use for assessing the pathways and timescales with that upper ocean temperature as well as salinity anomalies may be transmitted through the Indian and South Atlantic oceans, if the virtual fluid particles experience non-negligible along-track water property modifications.

Zusammenfassung

Lagrangesche Konnektivitätsstudien mit Hilfe von Ozeanmodellen stellen ein wichtiges Analysetool in der physikalischen Ozeanographie dar. Sie beruhen auf der Simulation von Trajektorien virtueller Fluidpartikel, und ihrer Auswertung hinsichtlich dominanter Ausbreitungspfade und -zeiskalen, sowie Volumen- oder Tracertransporte zwischen ausgewählten Ozeangebieten. Dennoch bestehen einige offene Fragestellungen bezüglich des Einflusses von (nicht vollständig aufgelösten) relativ kleinskaligen Prozessen auf großskalige Langrangesche Konnektivität. In dieser Doktorarbeit wurden verschiedene Aspekte der Frage untersucht, wie Lagrangesche Konnektivitätsstudien mit hochauflösenden Ozeanmodellen zu einem verbesserten Verständnis der Wassermassenausbreitung der globalen Umwälzbewegung beitragen können. Es wurden (i) Theorie und bisherige Anwendungen Lagrangescher Konnektivitätsstudien mit Ozeanmodellen zusammengefasst, und auf die Wichtigkeit hingewiesen Lagrangesche Analysen von rein advektiven Volumentransportpfaden und Lagrangesche Modellierung advektiv-diffusiver Tracerausbreitung zu unterscheiden; (ii) Lagrangesche Volumentransportpfade der globalen Umwälzbewegung im Südatlantik (Studie 1) und Indischen Ozean (Studie 2) in hochauflösenden Ozeanmodellen bestimmt und die damit verbundenen Netto-Wassermassentransformationen analysiert; und (iii) simulierte oberflächennahe Lagrange Ausbreitungspfade im Agulhasstromsystem mit beobachteten Driftertrajektorien hinsichtlich abgeleiteter Wirbel-Diffusivitäten verglichen (Studie 3).

In Studie 1 wurde die relative Bedeutung des Pazifik-Atlantik Einstroms durch die Drakepassage und des wirbelgetriebenen Indo-Atlantik Einstroms durch das Agulhasstromsystem für den Oberflächenstrom der globalen Umwälzbewegung im Atlantik analysiert. Dazu wurden Lagrangesche Trajektorien vom Nordbrasilstrom rückwärts in die Quellregionen gerechnet. Der aus ihnen ermittelte Beitrag des Pazifik-Atlantik Einstroms zum Gesamttransport der Oberflächenströmung der Umwälzbewegung ist vergleichbar mit dem des Indo-Atlantik Einstroms, und damit deutlich größer als bisherige Lagarangesche Studien mit grobauflösenden Ozeanmodellen vermuteten. Darüber hinaus weisen die durchgeführten Analysen darauf hin, dass ein Anstieg des Indo-Atlantik Einstroms auch zu einem erhöhten Beitrag von Wasser aus der Agulhasregion zum Gesamttransport der Oberflächenströmung im

tropischen Atlantik führt, während der Anteil des Pazifik-Atlantik Einstroms sinkt.
Studie 2 stellt die erste kohärente Lagrangesche Analyse der Oberflächenströmung der globalen Umwälzbewegung von dem Pazifischen Ozean in den Atlantik dar. Die Ergebnisse heben die Bedeutung des Indonesischen Durchstroms als dominante Quellregion für den Indo-Atlantik Einstrom hervor. Sie verdeutlichen auch, dass die Ausbreitungspfade zwischen der Inselkette Indonesiens und der Südspitze Afrikas sehr oberflächennah verlaufen und Fluidpartikel entlag dieser Wege salzreicher werden und abkühlen. Die Region südlich von Australien liefert einen ebenfalls nicht vernachlässigen Beitrag zum Indo-Atlantik Einstrom in den Atlantik. Die zugehörigen Ausbreitungspfade sind jedoch eher im Zwischenwasserbereich zu finden und die ihnen folgenden Fluidpartikel behalten zu großen Teilen ihre spezifischen Eigenschaften.
Studie 3 präsentiert eine detailierte Evaluierung von simulierten advektiven Lagrangen Trajektorien im Agulhasstromsystem bezüglich abgeleiteter räumlich variierender Diffusivitäten, welche ein Maß für den Einfluss von Wirbeln auf die Partikelausbreitung darstellen. Diffusivitäten die von Lagrangeschen Trajektorien aus einem hochauflösenden Modell abgeleitet wurden weisen eine räumliche Struktur und Magnitude auf, die gut zu Diffusivitäten passen die von beobachteten Driftertrajektorien abgeleitet wurden — ohne einer Implementierung zusätzlicher Diffusionsparametrisierungen in der Trajektorienberechnung.
Insgesamt zeigen diese Studien exemplarisch, wie Lagrangesche Konnektivitätsstudien mit hochauflösenden Ozeanmodellen unser Verständnis der globalen Umwälzbewegung hinsichtlich Volumentransportpfaden und -zeitskalen, sowie Netto-Wassermassentransformationen verbessern können. Gleichzeitig weisen sie jedoch auch darauf hin, dass Lagrangesche Analysen von advektiven Pfaden und -zeitskalen wahrscheinlich nur bedingt Aufschluss über die Ausbreitung potenzieller Temperatur- und Salzgehaltsanomalien geben, wenn die zu Grunde liegenden Partikeltrajektorien Modifikationen ihrer spezifischen Eigenschaften erfahren.

Contents

1 Introduction

The knowledge of how different oceanic regions are connected in terms of seawater pathways, as well as the associated timescales and transports of heat, dissolved substances and particulates, is of fundamental importance for many theoretical and practical applications in physical oceanography and related disciplines.

In physical oceanography, a prime example for the importance of hydrodynamic connectivity arises from the spreading of water masses as part of the global overturning circulation (GOC) [e.g., Broecker, 1991; Richardson, 2008]. Major features of the GOC are the production of cold and dense waters in the northern North Atlantic, their deep spreading into the Indian and Pacific basins (the lower limb of the GOC), the eventual upwelling of deep waters back into surface layers, as well as the return flow of warmer and lighter waters into the northern North Atlantic (the upper limb of the GOC). These processes greatly impact the oceanic uptake, transport, and storage of heat and climate relevant trace gases, thereby modulating climate variability on various spatial and temporal scales [e.g., Buckley and Marshall, 2016].

Seawater pathways related to the GOC have been traditionally assessed by analyzing the observed oceanic distribution of temperature and salinity [e.g., Lenz, 1845; Schott, 1902; Merz and Wüst, 1922; Wüst, 1949]; by studying the fate of transient chemical tracers such as Chlorofluorocarbons (CFCs) and Sulfur Hexafluorides (SF6) [e.g., Fine, 2011]; or by employing current-following, that is, Lagrangian, devices [e.g., Bower et al., 2009; Youngs et al., 2015]. There have been global Lagrangian observing programs such as the array of satellite-tracked surface drifting buoys from the Global Drifter Program [GDP, http://www.aoml.noaa.gov/phod/dac/index.php] or the ARGO array of free-drifting profiling floats [http://www.argo.ucsd.edu/]. By now the GDP drifter array is the highest spatial resolution ocean velocity data currently available [Lumpkin et al., 2017]. However, for a detailed and coherent assessment of large-scale connectivity, observational data is still too limited in space and time. Therefore, large-scale connectivity studies are increasingly performed by making use of the mathematically consistent and complete description of the oceanic flow field obtained from ocean general circulation models (OGCMs).

In principle, seawater pathways can be estimated from OGCMs by means of Lagrangian model studies, which involve the analysis of large sets of virtual particle trajectories calculated from the simulated three-dimensional and time-varying velocity fields [van Sebille et al., 2018], or by explicit tracer simulations [England and Maier-Reimer, 2001]. Yet, for many applications Lagrangian model studies

which are performed offline, that is, by using the stored velocity output after the actual OGCM integration, have become the preferential tool to assess connectivity. Persuasive arguments are lower computational costs compared to online simulated tracer spreading and a greater flexibility in the experimental design, including the possibility to calculate backward trajectories and conditional statistics from a posteriori defined subsets of particles [cf. van Sebille et al., 2018].

Lagrangian connectivity studies with ocean models significantly contributed to our current understanding of the spatio-temporal structure of the GOC. For instance, they have been employed to infer major global transport pathways [Speich et al., 2007], as well as many details of the circulation pattern in the North Atlantic [Gary et al., 2011; Burkholder and Lozier, 2011; Gary et al., 2012; Koszalka et al., 2013; Lozier et al., 2013; Burkholder and Lozier, 2014; Foukal and Lozier, 2016; Zou and Lozier, 2016; Berglund et al., 2017] and Southern Ocean [Döös et al., 2008; van Sebille et al., 2013; Viglione and Thompson, 2016; Drake et al., 2018]. They have been also used to explore individual aspects of the upper limb flow related to the Pacific-Indian [Speich et al., 2002; van Sebille et al., 2014] and Indian-Atlantic [Speich et al., 2001; Donners and Drijfhout, 2004; Biastoch et al., 2008c; van Sebille et al., 2011; Rimaud et al., 2012; Durgadoo et al., 2013; Rühs et al., 2013] inter-ocean exchanges.

Moreover, Lagrangian connectivity studies with ocean models have been of great benefit for interdisciplinary applications. For instance, they revealed substantial impact of ocean currents on population dynamics [e.g., Pineda et al., 2007; White et al., 2010; Kool et al., 2013] and hence ecosystem management. They have been used to assess pathways of small marine organisms such as larvae [Paris et al., 2005; Wood et al., 2014; Cetina-Heredia et al., 2015; Breusing et al., 2016; Torri et al., 2018], glass eels [Baltazar-Soares et al., 2014] and juvenile turtles [Scott et al., 2011; Scott et al., 2017]. Lagrangian connectivity studies have further been proven useful for assessing the massive accumulation of plastic garbage within the convergence zones of surface flow in all five subtropical basins and in the Arctic Ocean [van Sebille, 2015; Cózar et al., 2017; Hardesty et al., 2017]. And these are only selected examples of a continuously growing list of applications [cf. van Sebille et al., 2018].

Yet, despite their value as a unique tool in physical oceanography and interdiscipliary applications, Lagrangian connectivity studies with ocean models are still subject to several questions related to the (partially unresolved) impact of small-scale flow variability on large-scale Lagrangian connectivity measures and the suitability of Lagrangian connectivity studies to represent water mass spreading. In this dissertation I examine different aspects of the overall research question:

> *How can Lagrangian connectivity studies with high-resolution ocean models help improving our understanding of the spreading of water masses associated with the global overturning circulation?*

I focus on Lagrangian connectivity associated with the upper limb of the GOC within the South Atlantic and Indian Oceans, since (i) key regions of the GOC's upper limb in these basins have been shown to be greatly impacted by small-scale flow variability such as eddies, and (ii) these key regions are subject to ongoing changes in circulation pattern and thermohaline characteristics, but (iii) comprehensive Lagrangian connectivity studies of these circulation pattern as part of the large-scale GOC with high-resolution OGCMs are scarce. Specific related research challenges that are subject of this dissertation are further introduced in section 1.1. The individual studies performed to address these challenges and the resulting structure of this thesis are outlined in section 1.2.

1.1 Research challenges

The classical view of the large-scale spreading of water masses via the GOC has been that of the so-called great ocean conveyor as suggested first by Broeker and Peng [1982] and depicted in the influential paper by Broecker [1991] (Fig. 1.1). According to this schematic cold water sinks in the subpolar North Atlantic, subsequently spreads at depth along confined western boundary currents into the Indian and Pacific Oceans where it eventually upwells, and returns as warm upper ocean water through the Indonesian Archipelago and a passage south of Africa to the subpolar North Atlantic. The associated mass and heat transport was further assumed to be relatively coherent and to vary in response to changes in deep water formation caused by variable buoyancy forcing.

Since then, many authors refined this picture of the GOC [cf. Richardson, 2008; Lozier, 2010] by highlighting the role of the Southern Ocean in connecting the different basins through the Antarctic Circumpolar Current and linking the overturning cell associated with the deep water formation in the North Atlantic to a secondary deeper overturning cell associated with the formation of bottom water around Antarctica [Gordon, 1991; Lumpkin and Speer, 2007]; acknowledging a direct return flow of upper ocean water from the Pacific to the Atlantic Ocean through Drake Passage [Schmitz, 1995; Schmitz, 1996], as well as a westward path of upper ocean water south of Australia [Speich et al., 2007]; and including recirculations within the wind-driven oceanic gyres and large eddies as part of the lower and upper limb transports (Fig. 1.2). In particular, it has been shown that mesoscale perturbations control the inter-ocean exchange south of Africa [Biastoch et al., 2008c]. Further Lagrangian studies of the North Atlantic part of the GOC additionally revealed interior pathways of the subpolar-subtropical deep water transport [Bower et al., 2009; Gary et al., 2011] caused by eddy-driven recirculations [Lozier et al., 2013], and a subsurface instead of surface subtropical-subpolar gyre connection [Burkholder and Lozier, 2014] which inhibits a direct advective inter-gyre pathway for sea-surface temperature

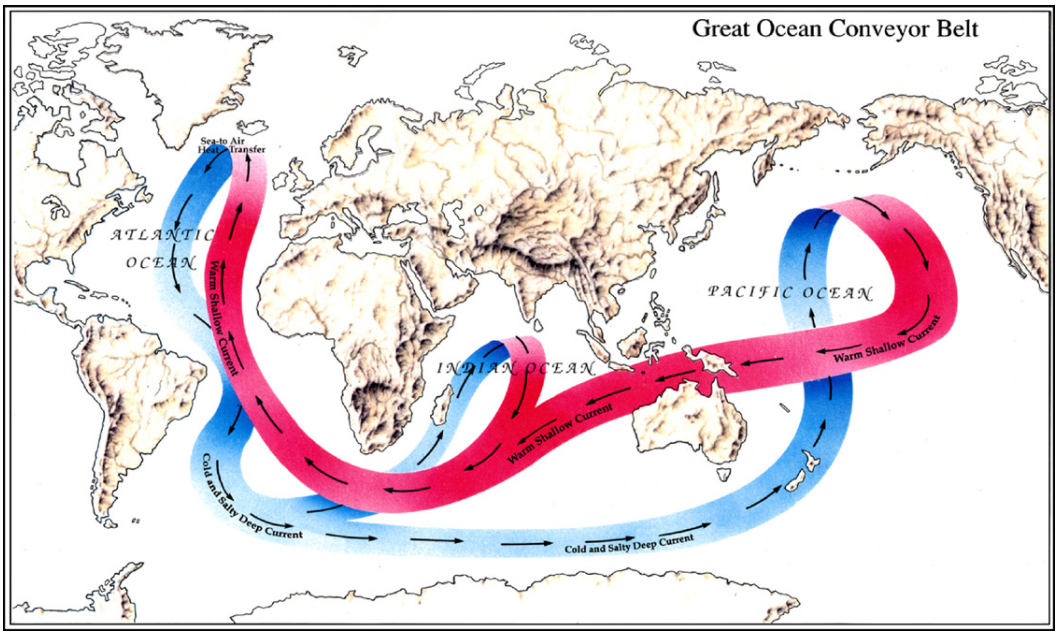

Fig. 1.1 *Broekers simple schematic of the great ocean conveyor belt in a version adopted from Richardson [2008].*

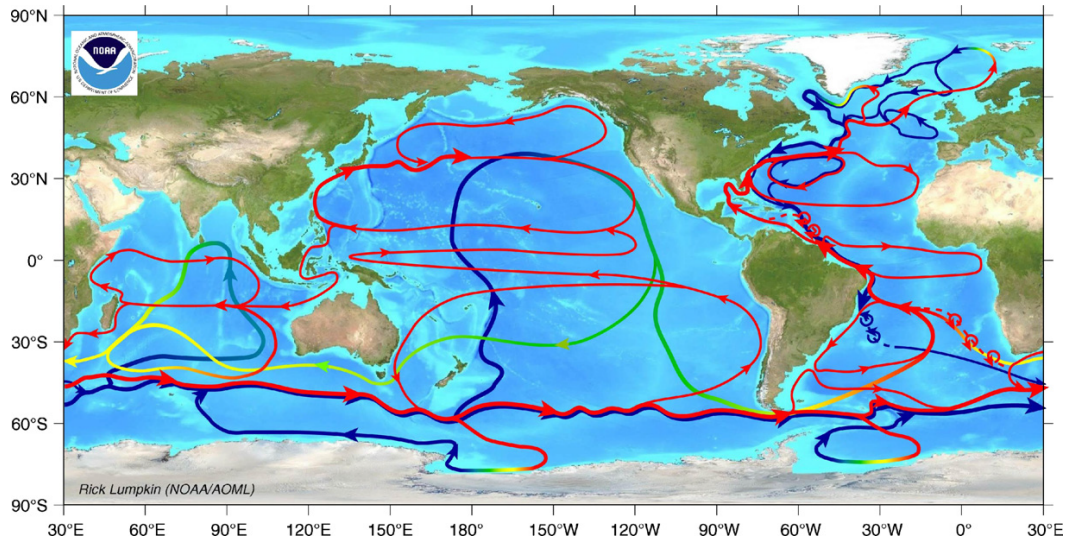

Fig. 1.2 *Schematic of the global overturning circulation as provided by Lumpkin and presented in Richardson [2008], including recirculating loops and large eddies that regionally take over the transport of the upper and deep limbs. Red arrows indicate light upper limb water, blue arrows dense deep (and bottom) waters.*

anomalies [Foukal and Lozier, 2016]. They also indicated that variability in deep water formation rates may not have a direct imprint on the southward advective export of newly formed deep water masses [Zou and Lozier, 2016]. Moreover, the classical view of water mass transformation only happening at distinct deep water formation and upwelling locations is untenable, since eddies have been shown to greatly enhance mixing [LaCasce, 2008] and hence potentially contribute to water mass transformation along all overturning pathways. Above all, variability in the overturning transport has been related to multiple forcing mechanism [Buckley and Marshall, 2016, and references therein], including changes in Southern Hemisphere winds and the eddy-driven inter-ocean exchange south of Africa [Biastoch et al., 2009; Beal et al., 2011; Durgadoo et al., 2013]. To sum up, the large-scale GOC is now accepted as a much more complex system with diverse pathways and less coherent transport of mass and heat that is fundamentally impacted by small-scale flow variability.

However, there are still many open questions to be solved, a particular one being the controversy about the relative importance of the different routes of the return flow feeding the GOC's upper limb in the Atlantic. Even though in dispute since the very first schematics of the overturning have been published [cf. Richardson, 2008, and references therein], there is still no final consensus on whether the colder and fresher inflow through Drake Passage or the warmer and saltier one south of Africa through the Agulhas Current system dominates. Previous studies addressed this issue, mostly, by making use of either inverse box model calculations based on distinct hydrographic data or Lagrangian analysis with coarse or eddy-permitting resolution. Both approaches seem inadequate in light of the fundamental impact of small-scale flow variability on the involved circulation pattern. While box-models by concept have difficulties to account for the eddy-driven inter-basin exchange south of Africa [Donners and Drijfhout, 2004], the Lagrangian analyzes were based on ocean models that did not sufficiently resolve eddies and thus did not feature a realistic representation of the GOC's upper limb return flow south of Africa [Biastoch et al., 2008c]. Hence, there is the need for a revision of the pathways supplying the GOC's upper limb transport in the South Atlantic by means of Lagrangian analysis with high-resolution eddy-rich model configurations. A detailed knowledge of these circulation pattern is also of crucial relevance for assessing potential large-scale impacts of ongoing changes in the Agulhas Current system, such as a strengthening of the Indo-Atlantic exchange [Biastoch et al., 2009; Cheng, 2018].

Acknowledging the important role of small-scale processes for the GOC also evokes another rather conceptual challenge for applications of large-scale Lagrangian connectivity analysis relying on the offline calculation of trajectories from OGCM output. In OGCMs the ocean is described by the so-called primitive equations, which are the Navier-Stokes equations combined with commonly adopted approximations resulting from scale considerations and a nonlinear equation of state that couples the two

active tracers temperature and salinity to the velocities [e.g Madec and NEMO-team, 2016]. Owing to the spatial and temporal discretizations in OGCM formulations, small-scale processes are not fully resolved in the gridded modeled velocity and tracer fields, and are instead parametrized following the turbulent closure hypothesis [cf. Durbin, 2018, and references therein for a review of the development in turbulence closure modeling]. That is, the sub-grid scale processes are formulated as turbulent fluxes (representing the fluxes associated with the mean correlation of small-scale perturbations obtained from Reynolds averaging of the Navier-Stokes equations) that can be expressed entirely in terms of resolved larger-scale features in the form of diffusive processes.

Lagrangian trajectories obtained by the offline advection of virtual fluid particles with the simulated flow of an OGCM only implicitly include the effect of such sub-grid scale parameterizations acting on the tracer and momentum equations through altered large-scale circulation pattern and along-track changes of temperature and salinity. This led to the notion that dispersal of simulated advective Lagrangian trajectories is not sufficiently diffusive compared to: (i) particle dispersal in the real ocean[1], and (ii) online simulated tracer spreading. The latter is directly inferred from the advection-diffusion equation for the tracer evolution evaluated at the integration time-step of the model simulation and thus explicitly includes the effect of the sub-grid scale parameterization, and captures flow features at higher temporal resolution than offline calculated trajectories.

To account for the unresolved physics, Lagrangian diffusion parameterizations were introduced [Griffa, 1996; Berloff and McWilliams, 2002; Monti and Leuzzi, 2010; Döös et al., 2011] and have been already employed in regional ocean circulation studies [de Dominicis et al., 2012; Koszalka et al., 2013; Rypina et al., 2016] (cf. chapter 5). They add an extra stochastic component to the trajectory calculation, even though there is still an ongoing debate about how to specify an appropriate stochastic model and how to fit the associated parameters to a specific OGCM output [cf. Rühs et al., 2018, and references therein].

Before regularly employing Lagrangian diffusion parameterizations also for large-scale connectivity studies, it should be critically discussed which kind of pathways are represented by simulated virtual particle trajectories with and without Lagrangian diffusion parameterizations, to avoid the misuse of one or the other. Moreover, there is the need for more thorough assessments of whether the impact of unresolved small-scale processes on Lagrangian trajectories indeed can be parametrized via a diffusive term and, if so, how much diffusion parameterization is actually needed so that trajectories calculated from a specific OGCM velocity output resemble observed particle or simulated tracer spreading.

[1] Note that this is equal to the notion that the dispersal of simulated advective Lagrangian trajectories is not sufficiently diffusive compared to observed tracer spreading, since Klocker et al. [2012] showed that, for a given velocity field, particle- and tracer-based estimates of eddy diffusivities are equivalent, as long as Lagrangian diffusivities are estimated from a sufficiently high number of trajectories (> 100) and by using their asymptotic and not their maximum values.

1.2 Thesis contributions and structure

As outlined above, there is the need for dedicated large-scale Lagrangian connectivity studies with high-resolution ocean models to further improve our understanding of the spatio-temporal structure of the GOC. Moreover, even though Lagrangian connectivity studies with ocean models are a unique and established tool in physical oceanography, there still exist several open questions regarding their implementation and interpretation. With this dissertation I address several facets of the specific challenges identified in section 1.1 by

(i) reviewing the theoretical background of Lagrangian connectivity studies with ocean models, thereby, contrasting the interpretation of Lagrangian trajectories as volume transport or tracer pathways, highlighting the different usage of pure Lagrangian analyzes and Lagrangian modeling approaches (the latter including diffusion parameterizations), and introducing most common evaluation techniques [chapter 2; partially published in van Sebille et al., 2018];

(ii) investigating large-scale spreading and transformation of water masses associated with the upper limb of the GOC in the South Atlantic [chapter 3; Rühs et al., manuscript in preparation] and Indian Ocean [chapter 4; Durgadoo et al., 2017] by making use of Lagrangian analyzes with high-resolution OGCMs that fully resolve mesoscale flow variability;

(iii) assessing the performance of Lagrangian simulations with OGCM output at different spatial and temporal resolution in the extended Agulhas region with respect to the question whether the offline simulated particle dispersal is sufficiently diffusive compared to observed particle spreading [chapter 5; Rühs et al., 2018].

The theory chapter contains a newly written summary of the review paper on Lagrangian model studies by van Sebille et al. [2018], in particular of those parts to which I contributed, but has been largely adjusted and complemented to better fit the scope of this thesis. The following three result chapters start with a prelude page including an outline of the novelties of the underlying study, the respective reference, as well as a short description of my specific contributions. The main part of each result chapter then consists of either the actual publication in its print version, or the to be submitted manuscript adjusted to the format of this thesis. Hence, each result chapter contains its own specific research questions or hypotheses, a thorough respective literature review, and a discussion of its results. In the final synthesis chapter I summarize and discuss the findings of all previous chapters in terms of answers to the overall research question formulated above and identify what has not or not sufficiently been addressed in this dissertation and may be subject of future studies.

2 Theoretical background of Lagrangian connectivity studies with ocean models

Lagrangian connectivity studies with ocean models comprise the analysis of the fate of virtual Lagrangian particles — representing small fluid parcels, small amounts of tracers, or even passively drifting objects — to identify their pathways, associated timescales and transports between distinct oceanic regions.
Any Lagrangian connectivity study performed with ocean model data consists of two steps: First, the actual calculation of Lagrangian particle trajectories from simulated Eulerian velocity fields, and second, the statistical evaluation of the set of trajectories in terms of connectivity measures.
This chapter gives an introduction to the theoretical concept of Lagrangian particle trajectories, their physical interpretation as volume or tracer transport pathways, and their use in studying the dispersal of drifting objects (section 2.1). It further summarizes the main numerical methods of Lagrangian particle trajectory calculation (section 2.2), as well as their statistical evaluation and validation (section 2.3).

Note that the content of this chapter constitutes a newly written summary of the review paper on Lagrangian model studies by van Sebille et al. [2018], in particular of those parts to which I contributed, but has been largely adjusted and complemented to better fit the scope of this thesis. It now includes, for instance, some best practice recommendations for particle trajectory calculations and a paragraph on water property changes along volume transport pathways.

2.1 What is a Lagrangian particle trajectory?

The fundamental concept behind all Lagrangian analysis is to describe fluid motion as the accumulation of continuum fluid parcel motion. Theoretically, each fluid parcel consists of a microscopic collection of molecules, and its velocity is formally determined as a mass weighted mean of the velocity of all these individual molecules [de Groot and Mazur, 1984]. Practically, by making the continuum hypothesis, a parcel is considered a macroscopically small fluid element (bigger than $1\ \mu m^3$, more than 10^{10} molecules [Olbers et al., 2012]) and labelled by the material coordinate

$\boldsymbol{a}$. The motion of such a material fluid parcel can be described by that of a classical point particle located at the center of mass of the fluid parcel, that is, in terms of its position vector $\boldsymbol{X}(\boldsymbol{a}, t)$ determined by the equations of motion derived from Newton's laws. As the particle moves it traces out a curve in space referred to as a Lagrangian particle trajectory (sometimes also called material pathline in the fluid mechanics literature [Batchelor, 1967]), whereby the particle's mass (or volume for a Boussinesq flow [1]) stays constant. The velocity of the Lagrangian particle is the time derivative of the trajectory, computed with the material coordinate held fixed, and equals the local Eulerian velocity at every point crossed in space and time:

$$\left(\frac{\partial \boldsymbol{X}(\boldsymbol{a}, t)}{\partial t}\right)_{\boldsymbol{a}} = \boldsymbol{v}(\boldsymbol{x}, t) \qquad \text{where } \boldsymbol{X}(\boldsymbol{a}, t) = \boldsymbol{x}. \tag{2.1}$$

To sum it up, a Lagrangian particle trajectory describes the pathway of an imaginary point particle that moves as though it is a small element with constant mass (or volume) of fluid.

A seawater parcel is comprised of fresh water and tracers of other matter, such as salts and biogeochemical components. While a seawater parcel maintains a constant mass (or volume), the concentration of each trace constituent (mass of tracer per parcel mass) is not necessarily constant, since tracers can be exchanged with adjacent seawater parcels through diffusive mixing. But what is diffusive mixing? In principal, the equations of motion are valid for all scales larger than approximately $1\ \mu m$ and the only process not governed by the therein described advection is molecular diffusion, which is negligible for most oceanic problems. This implies that tracer and advective mass (volume) transport pathways can be treated to a very good degree as identical in the real ocean. However, in ocean models the oceanic state is described by averages over much larger spatial (and temporal) scales and the effect of unresolved small-scale motions on tracer mixing is parametrized as diffusive transport. Depending on the model resolution as well as on the research question, this effect may or may not be negligible. Thus, in the presence of non-negligible diffusive tracer mixing, tracer and mass (volume) transport pathways are distinct in model simulations.
The dispersal of drifting objects such as crafts, marine organisms, or plastics is hardly ever purely flow following due to the additional influence of buoyancy, potential wind drag related to the body specific shape and weight, or even active swimming behavior. Hence, considering the argumentation outlined above, it can not be fully described by Lagrangian trajectories. Yet, in cases for which the object of interest

[1] The oceanic Boussinesq approximation assumes that density variations are negligible in the horizontal momentum and mass continuity equations so that therein the in situ density can be replaced with a constant reference density [Spiegel and Veronis, 1960]. This reduces the mass continuity equation to volume conservation, implying that Bussinesq flow has zero divergence. The full density as obtained by the equation of state then only appears in the vertical momentum equation, where it is coupled to gravitational acceleration.

can be approximated as dimensionless and immotile, Lagrangian particle trajectories may reveal and/or explain important dispersal characteristics. Furthermore, the calculation of Lagrangian particle trajectories can be easily expanded to more complex dispersal simulations which are, for instance, accounting for object dimensions in search and rescue applications, or active swimming behavior in biological applications.

2.2 How to calculate Lagrangian particle trajectories?

The basis of Lagrangain particle trajectory calculations is the integration of a discretized version of equation 2.1 for a given simulated Eulerian velocity field. When the nth particle is located at the point $\boldsymbol{X}^{(n)}(t) = \boldsymbol{x}$, one can update its position by

$$\boldsymbol{X}^{(n)}(t + \Delta t) = \boldsymbol{X}^{(n)}(t) + \int_{t}^{t+\Delta t} \boldsymbol{v}(\boldsymbol{x}(\tau), \tau)\, \mathrm{d}\tau, \tag{2.2}$$

However, there are many different ways of performing this trajectory calculation. In particular, one has to decide whether a pure Lagrangian analysis of the Eulerian velocity fields or a Lagrangian (stochastic) modeling approach of particle dispersion is desired, whether to perform the calculations offline or online, whether to use an analytical or time-stepping method for the temporal integration, and how to interpolate the gridded velocity field to an arbitrary point in space and time.

Within a pure Lagrangian analysis virtual fluid particles are simply advected with a simulated oceanic flow. By concept, the resulting advective Lagrangian trajectories capture all (and only) those flow features resolved in the underlying Eulerian velocity fields. Slight deviations may originate from spatial and temporal interpolation of the velocity fields performed prior to the actual Lagrangian calculations in order to reduce discontinuities (cf. discussion below).
To account for unresolved processes, Lagrangian diffusion parameterizations were introduced [e.g., Griffa, 1996; Berloff and McWilliams, 2002; Döös et al., 2011]. These add an additional stochastic component to the right hand side of the trajectory equation 2.2. However, in particular (but not only) for larger scale studies it is still an open question exactly when and how to implement stochastic terms, and introducing stochastic terms may break consistency with the underlying OGCM physics which may not always be desired (cf. section 5).

Online trajectory calculations are performed simultaneously with the ocean model simulation and are thus subject to velocity fields that update at the model integration

time step of only a few minutes or hours (depending on the spatial model resolution). Offline Lagrangian calculations are performed independently of the ocean model simulation and instead make use of stored model velocity output, which is typically available at daily, 5-day or monthly means. It is to note that the results inferred from offline Lagrangian calculations may be highly sensitive to the temporal resolution of the underlying model output [Poje et al., 2010; Blanke et al., 2012; Qin et al., 2014]. On the one hand, volume transports and particle transit times over various current systems seem to be well represented using velocity fields averaged over up to nine days [Qin et al., 2014]. On the other hand, there exist Lagrangian applications such as the analysis of along-trajectory variations of biogeochemical properties that require Eulerian model output at a daily or even hourly resolution [Chenillat et al., 2015].
Even though the online calculation has the advantage of velocity fields at higher temporal resolution, it is only feasible for very idealized, small scale, or coarse-resolution model simulations which can be easily repeated. Long term global scale ocean model simulations at eddy-resolving resolution are extremely costly and thus can not be easily repeated. Therefore, in these cases, the trajectory integration nearly always has to be performed offline. The offline calculation further allows for multiple complementary Lagrangian experiments, forward and backward integrations, and much longer integration times which can be achieved by looping through the original model output [e.g., Döös et al., 2008; Rühs et al., 2013; Thomas et al., 2015; Berglund et al., 2017; Drake et al., 2018]. Yet, looping eventually introduces sharp transitions in the tracer and velocity fields that can cause unphysical jumps in the particle trajectories. Looping thus only yields reasonable results if the Eulerian input fields are not subject to large (model) drift and the jumps in the fields between the end and the beginning are small enough to have a negligible net effect on the particle trajectory characteristics.

The temporal integration of the trajectory equation 2.2 can be obtained via explicit (and implicit) time-stepping, as well as in form of analytical solutions. For a given velocity field, these integration schemes would result in identical trajectories in the continuum, but differ in the discrete numerical implementations due to algorithmic differences and truncation errors.
The most simple explicit time-stepping method is the so-called Euler method, for which the velocity at a given point of the trajectory in space and time is multiplied by a time step Δt. Better accuracy of the trajectories can be obtained by using higher-order methods for the integration of equation 2.2, such as the 4^{th} order Runge-Kutta scheme [e.g., Butcher, 2016], where information of the velocity field at four increments between time steps t_n and t_{n+1} is used. In offline calculations Δt has mostly to be chosen smaller than the interval between consecutive stored velocity fields, thus necessitating temporal interpolation. This temporal interpolation of the velocity fields can be a large source of error, particularly when the interval

with which velocity fields are stored becomes longer than a few days [Valdivieso Da Costa and Blanke, 2004; Qin et al., 2014].
Analytical schemes calculate trajectories for a given steady-state non-divergent velocity field through analytic computation of three dimensional streamtubes [Blanke and Raynaud, 1997], without any intermediate time steps. If the velocity fields are time-evolving, it is possible to subsample them into piecewise steady fields, which are only kept constant in time for the specific period given by the temporal resolution of the input field. Another method allows for analytical trajectories in a time-dependent case that accounts for flow changes across time steps [de Vries and Döös, 2001; Döös et al., 2017]. The analytical integration method is self-consistent, since it respects the local three-dimensional non-divergence of the simulated flow, and thus prevents landfall of particles as long as no additional diffusion parameterization or custom behavior term is added.
Since trajectories are defined on continuous velocity fields (cf. equation 2.2) while ocean models work with discretized grids, where velocities are only known on either vertices or edges of the grid cells [Griffies et al., 2000], computing Lagrangian trajectories also requires spatial interpolation of the velocity fields. For example, on structured grids, the reconstruction of continuous velocity fields is achieved by linear, bilinear, trilinear, or spline interpolation, although more work needs to be done investigating the dependence of Lagrangian simulations on the accuracy of the chosen spatial interpolation scheme.

By now it exist a variety of tools with which Lagrangian particle trajectories can be inferred from modeled Eulerian velocity fields, either analytically or via time-stepping methods and with interpolation schemes of different complexity. To get an overview of the major Lagrangian tools and their specific advantages and disadvantages please refer to van Sebille et al. [2018]. Most tools were build for offline calculations, several allow for the addition of a stochastic component in the calculation procedure. In the end it depends on the research question, as well as on model specific requirements, which tool to use. Based on the discussion of van Sebille et al. [2018], combined with the results of Rühs et al. [2018] (section 5) and Wagner et al. [in preparation], the following is suggested here as a first guidance:

- **Volume transport pathways:** Diagnosing volume transport pathways requires a non-divergent velocity field, such as from a Boussinesq model, and a volume conserving purely advective trajectory integration scheme, such as an analytical one employed in the long established tools ARIANE [Blanke and Raynaud, 1997; Blanke et al., 1999, www.univ-brest.fr/lpo/ariane] and TRACMASS [Döös et al., 2013; Döös et al., 2017, tracmass.org] — without any additional diffusion parameterization or custom behavior terms. Representative sets of volume transport pathways are useful means to study the simulated large-scale water mass spreading and transformation. Even though explicit time-stepping

schemes are not strictly volume conserving, the resulting trajectories may yield a reasonable approximation of the volumetric connectivity (cf. section 2.3.3).

- **Tracer pathways:** To compute tracer transport pathways in the Lagrangian framework, one ideally uses a trajectory integration scheme with diffusion parameterization, that is, a Lagrangian modelling approach. Lagrangian codes allowing for the implementation of diffusion are, for instance, CMS [Paris et al., 2013, github.com/beatrixparis/connectivity-modeling-system] or PARCELS [Lange and van Sebille, 2017, oceanparcels.org]. However, as already indicated above, this approach additionally requires the knowledge of the diffusion tensor, which is a complex function of the often poorly understood subgrid scale flow, and thus a big potential source for errors. Purely advective integration schemes may thus yield reasonable and in some cases even desired approximations of tracer transport pathways if the resolution of the ocean model providing the velocity fields is high enough [e.g., Keating et al., 2011].

- **Object pathways:** Object pathways are not only determined by the oceanic flow field, but additionally greatly influenced by the objects specifications, such as its dimensions, buoyancy, and motility. Therefore, tools employed for the calculation of object pathways need to be able to incorporate object motion relative to the ambient currents, such as additional wind and wave induced drift or directional swimming [Staaterman and Paris, 2014; Phelps et al., 2015]. The respective flexibility in the trajectory calculation is, for instance, provided by PARCELS; other tools like CMS even have some build in modules for the simulation of larval dispersal. For best practice recommendations regarding the simulation and evaluation of larval dispersal see Ådlandsvik et al. [1992]. To get results as closely related to the observed circulation as possible, in many cases output from assimilation models is preferred, such as provided by Copernicus Marine Environment Monitoring Service (CMEMS, http://marine.copernicus.eu/). An additional source of uncertainty in the calculation of object pathways is a limited knowledge of the objects drift properties and behavior. Yet again, as already stated above, in particular in cases for which the object of interest can be approximated as dimensionless and immotile, advective(-diffusive) Lagrangian particle trajectories may reveal and/or explain important dispersal characteristics [e.g., Baltazar-Soares et al., 2014].

2.3 How to evaluate sets of Lagrangian particle trajectories?

In general, one simulated Lagrangian trajectory inherently carries information about the displacement and Lagrangian velocity of one particular virtual fluid particle. It is further possible to store along-pathway salinity, temperature, and biogeochemical tracers (if simulated), obtained from spatial and temporal interpolation of the respective gridded simulated Eulerian fields onto the particle positions; or to tag a particle by a certain initial and/or time-constant value, such as an associated volume transport.
However, in large-scale oceanography we are particularly interested in the spreading of tracers or water masses, defined as huge bodies of seawater with a common formation history, on the basin or even global scale. To simulate such a spreading, one has to account for the immense variety of possible individual particle pathways arising from large scale variability in ocean currents and oceanic turbulence, which requires very large numbers of particles. But even simulating the drift of one particular object requires large numbers of particles to account for uncertainties in the simulations with respect to slight changes in the initial conditions. This is why all Lagrangian model analyzes heavily rely on statistics of large sets of individual trajectories, whereby the determination of the exact number of trajectories required to address a certain question is a non-trivial task (cf. section 2.3.5).

The main tool for the statistical evaluation of sets of Lagrangian particle trajectories in terms of connectivity measures are binning techniques. The most prominent way to visualize trajectory data is to bin particle positions into spatial histograms; The resulting maps of particle density highlight most probable pathways (section 2.3.1). Yet, binning is not limited to spatial boxes as particles can be binned by virtually any variable that can be determined along a particle's path, such as depth, temperature, salinity, density, distance to origin, or time since release. This sort of binning can be useful to assess transit time distributions (section 2.3.2) or along-pathway water mass transformations (section 2.3.4). If each particle is tagged with a transport upon release and that transport is then conserved along the trajectory (cf. section 2.2), a spatial binning (and subsequent summing) of the individual transports can be further used to infer volume transport pattern between distinct oceanic regions (section 2.3.3).
In addition to its usage in directly assessing Lagrangian connectivity between distinct oceanic regions, binning of Lagrangian particle data is also used to infer general oceanic flow characteristics that determine particle dispersal, such as spatially-dependent maps of (eddy) dispersion and diffusivity, Lagrangian (eddy) time and length scales, or Lagrangian Coherent Structures. The concepts of (eddy) dispersion

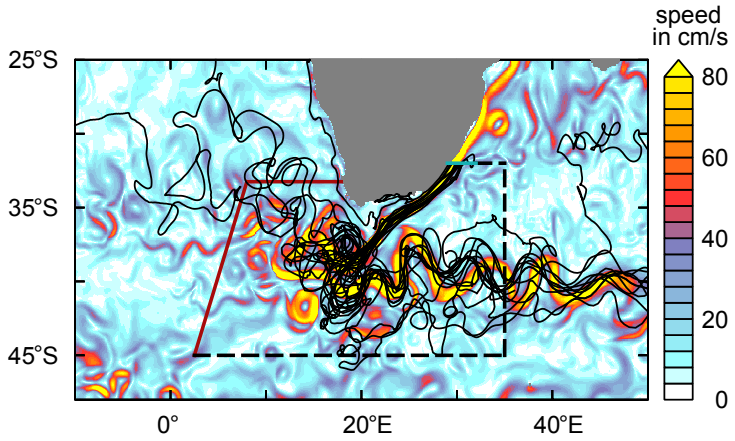

Fig. 2.1 *Exemplary Lagrangian analysis performed with the ARIANE tool using velocity fields from the eddy rich ocean model INALT01 (color shading: snapshot of 5-day mean current speed). Lagrangian particles were released in the Agulhas Current at 32°S (green line) and traced for 5 years towards predefined sample sections and beyond (black lines: exemplary trajectories); particles leaving through the Good Hope section (red lines) were assigned to Agulhas Leakage. Modified after van Sebille et al. [2018].*

and diffusivity and Lagrangian timescales are thoroughly described in section 5. For an introduction to Lagrangian Coherent Structures please refer to van Sebille et al. [2018] and references therein.

The following subsections provide an overview of the different Lagrangian connectivity measures and their implementation in the context of a minimalistic exemplary Lagrangian experiment addressing the Indian to Atlantic Ocean connectivity via Agulhas Leakage. For this Lagrangian experiment the ARIANE tool was applied to the three-dimensional 5-day mean non-divergent velocity fields at eddy-rich resolution (1/10°) obtained from a hindcast (1948 - 2009, experiment identifier KJD308) with the global nested ocean general circulation model configuration INALT01 [Durgadoo et al., 2013]. Lagrangian particles were released in the Agulhas Current (AC) at 32°S (green line in Fig. 2.1) every 5 days for the years 1948 to 2005 proportional to the current volume transport, each particle associated with a fraction of this transport (at maximum 0.1 Sv). Subsequently, the particles were advected along analytically computed 3D time-varying streamlines, representing volume transport pathways, and traced for at maximum 5 years towards predefined control sections and beyond. All particles leaving the domain through the Good Hope section (red line in Fig. 2.1) are accounted for Agulhas Leakage.

2.3.1 Predominant particle pathways

A common way to visualize major spreading pathways of a set of Lagrangian particles is to spatially bin all particle positions [e.g., Hüttl-Kabus and Böning, 2008; Rühs et al., 2013]. The resulting maps of particle density can be further transferred into

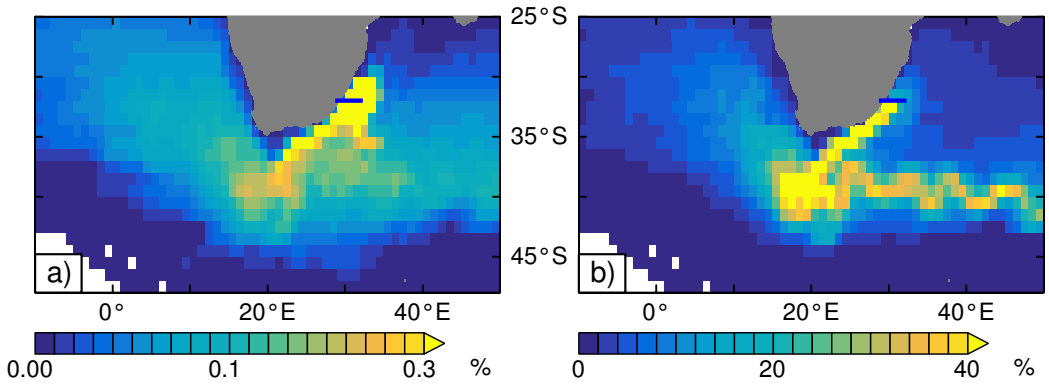

Fig. 2.2 *Major spreading pathways of Lagrangian particles released in the AC at 32°S (blue line) in the year 2000 as part of the exemplary Lagrangian analysis depicted in Fig. 2.1. The pathways are visualized by means of probability distributions inferred from spatial binning of the particle positions (bin size: 1° × 1°, vertical extend over whole water column) by either a) considering all particle positions (counting particles per bin at each time step, summing particle counts over whole integration period, and dividing by the total number of particle counts for all bins), so that the probability of all bins sum up to 100%; or b) considering each particle only once per bin (counting number of different particles reaching each bin during the whole integration period, and dividing by the total number of particles), so that the probability for each bin ranges between 0 and 100%. Modified after van Sebille et al. [2018].*

probability maps through normalising each bin-value by the total number of particle positions [e.g., Gary et al., 2011]. Alternatively we can produce probability maps by counting the visit of a particular particle only once per bin — also called *first arrival mode* — and then normalizing by the total number of particles [instead of the total number of particle positions, e.g., van Sebille et al., 2013; Appen et al., 2014]. All methods offer useful and complementary means to identify flow structures.

Figure 2.2 illustrates the use of both normalizing methods for studying the flow responsible for the spreading of particles originating in the AC at 32°S. Figure 2.2b is showing the probability derived from first arrival mode. Obviously, bins located within the AC downstream of the release section show the highest probabilities, followed by the areas around the Agulhas Return Current (ARC), and the Agulhas Ring corridor. Hence, this probability distribution highlights predominant spreading pathways along the major currents and via mesoscale eddies. Figure 2.2a shows the probability derived from the procedure described at first, that is, by allowing for multiple counts of the same particle in a certain bin (implying that high probabilities may result from many particles and/or slow current speed and/or recirculation pattern). This probability distribution differs from the first one in that it has relatively high values upstream from the release section and in the area between the AC and ARC, but relatively low probabilities within the ARC. In combination, the two probability distributions reveal that (i) the areas in between the AC and ARC and upstream the release section are reached by a small amount of particles several times, most probably due to recirculation pattern; and (ii) there are quite a few particles entering bins located within the ARC, even though they are also leaving them again relatively fast as a consequence of high current speeds.

One consideration in the choice of the bin size of the histogram grid is aliasing. If either the bin size is chosen to small or the period between subsequent stored particle positions Δt_{out} is too long, trajectories may pass through more than one histogram bin within the period Δt_{out} and thus may not be adequately accounted for. As a rule of thumb, at best, one should choose a minimum bin width $\Delta s > v_{max}\Delta t_{out}$, whereby v_{max} is a representative maximum speed of the study domain (Δt_{out} should not be confused with the trajectory integration time step Δt, which in most cases is smaller than Δt_{out}). For instance, for an open ocean region with v_{max} = 0.1 ms^{-1} and trajectory data available every Δt_{out} = 5 days, Δs = 43200 m.

2.3.2 Transit time distributions

The time taken for seawater to transit between defined regions or reservoirs, also referred to as the age of seawater with respect to a region in which its age is prescribed to zero[2], is a property of the flow that provides useful understanding of ocean circulation pattern [Deleersnijder et al., 2001], the overall distribution of temperature and salinity, replenishment rates of nutrients in the upper layers, as well as the uptake and storage of trace gases [Talley et al., 2011].
However, the different Lagrangian particles constituting together a certain water mass may transit between two regions by distinct pathways, traveling for different lengths of time. As such, the age is in fact a probability distribution: the transit time distribution (TTD) that an individual particle might take to travel between the two regions [e.g., Holzer and Hall, 2000; Deleersnijder et al., 2001]. Given a sufficient number of Lagrangian particle trajectories, a TTD between two regions can be estimated from a histogram of individual transit times (see Fig. 2.3 for an examplary TTD in the Agulhas region).
The structure resulting from the mean (first moment), variance (second central moment), width, and modal values of TTDs is used to understand the inherent timescales of ocean circulation. While the width and variance of a TTD capture information on the range and complexity of connecting pathways, the modal value is associated with the most dominant pathway which is followed by the bulk of particles [e.g., Rühs et al., 2013].

Evaluating the time since particles were last within the surface mixed-layer of the ocean yields the ventilation timescale on which the ocean interacts with the atmosphere. It is of particular climatic relevance since, among others, it influences the effectiveness of deep-ocean storage of chemical tracers such as anthropogenic carbon or CFCs. Ventilation timescales have been estimated from Lagrangian ana-

[2] In many studies the age of seawater is uniquely defined with respect to the last surface mixed-layer contact [e.g., Talley et al., 2011], however, I here adopt the broader definition presented in the review of Deleersnijder et al. [2001], and specifically distinguish water ages calculated with respect to zero description at different reference regions, leading to different associated dynamic timescales.

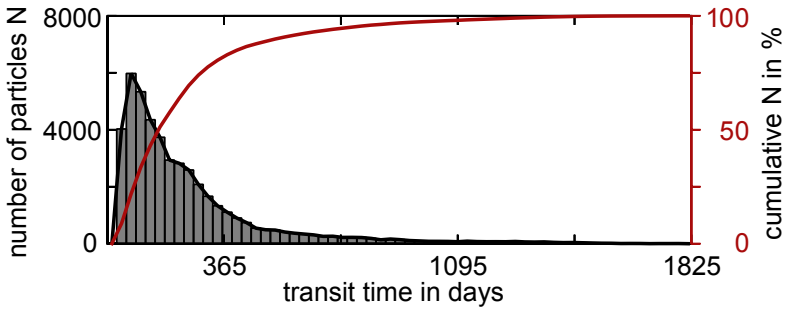

Fig. 2.3 *Transit time distribution for particles released in the AC at 32°S in the year 2000 and traced towards the GoodHope line as part of the exemplary Lagrangian experiment depicted in Fig. 2.1. Modified after van Sebille et al. [2018].*

lyzes for the global ocean [Blanke et al., 2002] as well as for specific water masses [e.g., Gary et al., 2012; Koch-Larrouy et al., 2010].

By considering the entry and exit of Lagrangian particles from a certain reservoir, their transit times can be interpreted as residence timescales. For a marginal sea with one point of exchange, such as the Baltic Sea, this has been used as an alternative to the classic box model approach for the determination of the turnover time [Jönsson et al., 2004] defined as the time it takes to replenish the water (or tracers) of a reservoir [Talley et al., 2011]. Where there are multiple points of exchange, such as the Arctic Ocean, the approach can be used to determine the timescales on which these gateways interact [Lique et al., 2010].

Lagrangian transit times are also used to evaluate possible timescales on which anomalies in a certain region may influence the flow downstream via advection [e.g., Speich et al., 2001; van Sebille et al., 2011; Rühs et al., 2013]. However, it is to note that signal propagation often also happens on so-called radiative timescales which result from wave dynamics and are generally faster than advective timescales. For instance, it has been shown that Agulhas-induced anomalies are conveyed into the western tropical Atlantic via Rossby and Kelvin waves within only a few months — which is several orders of magnitude faster than the estimated advective signal propagation [Biastoch et al., 2008a].

Transit times between distinct oceanic regions are also of major importance for biological connectivity. Many marine species are sedentary as adults and only experience significant dispersal during their larval phase [e.g., Lester and Ruttenberg, 2005]. Thus, under the assumption that larval dispersal is mostly passive, transit times shorter than the estimated larval duration allow for biological connectivity between the regions of interest, whereas much larger transit times most likely prohibit direct biological connectivity.

One difficulty with the determination of TTDs is that the timescale of interest, such as the ventilation timescale of deep waters (which can be on the order of thousands of years), often largely exceeds the length of available OGCM output. Hence,

the velocity fields must be looped to calculate the full TTD, which is practically doable but does not always yield meaningful results (cf. section 2.2). If the available OGCM output at least covers the modal value of the TTD, the full TTD could also be estimated by fitting techniques as done in van Sebille et al. [2011].

2.3.3 Volumetric connectivity

Among the first uses of basin-scale Lagrangian particle tracking was to assess seawater volume transports between distinct sites in the ocean, resulting in an effective way of quantifying Lagrangian connectivity. These applications require that each particle is tagged with a transport upon release, and that this transport is subsequently conserved along the trajectory. One can then reconstruct volumetric connectivity by summing the transports of those particle trajectories that connect selected oceanic sites. Moreover, the associated volume transport pathways can be visualized by the so-called Lagrangian streamfunctions, which can be inferred from transport-weighted binned particle positions.
Figure 2.4 visualizes how these Lagrangian volumetric connectivity measures can be used to determine Agulhas Leakage (based on the Lagrangian experiment described above and visualized in Fig. 2.1). After having calculated volume transport pathways between the AC at 32°S and the predefined control sections, Agulhas Leakage was estimated for each release year by summing the transports of only those trajectories that crossed the approximated GoodHope section (red lines) within maximal 5 years after their release (and normalizing the cumulative transport by the number of releases per year). This method has been extensively used to quantify Agulhas Leakage for various applications [e.g., Biastoch et al., 2008c; van Sebille et al., 2010; Durgadoo et al., 2013].

The concept of volumetric connectivity is closely tied to the analytical integration method and was introduced by Blanke and Raynaud [1997] and Blanke et al. [1999]. If the Eulerian velocity field is locally divergence free — as it is for any Boussinesq flow — and the trajectory calculation scheme respects the volume conservation — as the analytical schemes do — each trajectory can be indeed tagged with a fraction of the current volume transport through a defined 'release' section which stays constant during the integration. In practice, upon release, particles are grouped in regions where the transport is the highest so that no partial transport exceeds a prescribed maximum transport (e.g., 0.1 Sv). This maximum transport determines the accuracy of all derived volumetric connectivity measures [Valdivieso Da Costa and Blanke, 2004].
For the visualization of major volume transport pathways, the volume transports associated with each trajectory are recorded and summed at each grid-wall crossing to yield a three-dimensional transport field. This field can be further integrated

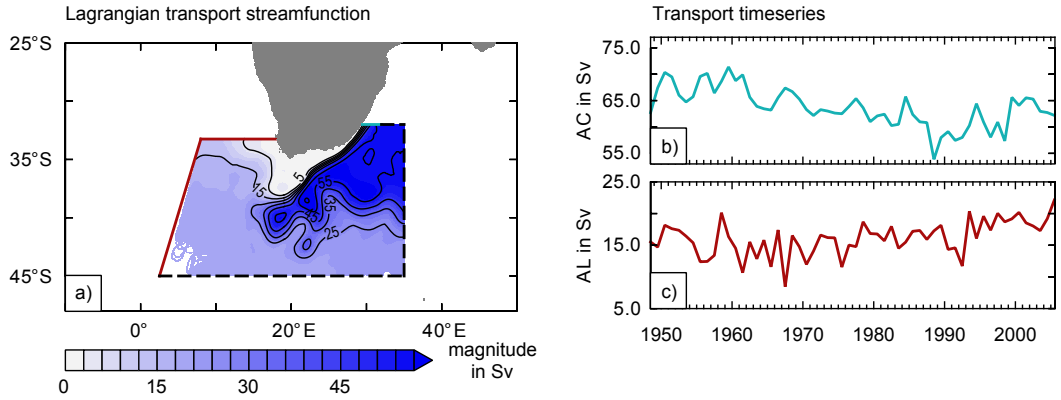

Fig. 2.4 *Quantitative Lagrangian analysis to determine Agulhas Leakage: a) Magnitude of horizontal Lagrangian streamfunction (contours, in Sv) for all trajectories initialized in the year 2000 and traced towards the control sections (black and red lines). b) Time series of the annual mean Agulhas Current (AC) transport at 32°S. c) Estimated time series of annual Agulhas Leakage (AL) transport. Modified after van Sebille et al. [2018].*

vertically (zonally) to a two-dimensional non-divergent field of volume fluxes that finally can be described by the horizontal (meridional) Lagrangian transport streamfunction. The unique feature of these 'conditional' Lagrangian streamfunctions is that they can be constructed for only that part of the flow that connects the section where particles are released with a chosen section where they are received. Subsampling of trajectories allows for any desired flow decomposition. This concept has been applied to study, for instance, the cold and warm water routes into the Atlantic [Speich et al., 2001; Speich et al., 2002; Drijfhout et al., 2003], Indian Ocean sources of Agulhas leakage [Durgadoo et al., 2017], the decomposition of the Deacon Cell [Döös et al., 2008], and the Atlantic MOC [Thomas et al., 2015]. It is noteworthy that the Lagrangian streamfunction is based on trajectories with varying residence times ranging from hours to months or even years, while Eulerian streamfunctions are snapshots or time-averages. Yet, when releasing particles at sufficient resolution at all entry sections into a certain domain and integrating the trajectories until all particles left this domain, the resulting total Lagrangian streamfunction has been shown to be almost identical to the Eulerian streamfunction [Berglund et al., 2017].

Even though integration schemes relying on explicit time-stepping are strictly speaking not volume conserving, a carefully chosen seeding strategy may enable the approximations of volume transport streamfunctions and connecting transports even from advective trajectories calculated with those schemes (van Sebille et al. [2014] used CMS for a volumetric analysis of Pacific-to-Indian Ocean connectivity). In addition to locally non-divergent Eulerian velocity fields and a suited trajectory calculation scheme, further prerequisites for the calculation of Lagrangian streamfunctions are that initial sections are seeded with sufficiently large number of particles proportional to the current local flow strength (to resolve a large number of distinct pathways and adequately sample the flow) and sufficient integration time

is allowed for the particles to leave the domain through the defined final sections (otherwise the constraint of volume conservation would be violated). It also should be taken into account, that, when releasing particles at not only one but several consecutive time steps (in order to account for temporal variability in the flow field), the cumulative transport field arising from all trajectories has to be scaled by the total number of releases.

2.3.4 Water properties modification

From a Lagrangian connectivity perspective, pathways and timescales of the dispersal of virtual fluid particles are easily assessed. Yet, their importance often arise from the tracer (or object) they are transporting. For example, in climate science it is of major concern how different water masses contribute to the freshwater and heat transport through distinct oceanic sections. In addition to direct Lagrangian modeling of tracer spreading (or object dispersal), also Lagrangian analyzes of volume transport pathways can help addressing this issue through recording along-trajectory tracer changes.
As detailed above, the tracer content of a seawater parcel may change along its trajectory through non-negligible diffusive mixing. Dependent on the tracer there may also exist local sources and sinks. In case of temperature and salinity, the characteristics of Lagrangian trajectories representing volume transport pathways may change along their way due to the parametrized and spurious diffusion in the model, as well as through heat and freshwater fluxes at the ocean surface.
The information on the infinitesimal transport as well as the thermohaline properties for each individual particle trajectory at the entrance and exit sections of a predefined study domain allows for the quantification of the net water properties modification within that domain [e.g., Lique et al., 2010; Speich et al., 2007; Rimaud et al., 2012; Chenillat et al., 2015]. A more detailed analysis of the full record of along-trajectory temperature and salinity changes may even be used to infer horizontal pattern of Lagrangian temperature and salinity divergences in order to determine the geographical positions of major water property modifications [Berglund et al., 2017].

2.3.5 Validation of Lagrangian analyzes

The accuracy of Lagrangian trajectories computed from simulated velocity fields depends on the accuracy of the time integration scheme, as well as the accuracy of the interpolation scheme used to estimate velocity at the time and position of the particle. To test the accuracy of a certain calculation scheme one should use idealized and analytical test cases as described in van Sebille et al. [2018] and assess

how well the analytical solution can be reproduced with the implemented schemes. However, this part of validation is mainly performed during the development of a Lagrangian tool and has been, for instance, done comprehensively for the new community tool Parcels [Lange and van Sebille, 2017].

The usual way to assess the robustness of the results of a Lagrangian analysis is to perform the analysis with as many particles as reasonable and then repeat the analysis with a series of subsets of the trajectory ensemble to verify that the results do not change substantially with a different number of particles or different particle launch locations. The number of particles needed to achieve robust results is generally increasing with the complexity of the flow (hence with increasing model resolution) and may change in time and space depending on the spatially and temporally varying mixing [Simons et al., 2013].
To test the robustness of the results with respect to the potential impact of sharp transitions in the tracer and velocity fields introduced by looping (section 2.2), one can perform sensitivity experiments as described in Thomas et al. [2015] in which artificial jumps are introduced and analyzed.
Two methods to quantify differences between, for example, probability maps or transit time distribution, are a pointwise correlation between the binned histograms and subsequent calculation of the fraction of unexplained variance [Simons et al., 2013] and a Kolmogorov-Smirnov statistical test [van Sebille et al., 2009].

Finally, one can evaluate simulated ensemble particle movement against observed surface drifter (or ARGO float) dispersal [van Sebille et al., 2009; Döös et al., 2011; Rühs et al., 2018] or the evolution of a tracer field explicitly computed online in the ocean model [Gary et al., 2012].
Note though that a Lagrangian analysis and the derived connectivity measures are only as 'realistic' as the underlying simulated Eulerian velocity fields which, among others, depends on the temporal and spatial model output resolution — unless a Lagrangian modelling approach is employed in which additional terms are added to correct for missing dynamics in Eulerian fields. However, considering the difficulties associated with the formulation and tuning of such correction terms (cf. section 5), such a 'corrected' approach may not necessarily lead to more realistic results.

3

Study 1: Cold vs. warm water route — sources for the upper limb of the AMOC revisited in a high-resolution ocean model

The major aim of this study was to revisit the relative importance of the different sources for the upper limb of the Atlantic part of the global overturning circulation, that are, waters entering the South Atlantic from the Indian Ocean versus waters entering from the Pacific through Drake Passage, commonly referred to as the warm and cold water routes, respectively. To do so, backward trajectories from the North Brazil Current into the two source regions were calculated by using the simulated velocity fields of a high-resolution (1/20°) ocean model. The Lagrangian analyzes revealed a substantially higher volumetric contribution of waters originating at Drake Passage than estimated by previous Lagrangian analyzes of coarser resolution models. They further highlight that waters with Drake Passage and Agulhas origin can not be unambiguously distinguished by their temperature (as the common terminology may imply), but rather by their salinity when entering the South Atlantic. Moreover, waters of both origins experience substantial water property modifications along their transit through the South Atlantic. A first analysis of temporal changes in the ratio of the two contributions further indicates that an ongoing increase in Agulhas leakage may evoke an increase in the Agulhas contribution to the upper limb of the overturning, while the Drake Passage contribution decreases.

The chapter is written as a manuscript for submission to Ocean Science:

> **Rühs, S.**, Schwarzkopf, F., and A. Biastoch: *Cold vs. warm water route — sources for the upper limb of the AMOC revisited in a high-resolution ocean model*.

My personal contribution to the manuscript has been the following:
defining the research problem and methodology, performing Lagrangian trajectory calculations, analyzing simulated Lagrangian trajectory data sets, producing all figures, and writing the paper.

3.1 Introduction

Within the framework of the global overturning circulation, the South Atlantic is depicted as a conduit, exporting dense waters produced in the North Atlantic into the Indian and Pacific basins, and enabling the return flow of lighter waters back into the North Atlantic which in turn feed the deep water formation [Broecker, 1991; Richardson, 2008]. The resulting net equatorward heat transport within the South Atlantic and thus northward heat transport across the whole Atlantic [cf. Kelly et al., 2014] is unique among all ocean basins and has been long recognized for its importance in modulating European [e.g., Palter, 2015; Moffa-Sánchez and Hall, 2017] as well as global [e.g., Srokosz et al., 2012; Buckley and Marshall, 2016; Lynch-Stieglitz, 2017] climate variability. Even though variability in the overall overturning strength and associated heat transport have been mostly related to variability in deep water formation [e.g., Biastoch et al., 2008b; Yeager and Danabasoglu, 2014], the involved convection process is highly sensitive to the thermohaline properties of the northward upper layer return flow [Haarsma et al., 2011; Garzoli and Matano, 2011; Cimatoribus et al., 2012; Garzoli et al., 2013]. Consequently, a proper knowledge of its characteristics and the processes determining them are crucial for the understanding of variability in the overturning strength.

The northward return flow, that is, the upper limb of the meridional overturning circulation in the Atlantic (AMOC), is supplied by waters entering the South Atlantic south of America (Pacific-Atlantic route) and south of Africa via the Agulhas System (Indo-Atlantic route) [Garzoli and Matano, 2011]. The Pacific-Atlantic route is characterized by cold and fresh waters [Rintoul, 1991] flowing within the ACC through Drake Passage and following the Malvinas Current into the South Atlantic without any intermediate recirculation in other basins. Within the literature it has been also referred to as the direct cold water route [Speich et al., 2001]. The Indo-Atlantic route injects comparatively warm and salty waters into the South Atlantic [Gordon, 1986; Richardson, 2007] in form of large anticyclonic eddies (Agulhas rings), smaller cyclonic eddies, and filaments shed at the retroflection of the Agulhas Current, comprehensively termed Agulhas leakage [de Ruijter et al., 1999; Lutjeharms, 2006]. Agulhas leakage is composed of waters originating from the Indonesian Throughflow [Gordon, 1986; Le Bars et al., 2013], the Tasman leakage south of Australia [Speich et al., 2001; Speich et al., 2002], and waters originating indirectly from Drake Passage through a connection via the Antarctic Circumpolar Current (ACC) and subsequent circulation in the Indian Ocean subtropical gyre [Gordon et al., 1992]. The Indo-Atlantic route is commonly also referred to as the warm-water route [Speich et al., 2001] — even though the various origins of the contributors to the Indo-Atlantic route lead to a substantial range in its characteristics. See Durgadoo et al. [2017] for a comprehensive analysis of the Indian Ocean sources of Agulhas leakage including its thermohaline properties and transformation. Note that some

studies also referred to the indirect Drake Passage contribution as the indirect cold water route.
Due to their remarkably different water properties the ratio of the inflow through the Pacific-Atlantic and Indo-Atlantic routes greatly impacts the characteristics of the South Atlantic water masses and, consequently, the characteristics of those waters feeding the deep water formation.

However, there is no final consensus on the relative importance of the two routes [Garzoli and Matano, 2011]. Gordon [1986] postulated the Indo-Atlantic route to be the major source for the upper limb of the AMOC (warm water route hypothesis), while Rintoul [1991] found only a minor importance of the Indo-Atlantic route and suggested the Pacific-Atlantic route to be the dominant one (cold water route hypothesis). Both hypotheses have been supported by diverse studies since then. For instance, Speich et al. [2001], Holfort and Siedler [2001], Donners and Drijfhout [2004], Speich et al. [2007], and Dong et al. [2011] agreed with the warm water route hypothesis, whereas Schmitz [1995], Macdonald [1998], and Sloyan and Rintoul [2001] favored the cold water route hypothesis. The conflicting views on the relative importance of the two routes have been partially attributed to conceptual (such as slightly diverting definitions of the cold and warm water routes) and methodological differences. Most importantly, Donners and Drijfhout [2004] refuted the majority of studies in support of the cold water hypothesis by arguing that their common choice of using inverse box model calculations based on distinct hydrographic sections is generally not suited to estimate the highly variable and intermittent interbasin exchange South of Africa[1]. Since then, Lagrangian (model) analyzes have become the preferential tool to estimate Agulhas leakage [c.f., Richardson, 2007; Biastoch et al., 2008c; van Sebille et al., 2010] and the warm water route hypothesis has been prevailing. Still, the studies supporting it were mostly based on the evaluation of relatively coarse resolution non-eddying or eddy-permitting ocean model simulations. Besides, various studies [Biastoch et al., 2008c; Durgadoo et al., 2013] have demonstrated that the obtained estimates of the interocean exchange south of Africa is highly resolution dependent. They specifically pointed out that coarser non-eddying ocean models overestimate the strength of Agulhas leakage, thus necessitating a confirmation or revision of the warm water route hypothesis by means of Lagrangian analysis with higher resolution eddy-rich flow fields.
Moreover, despite the general agreement that the knowledge on the characteristic properties and transformation of the waters supplying the upper limb of the AMOC is of fundamental importance — including the individual roles played by surface, cen-

[1]Despite the variable and intermittent character of Agulhas leakage which is generally difficult to capture by discrete observations, the westward Agulhas leakage and strong eastward flow of the ACC partially occurs in the same density range, so that the ACC signal dominates in the derived net cross-section transports.

tral, and intermediate waters — respective thorough analyzes within the Lagrangian framework are scarce [Speich et al., 2001].
Finally, over the last decades, research on (potential) changes in the Agulhas region have become prominent, since (i) it has been shown that changes in the Agulhas region have the potential to influence the strength of the AMOC through different processes on various timescales [Weijer et al., 2002; Knorr and Lohmann, 2003; Biastoch et al., 2008a; Beal et al., 2011]; and (ii) simulations with ocean and coupled ocean-atmosphere models indicate a strengthening of Agulhas leakage over the last decades [Biastoch et al., 2009; Cheng, 2018], though a conclusive observational corroboration is still lacking [Backeberg et al., 2012; Le Bars et al., 2014]. This may be due to the fact that Agulhas leakage also experiences decadal variability most likely related to the Southern Annular Mode [Biastoch et al., 2009] that tend to mask the current increase in leakage. The increase in Agulhas leakage has been attributed to an increase in the Southern Hemisphere westerlies [Durgadoo et al., 2013; Biastoch et al., 2015] and is expected to continue under global warming conditions [Biastoch and Böning, 2013]. A potential related increase of salt input into the South Atlantic and its northward advection could introduce a stabilizing effect on the AMOC, opposing its anticipated weakening due to increasing freshwater input [Beal et al., 2011]. These causalities motivated several Lagrangian studies on the pathways and associated advective timescales of Agulhas waters into the North Atlantic [van Sebille et al., 2011; Rühs et al., 2013]. However, none of these studies investigated possible temporal changes of the connectivity measures or tried to also relate those to potential changes in the Pacific-Atlantic contribution.

In this study we revisit the relative importance of the Indo-Atlantic and Pacific-Atlantic routes for the AMOCs upper limb volume transport and water mass characteristics by assessing Lagrangian connectivity between the North Brazil Current (NBC) at 6°S and the two source regions in a realistic set-up of a high-resolution (1/20°) ocean model. In addition, for the first time, estimates of (potential) decadal changes in the individual contributions are presented. The NBC is chosen as reference region, since it merges all upper and intermediate northward flow of the tropical South Atlantic and thus channels the upper limb of the AMOC in the tropics. It has been further shown that its transport variability captures decadal AMOC changes and may be used as an index for the AMOC strength [Rühs et al., 2015]. Thus, choosing the NBC as reference region also allows for the investigation of potential decadal changes in the ratio of the two contributions.

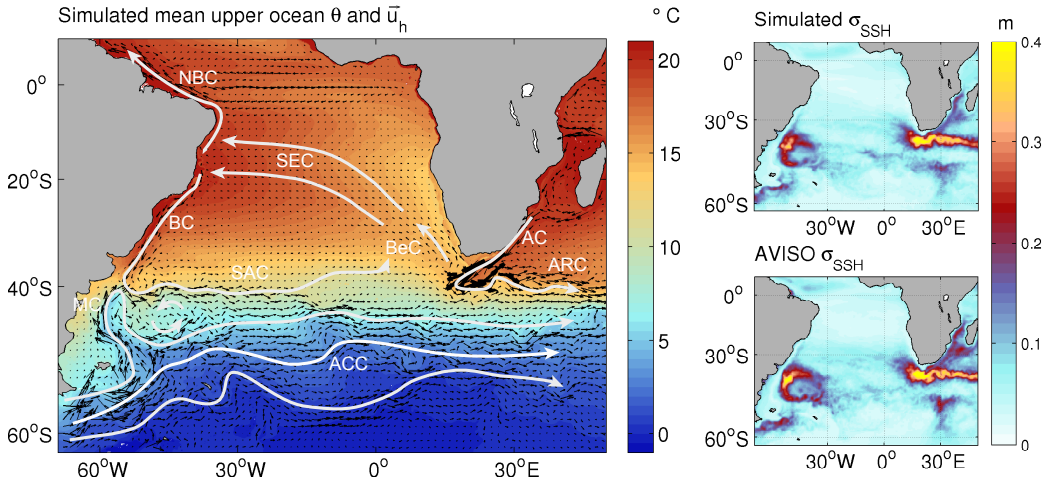

Fig. 3.1 *South Atlantic circulation pattern. (left) Simulated mean (2000–2009) upper ocean (averaged over upper 750 m depth) potential temperature θ (color shading) and horizontal velocity $\vec{u_h}$ (vectors); velocity components have been averaged onto a $1.5° \times 1.5°$ grid for plotting purposes; white arrows highlight major currents of interest for this study: Agulhas Current (AC), Agulhas Return Current (ARC), Benguela Current (BeC), Antarctic Circumpolar Current (ACC), Malvinas Current (MC), South Atlantic Current (SAC), South Equatorial Current (SEC), North Brazil Current (NBC) and Brazil Current (BC). (right) Standard deviation of sea surface height σ_{SSH} from simulations and AVISO (based on 5-day means in 2000–2009).*

3.2 Model data and method

The bases for this study are offline Lagrangian analyzes of simulated three-dimensional time-varying eddy-rich velocity fields. The underlying model simulation and its performance are described in section 3.2.1, whereas in section 3.2.2 the Lagrangian experiment set-up is specified.

3.2.1 Hindcast simulation with eddy–rich ocean model configuration INALT20

The analyzed model output stems from a hindcast experiment (1958–2009) performed with the global nested eddy-permitting to eddy-rich ocean/sea-ice model configuration INALT20, which is a successor of the well-established INALT01 [Durgadoo et al., 2013] with a southward extended and even higher resolution nest. INALT20 was developed within the DRAKKAR framework [Barnier et al., 2014] and consists of an ocean model formulated with the Nucleus for European Modelling of the Ocean [NEMO, version 3.6 stable, Madec and NEMO-team, 2016] coupled to the LIM2-VP sea-ice model [Fichefet and Maqueda, 1997]. The ocean is therein described by the primitive equations, that are, the Navier-Stokes equations along with a nonlinear equation of state, with commonly adopted approximations resulting from scale considerations including the Boussinesq approximation that effectively

reduces mass conservation to volume conservation. It is implemented on a horizontal tripolar Arakawa C-grid [Mesinger and Arakawa, 1976], which is Mercator-type south of 20°N. It has a global horizontal resolution of 1/4°, but is regionally refined between 63°S–10°N and 70°W–70°E via AGRIF two-way nesting [Debreu and Blayo, 2008] to its nominal resolution of 1/20°. This yields an effective resolution of 5.6–27.8 km in the global base model and 2.5–5.6 km in the nest, which allows to fully resolve mesoscale processes [c.f., Hallberg, 2013]. In the vertical it is composed of 46 z-levels, with grid spacing increasing from 6 m at the surface to maximum 250 m at depth. Bottom cells can be partially filled, thus allowing for an adjustment to a more realistic topography, which has been obtained by the interpolation from ETOPO1 [https://sos.noaa.gov/datasets/etopo1-topography-and-bathymetry/] to the respective horizontal resolution.
For the employed hindcast (experiment identifier KFS044), the model was initialized with temperature and salinity fields from the Levitus World Ocean Atlas 1998 [Levitus et al., 1998, https://www.esrl.noaa.gov/psd/]; spun up from rest for 30 years; and subsequently run with forcing from the interannually varying atmospheric fields (temperature, humidity, and horizontal wind components at 10 m height, long- and short-wave radiation, precipitation) of the Coordinated Ocean-Ice Reference Experiments data set version 2 [CORE; Large and Yeager, 2009; Griffies et al., 2009] for the period 1958–2009. Turbulent air-sea fluxes were calculated during the model integration through bulk formula using the prescribed atmospheric state, as well as the simulated sea surface temperatures and relative winds (absolute winds resulted in a slightly improved pattern of eddy kinetic energy, for example, in the Mozambique channel, but unfortunately also lead to too regular Agulhas rings pathways [Schwarzkopf et al., in preparation]). After a range of sensitivity studies, lateral boundary conditions were set to free slip in the base model and no slip in the nest. The momentum equations were discretized using the energy and enstrophy conserving [EEN; Arakawa and Hsu, 1990] advection scheme with Hollingsworth correction and a bi-Laplacian lateral diffusion operator. The evolution of tracers was simulated using the total variance dissipation [TVD; Zalesak, 1979] advection scheme and a Laplacian isoneutral diffusion operator. Viscosity and diffusivity coefficients vary horizontally according to the local grid size and are specified via their maximum values Ahm0 and Aht0, set to -6e9 (-1.5e11) m^4s^{-1} and 60 (300) m^2s^{-1} in the nest (base), respectively. No GM [Gent and McWilliams, 1990] parameterization of baroclinic eddies has been employed, since the horizotal resolution already allows for fully (partially) resolved mesoscale eddies in the nest (base). Vertical sub-grid scale physics have been parameterized using a turbulent kinetic energy [TKE; Gaspar et al., 1990; Madec et al., 1998] dependent closure scheme.

In this study we used the simulated 5-day mean velocity and tracer fields from the nested domain, which show a realistic representation of the mean flow and mesoscale eddy activity in the South Atlantic and adjacent Southern Ocean sector.

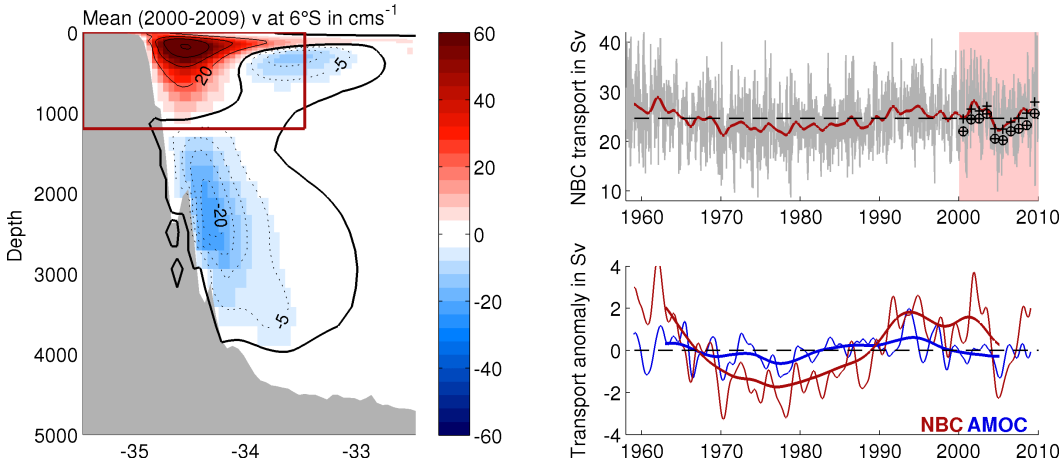

Fig. 3.2 *Simulated NBC and AMOC at 6°S. (left) Mean (2000–2009) meridional velocity v in the western tropical Atlantic; the NBC transport is defined by the integrated positive meridional (= northward) velocities between the coast and 33.5°W, and 0 –1200 m depth (red box). (upper right) 5-day mean (grey) and interannually lowpass-filtered (red) NBC transport time series; annual mean Lagrangian transport estimates without (crosses) and with (crosses in circles) correction for meanders are highlighted. (lower right) Interannual (thin) and decadal (thick) NBC (red) and AMOC (blue) transport anomalies (long-term mean subtracted).*

In the following we highlight those features of largest relevance for this study.
The simulated standard deviation of sea surface height (σ_{SSH}), which is a measure of surface geostrophic eddy variability, agrees well with the observed pattern and magnitude of σ_{SSH} derived from the Archiving, Validation, and Interpretation of Satellite Oceanographic (AVISO) data product (Fig. 3.1, right). In particular, it features the characteristic pattern of high σ_{SSH} at the Brazil-Malvinas-Confluence zone, as well as in the extended Agulhas Current system. It further captures elevated σ_{SSH} in the Mozambique channel, south of Madagascar, and east of Drake Passage. Also the strength and variability of NBC and AMOC are well represented. Figure 3.2 (left) shows a meridional velocity section at 6°S as well as the derived timeseries of the simulated NBC transport, obtained from the integration of the northward velocities between 0–1200 m depth and from the coast to 33.5°W [cf. Rühs et al., 2015, and references therein for a justification of the adopted NBC definition]. One can clearly identify the northward directed NBC with a subsurface maximum, its southward recirculation to the east, and the southward flowing Deep Western Boundary Current underneath. The mean (2000–2009) NBC transport of 25.5 $\pm$ 5.0 Sv (1 Sv $:= 10^6$ m^{3}s^{-1}, uncertainties are given in terms of one standard deviation) falls well into the observed range of 26.5 $\pm$ 3.7 Sv reported by Schott et al. [2005] based on repeated shipboard sections at 6°S (nine section ensemble with individual measurements between 1990 and 2004).
The simulated mean (2000–2009) AMOC strength, defined at each latitude as the maximum of the meridional overturning streamfunction, yields 14.8 $\pm$ 6.3 Sv at 6°S. Unfortunately, the lack of observational AMOC estimates hamper a model verifications at this latitude. Yet, first results of the SAMBA array [Meinen et al., 2013]

allow for some useful quantitative assessments at 34.5°S. Here, the simulated mean (2000–2009) AMOC transport of 13.6 ± 5.0 Sv fits well to the recently published observational estimates of 14.7 ± 8.3 Sv by Meinen et al. [2018] (based on daily data over the 2009–2017 period, with a ∼ 3 year gap from Dec. 2010 to Sep. 2013). The decadal variability of NBC and AMOC (Fig. 3.2, lower right) at 6°S features the characteristics already presented in Rühs et al. [2015]: the NBC and AMOC transports vary roughly in phase with overall decreasing transports in the 1960s and 1970s, and a recovering in the 1980s and the early 1990s, whereby the decadal NBC variability is more than twice as large in magnitude. This suggests that the conclusions of Rühs et al. [2015] also hold for this model simulation, i.e., that the basin-scale decadal variability of the AMOC is indeed captured in the NBC, but is additionally superimposed (and thus masked) by wind-driven gyre-variability.
It is also noteworthy that the model simulation adequately represents the distinct South Atlantic Current (SAC) north of the ACC, as well as the anticyclonic circulation of the Zapiola Gyre (Fig. 3.1, left), while coarser resolution models generally failed to separate the SAC from the ACC and did not resolve the Zapiola Anticyclone [cf. Stramma and England, 1999]. Finally, also the major currents providing the Indo-Atlantic and Pacific-Atlantic inflow of upper limb waters, that are, the Agulhas Current and the ACC, are satisfactorily represented. The mean (2000-2009) transport of the ACC through Drake Passage amounts to 116.2 ± 7.5 Sv. This value is not too far from the absolute transport of 134 ± 11.2 Sv reported by Cunningham et al. [2003], given that they estimated the error of this average transport to be between 15 and 27 Sv. In an accompanying study Schwarzkopf et al. [in preparation] show, that the total simulated Agulhas Current transport compares reasonably well with available observational estimates from the ACE [at 32°S, Bryden et al., 2005] and ACT [at 34°S, Beal et al., 2015] arrays.

3.2.2 Offline Lagrangian analysis of AMOC upper limb pathways with ARIANE

We used the ARIANE tool [version 2.2.6 by Blanke and Raynaud, 1997; Blanke et al., 1999] to perform three sets of offline Lagrangian experiments, one reference set (hereafter REF), and two sensitivity sets corresponding to a strong and weak phase of Agulhas leakage (hereafter highAL and lowAL).
ARIANE is a freely available FORTRAN software that infers Lagrangian particle trajectories from simulated three-dimensional volume-conserving velocity fields saved on a C-grid by advecting virtual fluid particles along analytically computed streamlines. The obtained trajectories thus represent volume transport pathways, which may experience along-track tracer and density changes.
For REF we released virtual fluid particles every 5 days for the years 2000–2009 over the full depth of the northward flowing NBC (0–1200 m depth, coast to 33.5°W) at

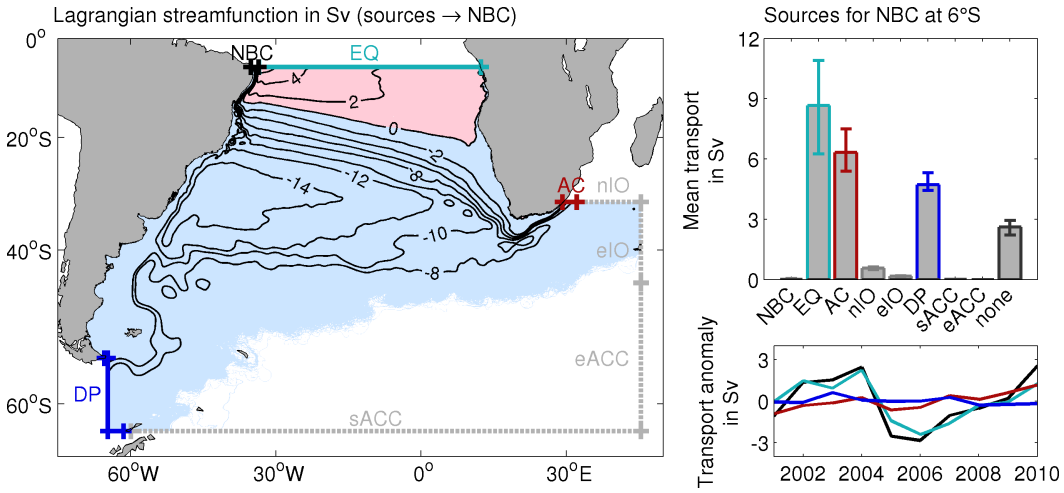

Fig. 3.3 *Sources for NBC transport inferred from the REF set of 10 Lagrangian experiments for which particles were released in the NBC at 6 °S every 5 days for years 2000 to 2009 and then traced backwards in time towards the indicated source sections for maximum 40 years. (left) Mean Lagrangian streamfunction representing volume transport pathways from all source sections towards the NBC. (upper right) Mean volumetric contributions of the individual sources to the NBC; whiskers indicate the range of transport estimates. (lower right) Timeseries of interannual variability of the total NBC transport (black line) and its individual contributions, that are, volumetric contribution of each Lagrangian experiment plotted against the respective release year (colored lines).*

6°S, yielding a set of 10 one-year release experiments with a total of O(10^6) particles. The number of particles seeded at each time step was proportional to the current NBC transport. Each particle was tacked with an individual partial volume transport (max. 0.01 Sv), so that the cumulative transport of all particles released at each time step reflects the current total NBC transport. Subsequently, the particles were advected backwards in time until the point where they entered the study domain through one of the predefined source sections displayed in Fig. 3.3, but at maximum for 40 years. During the trajectory integration the potential temperature and salinity fields were linearly interpolated onto the particle positions.

For the Lagrangian sensitivity experiments we followed the same procedure, but used only velocity fields from selected periods of weak and high Agulhas leakage transports. We released particles in the NBC at 6°S for years 1960–1969 (lowAL) and 2000–2009 (highAL), respectively, and then traced them backwards towards the predefined source sections by looping through the velocity data of each period for at maximum 40 years (instead of making use of the whole simulation period 1958–2009). Even though this looping technique has already been employed by various authors [e.g., Döös et al., 2008; Rühs et al., 2013; Thomas et al., 2015; Berglund et al., 2017; Drake et al., 2018], the obtained results have to be interpreted with caution. Looping may introduce unphysical jumps in the velocity and tracer fields and, consequently, also in the volume transport pathways and along-track tracer changes. Döös et al. [2008] and Thomas et al. [2015] showed that the errors in the pathways introduced by looping can be negligible if a sufficiently high number

of virtual fluid particles is considered and the (model) drift in the velocity fields is not too large (which we achieve by continuously seeding particles over 10 years and looping over a period of only 10 years). However, the analysis of along-track water mass transformation makes little sense for timescales exceeding the period of available data. Therefore, in this study, we employ the looping technique only for estimating sensitivities of the derived volumetric connectivity measures, but not for assessing along-track property modifications.

The highAL and lowAL periods were selected based on the timeseries of Agulhas leakage inferred from complementary offline Lagrangian experiments with ARIANE in forward mode following Durgadoo et al. [2013]: Virtual fluid particles were released in the Agulhas Current at 32 °S every 5 days for the years 1958–2005 proportional to the current volume transport, again each particle associated with a fraction of this transport. Subsequently, the particles were traced for at maximum 5 years towards predefined control sections. All particles leaving the domain through the so-called Good Hope section were marked as Agulhas leakage and their individual transports were subsequently combined to estimate a timeseries of Agulhas leakage referenced to the release year of the particles.

To quantitatively evaluate the pathways of the huge set of individual trajectories we followed Blanke et al. [1999] and calculated Lagrangian transport streamfunctions (Fig. 3.3). These represent time-integrated mean volume transport pathways derived from all trajectories entering and leaving the domain — particles still in domain were not considered (including them would have violated the constraint of volume conservation). Negative and positive values represent anticyclonic and cyclonic circulation pattern, respectively. A bundling of streamlines highlights most prominent pathways, closed streamlines indicate recirculation pattern. Subsampling of trajectories allows to determine conditional pathways, for example mean pathways for only those particles entering the South Atlantic through the Agulhas Current (AC section in Fig. 3.3).

3.3 Results and Discussion

This section first presents a thorough assessment of the Lagrangian trajectory set REF — representing the mean upper limb AMOC connectivity between the Indian/Pacific Oceans and the NBC over the last decades — in terms of a volumetric decomposition (section 3.3.1), transit times (section 3.3.2), volume transport pathways (section 3.3.3), and along-pathway water property modifications (section 3.3.4). It terminates with a short discussion of potential decadal and long-term changes in the derived connectivity measures associated with an increase in Agulhas leakage by a joint evaluation of the two trajectory sets lowAL and highAL (section 3.3.5).

3.3.1 Volumetric decomposition of NBC and AMOC upper limb transport at 6°S

From the Eulerian mean (2000–2009) NBC transport of 25.5 Sv, 2.4 Sv were identified as meanders within the framework of the Lagrangian analysis. Meanders consists of those particle trajectories that enter and leave the NBC section within one Lagrangian integration time-step of 5 days. Subtracting the meander associated transport yielded a new corrected Lagrangian mean (2000–2009) NBC transport estimate of 23.1 Sv (cf. Fig. 3.2, upper right), from which 8.7 Sv (38%) stem from the Equatorial Atlantic (EQ), 6.3 Sv (27%) from the Agulhas Current (AC), and 4.7 Sv (20%) from Drake Passage (DP) (Fig. 3.3). Other inflow sections from the Indian Ocean (nIO and eIO) constitute only a minor source of 0.8 Sv. On average 2.6 Sv could not be unequivocally attributed to one of the predefined sources, since the associated particles did not leave the study domain within the 40 years of integration (see discussion below).

If one examines the individual Lagrangian experiments of REF with 10 different release years, one detects a large interannual variability of the total NBC transport as well as in the individual volumetric contributions of the different sources, which necessitates the adopted strategy of multiple Lagrangian experiments with different release periods (Fig. 3.3, lower right). Most interannual volume transport variability in the NBC is related to variability in the EQ contribution, whereas changes in the AC and DP contributions are less pronounced.

Even though the order of the individual sources according to their total volume transport contribution does remain constant in all experiments and the EQ contribution is always the largest, the relative EQ contribution indeed varies between 31% and 43%. Interestingly, the relative DP contribution varies roughly anti-proportional to the relative EQ contribution, implying a moderation of the associated volume transport changes within the NBC; whereas the relative AC contribution nearly constantly increases from 25% in 2000 to 29% in 2009 (not shown). This increase in the AC contribution could be regarded as an indication that the increase of Agulhas leakage is indeed projected onto the NBC and upper limb of the AMOC in the tropical Atlantic. However, the here discussed Lagrangian analyzes are not sufficient to unequivocally determine a link between Agulhas leakage strength and the AC contribution to the NBC transport. In principle, a larger Agulhas contribution could stem from a preceded increase in Agulhas leakage transport and/or from a higher percentage of Agulhas leakage waters reaching the NBC due to changes in the subtropical gyre circulation — even if Agulhas leakage itself stays constant or decreases [cf. Tim et al., submitted to J. Geophys. Res. Ocean.]. In section 3.3.5, we discuss the possible impact of an ongoing increase in Agulhas leakage on the NBC and upper limb of the AMOC in more detail by making use of lowAL and highAL.

Some uncertainty in our analysis arises from the fact that on average 2.6 Sv of NBC waters could not be attributed to one of the predefined sources after 40 years of trajectory integration. Most particles still in the domain are found in the interior of the tropical gyre, but also a substantial number of particles remained within the subtropical gyre (not shown). This indicates that these particles did not reach any source section within the integration time due to (multiple) recirculation in the respective gyres.
To obtain a first estimate of where these waters may stem from, we extended the integration period for the respective particles to 80 years by cycling through the available velocity data for the period 1958–2009 (similar procedure as for the Lagrangian sensitivity experiments in lowAL and highAL described in section 3.2.2, but by making use of the whole velocity data set instead of restricted time periods). In the additional 40 years of integration, out of the 2.6 Sv, 0.8 Sv could be sampled at the DP, 0.4 Sv each at the AC and EQ, and 0.1 Sv at the IO and other minor southern sections (0.8 Sv still did not reach any section). This suggests that our analysis of the REF experiments with 40 years integration most likely underestimates the AC, EQ, and in particular the DP contribution (further support for this assumption follows below in section 3.3.2).

Of particular interest for this study are those sources contributing to the northward flow of the upper limb of the AMOC, which are the AC, DP, and IO contributions that amount 11.8 Sv when averaged over all Lagrangian experiments in REF[2]. Adding the 1.3 Sv that according to the extended experiments with 80 years of integration most likely also stem from AC, DP, and IO, yields an estimate for the Lagrangian mean upper limb transport at 6°S of 13.1 Sv. This number compares well with the simulated mean (2000–2009) Eulerian AMOC strength at 6°S of 14.8 $\pm$ 6.3 Sv, which gives us some confidence in the validity of our Lagrangian decomposition of the AMOCS upper limb with the NBC at 6°S as a reference point.
Our results — with and without the second integration cycle — seem to generally agree with the prevailing conception that the warm water route is the major source for the return flow. The AC contributions to the AMOCs upper limb transport at 6°S amounts to 53% (6.3 Sv from 11.8 Sv) in REF, and to 51% (6.7 Sv from 13.1 Sv) in the extended experiment. Nonetheless, we also obtained a DP contribution of 40% (4.7 Sv from 11.8 Sv) and 42% (5.5 Sv from 13.1 Sv), respectively, which, at least to our knowledge, is substantially higher than those inferred from all previous Lagrangian model studies investigating the relative importance of the cold and warm water routes. For instance, Speich et al. [2001], Donners and Drijfhout [2004], and

[2]The EQ contribution is not considered as part of the net northward upper limb flow at 6°S, since the southward inflow happens across the same zonal section and in the same depth range as the northward NBC outflow. We attribute this contribution to the more local tropical circulation, acknowledging that the NBC is not only part of the basin-scale AMOC but also of the wind-driven horizontal equatorial gyre circulation and the shallow overturning of subtropical-tropical cells [Rühs et al., 2015].

Speich et al. [2007] only estimated a direct cold water route contribution of 13%, 10%, and 6% respectively. Moreover, the results of section 3.3.5 suggest that the relative importance of the two routes is subject to temporal variability with phases in which the DP contribution indeed may have exceeded the AC contribution.
A possible reason for our remarkably different rating of the relative importance of the direct DP contribution could be the increased horizontal (and temporal) resolution of the underlying model data of this study compared to that of the previous ones. On the one hand, an increased resolution leads to a way more realistic representation of the current structure in the southern South Atlantic. Despite generally enhanced eddy-driven cross-frontal transports it allows for the separation of the SAC from the ACC as described in section 3.2.1, and a more detailed representation of the intricate flow pattern in the Malvinas-Brazil-Confluence zone. All these features potentially influence the existence and strength of the direct DP contribution (cf. section 3.3.3). On the other hand, coarser resolution models are likely to overestimate the AC contribution due to unrealistically high Agulhas leakage (cf. section 3.1), thereby reducing the relative importance of the DP contribution. More dedicated studies are needed to test the sensitivity of the relative DP and AC contributions to the listed factors, as well as to assess the potential impact of details in the model configuration and forcing.
Due to the reasoning outlined in section 3.2.2, for the rest of this study results are based on the REF experiments without cycling of the velocity fields (except for section 3.3.5, where lowAL and highAL are analyzed). Since the majority of DP and AC particles do reach the NBC within the REF integration period of 40 years (cf. section 3.3.2), we are convinced that the general scientific interpretation will not change with increasing integration time, even though exact numbers may do (as demonstrated above).

3.3.2 Transit times towards NBC at 6°S

The transit times of waters from the different sources to reach the NBC are crucial for understanding how these source waters and potential changes therein are transported downstream and thus impact the mean characteristics and variability of NBC waters and the upper limb of the AMOC. Figure 3.4 shows the transport-weighted distributions of the travel times needed by individual particles for the transit from the EQ, AC, and DP sections, respectively.
From the equatorial region the NBC is reached by the majority of particles ($> 50\%$) in less than 3 years, with 1 year being the most frequent transit time (modal value of the transit time distribution), which results from short pathways on which changes can be relatively fast and directly transmitted. This is one reason why interannual variability in the NBC mostly corresponds to variability of the EQ contribution, which is most probably a response to local variability in the wind forcing (cf. Rühs et al.

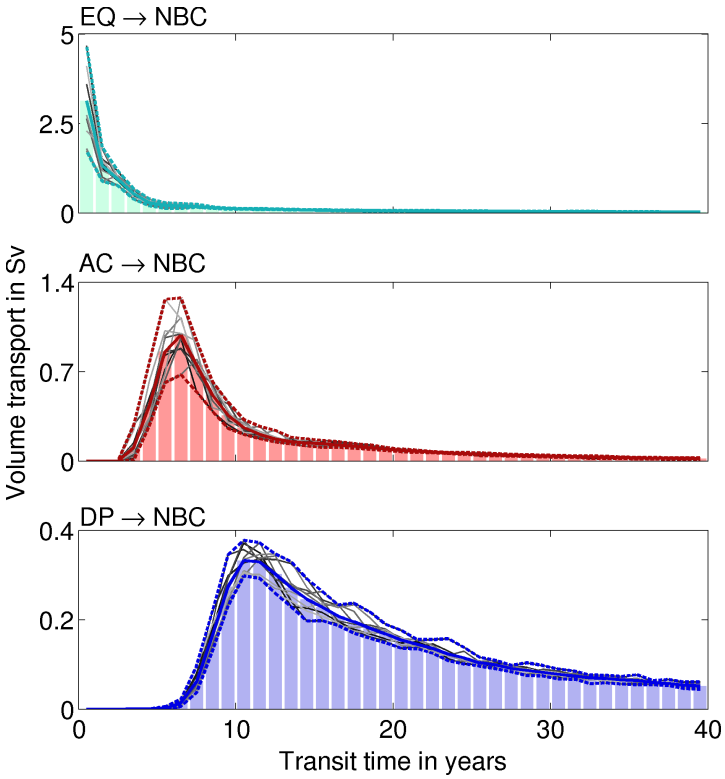

Fig. 3.4 *Transit times from the EQ (upper); AC (middle); and DP (lower) source region towards the NBC at 6°S. Bars and solid coloured lines represent mean transport-weighted transit time distributions, dashed coloured lines indicate the range of the 10 individual Lagrangian experiments in REF (displayed in thin grey solid lines).*

[2015]). From the AC and particularly DP the majority of particles ($> 50\%$) reach the NBC in 9 years and 18 years, and the most frequent transit times are 7 years and 12 years, respectively, hence they need considerably more time. Additionally to the shift to larger time scales the transit time distributions are broadening, in particular for waters with DP origin, representing longer and more diverse connecting pathways. The interannual variability of the volumetric AC and DP contributions thus constitute the accumulation of past changes at the source and potential additional circulation changes along the way. This may impede a direct imprint of variability at the DP and AC sources on the NBC.

The derived transit time distributions for the AC contribution match those derived by Rühs et al. [2013], which is not surprising, since their analysis was based on output from the ocean model configuration INALT01 which is the precursor of the here employed INALT20. As already stated in Rühs et al. [2013] the transit times appear slightly longer than those estimated by van Sebille et al. [2011], even though a detailed comparison is inhibited by differences in the applied methodologies and emphases of the studies. Our derived transit times from DP into the equatorial Atlantic can be compared to the transit times from DP towards 20°N estimated by Speich et al. [2001]. Most notably, they arrived at a multi-modal distribution and interpreted peaks at 19 years and 29 years as the representative time periods needed for DP waters to reach the North Atlantic on a relatively direct path and with one recirculation in the South Atlantic, respectively. The 19 years for the direct path are comparable to our 12 years, if following Rühs et al. [2013] and assuming the transit from 6°S to 20°N to account for another $\sim$ 6 years. But our analysis does not show a

second peak around 29 years. Here, most likely, the big difference in the horizontal and temporal resolution of the employed ocean models is crucial. Our analysis is based on a high-resolution fully eddying configuration, whereas Speich et al. [2001] used a coarse, non-eddying, one. Moreover, we used 5-day mean velocity fields of a realistically forced simulation, whereas Speich et al. [2001] used a monthly climatology. The increase in resolution and allowance for interannual variability most likely lead to more diverse recirculation pathways and associated transit times, thereby disintegrating the second peak in the transit time distribution.
Further note that the shape of the transit time distribution for the DP contribution shows a less distinct modal value and a broader tail than those for the AC and EQ distributions. This supports our assumption (cf. section 3.3.1) that a large part of the particles still in the domain after 40 years of integration probably could be attributed to the DP source and consequently reinforces the importance of the DP as a contributor to the upper limb of the AMOC.

3.3.3 AMOC upper limb pathways in the South Atlantic

In this section we have a closer look at the mean AMOC upper limb pathways in the South Atlantic by investigating the connection from the two major individual sources, that are the DP and AC regions, towards the NBC. This is done by the use of conditional Lagrangian streamfunctions, which were calculated considering only the respective subsets of trajectories and represent the associated net volume transport pathways.
From the Pacific, the majority ($\sim$ 3 Sv) of fluid particles later reaching the NBC through a direct path (without a detour through the Indian Ocean subtropical gyre) is entering the Atlantic through the northern part of DP, then follows a relative narrow path through the Malvinas Current, enters the subtropical gyre through the SAC and flows within the broad South Equatorial Current into the NBC (Fig. 3.5, right) as roughly described in Speich et al. [2001]. However, as already indicated by the relative broad transit time distribution, there are many different pathways for DP waters towards the NBC with different side-tracks: Some particles amounting to $\sim$ 1 Sv follow the ACC into the eastern South Atlantic, eventually making a little detour into the Agulhas region and finally entering the South Equatorial Current via the Benguela Current System. $\sim$ 1 Sv of DP waters is recirculated in the South Atlantic subtropical gyre at least once before finally entering the NBC. A comparison of the DP particle distributions at the NBC section with the local Eulerian mean cross-section velocities shows that DP particles can be found over the whole depth range and zonal extent of the NBC roughly proportional to the local current strength (Fig. 3.6, lower right). The DP particle distribution at the source section however does not directly reflect the Eulerian cross-section flow through Drake Passage (Fig. 3.6, upper right). The eastward ACC transport through Drake Passage is known to occur mainly within

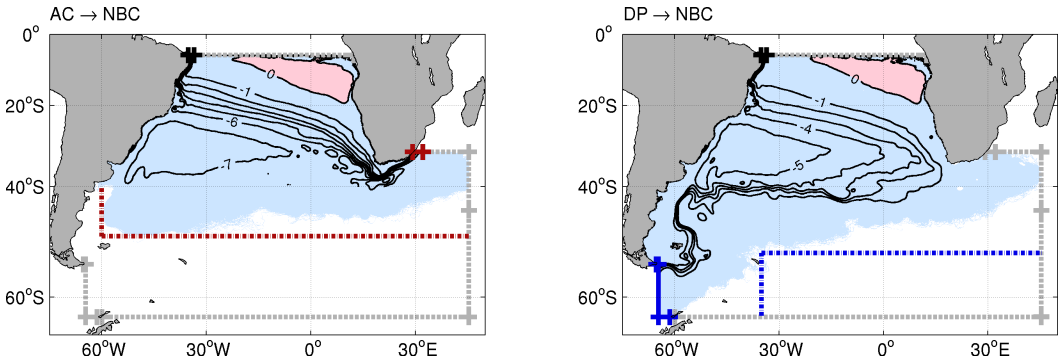

Fig. 3.5 *Mean Lagrangian streamfunction from all 10 Lagrangian REF experiments representing net volume transport pathways between AC (left) or DP (right) and the NBC in Sv; contour intervals of 1 Sv. Red (blue) dashed lines indicate areas from where particles of AC (DP) origin will leave the study domain before contributing to the northward upper limb flow in the South Atlantic.*

two jets corresponding to the Subantarctic Front and the Polar Front [Cunningham et al., 2003; Firing et al., 2011]. These two maxima are captured in the model simulation, but only from the northern one virtual fluid particles may directly enter the subtropical gyre and contribute to the South Atlantic branch of AMOCs upper limb. Particles that follow the ACC south of 53°S eastward beyond 35°W have zero chance to enter the subtropical gyre before leaving the Atlantic sector of the Southern Ocean south of Africa towards the Indian Ocean sector (at least in this model study). These imaginary borders also define the separation between the direct and indirect cold water route, which is located more eastern than reported by Speich et al. [2001] who identified it at about 50°S and 50°W. This difference is most probably again related to more diverse pathways in our higher resolution model simulation.

From the Indian Ocean the dominant volume transport pathway towards the NBC is from the AC via Agulhas leakage into the South Equatorial Current (Fig. 3.5, left), as already extensively described in previous studies [e.g., van Sebille et al., 2011; Rühs et al., 2013]. Some recirculation ($\sim$ 1 Sv) may occur in the subtropical gyre and in the Agulhas region itself. In terms of the depth distribution we get a similar picture as for the DP contribution: AC waters contributing to the NBC enter as surface and intermediate waters and later occupy the whole depth range of the NBC (Fig. 3.6, left). But in contrast to the DP contribution, waters later reaching the NBC also stem from the whole longitudinal range of the Agulhas Current. Particles stemming from the AC and eventually entering regions south of 50°S or west of 60°W do not reach the NBC.

A direct comparison of the pathways and depth distribution of the AC and DP upper limb contributions yields the following: Waters of both contributions enter the Cape Basin, follow the South Equatorial Current and are prone to eventual recirculation in the South Atlantic subtropical gyre, hence, they share part of their pathways. However, even though DP and AC waters can be found over the whole latitudinal and depth range of the South Equatorial Current, the bulk of DP waters is concentrated

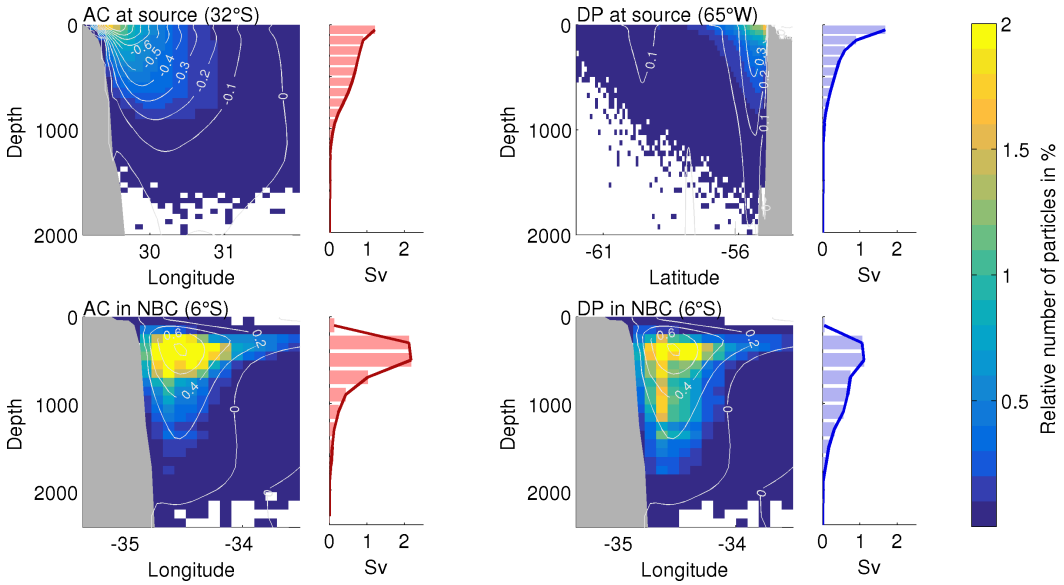

Fig. 3.6 *Depth distribution of REF particles at their source section and upon arrival in the NBC. Relative number of particles, i.e. local count divided by the total number of particles in the respective subset, from all 10 Lagrangian experiments per 0.1° × 50 m bin in % (color shading) with overlaid mean (2000-2009) Eulerian cross-section velocities in ms^{-1} (light-grey contours, contour interval at source 0.1 ms^{-1}, in NBC 0.2 ms^{-1}), and mean cumulative Lagrangian volume transport per 100 m depth bin (bar graphs) for AC waters at source (upper left); DP waters at source (upper right); c) AC waters in NBC (lower left); and d) DP waters in NBC (lower right).*

in a more southern (Fig. 3.5) and deeper (not shown) branch than the bulk of AC waters. Upon arrival in the NBC, waters with AC origin dominate in the upper 400 m the AMOC related volume transport, whereas below 400 m the DP contribution is stronger (Fig. 3.6) .

The shared pathways of waters with DP and AC origin have important consequences for the associated heat and freshwater transports, since they eventually allow for interior mixing of the two contributions and hence for water mass transformation, which is investigated in the following section.

3.3.4 AMOC upper limb water properties transformation within the South Atlantic

Figure 3.7 (left) visualizes the mean temperature (T) and salinity (S) characteristics of DP and AC waters at their respective source and within the NBC by means of histograms of Lagrangian particle frequency in TS space (0.5 °C × 0.05 psu bins). In their source regions, the DP contribution is relatively fresh (32.25–34.75) and cold (−2–11.0 °C) with potential density anomalies ($\sigma_\theta = \rho_\theta - 1000 kgm^{-3}$, in the following units are dropped for better readability) between 25.9 and 27.8, whereas the AC contribution is more salty (34.30–35.75) and spans a broader temperature range (2.5–29.0 °C) with σ_θ between 21.7 and 27.7. Note that there is no clear

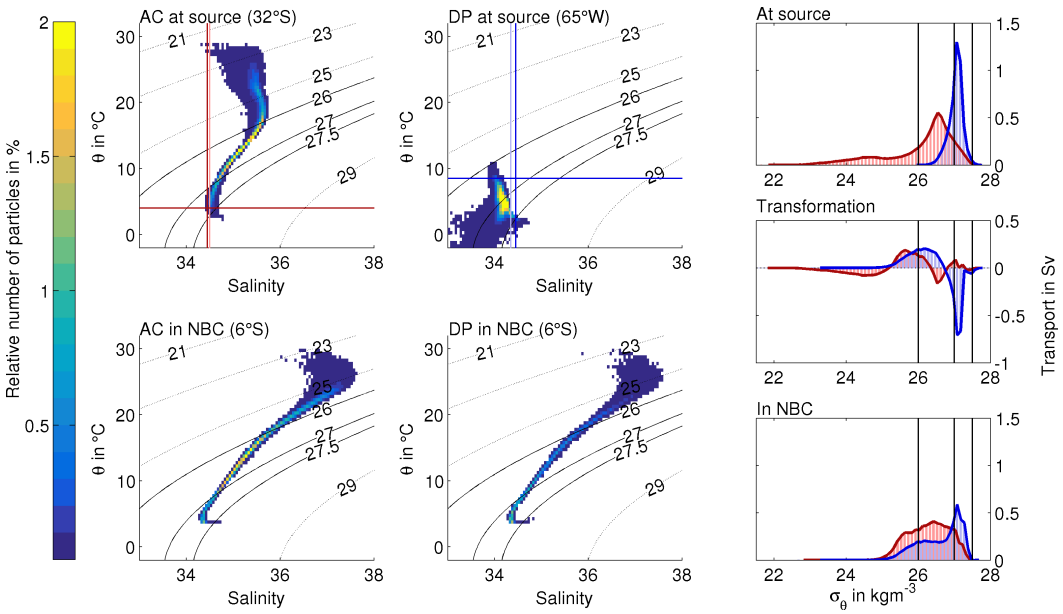

Fig. 3.7 *Mean potential temperature (θ) and salinity (S) characteristics, as well as transformation in density space of waters with AC and DP origin. (left, middle) Relative number of particles, i.e., local count divided by the total number of released particles in the respective subset, from all 10 Lagrangian experiments per 0.5 °C × 0.1 psu bin. (right) Mean volume transport per density class (in 0.1 kgm^{-3} bins) at source regions and in NBC, as well as volumetric water mass transformation (red: waters of AC origin, blue: waters of DP origin). Potential density levels used to separate surface, central, intermediate (and deep) waters are highlighted by solid black lines; dark blue (dark red) lines mark T and S values that constitute the upper (lower) limit for 99% of the DP (AC) water volume.*

separation of the two sources in temperature as the terminology *cold and warm water routes* may imply, since the AC contribution does not only consist of warm surface waters, but also of colder central and intermediate waters [Beal et al., 2006; Biastoch and Böning, 2013]. In our Lagrangian model analysis 99% of the DP (AC) contribution originally has temperatures colder (warmer) than 8.5 °C (4.0 °C) and 75% (11%) of DP (AC) waters can be found in the respective shared temperature range from 4.0 °C to 8.5 °C. However, the AC and DP water contributions can be well distinguished by the salinity in their source regions: 99% of the DP (AC) contribution originally has salinities lower (greater) than 34.45. Thus we may consider *fresh and salty routes* as an alternative more precise terminology, even though we would still recommend referring directly to the geographic origin to avoid ambiguities. Upon arrival in the NBC, fluid particles with DP origin cover nearly the same TS spectrum as those particles with AC origin, that are, temperatures from 3.5 °C to 30.0 °C and salinities from 34.25 to 37.60 (34.25 to 37.65 for AC waters), with corresponding σ_θ from 22.7 to 27.6 (23.0 to 27.6 for AC waters). The comparison of the initial and final TS spectra shows that substantial water mass transformation does occur on the transit through the South Atlantic. The bulk of waters entering the South Atlantic through AC and DP that later reach the NBC becomes more salty during the transit. Waters of DP origin additionally experience a substantial broadening of their

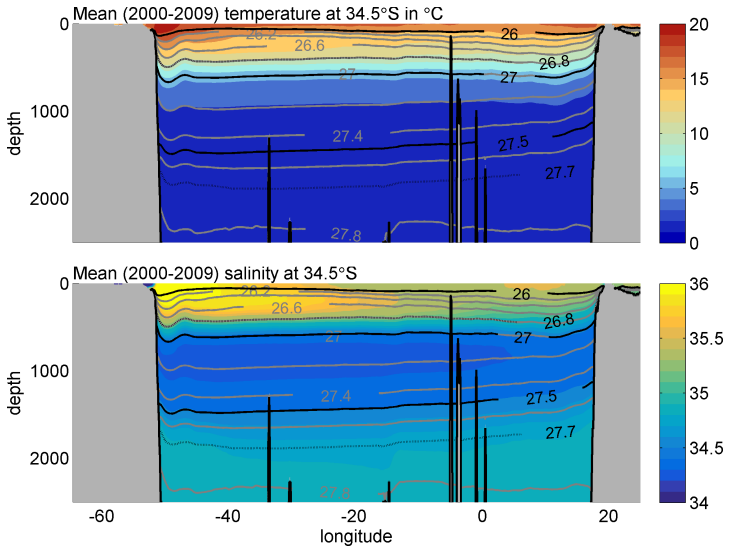

Fig. 3.8 *Mean (2000–2009) simulated Eulerian (upper) potential temperature θ, and (lower) salinity sections at 34.5°S (color shading). Potential density anomalies are overlaid in grey contours, those used as separation of surface, central, intermediate, and deep waters are printed in black.*

		in AC				in DP			
		surface	central	interm.	Σ	surface	central	interm.	Σ
in NBC	surface	(1.2)	0.0	0.0	1.2	(0.0)	0.5	0.4	0.9
	central	0.8	(3.4)	0.2	4.4	0.0	(1.0)	1.3	2.3
	interm.	0.0	0.3	(0.4)	0.7	0.0	0.1	(1.4)	1.5
	Σ	2.0	3.7	0.6	6.3	0.0	1.6	3.1	4.7

Tab. 3.1 *Net water mass transformation of surface, central, and intermediate waters with AC and DP origin between their entry into the South Atlantic and arrival in the NBC in Sv; water volumes without any net transformation into a different class are additionally listed in brackets.*

temperature spectrum associated with a general warming.

These property modifications are also eventually associated with water mass transformations in density space. To quantify those we binned the partial transports of all particles according to their potential density anomaly at their origins and upon arrival in the NBC, for each contribution separately (Fig. 3.7, upper and lower right). Then we compared the transport-weighted density distributions at the entry sections and the respective distributions in the NBC. The difference between the initial and final distributions quantifies the net transformation of the bulk of water (Fig. 3.7 , middle), which may be a result of multiple modification processes.

We additionally repeated this analysis for respective subsets of surface ($\sigma_\theta < 26.0$), central ($26.0 < \sigma_\theta < 27.0$), and intermediate ($27.0 < \sigma_\theta < 27.5$) waters. The exact numbers for the transformation analysis of the different classes depend on the applied density criteria. Here we chose to follow Macdonald [1993] and Holfort and Siedler [2001] for the definition of the separation of central and intermediate waters, since it fits to the simulated mean (2000-2009) thermohaline structure of the water column in the South Atlantic (Fig. 3.8). Other authors following Roemmich [1983] chose σ_θ =26.8, but in our simulation waters with $26.8 < \sigma_\theta < 27.0$ seem to fall in the central water range with a still relatively large vertical gradient in temperature and salinity. The general tendencies of our transformation analysis stay robust with respect to small changes in these criteria (not shown), so that the results are worth

a discussion.
The AC contribution to the upper limb of the AMOC originally consisted of 2.0 Sv surface, 3.7 Sv central, and 0.6 Sv intermediate waters. These waters showed a net transformation to 1.2 Sv surface, 4.4 Sv central, and 0.7 Sv intermediate waters upon arrival in the NBC. More specifically, 40% (0.8 Sv) of the surface waters became central waters, 8% (0.3 Sv) of the central waters became intermediate waters, and and a third (0.2 Sv) of the intermediate waters became central waters (Tab. 3.1). Hence, the bulk of AC waters experiences a slight net density gain during the transit towards the NBC.
The DP contribution to the upper limb of the SAMOC originally consisted of 1.6 Sv central, and 3.1 Sv intermediate waters. These showed a net transformation to 0.9 Sv surface, 2.3 Sv central, and 1.5 Sv intermediate water upon arrival in the NBC. More specifically, 31% (0.5 Sv) of central waters became surface waters (6% became intermediate waters), and 55% (1.7 Sv) of the intermediate waters became central or surface waters (Tab. 3.1). To sum it up, in contrast to AC waters, the bulk of DP waters experiences a net density loss during the transit towards the NBC.

Changes of temperature and salinity and thus density along volume transport pathways generally correspond to the mean effect of surface fluxes, such as direct warming by solar heat flux or precipitation and evaporation processes, and mixing with ambient waters due to parameterized and spurious tracer diffusion of the OGCM. The fact that both DP and AC waters show a salinification during their transit implies that they do not only mix with each other, but that mixing with other ambient waters and/or surface fluxes may play an important role, too.
To further investigate the transformation in the bulk AC and DP water volumes occurring during the transit and to determine their origin, we assessed which particles reached the mixed layer on their transit between the DP or AC and the NBC, and then investigated the net transformation of waters with and without mixed layer contact separately. In particular, we compare transport-weighted density as well as temperature and salinity distributions at the entry sections and the respective distributions in the NBC. Following the criterion used during the OGCM integration and also adopted in comparable Lagrangian studies [cf. Tim et al., submitted to J. Geophys. Res. Ocean.], we assume a particle having reached the mixed layer if its density (that equals the ambient density) differs by less than 0.01 kgm^{-3} from the density at 10m depth.
During the transit through the South Atlantic the surface mixed layer is reached at least once by 66% (3.1 from 4.7 Sv) and 49% (3.1 from 6.3 Sv) of DP and AC waters, respectively. That implies that these waters do gain their specific characteristics within the South Atlantic and — if adopting the common definition of a water mass as a body of water with common formation history — are strictly speaking not water masses with Indian Ocean or Pacific origin as may be suggested by their prior classification as AC or DP waters. Figure 3.9 maps the frequency distribution of the

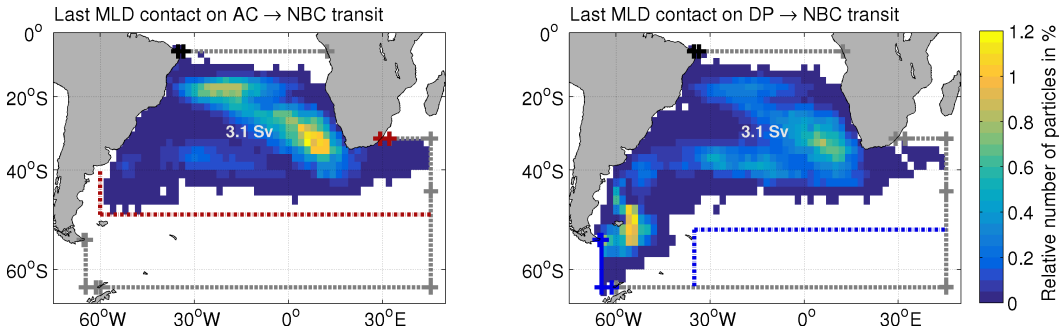

Fig. 3.9 *Horizontal distribution of the position of the last mixed layer contact for particles on the transit between AC (left) or DP (right) and NBC. Relative number of particles, i.e. local count divided by the total number of particles from all 10 REF experiments in the respective subset that are entering the mixed layer at least once during their transit, per 2° × 2° bin in % (color shading); Mean cumulative transports of particles reaching the mixed layer at least once during transit are printed in white.*

position of the last mixed layer contact for particles on the transit between AC (left) or DP (right) and the NBC. Regions of high frequency can be interpreted as the most probable formation regions for water masses of the NBC within the South Atlantic. Those can be found in the vicinity of the different mode water formation regions as depicted in [Hanawa and Talley, 2001], in particular in the eastern subtropical gyre where eastern subtropical mode water (ESTMW) is formed, and east of the Drake Passage (north of the Subantarctic Front) where Subantarctic Mode Water (SAMW) originates. Notably, the formation region of classical Subtropical Mode Water (STMW) located east of the western boundary current, that is the Malvinas Current, does not stand out in the frequency distribution, which suggest that STMW is no major contributor to NBC waters in the analyzed model simulation. Possible explanations for this could be that (i) the formation location of STMW is located more to the central southern boundary of the gyre where indeed some higher frequency can be observed (and which would fit to the new observational estimate of STMW thickness by Tsubouchi et al. [2016] yielding largest values between 40°W and 20°W), and/or (ii) most STMW gets re-entrained into the mixed layer in the eastern subtropical gyre and thus becomes itself part of the ESTMW. In any case, our findings match those of [Tim et al., submitted to J. Geophys. Res. Ocean.], who analyzed the same model simulation and found an only minor direct South Atlantic Central Water but strong eastern South Atlantic Central Water contributions to the upwelling water masses of Benguela. Relative high frequencies of last mixed layer contacts are further located at the subduction zones along the South Equatorial Current and in particular around 15°S, which have been shown to be important source regions for the equatorward subsurface flow related to the shallow overturning of the subtropical cell in the South Atlantic [Zhang, 2003; Schott et al., 2004; Hazeleger and Drijfhout, 2006].

The mixed layer contact of virtual fluid particles on their transit between the AC or DP and the NBC greatly impacts their characteristic properties. Most notably,

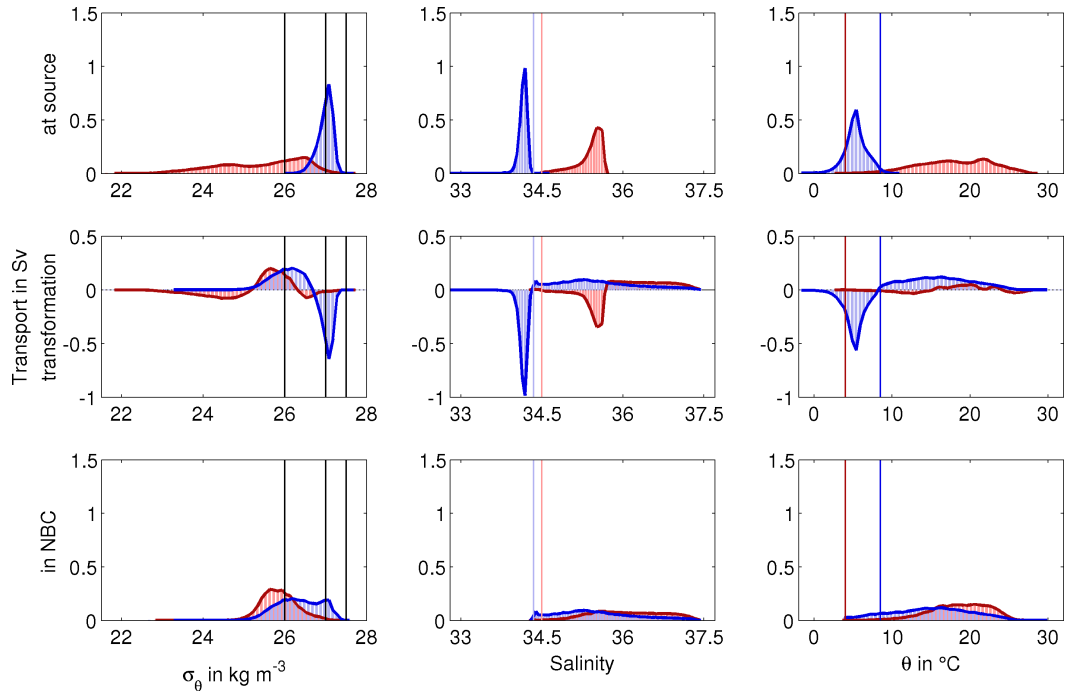

Fig. 3.10 *Mean transformation of waters with AC and DP origin that enter the mixed layer at least once during their transit. Mean volume transport per density (left, 0.1 kgm^{-3} bins), salinity (middle, 0.05 psu bins), and temperature (right, 0.5 °C bins) class at source region (upper) and in NBC (lower), as well as volumetric water mass transformation (middle) for waters of AC (red bars) and DP (blue bars) origin. From all 10 Lagrangian experiments only particle trajectories with at least one mixed layer contact during their transit are considered. Potential density levels used to separate surface, central, intermediate and deep waters are highlighted by solid black lines; dark blue (red) lines mark θ and S values that constitute the upper (lower) limit for 99 % of the DP (AC) waters, light blue (red) lines represent the 95 % limit (cf. Fig. 3.7).*

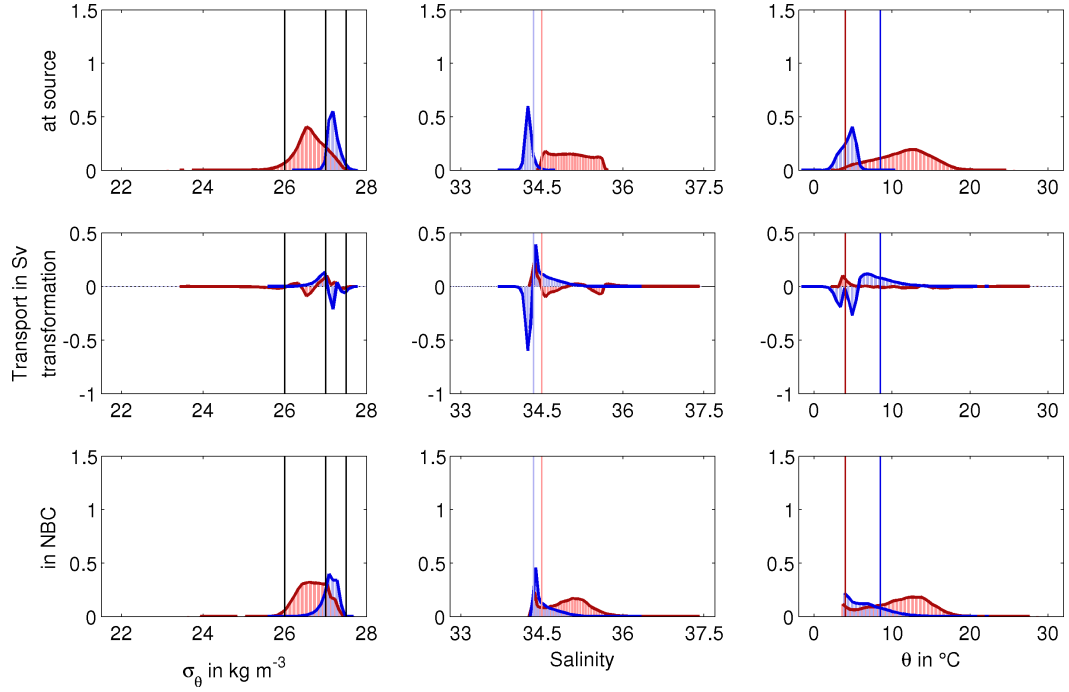

Fig. 3.11 *Same as Fig. 3.10 but for waters with AC and DP origin that that do not enter the mixed layer during their transit.*

the net transformation in density space of DP and AC waters (Fig. 3.7) is almost completely captured by those particles with mixed layer contact (Fig. 3.10), whereas water property modifications associated with particles without mixed layer contact are characterized by only minor changes in density space (Fig. 3.11).

Nearly all DP particles entering the South Atlantic in the central water range (see discussion above) and more than half (1.6 from 3.1 Sv) of those entering in the intermediate water range reach the mixed layer at least once during their transit. The bulk of these DP waters with mixed layer contact experience a substantial salinification (when entering the Atlantic 95% of the waters have salinities < 34.45, whereas upon arrival in the NBC 95% of the waters have salinities > 34.45) but even stronger warming during the transit. This results in a net decrease in density and in a corresponding shift towards central and surface waters. From the AC contribution, the particles entering the South Atlantic as surface waters, as well as 30% (1.1 from 3.7 Sv) of those entering as central waters reach the mixed layer during their transit. They enter the South Atlantic at a large range of relatively high temperatures which hardly changes during the transit. However, as DP waters, AC waters with mixed layer contact experience a net salinification, resulting in a net increase in density. Since this coherent increase in salinity of AC and DP waters can not be found for waters without mixed layer contact, we attribute the salinification to the impact of on average net evaporative surface fluxes over the subduction zones along the South Equatorial Current, as well as to mixing with ambient subtropical upper layer waters with high salinities.

Nearly half (1.5 from 3.1 Sv) of the DP waters that are entering the South Atlantic as intermediate waters, as well as nearly all intermediate and 70% (2.6 from 3.7 Sv) of the central AC waters do not experience any mixed layer contact during their transit towards the NBC. Interestingly, AC and DP waters without mixed layer contact show opposite transformations in temperature and salinity: DP waters are warming and becoming more saline, whereas AC waters are cooling and freshening. As a result the salinity and temperature distributions of both components show new common peaks in the temperature and salinity distributions, at 3.5–4.0 °C and 34.35–34.40, respectively. This result fits to the idea that intermediate and central waters of western and eastern Atlantic origin mix in the eastern South Atlantic and form new specifications of central and intermediate water (water masses in the same density range but with different temperature and salinity characteristics), as specifically shown by Rimaud et al. [2012] for different specifications of Antarctic Intermediate Water.

3.3.5 Potential decadal changes in AMOC upper limb connectivity measures

Figure 3.12 gives a first impression on the possible sensitivity of the volumetric NBC decomposition to the strength of Agulhas leakage. The underlying data stems from the two additional sets of Lagrangian experiments for which particles were released in the NBC at 6°S for years 1960 to 1969 (lowAL) and 2000 to 2009 (highAL), respectively, and then traced backwards towards the source sections (cf. Fig. 3.3) by cycling through the velocity data of each period for at maximum 40 years (more details on the experiments can be found in section 3.2.2).

We chose the 1960s and 2000s for our comparison, since both periods feature the same simulated Lagrangian mean NBC transport (23.1 Sv) and comparable upper limb transport (11.0 Sv in the 1960s and 12.0 Sv in the 2000s [3]) estimates, but are associated with notably different estimated mean values of Agulhas leakage that show an increase from 8.4 Sv in the 1960s to around 14.6 Sv in the 2000s[4]. The fundamental question is whether this increase in Agulhas leakage also evoked a corresponding increase in the AC contribution to the upper limb of the AMOC.

In highAL the AC contribution amounts to 7.0 Sv which constitutes 30% of the total NBC transport and 58% of the AMOC upper limb transport at 6°S; whereas the DP only contributes 4.1 SV, that is, 18% and 34% to the NBC and upper limb transports, respectively. In lowAL the volumetric decomposition is fundamentally different, since the DP contribution in this case slightly exceeds the AC contribution. The AC contribution only amounts to 5.1 SV, that is, 22% of the total NBC transport and 46% of the AMOC upper limb transport at 6°S; whereas the DP contribution provides 5.3 SV, that is, 23% and 48% to the NBC and upper limb transports, respectively. In highAL and lowAL on average 2.1 and 2.8 Sv remained in the domain after 40 years of integration, respectively, from which a large part probably would additionally add to the DP contribution under longer integration times (cf. section 3.3.1). The higher amount of unsampled particles in lowAL can be related to the generally longer transit time from DP to NBC than from AC to NBC: A circulation pattern with more pronounced DP contribution is associated with a shift of the total transit time distribution, that is, a transit time distribution inferred of particles from all sources, towards longer time scales (not shown); it consequently yields more particles still in the domain after 40 years of integration.

[3] These Lagrangian estimates of the upper limb strength are notably lower than the Eulerian AMOC strength in the respective periods, since within the limited integration period of 40 years not all AMOC contributions could be captured. With the absolute transport numbers also the exact values for the relative DP and AC contributions to the upper limb transport may change with longer integration times, even though the general findings are regarded as relatively robust (cf. section 3.3)

[4] Note that the mean Agulhas leakage transport for the 2000s has been calculated based only on the annual mean values from 2000 to 2005, since the applied methodology of Agulhas leakage estimation required a potential particle tracking towards the Good Hope section for at least 4 years and the employed model simulation only provided velocity output until 2009.

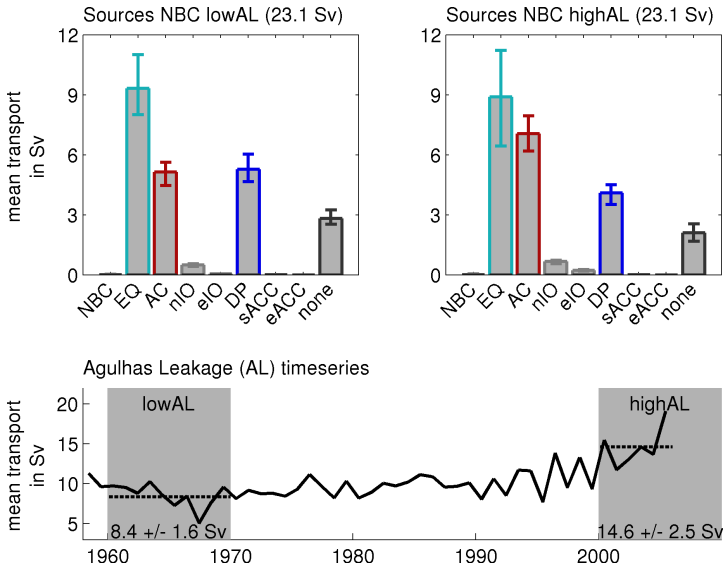

Fig. 3.12 *Sensitivity of NBC sources to the strength of Agulhas leakage (AL): (upper) mean volumetric contributions of the individual sources to the NBC inferred from lowAL and highAL (cf. Fig. 3.3); (lower) interannual variability of AL transport.*

These estimates suggest that the increase in Agulhas leakage between the 1960s and 2000s is indeed reflected in an increase of the AC contribution to the upper limb of the AMOC and is further accompanied by a decrease in the DP contribution.
It is noteworthy, that the increase in the AC contribution to the AMOC's upper limb is not directly proportional to the increase in Agulhas Leakage, but slightly weaker. This fits to the findings of Durgadoo [2013], who assessed the impact of Southern Hemisphere wind changes on the strength and fate of Agulhas leakage. He showed that the simulated wind-driven increase in Agulhas leakage goes along with a strengthening of the South Atlantic subtropical gyre. This strengthening leads to a favored re-circulatory route at the bifurcation point of the South Equatorial Current at the coast off Brazil. Consequently, less Agulhas leakage waters feed into the North Brazil Current. The strengthened re-circulatory route could also be regarded as one potential reason for the simulated decrease in the DP contribution. However, due to the conceptual limitations of the here presented analysis, the results are not yet conclusive and should be rather regarded as a motivation for future studies.

3.4 Summary and conclusions

In this study we revisited the relative importance of waters entering the South Atlantic from the Indian Ocean through the Agulhas Current (AC) system and waters entering directly from the Pacific through Drake Passage (DP) — commonly referred to as the warm and cold water routes, respectively — for the northward transport and thermohaline characteristics of the upper limb of the AMOC. To do so we performed Lagrangian analyzes between the two source regions and the North Brazil Current (NBC) at 6°S, which channels the upper limb flow in the tropics, in a realistically forced high-resolution (1/20°) ocean model.

Even though our results generally agree with the prevailing conception that, currently, the AC contribution is with around 50% the major source for the upper limb of the AMOC, they also suggest a non-negligible DP contribution of at least 40% — which is a substantially higher value than estimated by previous Lagrangian studies with coarser resolution models. The importance of the DP for the upper limb of the AMOC is further strengthened by the presented first estimates of (potential) changes in the DP and AC contributions, indicating that the ratio of the two sources is subject to temporal variability with phases in which the DP contribution indeed may have exceeded the AC contribution. This analysis additionally indicates that an ongoing increase in Agulhas leakage may indeed evoke an increase in the Agulhas contribution to the upper limb of the AMOC while the Drake Passage contribution decreases. Moreover, our study highlights that waters with DP and AC origin cannot be clearly distinguished by the temperature at their source (as the commonly adopted terminology may imply), but by their salinity. It further reveals substantial property transformations of AC and DP waters during their transit towards the NBC. The bulk of DP waters experiences a net density loss, the bulk of AC waters a slight net density gain. These transformations in density space are nearly completely captured by those Lagrangian particle trajectories reaching the surface mixed layer at least once during the transit, which amount to 66% (3.1 from 4.7 Sv) and 49% (3.1 from 6.3 Sv) for DP and AC waters, respectively. Upon arrival in the NBC waters of both origins can be found over the whole depth of the current and in the same temperature and salinity range.

The non-negligible water mass transformations indicate that the advective pathways and timescles inferred for the water volume transport between the two source regions and the NBC are limited in their use for assessing the pathways and timescales with that upper ocean temperature as well as salinity anomalies are transmitted through the South Atlantic oceans. However, more work is needed to better understand where and how the water mass transformation and mixing of the two contributions occurs and how changes in the Pacific-Atlantic and Indo-Atlantic exchange are related and eventually projected onto the return flow characteristics. This is particularly important for a better assessment of the potential impact of the observed warming in the extended Agulhas region and the estimated increase in Agulhas leakage over the last decades.

Finally, even though in this study we focused on the importance of the ratio of the DP and AC contributions for the upper limb of the AMOC, the ratio of the two inflows generally impacts the thermohaline structure of the whole South Atlantic, with consequences also on a more regional scale, for instance, for the Benguela upwelling region [Tim et al., submitted to J. Geophys. Res. Ocean.] or the tropical Atlantic [Lübbecke et al., 2015; Castellanos et al., 2017].

Acknowledgments

The OGCM and trajectory simulations were performed at the High Performance Computing Centers in Hannover (HLRN). The project received funding by the Cluster of Excellence 80 “The Future Ocean” within the framework of the Excellence Initiative by the Deutsche Forschungsgemeinschaft (DFG) on behalf of the German federal and state governments (Siren Rühs, Grant CP1412), and by the German Federal Ministry of Education and Research (BMBF) for the SPACES-AGULHAS project (Arne Biastoch and Franziska Schwarzkopf, Grant 03F0750A). The authors further wish to thank Sabrina Speich, Susan Lozier, and Erik van Sebille for inspiring discussions that added value to this manuscript.

4 Study 2: Indian Ocean sources of Agulhas leakage

This study presents a Lagrangian decomposition of Agulhas leakage waters into their different sources from the Indian Ocean performed in a high-resolution (1/12°) ocean model. It constitutes the first detailed and coherent Lagrangian analysis of large-scale connectivity associated with the upper limb return flow of the global overturning circulation from the Pacific via the Indian Ocean into the Atlantic. The analysis highlights the dominant contribution of surface-bound Indonesian Throughflow waters to the Pacific–Atlantic connection and further reveals that the Indian Ocean does not act as a passive connector, but salinifies and cools the bulk of these waters during their transit. However, it also reports a relative high contribution of intermediate water with origin South of Australia, which largely maintain their properties through their transit. These findings are of particular interest considering the question whether the currently observed increased heat transport across the Indonesian Throughflow could be observed in the South Atlantic within the coming decades.

The chapter has been published in the Journal of Geophysical Research: Oceans:

Durgadoo, J. V., **Rühs, S.**, Biastoch, A., and C. W. Böning (2017): *Indian Ocean sources of Agulhas leakage*. Journal of Geophysical Research: Oceans, 122(4), 3481–3499, doi:10.1002/2016JC012676.

My personal contribution to the publication has been the following:
assisting with Lagrangian trajectory calculations, suggesting to include water mass transformation analysis, refining methodology of pathway analysis by means of Lagrangian streamfunctions, writing respective parts of method section, and contributing to overall writing process from the first draft to the final version of the paper.

AGU PUBLICATIONS

JGR

Journal of Geophysical Research: Oceans

RESEARCH ARTICLE

10.1002/2016JC012676

Indian Ocean sources of Agulhas leakage

Jonathan V. Durgadoo[1], Siren Rühs[1], Arne Biastoch[1], and Claus W. B. Böning[1]

[1]GEOMAR Helmholtz Centre for Ocean Research Kiel, Kiel, Germany

Key Points:
- A study of pathways, timescales, and water transformations of Indian Ocean sources of Agulhas leakage
- On-route, Indonesian Through-Flow cools and salinificates, while Tasman leakage is deeper and experiences no change in properties
- The Pacific contributes at least 7.9 Sv to the total Agulhas leakage of about 14 Sv

Correspondence to:
J. V. Durgadoo,
jdurgadoo@gmail.com

Citation:
Durgadoo, J. V., S. Rühs, A. Biastoch, and C. W. B. Böning (2017), Indian Ocean sources of Agulhas leakage, *J. Geophys. Res. Oceans, 122*, doi:10.1002/2016JC012676.

Received 30 DEC 2016
Accepted 4 APR 2017
Accepted article online 13 APR 2017

Abstract We examine the mean pathways, transit timescales, and transformation of waters flowing from the Pacific and the marginal seas through the Indian Ocean (IO) on their way toward the South Atlantic within a high-resolution ocean/sea-ice model. The model fields are analyzed from a Lagrangian perspective where water volumes are tracked as they enter the IO. The IO contributes 12.6 Sv to Agulhas leakage, which within the model is 14.1 $\pm$ 2.2 Sv, the rest originates from the South Atlantic. The Indonesian Through-flow constitutes about half of the IO contribution, is surface bound, cools and salinificates as it leaves the basin within 10–30 years. Waters entering the IO south of Australia are at intermediate depths and maintain their temperature-salinity properties as they exit the basin within 15–35 years. Of these waters, the contribution from Tasman leakage is 1.4 Sv. The rest stem from recirculation from the frontal regions of the Southern Ocean. The marginal seas export 1.0 Sv into the Atlantic within 15–40 years, and the waters cool and freshen on-route. However, the model's simulation of waters from the Gulfs of Aden and Oman are too light and hence overly influenced by upper ocean circulations. In the Cape Basin, Agulhas leakage is well mixed. On-route, temperature-salinity transformations occur predominantly in the Arabian Sea and within the greater Agulhas Current region. Overall, the IO exports at least 7.9 Sv from the Pacific to the Atlantic, thereby quantifying the strength of the upper cell of the global conveyor belt.

1. Introduction

In the global ocean circulation, the Indian Ocean (IO) constitutes a connector between the Pacific and Atlantic Oceans. *Broeker*'s [1991] simple but profound schematic of the Great Ocean Conveyor Belt already illustrates the importance of the IO. In the upper ocean, warm tropical waters are imported from the Pacific through the Indonesian Archipelago into the IO and exported south of Africa into the Atlantic where eventually convective overturning occurs at high northern latitudes. The newly formed deep water subsequently spreads southward and is redistributed into the Indian and Pacific Oceans after looping around Antarctica. In this study, we investigate whether the IO simply acts as a passive connector between the Pacific and Atlantic oceans or whether it additionally actively modifies the waters that it communicates across. Since 1991, numerous authors have revised *Broeker*'s depiction, highlighting the complex and eddying nature of both the upper and deep routes [*Richardson*, 2008; *Lozier*, 2010]. Among others, it is now recognized that the route through the IO occurs both north and south of Australia, namely via the Indonesian Through-flow and Tasman leakage (Figure 1).

Water entering the IO from the Indonesian Archipelago, so-called Indonesian Through-flow (ITF), must navigate a complex route. The main entry point from the Pacific Ocean is through Makassar Strait between Borneo and Sulawesi, with over 75% of the ~15 Sv that eventually traverses into the IO [*Sprintall et al*., 2009; *Tillinger and Gordon*, 2009]. The volume transport of ITF displays a relationship with phases of the El-Niño Southern Oscillation. In the negative phase, an enhancement in through-flow has been reported [*Meyers*, 1996; *Liu et al*., 2015], with more waters of south Pacific origin entering Makassar Strait [*van Sebille et al*., 2014]. Further interannual variations in ITF originate from coastal Kelvin waves propagating along the eastern IO basin, and are related to the Indian Ocean Dipole [*Liu et al*., 2015]. Based on 3 decades (since 1984) of repeated expendable bathythermograph measurements between Fremantle (southwest Australia) and Sunda Strait (between the islands of Sumatra and Java) and surface winds measurements, *Wijffels et al*. [2008] and *Liu et al*. [2015] reported a positive trend in geostrophic ITF transport of 1 Sv/decade. ITF waters enter the IO as a tongue of relatively fresh surface waters and saltier intermediate waters [*Gordon et al*., 1997] and feed into the South Equatorial Current. High-resolution numerical experiments with artificial opening and closing of the ITF passages provide evidence of a codependency between ITF transport and Agulhas leakage further downstream [e.g., *Le Bars et al*., 2013].

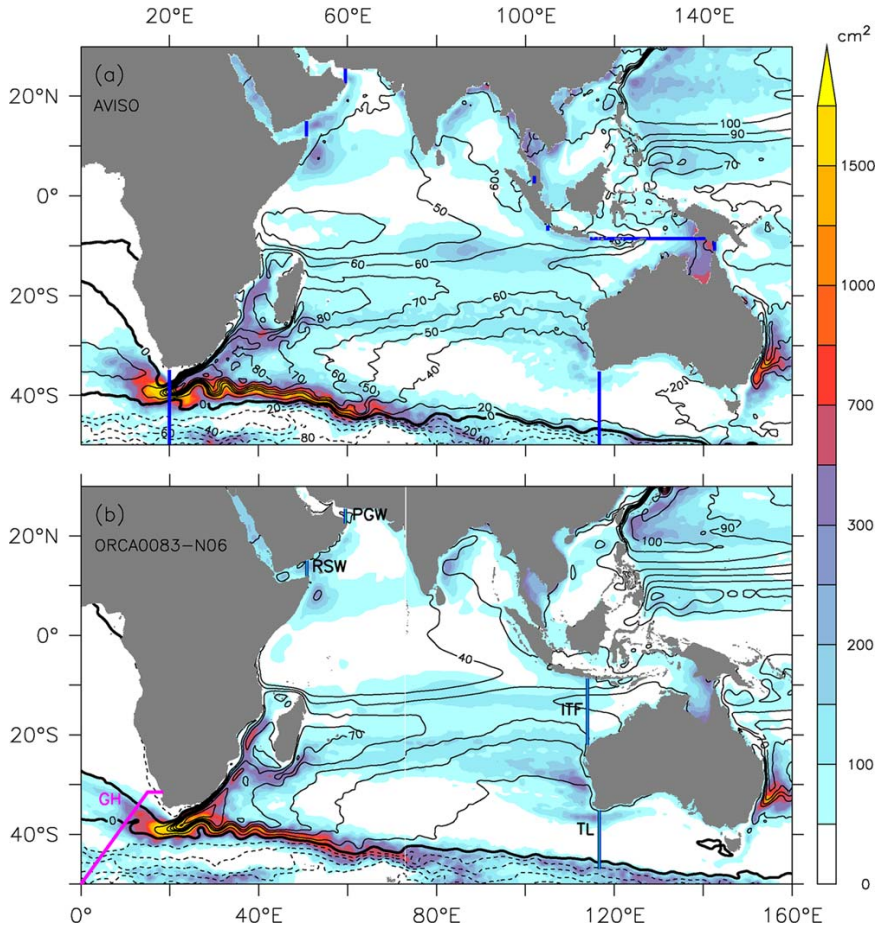

Figure 1. Representation of the mean circulation (contours of sea surface height, cm) and mesoscale variability (shading of sea surface height variance, cm^2) for the period 2000–2010 from (a) altimetric observations, AVISO, (b) model, ORCA0083. Sections in Figure 1a denote the final sections used for the quantitative Ariane experiments; sections at 20°E and 116.6°E extend to Antarctica. Sections in Figure 1b highlight the initial seeding sections used for the four main quantitative Ariane experiments. GoodHope (GH) is the section along which Agulhas leakage is commonly monitored.

The interconnectivity of the three southern hemisphere subtropical gyres allows for the secondary inflow of waters into the IO from the Pacific Ocean south of Australia, so-called Tasman leakage [*Ridgway and Dunn*, 2007; *Speich et al*., 2007]. Westward flow, in parts originating from the East Australian Current, is typically observed between Tasmania and the Subtropical Front [*Speich et al*., 2002]. Early observational and modeled estimates of this leakage give 0–13 Sv of thermocline and intermediate waters flowing westward south of Tasmania [*Rintoul and Sokolov*, 2001; *Speich et al*., 2002]. More recent studies constrain these estimates to around 4–5 Sv in the mean [*van Sebille et al*., 2012, 2014]. Derived from observational subsurface autonomous floats, *Rosell-Fieschi et al*. [2013] reported a westward transport of 5.2 $\pm$ 1.8 Sv at 115°E at intermediate depth. Despite the fact that both interocean exchanges north and south of Australia being of Pacific origin could arguably be related to large scale wind patterns [e.g., *Feng et al*., 2011], *van Sebille et al*. [2014] noted no obvious link between the two. Little is known on the spreading of Tasman leakage in the IO, but it is assumed to partly contribute to Agulhas leakage.

Other sources of surface and intermediate waters for the IO are from the marginal seas in the northwestern part of the basin (Figure 1). Resulting from extreme evaporation, warm, and saline water are formed in the Red Sea and Persian Gulf. These dense waters mix in the Gulfs of Aden and Oman due to high mesoscale activities [*Fratantoni et al*., 2006; *Al Saafani et al*., 2007; *L'Hégaret et al*., 2015]. In the Arabian Sea, they level

at depth between 200 and 900 m and spread equatorward [*Prasad et al*., 2001; *Bower et al*., 2002; *Chowdary et al*., 2005]. An analysis of historical hydrographic sections showed that the high salinities relative to the ambient waters could be traced within the Mozambique Channel and downstream in the Agulhas Current [*Beal et al*., 2000; *Roman and Lutjeharms*, 2007]. South of Africa, the high salinity waters undergo additional mixing and share the similar density classes as the relatively fresher but colder Antarctic Intermediate Water [*Beal et al*., 2006]. In the Cape Basin, *You et al*. [2003] reported about 0.4 ± 1 Sv of Red Sea Water entering the South Atlantic.

The outflow from the Indian Ocean into the Atlantic Ocean passes through a vigorous western boundary current regime southeast of Africa (Figure 1). The Agulhas Current transports warm and saline surface and intermediate water southward [*Lutjeharms*, 2006], with a typical transport of 84 ± 24 Sv (estimated from 3 years of mooring data) [*Beal and Elipot*, 2016]. The prominent contributors of water of the Agulhas Current are from the Mozambique Channel (16.7 ± 15.8 Sv, 6 years of mooring data) [*Ullgren et al*., 2012], from the South East Madagascar Current (37 ± 10 Sv, four hydrographic sections) [*Nauw et al*., 2008], and the rest from recirculations along the Agulhas Return Current [*Lutjeharms and Ansorge*, 2001; *Lutjeharms*, 2006]. The large standard deviations in transport value stem from the dominance of the mesoscale in this region (Figure 1). South of Africa, the Agulhas Current overshoots the shelf break and abruptly retroflects back into the Indian Ocean. The majority (∼2/3–3/4) of the original Agulhas Current transport flows eastward as the Agulhas Return Current [*Lutjeharms*, 2006]. The remainder, roughly 15 Sv [*Richardson*, 2007], flows westward as Agulhas leakage mostly in form of mesoscale eddies, and constitutes the so-called warm and salty export into the South Atlantic that *Broeker* [1991] described.

Agulhas leakage in the Cape Basin can therefore in principle be decomposed into its various constituents: coming from the Pacific north and south of Australia, the marginal seas, and via the disparate sources of the Agulhas Current. The Cape Basin is, however, a cauldron, where waters of IO origin mix with ambient South Atlantic water and with waters from Drake Passage [*Stramma and England*, 1999], making it a challenge to identify and more importantly volumetrically quantify individual water masses from classical potential temperature-salinity plots.

The aim of this study is to decompose the exhaust of the IO, Agulhas leakage, into its individual sources using a high-resolution global ocean sea-ice model. We focus on waters of IO origin, determine and compare their pathways and associated timescales, and assess changes in properties along their way from the Pacific and marginal seas toward the Atlantic. The spreading of individual water masses in the IO has been described in the past using historical hydrography data sets, simple and coarse-resolution models [e.g., *You and Tomczak*, 1993; *You*, 1998; *Haines et al*., 1999; *Joseph and Swathi*, 1999; *Beal et al*., 2000; *Song et al*., 2004]. We use a Lagrangian analysis approach that allows us to follow entire water volumes (which may comprise of different water masses) and to provide quantitative measures by closing the IO inflow-outflow budget. For this study, we seek an understanding of the mean flow and do not resolve any variability on seasonal, interannual, decadal, or longer timescales. Nonetheless, it is important to note that the circulation of the IO is subject to changes on a range of timescales. For example, owing to the seasonality of the Asian monsoon winds, the upper ocean current system of the northern IO reverses biannually [*Schott and McCreary*, 2001]. On interannual timescales strong imprints of the Indian Ocean Dipole and the El Niño Southern Oscillation are observed [*Saji et al*., 1999; *Behera et al*., 2006; *Ummenhofer et al*., 2013]. As underlined by *Haines et al*. [1999], in order to adequately resolve the mean circulation, it is important that the Eulerian velocity fields used for the Lagrangian analysis incorporate the full temporal variability of the IO.

2. Methods

2.1. Model Output

The ORCA0083 configuration of the NEMO model (version 3.6) [*Madec*, 2016] is used for this study. This configuration, developed within the European DRAKKAR consortium [*The DRAKKAR Group*, 2007], simulates the ocean/sea-ice circulation nominally at 1/12° globally, which is eddy resolving between roughly 50°S and 50°N [*Hallberg*, 2013]. ORCA0083 uses an Arakawa-C staggered grid arrangement in the horizontal, and has 75 vertical levels, with 46 levels in the top 1000 m and spacing increasing from 1 m at the surface to a maximum of 204 m at depth. The experiment used for this study is the ORCA0083-N06, which was run by the National Oceanography Centre, Southampton, UK. The treatment of tracers is implemented using a

Laplacian operator for isoneutral horizontal diffusion (eddy diffusion of 125 m^2/s) and the total variance dissipation scheme for advection. Geopotential horizontal diffusion on momentum uses a bi-Laplacian operator (eddy viscosity of $-1.25e10$ m^4/s) and a vector form advection scheme conserving energy and enstrophy. Subgrid-scale vertical mixing is calculated through the turbulent eddy kinetic dependent diffusion scheme. This experiment started from rest with tracer fields initialized using a combined product derived from PHC2.1 [*Steele et al*., 2001], Medatlas [*Jourdan et al*., 1998], and *Levitus et al*. [1998], and was forced using the Drakkar Forcing Set (DFS5.2) [*Brodeau et al*., 2010; *Dussin et al*., 2014] for the period 1958–2012.

The first 5 years (1958–1962) of the simulation are treated as the initialization phase, so that for this study, 50 years output (1963–2012) are used. We note that a 5 years initialization phase is likely not sufficient to spin the whole overturning. However, it is sufficient for the circulation of the upper 1000 m in the IO (dynamic height fields difference between the first and last decades of the 50 years shows no major discrepancies, not shown). The three-dimensional velocity and tracer fields were stored at temporal resolution of 5 day means. *Qin et al*. [2014] showed that for offline Lagrangian analyses within models of similar horizontal resolution as ORCA0083, degradation in flow characteristics occurs when using model output with temporal resolution beyond 9 day average. The model's representation of the mean flow and of the variability of the IO region is adequate (Figures 1 and 2a). The region of high sea-surface-height variability in the source region of the Agulhas Current, which most nested configurations fail to reproduce adequately [*Biastoch et al*., 2008; *Durgadoo et al*., 2013], is well resolved by this simulation. Further details and overall evaluation of the model experiment can be found in *Moat et al*. [2016] and *Schulze* [2016].

2.2. Lagrangian Analysis of the Model Fields

Tracking water within the Eulerian output fields of the model was performed offline using the Ariane Lagrangian package [*Blanke and Raynaud*, 1997]. Ariane advects particles within the model fields by displacing them along analytically computed three-dimensional streamlines, taking advantage of the volume conservation property of the model, which implies that the velocity field has to be locally nondivergent. Unlike other explicit time-stepping methods, the analytical integration scheme yields unique and identical trajectory solutions both forward and backward in time.

Ariane runs in two complementary modes: quantitative and qualitative. In its quantitative mode, Ariane seeds particles along predefined sections at every time step (in this case, 5 day), whereby each particle is assigned a partial transport. The number of particles at each time-step is dependent on the transport across a particular section, such that the stronger the flow, the more particles are seeded; the cumulative transport of all particles represents the instantaneous Eulerian transport [*Blanke and Raynaud*, 1997]. Subsequently, the particles are advected forward or backward in time. Finally, they are captured when they cross edges of a predefined domain, and their transports are summed up. This mode is most useful to determine the connectivity between the seeding section and the edges of the predefined domain. A prime example where Ariane is successfully used in this mode is in measuring Agulhas leakage, defined by the portion of the Agulhas Current entering the Atlantic across the GoodHope line [*Durgadoo et al*., 2013; *Biastoch et al*., 2015].

Blanke et al. [1999] introduced the concept of the Lagrangian streamfunction based on the fact that Ariane respects mass conservation (nondivergent flow). As particles are advected in the quantitative mode their infinitesimal transports are summed at each velocity grid cell wall they cross. The resulting three-dimensional transport field can then be integrated vertically to obtain a two-dimensional locally nondivergent flow field that can be described by a horizontal streamfunction. Such a Lagrangian streamfunction thus represents the horizontal flow of the entire water volume that entered and left the study domain. Prerequisites are that first initial sections are seeded with sufficiently large number of particles, and second sufficient time is allowed for the particles to leave the domain across the defined final sections.

In the qualitative mode of Ariane, seeding positions are obtained by either first running a quantitative experiment or by user-defined start positions. Here, the former is favored since the particle positions derived from a quantitative experiment has the advantage of being tagged by partial transports. Furthermore, in qualitative mode, spatial and temporal information of individual particle trajectories are stored. Such information can subsequently be analyzed to assess pathways, timescales (e.g., *Rühs et al*. [2013] and

Lübbecke et al. [2015] for Agulhas water spreading in the Atlantic), and along-track changes in tracer properties.

Four main sets of Lagrangian experiments were performed for this study, each corresponding to the start positions of the particles at four different initial sections. These initial sections, illustrated in Figure 1b, capture water entering the IO basin from the Pacific Ocean (ITF and TL) and the marginal seas adjacent to the IO, namely from the Gulfs of Oman (PGW) and Aden (RSW).

1. PGW—meridional section at the mouth of the Gulf of Oman along 59.5°E; 22.5°N-25.4°N, where water enters the Arabian Sea.
2. RSW—meridional section at the mouth of the Gulf of Aden along 50.8°E; 11.9°N–15°N, where water enters the Arabian Sea.
3. ITF—meridional section along 114°E; between Australia (22°S) and Java (8.7°S). The Indonesian Throughflow is a collective term consisting of water transport across the Indonesian Archipelago through various Straits. Along 114°E, flow across 5 of the 7 Straits are captured, namely Lombok, Flores, Ombai, Timor, and Torres. Considering ITF collectively enables consistent analysis of pathways and timescales across the IO basin. Separate experiments for the two remaining Straits, Sunda, and Malacca, were performed, and shall be mentioned briefly in the results.
4. TL—meridional section along 116.6°E; between Antarctica and Australia (35.2°S). Strictly speaking, Tasman leakage occurs south of Tasmania [*Ridgway and Dunn*, 2007]. Here, since a sizable portion of the westward flowing water along this longitude between Australia and the Subtropical Front indeed originate from south of Tasmania [*van Sebille et al.*, 2014], the nomenclature was deemed appropriate. The westward flowing Antarctic Coastal Current was not considered as part of TL, since it is confined south of the Antarctic Circumpolar Current and thereby does not enter the IO basin.

These four initial sections were designed to satisfy two criteria. First, the transport across each section is representative of the flow of the entire water column, including the respective water masses (as ordinarily measured along their typical isopycnals) after which they are named. Second, the sections are offset from the original water mass source, so as to minimize the effect of recirculations on timescales between the area where they originate and when they enter the IO.

The quantitative mode requires a closed domain to be defined, containing an initial section and several other final sections along which particles are captured. These final sections are shown in Figure 1a. The sections at 20°E and 116.6°E (TL) extend to the Antarctic continent. This domain was used for the quantitative experiments for PGW, RSW, and TL. For the ITF experiment, the final sections extending from Java to Papua (along 8.6°S) and New Guinea to Australia (along 142.5°E) were replaced with the initial section shown in Figure 1b.

So as to capture the interannual and decadal variability of the flow, it is necessary to seed particles over at least a few decades. In order to optimize the seeding strategy, and thereby allowing more particles to be seeded and integrated over a longer period of time, a series of preanalysis experiments was undertaken. In this preanalysis, particles were successively seeded full-depth along each initial section every 5 days over a period of 5 years, and were advected forward for a total of 25 years in quantitative mode. The initial positions of particles that, within 25 years, exited the domain south of Africa at 20°E were subsequently analyzed. It was found that over 99% of the particles reaching 20°E originated from PGW, RSW, ITF, and TL in the upper 500, 1500, 1500, and 1600 m, respectively (not shown). Furthermore, for the TL preanalysis experiment, the particles reaching 20°E originated from between Australia and 47°S, which roughly delineates the subtropical regime from the Antarctic Circumpolar Current (Figure 1). Repeating this preanalysis in reverse yields the same result (backward tracking of particles from 20°E to the four source regions). Results from the preanalysis experiments informed the design of the full set of Lagrangian experiments assessed here.

The four main sets of Lagrangian experiments were constructed as follows. Seeding across each initial section was refined based on the depth and latitude criteria described above. In quantitative mode, 1.5×10^6, 2.2×10^6, 10.1×10^6, and 10.0×10^6 particles were seeded every 5 days over a period of 30 years (1963–1992), corresponding to a total mean transport of 1.0, 3.6, 17.6, and 16.0 Sv across the PGW, RSW, ITF, and TL initial sections, respectively. The maximum accuracy achieved in this study is in the order of 0.1 Sv, therefore all transports reported here are rounded to 1 decimal place. The particles were then integrated forward for 100 years. Less than 3% of the initially seeded particles remained in the IO domain by the end of the

100 years. The long integration period was achieved by cycling twice through the input data, a practice previously employed for other studies of this kind [*van Sebille et al*., 2011; *Rühs et al*., 2013]. Out of 38.2 Sv (sum of the time-mean transport across the four initial sections), 23.2 Sv (60%, 3.8×10^6 particles) reached 20°E within 100 years, that is 0.3, 1.4, 10.9, and 10.6 Sv from PGW, RSW, ITF, and TL, respectively.

Subsequently, only those particles that exited the IO domain across 20°E were placed back at their respective initial seeding sections and advected forward in quantitative and qualitative modes for 100 years. The positions of the trajectories were stored every 5 days. Additionally, the modeled ambient temperature and salinity interpolated at the trajectory locations were stored at the same temporal frequency. Even though cycling through the input data allows for the analysis of longer pathways and timescales, the analysis of along-track tracer characteristics ought to be restricted to the length of input data available, that is, 50 years (see section 3.4).

3. Results and Discussion

3.1. Pathways from the Marginal Seas and the Pacific to the South Atlantic

We generated the Lagrangian streamfunctions after 100 years of integration, and in order to obtain a closed volumetric budget, particles remaining in the domain were omitted. Figure 2 shows the Lagrangian streamfunction for each experiment for all particles, while Figure 3 shows the same but for only those particles that exited the domain across 20°E within 100 years. In the first case, the isolines connect the initial seeding section with all other sections of the domain, and in the second case, they highlight only the flow from the seeding section to the section at 20°E south of Africa.

The 50 year mean Eulerian streamfunction, derived from annual average velocity fields, portrays the overall barotropic circulation of the IO basin (Figure 2a). Prominently, the two gyres of the south IO, roughly delineated along 10°S, are seen: the broad counter-clockwise south Indian subtropical gyre between 40°S and 10°S, and the narrow clockwise tropical gyre between 10°S and the Equator. Their associated western boundary currents, namely the Agulhas Current [*Lutjeharms*, 2006], the North and South East Madagascar Currents [*Swallow et al*., 1988], and the East African Coastal Current [*Swallow et al*., 1991], are also visible. North of the Equator, the circulation is strongly influenced by seasonal reversal of winds. A weak clockwise circulation illustrates a stronger summer (southwest) monsoon on average.

The total Lagrangian streamfunction (Figure 2b) portrays the vertically integrated flow of the four IO water sources. The resemblance to the Eulerian mean both in structure and magnitude suggests that it adequately captures the Eulerian circulation, hence validating the method. Generally, a congruity between the Eulerian and Lagrangian streamfunctions indicates that the prerequisites mentioned previously are sufficiently fulfilled. The biggest differences between the two fields probably stem from the fact that deep-water inflow (e.g., from the Atlantic across 20°E) is not considered and particle trajectories with potentially longer residence times in the IO (e.g., local recirculations in the Southwest IO) are prohibited to some degree by the experiment design (section 2.2). Also, it is worth noting that the Eulerian streamfunction portrays the circulation of the 50 year mean, while the Lagrangian streamfunction is based on trajectories with various residence times, up to 100 years [*Döös et al*., 2008]. The Lagrangian streamfunctions based on each individual experiments (Figures 2c–2f), showing the spreading of waters from the different source regions, are described next.

Water from the marginal seas entering the northwestern IO from the Gulfs of Oman and Aden show similar pathways (experiments PGW and RSW, Figures 2c and 2d). As they enter the Arabian Sea, these waters are advected equatorward and experience strong recirculation associated with seasonally varying flows [*Chowdary et al*., 2005; *Schott et al*., 2009]. Clearly distinguishable is the clockwise Great Whirl roughly centered at 9°N off Somalia, which recirculates both PGW and RSW waters predominantly during the southwest monsoon [*Beal and Donohue*, 2013]. At the mouth of the Gulf of Aden, RSW either veers immediately southward between the horn of Africa and the island of Socotra, or is advected westward into the Arabian Sea and into the interior of the northern IO. The former occurs during the northeast (winter) monsoon, while the latter during the southwest (summer) monsoon [*Fischer et al*., 1996; *Schott and Fischer*, 2000; *Prasad et al*., 2001]. *Beal et al*. [2000] analyzed historical hydrographic data, and reported a preferred spread of Red Sea Water along the African west coast through the Mozambique Channel. In contrast, the lack of direct contours in Figure 2d suggests the main RSW pathway consist first of an equatorial detour before reaching the

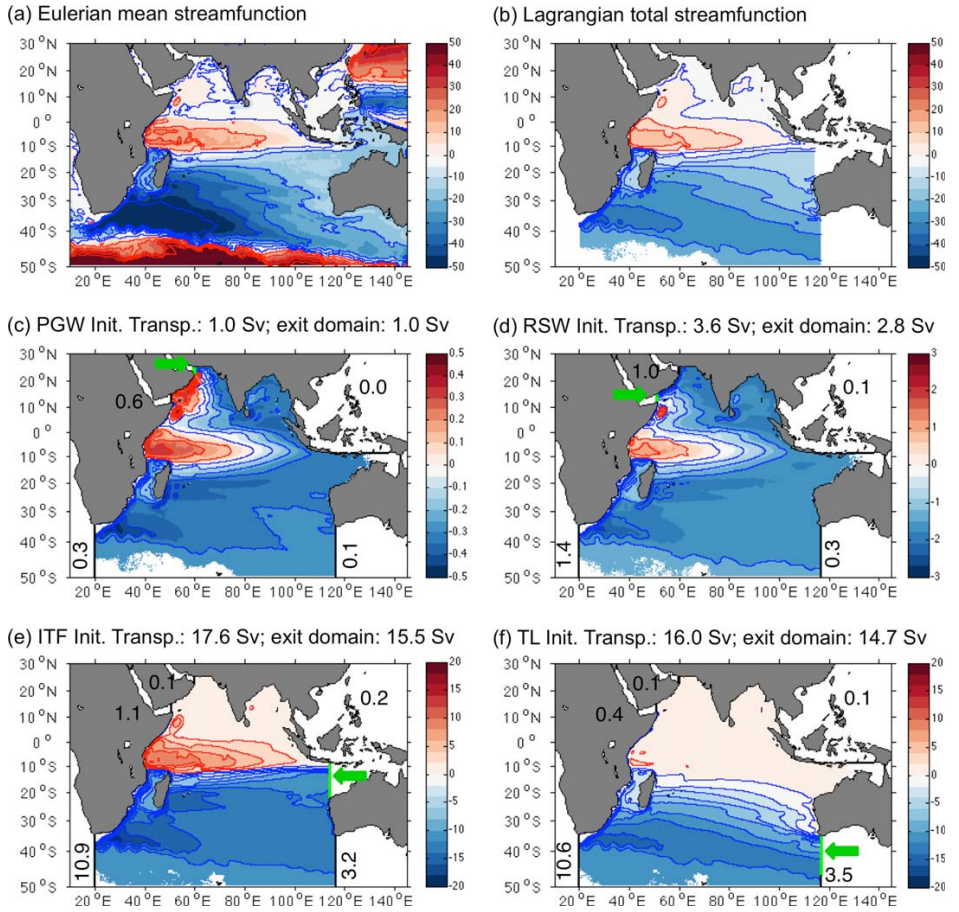

Figure 2. (a) Mean barotropic streamfunction from the Eulerian fields averaged over the period 1963–2012. (b–f) Lagrangian streamfunction derived only from particles that exited the domain within 100 years; reference set to 0 over Africa (20°E, Equator). (c–f) Streamlines showing the connection between the initial sections (PGW, RSW, ITF, and TL, highlighted by the green arrows) and the other final sections of the domain (black lines). Figure 2b is the sum of the four components shown in Figures 2c–2f. All units are in Sv.

Mozambique Channel. Dense water overflows are generally poorly resolved in z-level models and require special treatment [*Legg et al*., 2009]. ORCA0083-N06 contains no such special treatment for the overflows from the Gulfs; hence, Red Sea Water entering the Arabian Sea is lighter than expected. Being more surface bound in the model, waters from the Gulf of Aden is more prone to be affected by the seasonally changing circulation. And since the summer monsoon dominates the annual cycle, a preferred pathway into the Arabian Sea is likely. Furthermore, another difference between our study and that of *Beal et al*. [2000] is that we consider RSW as water exiting the Gulf of Aden over the full water column down to 1500 m, while *Beal et al*. [2000] focused on the spread of "pure" Red Sea Water along its typical density surfaces. Closed contours in the Bay of Bengal indicate some degree of spreading and residence there.

Along the Equator, water from both PGW and RSW broadly spread eastward, congruent with the South Equatorial Counter Current. Thereafter, between 10°S and 20°S, they flow back toward Madagascar within the South Equatorial Current and split. The bunching of streamlines north of Madagascar and through the Mozambique Channel highlights the preferred pathway toward the Agulhas Current. Averaged over the 30 years of seeding, 1.0 and 3.6 Sv, enter the Arabian Sea from the Gulfs of Oman and Aden, respectively. In the model about 0.17 and 0.15 Sv (Eulerian means over 50 years) exits the Persian Gulf at the Strait of Hormuz and the Red Sea at Bab al-Mandab Strait, respectively. These values fall within the reported observational range of 0.17–0.25 Sv for the Persian Gulf [e.g., *Bower et al*., 2000] and of 0.05–0.6 Sv for the Red Sea

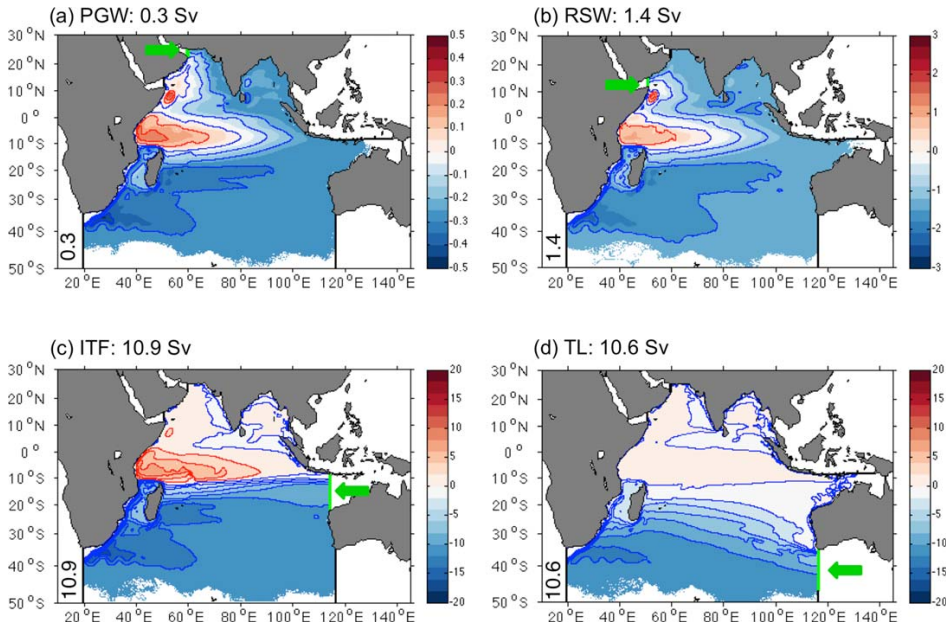

Figure 3. Similar to 2c–2f, but highlighting only the connectivity between initial sections (green arrows) and 20°E, that is no transport across the other final sections. 0.3, 1.4, 10.9, and 10.6 Sv from the initial sections PGW, RSW, ITF, and TL, respectively, reach 20°E within 100 years. All units are in Sv; Lagrangian streamfunction reference set to 0 over Africa (20°E, Equator).

[e.g., *Sofianos and Johns*, 2002]. Downstream of both Straits, mesoscale activities enhance the flow further. For example, *Fratantoni et al.* [2006] roughly estimated an additional 2–3 Sv flow through the Socotra Passage resulting from the propagation of Somali Current rings into the Gulf of Aden. Within 100 years, 0.3 and 1.4 Sv exit south of Africa from PGW and RSW, respectively.

Water entering the IO basin across 114°E from the Indonesian Archipelago is concentrated primarily in the top 600 m between the island of Java and 13°S. A shallower secondary core is centered at 21°S. Averaged over the 30 years of seeding, 17.6 Sv enters the basin in the top 1500 m (Figure 2e). This value falls within the observational range of 10.7–18.7 Sv [*Sprintall et al.*, 2009]. The major source of water at 114°E is through the Lombok, Ombai, and Timor Straits, with 3.3, 3.3, and 7.4 Sv, respectively (Eulerian means over 50 years); these values are also in agreement with *Sprintall et al.* [2009]. The bulk of the water is transported westward in a narrow band along 11°S till about 100°E, and is subsequently broadened feeding different branches of the South Equatorial Current. At the Mascarene plateau (59°E), two distinct branches of the South Equatorial Current are seen at 12°S and 16°S. The equatorward branch feeds the North East Madagascar Current, and bifurcates flowing through the Mozambique Channel and into the East African Coastal Current where it recirculates around the tropical gyre. Entry into the northern IO occurs along the African coast. The poleward branch feeds the South East Madagascar Current. In the southwest IO, streamlines from the Mozambique Channel and south of Madagascar converge in the Agulhas Current, and downstream either exit the domain or recirculate. Streamlines connecting the ITF section to the TL section indicate water exiting the IO basin south of Australia within 100 years either along the Agulhas Return Current and Subtropical Front (2.7 Sv), typically after first negotiating the retroflection south of Africa, or directly via the Leeuwin Current (0.5 Sv). About 60% (10.9 Sv) of ITF cross 20°E south of Africa within 100 years, with the most direct route being through the Mozambique Channel.

South of Australia (TL), 16.0 Sv entering the IO basin feed the broad westward flow of the south Indian subtropical gyre (Figure 2f). Most streamlines originating between Australia and 40°S spread either north or south of Madagascar, while those south of 40°S directly reach the Agulhas Current. Very little penetration of TL waters is observed in the northern IO, with only ∼3% being transported across the domain sections north of 10°S. This is likely due to the fact that TL waters are concentrated at intermediate depths (discussed

further in the subsequent sections), hence less prone to recirculate in the relatively shallow tropical gyre. More than 65% (10.6 Sv) of TL water exit south of Africa, and about 20% (3.5 Sv) recirculate leaving the domain again between 47°S and Antarctica.

Within 100 years, a total of 23.2 Sv from the four source regions reach south of Africa at 20°E. Figure 3 highlights only the pathways connecting each individual component to the section at 20°E. Since by design (preanalyses in section 2.2), water entering the IO basin are predisposed to leave the domain at 20°E if allowed sufficient time, the overall pathway depicted in this subset is similar to that shown in Figures 2c–2f. Most notable differences are: (1) Detours north of the Equator are less prominent in the cases of ITF and TL. (2) Recirculation of TL in the southwest IO is much weaker. This indicates that the pathway between TL and 20°E is for the most part direct and via the South East Madagascar Current.

Figure 4 schematically summarizes the most likely pathways shown in Figure 3 from the four source sections toward 20°E and subsequently into the Atlantic. Additionally, the origins of the contributions from ITF and TL are further decomposed. The partitioning of ITF waters coming across Lombok, Ombai, and Timor Straits and reaching 20°E within 100 years reflects that of the total transport across the ITF initial section, namely roughly 60% (cf. Figure 2e and the Eulerian means for the transport across the Straits given above). For TL, a large portion of the 10.6 Sv comes from recirculations across the initial section [*Sallée et al*., 2006]. The portion originating from between Tasmania and 50°S as Tasman leakage (3.1 Sv) commensurate previous findings [*van Sebille et al*., 2012, 2014; *Rosell-Fieschi et al*., 2013].

Of the 23.2 Sv that flows across 20°E within 100 years, 90% flows either through the Mozambique Channel or southeast of Madagascar. Waters from PGW, RSW, and ITF flow preferably along the South Equatorial Current and through the Mozambique Channel, while TL waters predominantly either are incorporated within the South East Madagascar Current or flow directly westward. After crossing 20°E, a little more than 50% of the waters proceed to leave the IO basin across GoodHope, the rest retroflects. Of the 12.2 Sv entering the Atlantic, over 96% were previously within the Agulhas Current, and can therefore be referred to as part of Agulhas leakage (as opposed to the more general term "Indian Ocean leakage").

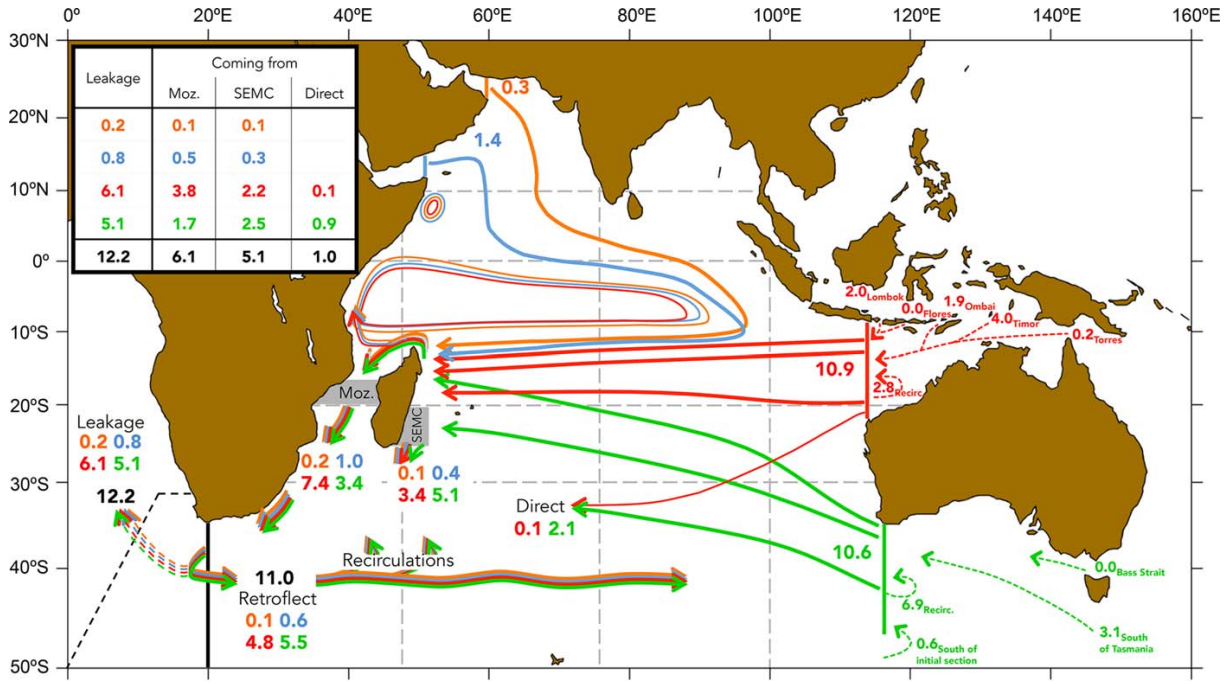

Figure 4. Schematic of the major pathways of water crossing 20°E within 100 years from the Indian Ocean. Of the 23.2 Sv from the four source regions, PGW (orange), RSW (blue), ITF (red), and TL (green), 12.2 Sv enters the Atlantic across the GoodHope section (dashed black line), the rest retroflects (11.0 Sv). Agulhas leakage within the model is 14.1 ± 2.2 Sv (see text for details). Sizes of arrows vary for clarity purposes. The table details the decomposition of leakage. Dashed arrows itemize the upstream sources of ITF and TL. Transport numbers are in Sv.

The ratio of water last seen leaving the grey shaded boxes (Figure 4) in the Mozambique Channel (Moz), southeast of Madagascar (SEMC), and arriving directly at 20°E without going through the Channel or southeast Madagascar are 5:4:1 (total of 23.2 Sv). There are no direct routes from the marginal seas to 20°E within 100 years, and water from the Gulfs of Oman and Aden flows either through the Mozambique Channel or through the Southeast Madagascar Current. Moreover, comparing the volume transports of particles' first entry into the grey shaded boxes and those last seen leaving them, there is a 20–25% chance that water entering the Channel or the South East Madagascar Current will recirculate within the southwest IO gyre, re-enter the Channel or the Southeast Madagascar Current, before eventually exiting at 20°E (also seen in Figure 3). The exception is for water from TL arriving southeast of Madagascar, where recirculation is negligible (weaker recirculation in the southwest IO in Figure 3d).

Agulhas leakage is commonly defined as the portion of the Agulhas Current, for example, at 32°S that leaks into the Atlantic across the GoodHope section within 3–5 years, and is intuitive measured in models using a Lagrangian framework [*Durgadoo et al.*, 2013; *Biastoch et al.*, 2015; *Lübbecke et al.*, 2015]. In the present model, employing this definition and over the period 1963–2008, the mean value of Agulhas leakage is 14.1 Sv with an annual standard deviation of 2.2 Sv. This value falls well within the expected range [*Richardson*, 2007]. In the schematic (Figure 4), we show that Agulhas leakage can be decomposed on average as ∼1 Sv arriving from the marginal seas of the northwest IO and ∼11 from the Pacific through the Indonesian Archipelago (∼6 Sv) and south of Australia (∼5 Sv), totalling ∼12 Sv. The missing ∼2 Sv could stem first from the so-called cold-water-route at intermediate depths from the south Atlantic [*Rimaud et al.*, 2012; *Rusciano et al.*, 2012] and second from the two remaining Straits not covered by the ITF section, namely Sunda and Malacca. As mentioned in section 2.2, separate Lagrangian experiments were additionally performed for the two Straits. They contribute ∼0.4 Sv to Agulhas leakage. To estimate the portion of South Atlantic origin, a backward experiment was performed where particles were seeded along the GoodHope section between Africa and 50°S in the top 2000 m for 30 years and advected backward in time for a total of 80 years to determine their origins. Of the ∼14 Sv of Agulhas leakage seeded, ∼0.9 Sv originated poleward of 50°S across 0°E from the South Atlantic, ∼0.8 Sv originated from below the GoodHope section deeper than 2000 m. Thereby, all the constituents of Agulhas leakage are accounted for.

Typically, 20–25% of Agulhas Current water leaks into the Atlantic. The Eulerian mean Agulhas Current transport at 32°S (Figure 2a) in the model is ∼63 Sv (falls within observational uncertain range of *Beal and Elipot* [2016]), of which ∼14 Sv leaks (classical definition), meeting the expectation. From the total Lagrangian streamfunction (Figure 2b) the Agulhas Current at 32°S is 33 Sv (of which, PGW: 0.4 Sv, RSW: 2.2 Sv, ITF 16.4 Sv, TL: 14 Sv; Figures 2c–2f), meaning that the current draws about half of its water from the four source regions considered here. The remainder is drawn from water recirculating along the Agulhas Return Current and Subtropical Front [*Lutjeharms and Ansorge*, 2001; *Lutjeharms*, 2006].

3.2. Timescale Across the IO and Into the South Atlantic

The timescales associated with the flow from the source regions toward GoodHope are shown in Figure 5. Each box plot shows the temporal distribution in transport first crossing the respective latitudes and longitudes of only those particles that cross the GoodHope section as Agulhas leakage (12.2 Sv in total).

The westward transport of water from ITF and TL is mainly achieved by the mean flow with the core of the ITF waters being in the top 500 m and TL below that. Within the IO subtropical gyre between 60°E and 100°E the fastest modeled mean speeds are ∼0.1 m s^{-1} in the top 500 m and ∼0.02 m s^{-1} between 500 and 1000 m (not shown). Therefore, between the ITF and TL initial sections and 77°E, approximately 4200 km apart, a particle traveling at these speeds, would take ∼1.3 years in the top 500 m and ∼6.7 years below that. These values are consistent with the fastest timescales shown at 77°E, indicated by the lower edges of the boxes in Figure 5b, where 25% of the transports reach the section in less than 1.2 and 6.4 years, respectively. This and the narrow interquartile ranges of the boxes, suggest that only minor stirring occurs until 77°E.

Waters from PGW being more surface-bound than those from RSW are likely to recirculate and linger in the northern IO. The bulk of the RSW waters (75% of it) cross the Equator twice as fast as PGW waters. Detours in the Bay of Bengal further account for the long timescales in the northern IO. The slowest particles are delayed by more than 2 decades between the Equator and 20°S due to residence within the tropical gyre.

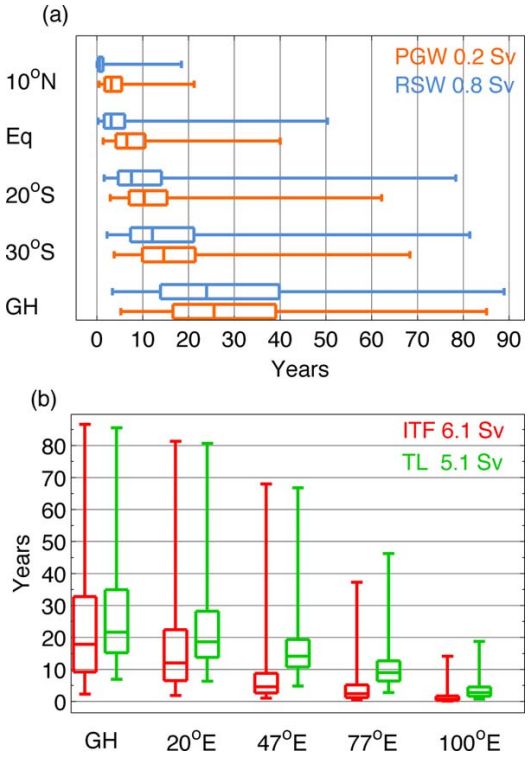

Figure 5. Transit time within the Indian Ocean of water eventually entering the Atlantic within 100 years from PGW (0.2 Sv, orange), RSW (0.8 Sv, blue), ITF (6.1 Sv, red), and TL (5.1 Sv, green). Each box plot shows the temporal spread in transport reaching the respective lines of longitudes and latitudes (grey dash lines in Figure 4). The edges of the boxes delineate the 25 and 75 percentiles, and the medians are indicated as lines across the boxes. The tails encompass 99% of the transport from the respective sources reaching GoodHope (GH) as part of Agulhas leakage.

In the southwest IO south of 20°S between 20°E and 47°E, the elongated boxes and extended tails indicate that the recirculatory and highly eddying nature of the flow there affect timescales of water from all origins (cf. Figure 1).

At GoodHope, the fastest waters are from ITF, with 25% of the volume transport arriving within the first decade. The relatively direct pathways of water of Pacific origin in contrast to those from the marginal seas are evident from the length of the respective lower tails in Figure 5. About half of the water transported into the Atlantic from all sources occurs within 25 years. Worth noting is that within 50 years, which is the length of one cycle of model data used, over 75% of the transport across GoodHope are accounted for.

3.3. Depth Structure of Waters Entering the South Atlantic

Within the Lagrangian framework, it is possible to examine the depth characteristics of waters of disparate sources along the GoodHope section as they enter the South Atlantic and before. The depth distribution of particles that cross GoodHope as Agulhas leakage and were last seen leaving the Mozambique Channel (across 20°S) or the Southeast Madagascar Current (across 25°S, 47–52°E) are shown in Figure 6. The mean flow is in both cases intensified along the coast to the left (cf. Figure 1), in the Mozambique Channel in the upper 500 m and southeast of Madagascar below that. The dominance of waters of ITF origin in the Mozambique Channel (3.8 out of 6.1 Sv) and of waters of TL origin southeast of Madagascar (2.5 out of 5.1 Sv) is evident and in line with the results described in section 3.2 for the entire transport reaching 20°E within 100 years. Southeast of Madagascar, there is additionally a clear delineation in the vertical between the waters of Pacific origin above and below 500 m. Red Sea Water, as a water mass, is typically found in the southwest IO at intermediate depths [*You*, 1998; *Beal et al.*, 2000; *You et al.*, 2003]. Here, in the upper layer above 750 m, waters of RSW origin can be found on either side of Madagascar. At intermediate depth, however, a sizable amount of RSW water can only be detected in the Channel corroborating previous reports [e.g., *You*, 1998; *Beal et al.*, 2000). The contribution of PGW is small and confined to the surface. Within the Agulhas Current, unlike the quasi-instantaneous observations of *Beal et al.* [2006], who found distinct water of distinct origins on either side of the current's core, here, no such clear demarcation is noted (not shown).

Agulhas leakage waters cross GoodHope mostly between 8°E and 18°E in the top 1250 m (Figure 6a), consistent with the broad fan of enhanced sea surface height variability in Figure 1b. In contrast to the relatively clear depth separation of ITF waters overlying TL waters within the subtropical gyre and southeast of Madagascar, at GoodHope (similar to within the Agulhas Current further upstream), these two water sources are mixed throughout the water column. Nonetheless, integrated across the section, ~4.5 Sv of ITF waters are concentrated in the top 500 m, while the same amount of TL waters are mostly centered between 250 and 1000 m. *van Sebille et al.* [2010] previously examined the question of what determines the fate of Agulhas water crossing 20°E. At that longitude, they noted a fairly similar spread in waters leaking into the

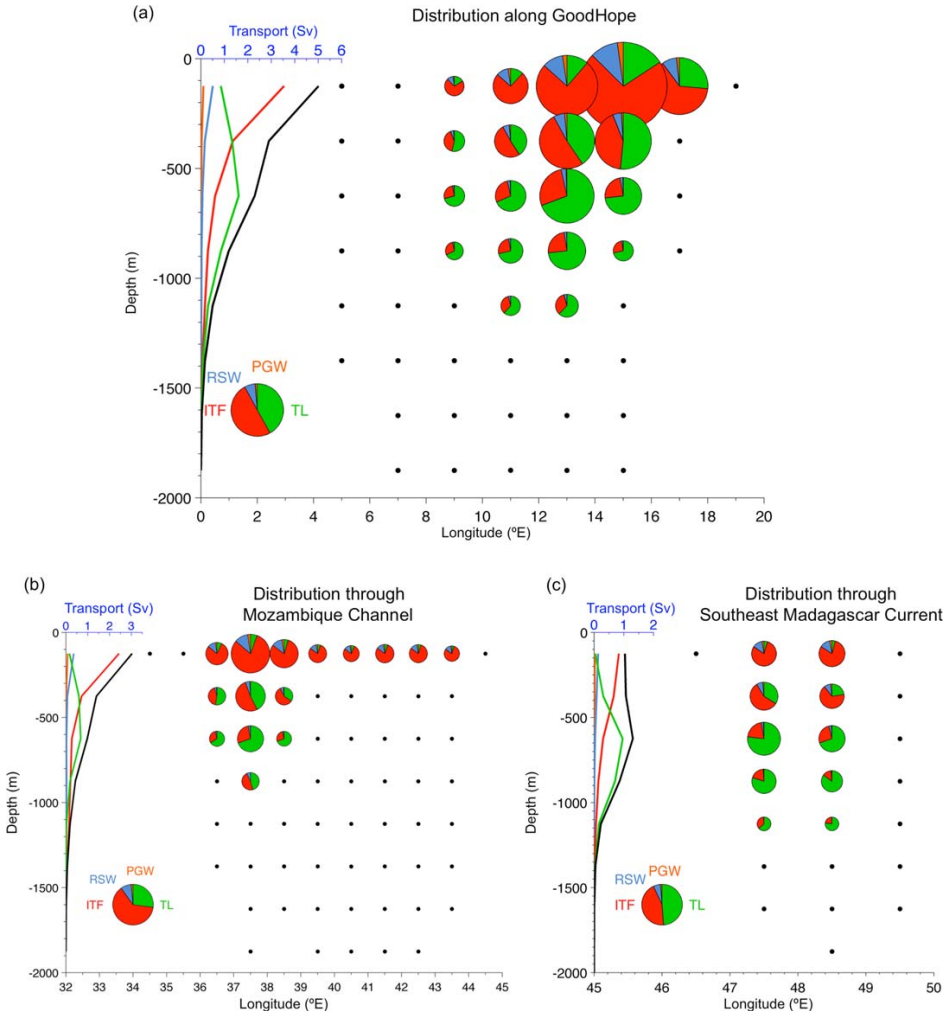

Figure 6. Transport depth-longitude distribution of waters from four origins that exit the Indian Ocean within 100 years across the (a) GoodHope section, and having passed through the (b) Mozambique Channel or (c) Southeast Madagascar Current immediately prior exiting (grey shaded boxes in Figure 4). Color coding given in legend. Each pie chart represents the transport through 1° or 2° of longitude × 250 m, with 1 Sv scaled to represent size of the pie chart in the legend. Pie charts with total transports less than 0.1 Sv are indicated by dots instead. The left plots show the zonally integrated transport as a function of depth, with the black curve showing the sum of the four components. Partitioning shown in the legend correspond to the total depth-integrated transport of (a) 12.2 Sv (0.2, 0.8, 6.1, and 5.1 Sv for PGW, RSW, ITF, and TL respectively); (b) 6.1 Sv (0.1, 0.5, 3.8, and 1.7 Sv for PGW, RSW, ITF, and TL respectively); and (c) 5.1 Sv (0.1, 0.3, 2.2, and 2.5 Sv for PGW, RSW, ITF, and TL respectively).

Atlantic and to those returning to the IO. This lent support to the mechanism of ring shedding by loop occlusion [*Ou and de Ruijter*, 1986] as the dominant factor in determining the fate of water crossing 20°E. With the exception of TL, values shown in Figure 4 suggest more water of PGW, RSW, and ITF origins to enter the Atlantic than to retroflect. It is important here to keep in mind the transport still left in the domain after 100 years of integration, which provides an upper bound of the uncertainties in this discussion (headers in Figures 2c–2f). A detailed look at the overall depth distribution at 20°E of waters leaking in contrast to those retroflecting shows a general agreement with the conclusion of *van Sebille et al*. [2010]. This distribution is unchanged from that upstream within the Agulhas Current. In the upper 250 m all sources but TL exhibit a preference for leaking. This is likely because of the surface-intensified cyclonic relative vorticity [*van Sebille et al*., 2010]. Below 500 m, waters of TL origin have a slight tendency to more likely retroflect than leak.

3.4. Water Properties Modification Within the Indian Ocean

From a Lagrangian connectivity perspective, we have investigated thus far the advective pathways and timescales of water from the source regions to the Atlantic. The question remains: to what extent does the Indian Ocean modify the water mass characteristics of the inflowing waters before exporting them? Here we consider the memory of the bulk water volume as opposed to that of individual particles or water masses.

Every 5 days, potential temperature (θ) and salinity (S) were linearly interpolated from the tracer fields onto each particle location. Inherently the tracer field incorporate the simulated and parameterized turbulent motions of the model, including the air-sea fluxes (described in section 2.1). For the purpose of examining the modification of water characteristics within the IO, only the first 50 years of the trajectories were considered. We noted from Figure 5 that more than 75% of water from the Pacific and the marginal seas reaches the Atlantic within 50 years. Figure 7 shows normalized transports binned according to potential temperature θ, salinity S, potential density anomaly σ_0, and depth of particles at their origins, at the first time they cross meridional and zonal sections across the IO, and finally as they exit across GoodHope within 50 years (sections shown in Figure 4). In the upper plot of Figure 7, the two distributions for "Init" are equivalent.

Waters from the marginal seas of the IO are typically characterized by their high salinities [*Beal et al*., 2000; *Bower et al*., 2000; *Chowdary et al*., 2005]. Initially waters from the Gulfs of Oman and Aden have distinct characteristics ($\theta > 20$°C; S > 35.5), as evidenced by the shapes of the respective distributions (Figures 7a and 7b) being narrow and single peaked. Since only first crossing is considered, the broadening of the respective salinity distributions along 10°N indicates that these waters rapidly mix with ambient waters of the Arabian Sea. From this point, they become indistinguishable. Between 10°N and the Equator, while the potential temperature distributions of PGW and RSW waters remain alike, a salient freshening is noted. Furthermore, the initial θ–S signatures of the waters are lost. The densest RSW waters at intermediate depths ($\sigma_0 > 25$ kg/m^3) however maintain some of their relatively high salinity signatures. During the transit within the southern IO, the salinities remain relatively similar, but a gradual cooling occurs. Waters that do not directly exit at GH, and instead first recirculate within the south IO subtropical gyre undergo further erosion in properties.

Pacific waters through the Indonesian Archipelago are characterized by their relatively lower salinities (S < 35.5) and broad potential temperature distribution. The direct and fast (cf. Figure 5) westward advection within the South Equatorial Current results in little change in water properties. Upon reaching Madagascar along 47°E and further west, shifts in distributions are noted indicating mixing (Figure 7c).

Waters entering the IO south of Australia are predominantly confined at intermediate depths between 500 and 1000 m, and undergo only slight changes in properties as they transit westward across the basin. The reduction in amplitude and slight broadening of the distributions (Figure 7d) indicate minor erosion of properties and mixing with surrounding water masses below and above.

Within the model, waters from the Gulf of Oman lose their initial characteristics rapidly within the Arabian Sea. South of the Equator, their high salinity signature is no longer detectable. This is similar to surface waters from the Gulf of Aden. At intermediate depths, a very small amount of high salinity waters from the Red Sea persists into the southern IO (model deficit discussed in section 3.1). In contrast to the rapid decay of waters from the marginal seas, waters from the Pacific north and south of Australia maintain their properties for most of their westward crossing. At GoodHope, the properties of waters originating from the Gulfs and from the ITF are almost indistinguishable (Figures 7a–7c), consistent with the volumetric depth distribution (Figure 6a). In contrast, the properties of waters from south of Australia cross GoodHope almost intact.

In general, water modification is possible by either mixing with ambient waters or via surface fluxes. We first consider the former. Salinity fields in the IO along the isopycnals at which water from the four source regions enter the basin show that the largest gradients occur in the northern IO (Figure 8). Waters from the Gulfs enter a region of sharp contrast in the Arabian Sea favoring immediate isopycnal mixing. ITF enters the IO basin over a relatively broad range of densities in the upper 500 m. At its surface and subsurface-intensified core (σ_0 22–23 kg/m^3), it enters the basin in regions of weaker salinity gradients. Along isopycnal mixing starts to occur at about 80°E and is gradual until Madagascar (47°E). Weak gradients in the southern IO, in addition to little to no contact with the surface and weak recirculations in the southwest IO, result in water from TL transiting the basin experiencing only minor erosion.

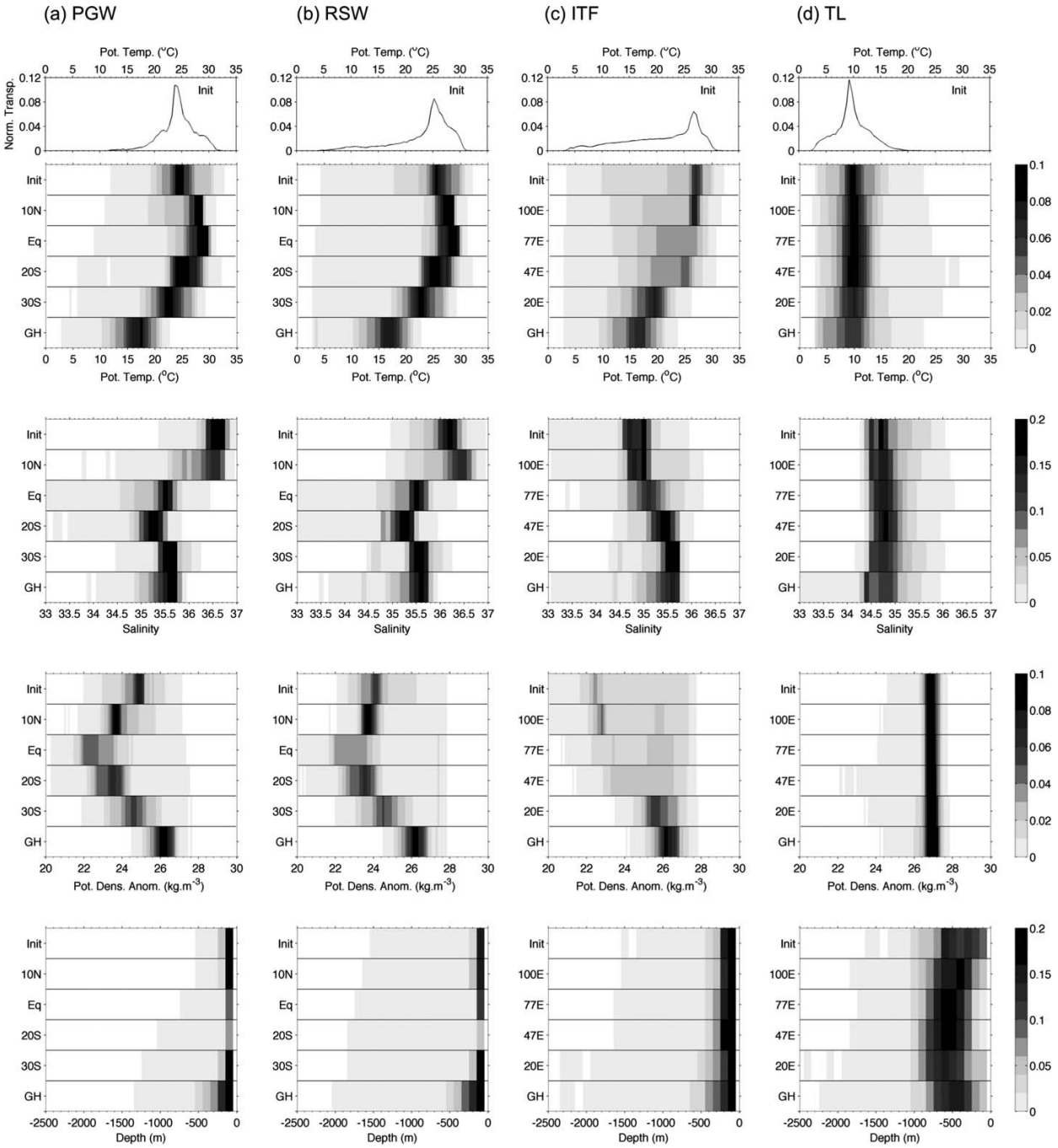

Figure 7. Normalized transports (units Sv/Sv) binned by potential temperature (upper plot, °C), salinity (middle-upper plot), potential density anomaly (σ_0, middle-lower plot, kg/m^3), and depth (lower plot, m) at the initial positions (Init), at the first crossing of 4 meridional/zonal sections across the Indian Ocean basin (sections shown in Figure 4), and at GoodHope (GH). In the upper plot, the potential temperature "Init" histogram and the "Init" strip are equivalent, in that the horizontal strip is a top view of the histogram. The transport distributions were normalized by the total transport of each component: (a) 0.1 Sv, (b) 0.5 Sv, (c) 4.6 Sv, and (d) 3.7 Sv entering the Atlantic within 50 years from PGW, RSW, ITF, and TL, respectively. The bin intervals are 0.5°C, 0.1, 0.1 kg/m^3, and 100 m, respectively.

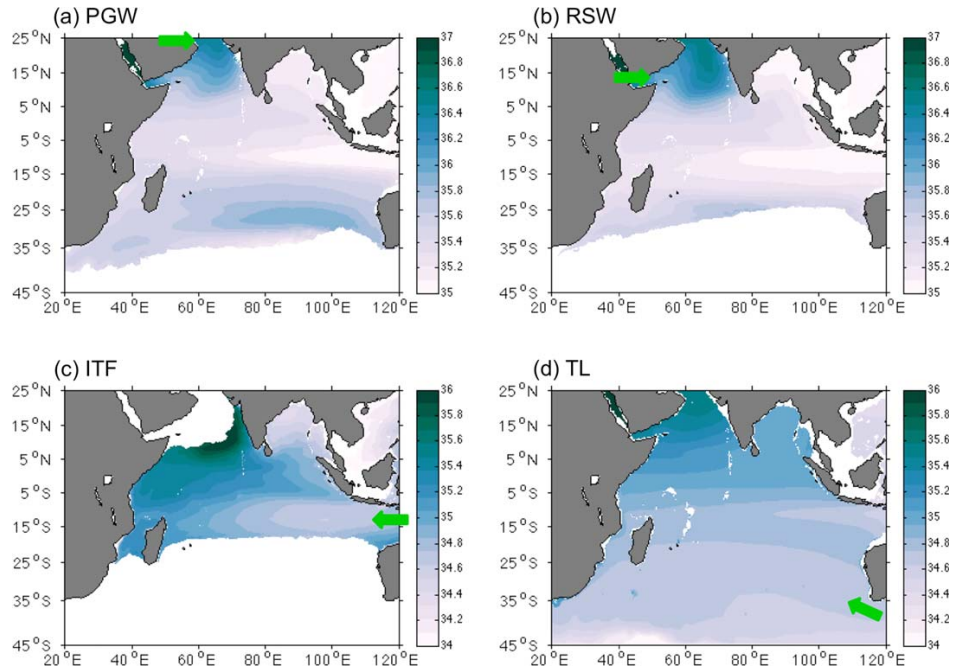

Figure 8. Salinity from the Eulerian fields averaged over density classes representative of the bulk of water entering the Indian Ocean basin (initial sections, green arrows) for the period 1963–1992 from PGW (σ_0 = 24.5–25.5 kg/m^3), RSW (σ_0 = 23.5–24.5 kg/m^3), ITF (σ_0 = 22.0–23.0 kg/m^3), and TL (σ_0 = 26.5–27.5 kg/m^3).

Biastoch et al. [2015] calculated the heat transport across GoodHope within a model with different atmospheric forcing by integrating full-depth from Africa to the dynamic boundary delineated by the Subtropical Front. Applying the same method, we obtain 0.35 ± 0.04 PW (1963–2012, using annual-mean values), which roughly agrees with their estimate. Does the heat exported across GoodHope come from the Pacific, or mostly set by surface fluxes within the IO basin? Waters from the Gulfs and ITF lie predominantly in the upper 250 m (lower plot Figure 7) and therefore experience modifications resulting from surface fluxes. Within the model and in agreement with observations (not shown), the net surface heat flux exhibits a flux into the ocean in the northern IO, and flux to the atmosphere within the subtropical gyre and the greater Agulhas Current system. Since volume is conserved for all particles, integrating under the curves of Figure 7 (upper plot) yields normalized transport weighed potential temperature (TWT) values for the bulk of the water from the four origins. At the source (init), the waters entering the IO have a TWT of 16°C (PGW = 24°C, RSW = 23°C, ITF = 21°C, TL = 10°C). Overall, at GoodHope, the waters are 3°C cooler (PGW = 16°C, RSW = 15°C, ITF = 15°C, TL = 9°C), suggesting that the IO cools the waters it receives. Figure 7 shows that this cooling occurs over the greater Agulhas Current system, consistent with the model's net heat flux to the atmosphere. In the Arabian Sea, north of the Equator, the temperature distributions of PGW and RSW indicate heat gain, which is also consistent with the sign of the net heat flux there. This therefore suggests that exchange with the atmosphere over the IO basin is an important factor determining the heat exported to the South Atlantic.

The fresh water export of the IO is −192 ± 34 mSv (also calculated following *Biastoch et al.* [2015] and agree with their value), and for the most part, waters from the ITF salinificate, while those from the Gulfs freshen.

4. Summary and Conclusions

We investigated the mean pathways, transit timescales, and transformation of waters flowing from the Pacific Ocean and the marginal seas through the Indian Ocean (IO) on their way toward the South Atlantic. Lagrangian analyses of Eulerian fields from a high-resolution ocean/sea-ice model were performed. Particles were released over a period of 30 model years along sections that define the entry points of water into the IO basin: at the mouths of the Gulfs of (1) Oman and (2) Aden, (3) north and (4) south of Australia. The

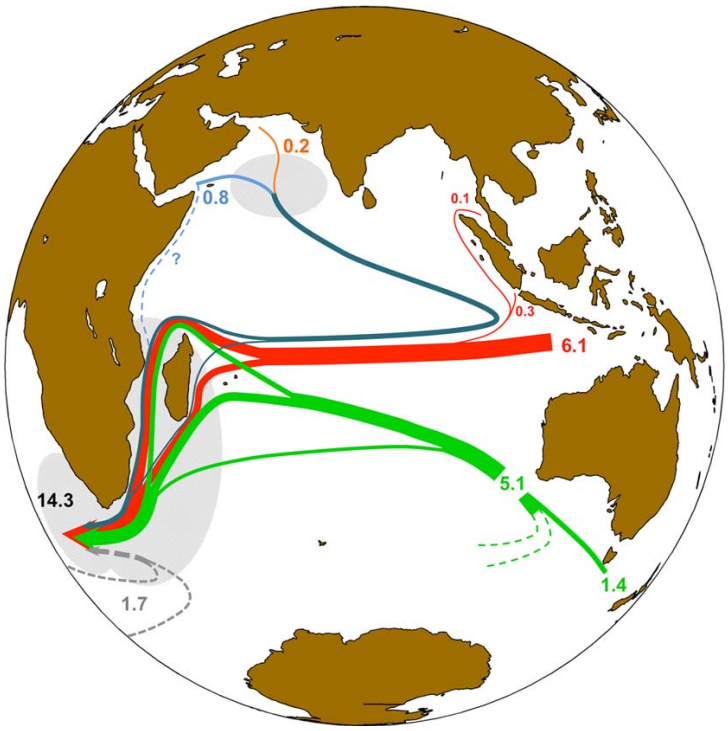

Figure 9. Schematic decomposition of sources of Agulhas leakage and their mean pathways within the Indian Ocean. Line/arrow thickness represents the different transport (Sv) contribution (see table in Figure 4). Indonesian Through-flow (red) additionally receives water from Sunda and Malacca Straits. Waters from south of Australia (green) consist of Tasman leakage and recirculations. Waters from the Gulfs (blue and orange), leaving the Arabian Sea share similar properties (represented thereafter in teal). A possible route from the Gulf of Aden along western Africa is shown but not quantified (dashed blue, see text for details). Finally, Agulhas leakage also receives water from the Atlantic (dashed grey arrow). Grey shaded areas denote region where strongest changes in water properties occur.

experiments were design so as to decompose and quantify the constituents of the exhaust of the IO, namely Agulhas leakage, and to determine whether the IO acts as a passive connector or plays an active role as a modifier.

Agulhas leakage (AL) in the model is roughly 14 Sv, which is within the observed range (section 3.1). Based on results from this study, Figure 9 shows the volumetric decomposition and the pathways of the sources of AL. The principal contributor of AL comes from north of Australia as Indonesian Through-Flow (ITF, 45%, 6.5 Sv). More than half of that water flows through the Mozambique Channel within 5 years, where it is mostly confined in the upper 500 m along the African coast. Waters from Sunda and Malacca Straits were not explicitly discussed here. They contribute around 0.4 Sv to AL. The second contributor of AL, 5.1 Sv, originates from south of Australia, of which 30% (1.4 Sv) come directly from the Pacific as Tasman leakage, and the rest from recirculations from the frontal regions of the Southern Ocean. Within the IO, these waters sit at intermediate depths and slowly transit westward within the subtropical gyre, reaching the Agulhas Current in about 2 decades mostly via the Southeast Madagascar Current (50%). About 20% flows directly into the Agulhas Current. In the model waters from the Gulfs contributing to AL (1.0 Sv) have similar pathways, which first consist of a detour toward the northeastern IO before subsequently converging within the boundary currents on either side of Madagascar. Deficits in the model result in a negative density bias (lighter than observed) for waters entering the IO from the Gulf of Aden. Therefore, their pathways north of 10°S portrayed in Figure 9 may be overly influence by the seasonally reversing upper ocean circulation there. Consequently, while our results do not suggest a direct route from the Gulf of Aden along western Africa (blue dashed line in Figure 9) as reported by *Beal et al*. [2000], we cannot discount it as a possible route. Finally, also not explicitly considered in this study, about 1.7 Sv of AL originate from the South Atlantic, possibly from mode water recirculation and from Drake Passage.

In the Cape Basin, we showed in Figures 6a and 7 that the source waters of AL are well mixed throughout the water column. On route, however, each individual component loses their original temperature and salinity characteristics at different locations due to mixing with ambient waters and/or surface fluxes. This occurs in the Arabian Sea for water from the Gulfs and in the larger Agulhas Current system for waters from the Gulfs and ITF (grey shading in Figure 9). However, water from south of Australia experiences very little modifications in properties during transit. The location and degree of mixing depend on the characteristics of the ambient waters such that the stronger the isopycnal gradient, the more potential for mixing (Figure 8). Therefore, the IO acts not only as a connector, but also as a modifier of water it receives from the Pacific and the marginal seas.

More profoundly Figure 9 shows that the IO exports 7.9 Sv from the Pacific to the Atlantic within 100 years. From a simple *Broeker* [1991] circulation point of view, this value therefore corresponds to the strength of the upper cell of the global conveyor belt. In other words, irrespective of the driving mechanisms, at least 7.9 Sv is the Pacific contribution to the so-called Atlantic warm-water route within this model. Due to the Lagrangian experiment design and in particular the duration of the integration, this value is given as a lower bound.

Of interest is to understand how an anomaly in properties in one of the sources would be communicated across the IO basin. For example, since the turn of the century, *Lee et al*. [2015] found an increase of about 0.2 PW in heat transport across the ITF (interannual heat transport difference 2003–2012), which also coincided with stronger through-flow, resulting from a prolonged negative phase of the Interdecadal Pacific Oscillation [*England et al*., 2014]. Our model simulates this increase as well. The question is whether (part of) this additional heat could be observed in the South Atlantic within the coming 1–2 decades? We found here that in the mean the IO cools and salinificates water coming from the ITF. Furthermore, based on our results, the efficiency at which the IO can communicate an anomaly across depends on the amplitude and duration of the anomaly, in addition to the characteristic of the ambient waters. In order to further address this question, sensitivity model experiments could be designed similar to *Lübbecke et al*. [2015] who assessed a warming signal transported across the South Atlantic from an increase in transport of Agulhas leakage.

Acknowledgments
The model data used for this study were kindly provided through collaboration within the DRAKKAR framework by the National Oceanographic Centre, Southampton, UK. We especially thank A.C. Coward and colleagues for making the data available. The Ariane-v2.2.6 Lagrangian package used can be obtained from http://www.univ-brest.fr/lpo/ariane/. Altimetry data for model validation were downloaded from http://aviso.oceanobs.com/. This work received funding from the Helmholtz Association and the GEOMAR Helmholtz Centre for Ocean Research Kiel (J.V.D., grant IV014/GH018), and the Cluster of Excellence "Future Ocean" (S.R., grant CP1412). The "Future Ocean" is funded within the framework of the Excellence Initiative by the Deutsche Forschungsgemeinschaft (DFG) on behalf of the German federal and state governments. The authors thank S. Lozier and C. Ummenhofer for helpful discussions of the results.

References

Al Saafani, M. A., S. S. C. Shenoi, D. Shankar, M. Aparna, J. Kurian, F. Durand, and P. N. Vinayachandran (2007), Westward movement of eddies into the Gulf of Aden from the Arabian Sea, *J. Geophys. Res.*, *112*, C11004, doi:10.1029/2006JC004020.

Beal, L. M., and K. A. Donohue (2013), The Great Whirl: Observations of its seasonal development and interannual variability, *J. Geophys. Res. Oceans*, *118*, 1–13, doi:10.1029/2012JC008198.

Beal, L. M., and S. Elipot (2016), Broadening not strengthening of the Agulhas Current since the early 1990s, *Nature*, *540*, 570–573, doi:10.1038/nature19853.

Beal, L. M., A. Ffield, and A. L. Gordon (2000), Spreading of Red Sea overflow waters since of the thickness influence, *J. Geophys. Res.*, *105*, 8549–8564.

Beal, L. M., T. K. Chereskin, Y. D. Lenn, and S. Elipot (2006), The sources and mixing characteristics of the Agulhas Current, *J. Phys. Oceanogr.*, *36*(11), 2060–2074, doi:10.1175/JPO2964.1.

Behera, S. K., et al. (2006), A CGCM study on the interaction between IOD and ENSO, *J. Clim.*, *19*(9), 1688–1705, doi:10.1175/JCLI3797.1.

Biastoch, A., J. R. E. Lutjeharms, C. W. Böning, and M. Scheinert (2008), Mesoscale perturbations control inter-ocean exchange south of Africa, *Geophys. Res. Lett.*, *35*, L20602, doi:10.1029/2008GL035132.

Biastoch, A., J. V Durgadoo, A. K. Morrison, E. van Sebille, W. Weijer, and S. M. Griffies (2015), Atlantic multi-decadal oscillation covaries with Agulhas leakage, *Nat. Commun.*, *6*, doi:10.1038/ncomms10082. [Available at https://www.nature.com/articles/ncomms10082.]

Blanke, B., and S. Raynaud (1997), Kinematics of the Pacific Equatorial Undercurrent: An Eulerian and Lagrangian approach from GCM results, *J. Phys. Oceanogr.*, *27*, 1038–1053, doi:10.1175/1520-0485(1997)027 < 1038:KOTPEU>2.0.CO;2.

Blanke, B., M. Arhan, G. Madec, and S. Roche (1999), Warm water paths in the equatorial atlantic as diagnosed with a general circulation model, *J. Phys. Oceanogr.*, *29*(11), 2753–2768, doi:10.1175/1520-0485(1999)029 < 2753:WWPITE>2.0.CO;2.

Bower, A. S., H. D. Hunt, and J. F. Price (2000), Character and dynamics of the Red Sea and Persian Gulf outflows, *J. Geophys. Res.*, *105*, 6387–6414.

Bower, A. S., D. M. Fratantoni, W. E. Johns, and H. Peters (2002), Gulf of Aden eddies and their impact on Red Sea Water, *Geophys. Res. Lett.*, *29*(21), 2025, doi:10.1029/2002GL015342.

Brodeau, L., B. Barnier, A.-M. Treguier, T. Penduff, and S. Gulev (2010), An ERA40-based atmospheric forcing for global ocean circulation models, *Ocean Modell.*, *31*(3), 88–104, doi:10.1016/j.ocemod.2009.10.005.

Broeker, W. (1991), The Great Ocean Conveyor, *Oceanography*, *4*(2), 79–89, doi:10.5670/oceanog.1991.07.

Chowdary, J. S., C. Gnanaseelan, B. Thompson, and P. S. Salvekar (2005), Water mass properties and transports in the Arabian Sea from Argo observations, *J. Atmos. Ocean Sci.*, *10*(3), 235–260, doi:10.1080/17417530600752825.

Döös, K., J. Nycander, and A. C. Coward (2008), Lagrangian decomposition of the Deacon Cell, *J. Geophys. Res.*, *113*, C07028, doi:10.1029/2007JC004351.

Durgadoo, J. V., B. R. Loveday, C. J. C. Reason, P. Penven, and A. Biastoch (2013), Agulhas leakage predominantly responds to the Southern Hemisphere Westerlies, *J. Phys. Oceanogr.*, *43*(10), 2113–2131, doi:10.1175/JPO-D-13-047.1.

Dussin, R., B. Barnier, and L. Brodeau (2014), The making of Drakkar forcing set DFS5, *DRAKKAR/MYOcean Rep. 05-10-14*, LGGE, Grenoble, France.

England, M. H., S. McGregor, P. Spence, G. A. Meehl, A. Timmermann, W. Cai, A. Sen Gupta, M. J. McPhaden, A. Purich, and A. Santoso (2014), Recent intensification of wind-driven circulation in the Pacific and the ongoing warming hiatus, *Nat. Clim. Change*, *4*(3), 222–227, doi:10.1038/nclimate2106.

Feng, M., C. Böning, A. Biastoch, E. Behrens, E. Weller, and Y. Masumoto (2011), The reversal of the multi-decadal trends of the equatorial Pacific easterly winds, and the Indonesian Throughflow and Leeuwin Current transports, *Geophys. Res. Lett.*, *38*, L11604, doi:10.1029/2011GL047291.

Fischer, J., F. Schott, and L. Stramma (1996), Currents and transports of the Great Whirl-Socotra Gyre system during the summer monsoon, August 1993, *J. Geophys. Res.*, *101*, 3573–3587.

Fratantoni, D. M., A. S. Bower, W. E. Johns, and H. Peters (2006), Somali Current rings in the eastern Gulf of Aden, *J. Geophys. Res.*, *111*, C09039, doi:10.1029/2005JC003338.

Gordon, A. L., S. Ma, D. B. Olson, P. Hacker, A. Ffield, L. D. Talley, D. Wilson, and M. Baringer (1997), Advection and diffusion of Indonesian Throughflow Water within the Indian Ocean South Equatorial Current, *Geophys. Res. Lett.*, *24*, 2573–2576.

Haines, M. A., R. A. Fine, M. E. Luther, and Z. Ji (1999), Particle trajectories in an Indian Ocean Model and sensitivity to seasonal forcing, *J. Phys. Oceanogr.*, *29*(4), 584–598, doi:10.1175/1520-0485(1999)029 < 0584:PTIAIO>2.0.CO;2.

Hallberg, R. (2013), Using a resolution function to regulate parameterizations of oceanic mesoscale eddy effects, *Ocean Modell.*, *72*, 92–103, doi:10.1016/j.ocemod.2013.08.007.

L'Hégaret, P., R. Duarte, X. Carton, C. Vic, D. Ciani, R. Baraille, and S. Corréard (2015), Mesoscale variability in the Arabian Sea from HYCOM model results and observations: Impact on the Persian Gulf Water path, *Ocean Sci.*, *11*(5), 667–693, doi:10.5194/os-11-667-2015.

Joseph, B., and P. S. Swathi (1999), Lagrangian particle transport in the Indian Ocean: A model study tank, *J. Geophys. Res.*, *104*, 5211–5224.

Jourdan, D., E. Balopoulos, M.-J. Garcia-Fernandez, and C. Maillard (1998), Objective analysis of temperature and salinity historical data set over the Mediterranean basin, in *IEEE Oceanic Engineering Society. OCEANS'98. Conference Proceedings (Cat. 98CH36259)*, vol. 1, pp. 82–87, IEEE. [Available at http://ieeexplore.ieee.org/stamp/stamp.jsp?arnumber=725649.]

Le Bars, D., H. A. Dijkstra, and W. P. M. De Ruijter (2013), Impact of the Indonesian Throughflow on Agulhas leakage, *Ocean Sci.*, *9*(5), 773–785, doi:10.5194/os-9-773-2013.

Lee, S.-K., W. Park, M. O. Baringer, A. L. Gordon, B. Huber, and Y. Liu (2015), Pacific origin of the abrupt increase in Indian Ocean heat content during the warming hiatus, *Nat. Geosci.*, *8*, 445–449, doi:10.1038/ngeo2438.

Legg, S., et al. (2009), Improving oceanic overflow representation in climate models: The Gravity Current Entrainment Climate Process Team, *Bull. Am. Meteorol. Soc.*, *90*(5), 657–670, doi:10.1175/2008BAMS2667.1.

Levitus, S., M. Conkright, T. P. Boyer, T. O'Brian, J. Antonov, C. Stephens, L. S. D. Johnson, R. Gelfeld (1998), World ocean database 1998, *Tech. Rep. NOAA Atlas NESDIS 18*, U.S. Gov. Print. Off., Washington, D. C.

Liu, Q.-Y., M. Feng, D. Wang, and S. Wijffels (2015), Interannual variability of the Indonesian Throughflow transport: A revisit based on 30 year expendable bathythermograph data, *J. Geophys. Res. Oceans*, *120*, 8270–8282, doi:10.1002/2015JC011351.

Lozier, M. S. (2010), Deconstructing the conveyor belt, *Science*, *328*(5985), 1507–1511, doi:10.1126/science.1189250.

Lübbecke, J. F., J. V. Durgadoo, and A. Biastoch (2015), Contribution of increased agulhas leakage to tropical Atlantic warming, *J. Clim.*, *28*(24), 9697–9706, doi:10.1175/JCLI-D-15-0258.1.

Lutjeharms, J. R. E. (2006), *The Agulhas Current*, Springer, Berlin Heidelberg.

Lutjeharms, J. R. E., and I. J. Ansorge (2001), The Agulhas Return Current, *J. Mar. Syst.*, *30*(1–2), 115–138, doi:10.1016/S0924-7963(01)00041-0.

Madec, G., and the NEMO team (2016), *NEMO ocean engine*, Note du Pôle de modélisation, Institut Pierre-Simon Laplace (IPSL), *27*, France. [Available at http://www.nemo-ocean.eu/About-NEMO/Reference-manuals.]

Meyers, G. (1996), Variation of Indonesian throughflow and the El Niño-Southern Oscillation, *J. Geophys. Res.*, *101*, 12,255–12,263.

Moat, B. I., et al. (2016), Major variations in subtropical North Atlantic heat transport at short (5 day) timescales and their causes, *J. Geophys. Res. Oceans*, *121*, 3237–3249, doi:10.1002/2016JC011660.

Nauw, J. J., H. M. van Aken, A. Webb, J. R. E. Lutjeharms, and W. P. M. de Ruijter (2008), Observations of the southern East Madagascar Current and undercurrent and countercurrent system, *J. Geophys. Res.*, *113*, C08006, doi:10.1029/2007JC004639.

Ou, H., and W. de Ruijter (1986), Separation of an inertial boundary current from a curved coastline., *J. Phys. Oceanogr.*, *16*, 280–289.

Prasad, T. G., M. Ikeda, and S. P. Kumar (2001), Seasonal spreading of the Persian Gulf Water mass in the Arabian Sea, *J. Geophys. Res.*, *106*, 17,059–17,071.

Qin, X., E. van Sebille, and A. Sen Gupta (2014), Quantification of errors induced by temporal resolution on Lagrangian particles in an eddy-resolving model, *Ocean Modell.*, *76*, 20–30, doi:10.1016/j.ocemod.2014.02.002.

Richardson, P. L. (2007), Agulhas leakage into the Atlantic estimated with subsurface floats and surface drifters, *Deep Sea Res., Part I*, *54*(8), 1361–1389, doi:10.1016/j.dsr.2007.04.010.

Richardson, P. L. (2008), On the history of meridional overturning circulation schematic diagrams, *Prog. Oceanogr.*, *76*(4), 466–486, doi:10.1016/j.pocean.2008.01.005.

Ridgway, K. R., and J. R. Dunn (2007), Observational evidence for a Southern Hemisphere oceanic supergyre, *Geophys. Res. Lett.*, *34*, L13612, doi:10.1029/2007GL030392.

Rimaud, J., S. Speich, B. Blanke, and N. Grima (2012), The exchange of Intermediate Water in the southeast Atlantic: Water mass transformations diagnosed from the Lagrangian analysis of a regional ocean model, *J. Geophys. Res.*, *117*, C08034, doi:10.1029/2012JC008059.

Rintoul, S. R., and S. Sokolov (2001), Baroclinic transport variability of the Antarctic Circumpolar Current south of Australia (WOCE repeat section SR3), *J. Geophys. Res.*, *106*, 2815–2832.

Roman, R. E., and J. R. E. Lutjeharms (2007), Red Sea Intermediate Water at the Agulhas Current termination, *Deep Sea Res., Part I*, *54*(8), 1329–1340, doi:10.1016/j.dsr.2007.04.009.

Rosell-Fieschi, M., S. R. Rintoul, J. Gourrion, and J. L. Pelegrí (2013), Tasman leakage of intermediate waters as inferred from Argo floats, *Geophys. Res. Lett.*, *40*, 5456–5460, doi:10.1002/2013GL057797.

Rühs, S., J. V. Durgadoo, E. Behrens, and A. Biastoch (2013), Advective timescales and pathways of Agulhas leakage, *Geophys. Res. Lett.*, *40*, 3997–4000, doi:10.1002/grl.50782.

Rusciano, E., S. Speich, and M. Ollitrault (2012), Interocean exchanges and the spreading of Antarctic Intermediate Water south of Africa, *J. Geophys. Res.*, *117*, C10010, doi:10.1029/2012JC008266.

Saji, N. H., B. N. Goswami, P. N. Vinayachandran, and T. Yamagata (1999), A dipole mode in the tropical Indian Ocean, *Nature*, *401*(6751), 360–363.

Sallée, J. B., N. Wienders, K. Speer, and R. Morrow (2006), Formation of subantarctic mode water in the southeastern Indian Ocean, *Ocean Dyn.*, *56*(5–6), 525–542, doi:10.1007/s10236-005-0054-x.

Schott, F. A., and J. Fischer (2000), Winter monsoon circulation of the northern Arabian Sea and Somali Current, *J. Geophys. Res.*, *105*, 6359–6376.
Schott, F. A., and J. P. McCreary (2001), The monsoon circulation of the Indian Ocean, *Prog. Oceanogr.*, *51*(1), 1–123, doi:10.1016/S0079-6611(01)00083-0.
Schott, F. A., S.-P. Xie, and J. P. McCreary (2009), Indian Ocean Circulation and climate variability, *Rev. Geophys.*, *47*, 1–46, doi:10.1029/2007RG000245.
Schulze, L. M. (2016), Freshwater fluxes and vertical mixing in the Labrador Sea, doctoral thesis, 198 pp., Univ. of Southampton, Ocean & Earth Sci., Southampton, U. K. [Available at http://eprints.soton.ac.uk/391105/.]
Sofianos, S. S., and W. E. Johns (2002), An Oceanic General Circulation Model (OGCM) investigation of the Red Sea circulation, 1. Exchange between the Red Sea and the Indian Ocean, *J. Geophys. Res.*, *107*(C11), 3196, doi:10.1029/2001JC001184.
Song, Q., A. L. Gordon, and M. Visbeck (2004), Spreading of the Indonesian Throughflow in the Indian Ocean*, *J. Phys. Oceanogr.*, *34*, 772–792, doi:10.1175/1520-0485(2004)034<0772:SOTITI>2.0.CO;2.
Speich, S., B. Blanke, P. de Vries, S. S. Drijfhout, K. Döös, A. Ganachaud, and R. Marsh (2002), Tasman leakage: A new route in the global ocean conveyor belt, *Geophys. Res. Lett.*, *29*(10), 1416, doi:10.1029/2001GL014586.
Speich, S., B. Blanke, and W. Cai (2007), Atlantic meridional overturning circulation and the Southern Hemisphere supergyre, *Geophys. Res. Lett.*, *34*, L23614, doi:10.1029/2007GL031583.
Sprintall, J., S. E. Wijffels, R. Molcard, and I. Jaya (2009), Direct estimates of the Indonesian Throughflow entering the Indian Ocean: 2004–2006, *J. Geophys. Res.*, *114*, C07001, doi:10.1029/2008JC005257.
Steele, M., R. Morfley, and W. Ermold (2001), PHC: A global ocean hydrography with high-quality Artic Ocean, *J. Clim.*, *14*, 2079–2087, doi:10.1175/1520-0442(2001)014 < 2079:PAGOHW>2.0.CO;2.
Stramma, L., and M. England (1999), On the water masses and mean circulation of the South Atlantic Ocean, *J. Geophys. Res.*, *104*, 20,863.
Swallow, J., M. Fieux, and F. Schott (1988), The boundary currents east and north of Madagascar: 1. Geostrophic currents and transports, *J. Geophys. Res.*, *93*, 4951.
Swallow, J. C., F. Schott, and M. Fieux (1991), Structure and transport of the East African Coastal Current, *J. Geophys. Res.*, *96*, 22,245.
The DRAKKAR Group (2007), Eddy-permitting ocean circulation hindcasts of past decades, in CLIVAR Exchanges, vol. 12, pp. 8–14. [Available at http://www.clivar.org/node/193.]
Tillinger, D., and A. L. Gordon (2009), Fifty years of the Indonesian Throughflow, *J. Clim.*, *22*(23), 6342–6355, doi:10.1175/2009JCLI2981.1.
Ullgren, J. E., H. M. van Aken, H. Ridderinkhof, and W. P. M. de Ruijter (2012), The hydrography of the Mozambique Channel from six years of continuous temperature, salinity, and velocity observations, *Deep Sea Res., Part I*, *69*, 36–50, doi:10.1016/j.dsr.2012.07.003.
Ummenhofer, C. C., F. U. Schwarzkopf, G. Meyers, E. Behrens, A. Biastoch, and C. W. Böning (2013), Pacific Ocean contribution to the asymmetry in Eastern Indian Ocean variability, *J. Clim.*, *26*(4), 1152–1171, doi:10.1175/JCLI-D-11-00673.1.
van Sebille, E., P. J. van Leeuwen, A. Biastoch, and W. P. M. De Ruijter (2010), On the fast decay of Agulhas rings, *J. Geophys. Res.*, *115*, C03010, doi:10.1029/2009JC005585.
van Sebille, E., L. M. Beal, and W. E. Johns (2011), Advective time scales of Agulhas leakage to the North Atlantic in surface drifter observations and the 3D OFES model, *J. Phys. Oceanogr.*, *41*(1947), 1026–1034, doi:10.1175/2011JPO4602.1.
van Sebille, E., M. H. England, J. D. Zika, and B. M. Sloyan (2012), Tasman leakage in a fine-resolution ocean model, *Geophys. Res. Lett.*, *39*, L06601, doi:10.1029/2012GL051004.
van Sebille, E., J. Sprintall, F. U. Schwarzkopf, A. Sen Gupta, A. Santoso, M. H. England, A. Biastoch, and C. W. Böning (2014), Pacific-to-Indian Ocean connectivity: Tasman leakage, Indonesian Throughflow, and the role of ENSO, *J. Geophys. Res. Oceans*, *119*, 1365–1382, doi:10.1002/2013JC009525.
Wijffels, S. E., G. Meyers, and J. Stuart Godfrey (2008), A 20-Yr average of the Indonesian Throughflow: Regional currents and the interbasin exchange, *J. Phys. Oceanogr.*, *38*, 1965–1978, doi:10.1175/2008JPO3987.1.
You, Y. (1998), Intermediate water circulation and ventilation of the Indian Ocean derived from water-mass contributions, *J. Mar. Res.*, *56*, 1029–1067, doi:10.1357/002224098765173455.
You, Y., and M. Tomczak (1993), Thermocline circulation and ventilation in the Indian Ocean derived from water mass analysis, *Deep Sea Res., Part I*, *40*(1), 13–56, doi:10.1016/0967-0637(93)90052-5.
You, Y., J. R. E. Lutjeharms, O. Boebel, and W. P. M. de Ruijter (2003), Quantification of the interocean exchange of intermediate water masses around southern Africa, *Deep Sea Res., Part II*, *50*(1), 197–228, doi:10.1016/S0967-0645(02)00384-3.

5

Study 3: Eddy diffusivity estimates from Lagrangian trajectories simulated with ocean models and surface drifter data

This study presents an analysis of near-surface lateral eddy diffusivity estimates obtained from Lagrangian trajectories simulated with an eddy-rich and an eddy-poor ocean model for the greater Agulhas system. Moreover, it includes the first comprehensive comparison of Lagrangian eddy diffusivity estimates from simulated Lagrangian trajectories and observed drifter trajectories for that region. Notably, Lagrangian eddy diffusivities from the high-resolution model are consistent with the pattern and magnitude of drifter-based eddy diffusivity estimates — without the need for an additional diffusion parametrization in the trajectory calculation. It further emphasizes the fact that the implementation of such a diffusion parametrization for trajectories simulated in coarser resolution models is a non-trivial task, since one has to consider spatial variability of the diffusivity parameter, which does not necessarily scale with variability in eddy kinetic energy, as well as possible Eulerian subgrid-scale parameterizations.

The chapter has been published in the Journal of Physical Oceanography:

Rühs, S., Zhurbas, V., Koszalka, I. M., Durgadoo, J. V., and A. Biastoch (2018): *Eddy diffusivity estimates from Lagrangian trajectories simulated with ocean models and surface drifter data - a case study for the greater Agulhas system*. Journal of Physical Oceanography, 48(1), 175–196, doi:10.1175/JPO-D-17-0048.1.

My personal contribution to the publication has been the following:
defining the research problem and methodology, performing Lagrangian trajectory calculations, performing and analyzing diffusivity calculations from simulated trajectories, comparing diffusivity estimates from simulated and observed particle dispersal, producing all figures, and writing the paper.

Eddy Diffusivity Estimates from Lagrangian Trajectories Simulated with Ocean Models and Surface Drifter Data—A Case Study for the Greater Agulhas System

SIREN RÜHS

GEOMAR Helmholtz Centre for Ocean Research Kiel, Kiel, Germany

VICTOR ZHURBAS

Shirshov Institute of Oceanology, Moscow, Russia

INGA M. KOSZALKA

GEOMAR Helmholtz Centre for Ocean Research Kiel, and Christian-Albrechts University of Kiel, Kiel, Germany

JONATHAN V. DURGADOO AND ARNE BIASTOCH

GEOMAR Helmholtz Centre for Ocean Research Kiel, Kiel, Germany

(Manuscript received 10 March 2017, in final form 10 October 2017)

ABSTRACT

The Lagrangian analysis of sets of particles advected with the flow fields of ocean models is used to study connectivity, that is, exchange pathways, time scales, and volume transports, between distinct oceanic regions. One important factor influencing the dispersion of fluid particles and, hence, connectivity is the Lagrangian eddy diffusivity, which quantifies the influence of turbulent processes on the rate of particle dispersal. Because of spatial and temporal discretization, turbulence is not fully resolved in modeled velocities, and the concept of eddy diffusivity is used to parameterize the impact of unresolved processes. However, the relations between observation- and model-based Lagrangian eddy diffusivity estimates, as well as eddy parameterizations, are not clear. This study presents an analysis of the spatially variable near-surface lateral eddy diffusivity estimates obtained from Lagrangian trajectories simulated with 5-day mean velocities from an eddy-resolving ocean model (INALT01) for the Agulhas system. INALT01 features diffusive regimes for dynamically different regions, some of which exhibit strong suppression of eddy mixing by mean flow, and it is consistent with the pattern and magnitude of drifter-based eddy diffusivity estimates. Using monthly mean velocities decreases the estimated diffusivities less than eddy kinetic energy, supporting the idea that large and persistent eddy features dominate eddy diffusivities. For a noneddying ocean model (ORCA05), Lagrangian eddy diffusivities are greatly reduced, particularly when the Gent and McWilliams parameterization of mesoscale eddies is employed.

1. Motivation

Over the past decades, the Lagrangian analysis of fluid motion by following floating instruments has been used to investigate ocean general circulation patterns (e.g., Davis 1991a,b; Poulain 2001; Lumpkin and Johnson 2013; Lumpkin et al. 2017). Additionally, an increasing number of Lagrangian analyses are performed by advecting virtual fluid particles with the simulated flow fields of ocean models (van Sebille et al. 2018). They are employed in large-scale oceanography to study the sources, fates, and transformations of water masses (Speich et al. 2001; Lique et al. 2010; Koszalka et al. 2013a,b; Gary et al. 2014; Durgadoo et al. 2017) and are particularly suited to quantify connectivity between different oceanic sites, that is, preferential linking pathways (e.g., Rühs et al. 2013; van Sebille et al. 2013, 2014) and associated time scales (e.g., Blanke et al. 2002; van Sebille et al. 2011; Koszalka et al. 2013a;

Denotes content that is immediately available upon publication as open access.

Supplemental information related to this paper is available at the Journals Online website: https://doi.org/10.1175/JPO-D-17-0048.s1.

Corresponding author: Siren Rühs, sruehs@geomar.de

DOI: 10.1175/JPO-D-17-0048.1

Rühs et al. 2013), as well as volume, freshwater, and heat transports (e.g., Blanke et al. 2001; Biastoch et al. 2008b; Döös et al. 2012).

One important factor influencing large-scale (~1000 km) connectivity is the average rate at which particles disperse. Turbulent processes, such as mesoscale (10–100 km) eddies and jets, cause fluid particles to disperse quickly and increase the rate of mass, momentum, and tracer spreading, leading to accelerated mixing (LaCasce 2008). Turbulent flow is often described via Reynolds decomposition in terms of a long-term (or slowly varying) mean velocity and the residual eddy component. Analogously, the concept of Lagrangian eddy diffusivity is used to quantify the rate of dispersal related to the cumulative effect of eddies. Depending on the definition of the mean flow, the residual eddy component may include not only mesoscale, but also seasonal-to-interannual (Rieck et al. 2015; Laurindo et al. 2017; Uchida et al. 2017) or smaller-scale (if resolved but not low-pass filtered) variability, or may specifically refer to processes not resolved by a certain flow field (Rypina et al. 2016). In this study, we focus primarily on mesoscale eddy variability.

Owing to spatial and temporal discretization, turbulent processes are not fully resolved in modeled velocity fields, but are parameterized instead. Simulated advective Lagrangian trajectories capture the resolved turbulence but only implicitly include the effect of subgrid-scale parameterizations acting on the tracer and momentum equations, that is, by altered large-scale circulation patterns and along-track changes of temperature and salinity. This led to the notion that dispersal of advective Lagrangian trajectories is not sufficiently diffusive compared to particle dispersal in the real ocean. To circumvent this issue, Lagrangian diffusion parameterizations were introduced (Griffa 1996; Berloff and McWilliams 2002; Monti and Leuzzi 2010; Döös et al. 2011). These add an additional stochastic component to the advective particle displacements (or velocities or accelerations) and have already been employed in regional ocean circulation studies (De Dominicis et al. 2012; Koszalka et al. 2013b; Rypina et al. 2016).

However, compared to the vast number of large-scale Lagrangian applications with ocean models, there are few comprehensive validations of eddy diffusivities associated with the simulated particle dispersal. Numerous studies presented eddy diffusivity estimates derived from drifter data (e.g., Krauss and Böning 1987; Davis 1991a,b; Swenson and Niiler 1996; Poulain 2001; Lumpkin and Flament 2001; Bauer et al. 2002; Zhurbas and Oh 2004; Sallée et al. 2008; Koszalka et al. 2011; Zhurbas et al. 2014; Peng et al. 2015). Likewise, several studies addressed the diffusivity estimation using Lagrangian trajectories simulated with velocity fields from eddy-resolving ocean models (e.g., McClean et al. 2002; Koszalka and LaCasce 2010; Griesel et al. 2010, 2014; Chen et al. 2014; Wolfram et al. 2015). Yet there are only a handful of publications aiming at a quantitative comparison of eddy diffusivity estimates from drifter data and simulated trajectories (De Dominicis et al. 2012; Rypina et al. 2012, 2016). Additionally, the relations between Lagrangian eddy diffusivity estimates and the optimal choice of diffusivities to be used in stochastic Lagrangian parameterizations and in the Eulerian diffusion parameterizations employed in OGCM tracer equations are not well understood (van Sebille et al. 2018). Unresolved issues concern the difficulty to unequivocally define the mean flow and residual eddy component (Griesel et al. 2014), the spatial variability of eddy diffusivities associated with different turbulence regimes (Berloff and McWilliams 2002; Koszalka et al. 2011), and the sensitivity of model-based eddy diffusivity estimates to the temporal and spatial model resolution (Keating et al. 2011; Wolfram et al. 2015; van Sebille et al. 2018).

In this study, we address this gap by jointly assessing lateral near-surface eddy diffusivity estimates obtained from real drifter data and trajectories simulated with the velocity output from ocean general circulation models (OGCMs) at varying horizontal and temporal resolutions for the greater Agulhas system. The greater Agulhas system, located around the southern tip of Africa, is known for its vigorous eddy activity and its importance for interbasin exchange of heat, salt, and momentum between the Indian and Atlantic Oceans (e.g., Beal et al. 2011). It features different dynamic regimes in a confined region (Fig. 1): the Agulhas Current (AC), a strong but stable western boundary current in the Indian Ocean; the Agulhas Retroflection (AR) into the eastward-flowing Agulhas Return Current (ARC); and associated shedding of Agulhas eddies (Lutjeharms 2006) that travel into the eastern South Atlantic Gyre (eSAG). Hence, it constitutes a good test region for evaluating spatially variable eddy diffusivity characteristics. In particular, we address the following questions:

1) What are the characteristics of lateral near-surface eddy diffusivities estimated from 2D trajectories simulated with an eddy-resolving OGCM?
2) How do these diffusivity estimates compare to those derived from surface drifter data?
3) How sensitive are the diffusivity estimates to the temporal and horizontal resolutions of the underlying Eulerian OGCM velocity fields? And what is the

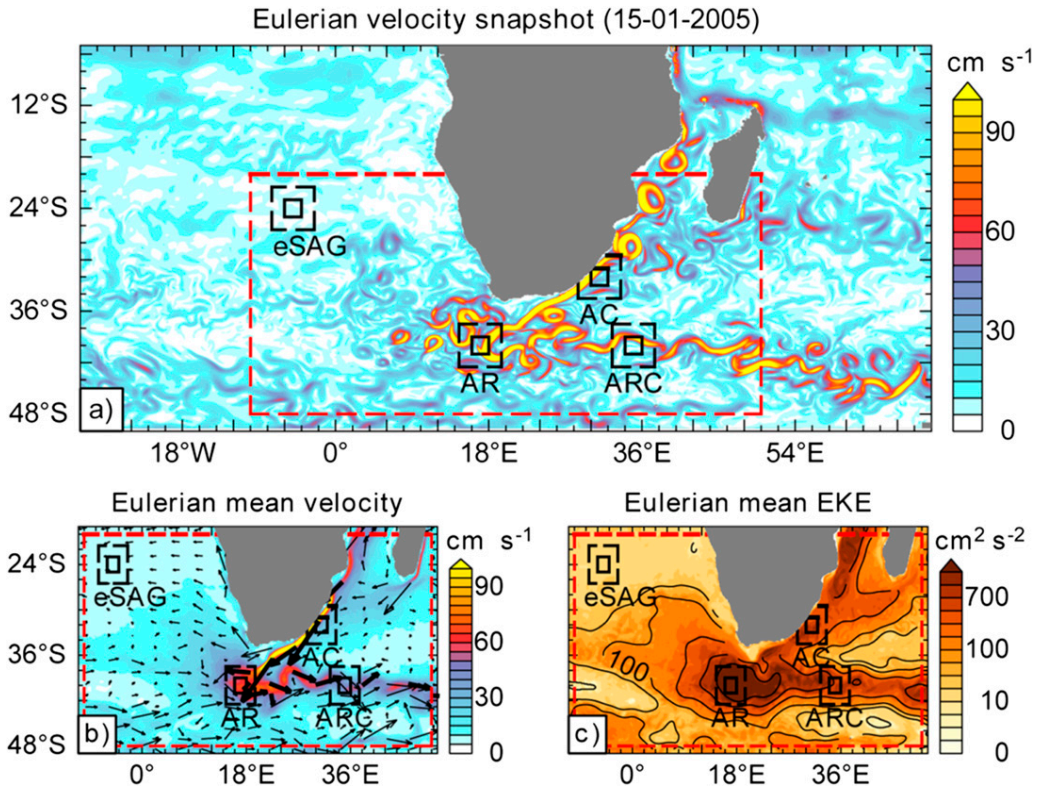

FIG. 1. Eulerian fields simulated with the eddy-resolving ocean model configuration INALT01-KJD308. (a) Snapshot of the daily mean current speed at 15-m depth (15 Jan 2005). (b) Long-term mean (1996–2006) Eulerian velocity speed (color shading) and direction (vectors). Velocity vectors for speeds $>50\,\mathrm{cm\,s^{-1}}$ are displayed thick and at half-length compared to vectors for speeds $<50\,\mathrm{cm\,s^{-1}}$. (c) Long-term mean (1996–2006) Eulerian EKE. Contours are displayed for 50, 100, 300, 700, and $1300\,\mathrm{cm^2\,s^{-2}}$. In all plots, the red dashed frame surrounds the region in which virtual fluid particles were released. The black dashed and solid frames enclose the $5° \times 5°$ and $2° \times 2°$ bins used for the diffusivity calculations and plotting, respectively, for the AC, AR, ARC, and eSAG.

impact of the Gent and McWilliams (GM) parameterization for baroclinic eddies in a noneddying OGCM on the diffusivity estimates?

This manuscript is structured as follows: In section 2, we describe the employed OGCMs, the offline-performed Lagrangian experiments, the applied method for eddy diffusivity estimation, and the primary observational reference dataset. In section 3, we present and discuss the results: eddy diffusivity estimates obtained from trajectories simulated with 5-day mean velocity output of an eddy-resolving OGCM (section 3a), a comparison of those simulation-based estimates to the observation-based estimates (section 3b), and the sensitivity of the simulation-based diffusivity estimates to the temporal and lateral OGCM output resolution, including the impact of an applied GM parameterization (section 3c). In section 4, we further compare our diffusivity estimates with eddy diffusivity estimates based on different methods and discuss possible implications of our results for eddy parameterization approaches. Section 5 lists our conclusions.

2. Data and methods

One major goal of this study is to compare eddy diffusivity estimates obtained from trajectories simulated with ocean models to those obtained from observed surface drifter data. Therefore, we calculated 2D Lagrangian trajectories resembling surface drifter tracks from the simulated flow fields of an eddy-resolving and a noneddying global OGCM configuration, INALT01 and ORCA05, respectively. Subsequently, we derived eddy diffusivities from those simulated trajectories as well as from the Global Drifter Program (GDP; Lumpkin and Pazos 2007) data following the method employed by Zhurbas et al. (2014). Zhurbas et al. (2014) already presented global maps of drifter-derived eddy diffusivities, and our updated version of their estimates for

the Agulhas region serves as the primary observational reference in this study.

a. GDP data

The GDP array of satellite-tracked surface drifting buoys is the highest spatial resolution ocean velocity data currently available, and it is the cornerstone of our knowledge of near-surface submesoscale and mesoscale turbulence and turbulent diffusive regimes (Lumpkin et al. 2017). Each drifter consists of a surface buoy with a transmitter and a temperature sensor, and a subsurface drogue, centered at 15-m depth measuring near-surface mixed layer currents. For this study, we used the latitude, longitude, and drifter velocity components at 6-h intervals obtained by objective interpolation updated through 2012 (http://www.aoml.noaa.gov/phod/dac/gdp.html; Hansen and Poulain 1996). Only trajectory segments with the drogue attached were considered (Lumpkin et al. 2013), and the trajectory data were low-pass filtered prior to the diffusivity calculations to remove variability in drifter positions and velocities with periods smaller than 2 days mostly caused by inertial oscillations.

b. Lagrangian trajectories from ocean model simulations

1) Ocean model simulations

The global ocean/sea ice model configurations INALT01 and ORCA05 were developed under the DRAKKAR framework (Barnier et al. 2007, 2014). They were formulated with the Nucleus for European Modelling of the Ocean (NEMO, version 3.1.1; Madec 2008) and implemented on a horizontal tripolar Arakawa C-grid (Mesinger and Arakawa 1976), which is Mercator-type south of 20°N. Both configurations employed have 46 vertical levels, with grid spacing increasing from 6 m at the surface to 250 m at depth and partially filled bottom cells.

ORCA05 is a well-validated global configuration (e.g., Danabasoglu et al. 2014) with a nominal horizontal resolution of 0.5° (~43 km in the Agulhas region), which realistically represents the mean flow and interannual-to-decadal variability of the large-scale circulation (Biastoch et al. 2008a). It classifies as a noneddying OGCM configuration, since to fully capture the mesoscale variability in the Agulhas region, horizontal resolutions of 0.25° and finer are needed (Hallberg 2013).

INALT01 is a two-way nested model configuration that is based on the global ORCA05 configuration described above, but it is regionally refined between 50°S–8°N and 70°W–70°E to its nominal horizontal resolution of 0.1° (~9 km in Agulhas region) to capture the complex mesoscale dynamics of the greater Agulhas system (Durgadoo et al. 2013). Figure 1a shows a snapshot of the daily mean current speed at 15-m depth, illustrating the ability of the model to represent, for example, Mozambique Channel eddies and Agulhas rings. INALT01 has been employed by a variety of studies investigating the local dynamics (Cronin et al. 2013; Loveday et al. 2014) and large-scale impact (Lübbecke et al. 2015; Biastoch et al. 2015) of the greater Agulhas system.

Both ocean/sea ice models were spun up for 20 years before the actual simulations were performed using interannually varying (years 1948–2007) or climatological atmospheric forcing fields from the Coordinated Ocean–Ice Reference Experiments version 2b (CORE v2b; Large and Yeager 2009; Griffies et al. 2009). The evolution of tracers was simulated using a Laplacian isoneutral diffusion operator and the total variance dissipation (TVD; Zalesak 1979) advection scheme. The momentum equations were formulated using a bi-Laplacian lateral diffusion operator and the energy- and enstrophy-conserving (EEN; Arakawa and Hsu 1990) advection scheme. Diffusivity and viscosity coefficients vary horizontally according to the local grid size and are specified via their maximum values A_{ht0} and A_{hm0} (Table 1), respectively. Further details of the INALT01 and ORCA05 simulations employed in this study are described in Durgadoo et al. (2013).

Table 1 contains a summary of the model simulations providing velocity data used for six Lagrangian experiments performed for this study. Note that 1) one simulation with the eddying INALT01 configuration yielded three different Lagrangian experiments that differ only in the temporal resolution of the velocity fields used for the trajectory integration (SIMeddy-1d, SIMeddy-5d, and SIMeddy-1m); and 2) for the noneddying ORCA05 configurations, two simulations and respective Lagrangian experiments were analyzed, one with (SIMpareddy-5d) and one without (SIMnoeddy-5d) GM parameterization of baroclinic eddies (Gent and McWilliams 1990). The GM parameterization mimics the impact of baroclinic eddies on tracer fluxes by adding an extra term to the tracer equation, which represents eddy-induced advection (Gent et al. 1995; Gent 2011); it is determined by the GM coefficient, which is computed from the growth of the baroclinic instability as described in Treguier et al. (1997), and is allowed to vary horizontally and temporally with a cap of $1000\,\mathrm{m^2\,s^{-1}}$.

2) Lagrangian trajectory integration

The trajectory integration was performed using the offline Lagrangian community tool ARIANE (version

TABLE 1. Summary of the global OGCM simulations, which provided the velocity fields used for six Lagrangian experiments performed in this study. All OGCM simulations used a Laplacian isoneutral diffusion of tracers (with different values for the isopycnal diffusivity coefficient A_{ht0}) and a bi-Laplacian lateral diffusion of momentum (with different values for the horizontal viscosity coefficient A_{hm0}).

Lagrangian experiment	OGCM configuration/ simulation	Horizontal resolution	Subgrid-scale parameterizations ($[A_{ht0}] = m^2 s^{-1}$; $[A_{hm0}] = m^4 s^{-1}$)	Spinup	Forcing type/ period	Temporal output resolution/ period
SIMeddy-1d	INALT01/ KJD308	Base: 1/2°; Nest: 1/10°	Base: $A_{ht0} = 600$, $A_{hm0} = -12 \times 10^{11}$; Nest: $A_{ht0} = 200$, $A_{hm0} = -2.125 \times 10^{10}$	Base: Forcing 1978–97 (JD305); Nest: No spinup, initialized with base model fields	Hindcast/1948–2007 (1-day mean fields only between 1995 and 2007)	1-day mean/ 1996–2007
SIMeddy-5d						5-day mean/ 1996–2007
SIMeddy-1m						Monthly mean/ 1996–2007
SIMeddy-5d-clim	INALT01/ KJD309				Climatological/ 60 years	5-day mean/ years 49–60
SIMnoeddy-5d	ORCA05/ JD308	Globally 1/2°	$A_{ht0} = 600$, $A_{hm0} = -12 \times 10^{11}$	Forcing 1978–97 (JD305)	Hindcast/1948–2007	5-day mean/ 1996–2007
SIMpareddy-5d	ORCA05/ JD409		$A_{ht0} = 600$, $A_{hm0} = -12 \times 10^{11}$,GM	Forcing 1978–97 (JD405)	Climatological/ 60 years	5-day mean/ years 49–60

2.2.6; Blanke and Raynaud 1997). Lagrangian particles were released homogenously over the greater Agulhas system (Fig. 1) at ~15-m depth, every 0.5° in both latitudinal and longitudinal directions, every 30 days for 10 years (beginning 1200 UTC 15 January 1996), yielding nearly 900 000 particles for each Lagrangian experiment. Subsequently, particles were advected forward in time for 60 days with the modeled horizontal velocities (for SIMpareddy-5d, the Eulerian velocity combined with the eddy-induced velocity from the GM parameterization was used), whereby particle positions were stored daily. As drogued surface drifters' behavior should be mimicked, particles were kept at the same depth over the whole integration period. No additional stochastic Lagrangian parameterization was employed.

The resulting trajectories represent pathways determined by the resolved Eulerian flow, or, in the case of SIMpareddy-5d, by the resolved Eulerian flow combined with the mesoscale eddy-induced velocity from the GM parameterization. It has been shown that including the mesoscale eddy-induced transport yields a more realistic picture of the mean overturning circulation, particularly in the Southern Ocean, where the eddy-induced meridional velocity counteracts the Eulerian meridional velocity (e.g., Drijfhout et al. 2003). However, while parameterizing the advective effect of baroclinic eddies where they are not resolved by the model, GM also suppresses the explicit generation of physical as well as numerical mesoscale variability (Hallberg 2013) by flattening isopycnals. Thus, it is worth comparing eddy diffusivity estimates from Lagrangian experiments in noneddying ocean model simulations with and without GM parameterization.

c. *Lagrangian eddy diffusivity estimation*

Lagrangian eddy diffusivities can be estimated from both single-particle and particle-pair/cluster statistics (LaCasce 2008). While particle-pair/cluster statistics are additionally suited to infer the spatial spectra of mesoscale currents, they also require a simultaneous deployment of a large number of particles in a confined area. Because GDP data presently fulfill this requirement only in a few regions and thus cannot be used to infer spatial variability of eddy diffusivity estimates via particle-pair or cluster statistics, we employed single-particle statistics.

1) THEORETICAL BACKGROUND OF SINGLE-PARTICLE DIFFUSIVITY ESTIMATION

The concept of Lagrangian diffusivity estimation was introduced by Taylor (1922), who determined scalar single-particle diffusivities by integrating the ensemble-mean Lagrangian velocity autocorrelation function:

$$k^{\text{Taylor}} = \lim_{t\to\infty} k(t), \quad \text{with} \tag{1}$$

$$k(t) = 0.5\frac{d}{dt}\langle \mathbf{d}(t)^2\rangle_L = \langle \mathbf{v}_L(t)\cdot\mathbf{d}(t)\rangle_L = \int_{t_0}^{t} \langle \mathbf{v}_L(t)\cdot\mathbf{v}_L(\tau)\rangle_L \, d\tau, \tag{2}$$

whereby $\mathbf{d}(t) = \mathbf{x}(t) - \mathbf{x}(t_0) = \int_{t_0}^{t} \mathbf{v}_L(\tau)d\tau$ represents the particle displacement, $\mathbf{v}_L(t) = \partial\mathbf{x}/\partial t$ is the Lagrangian

velocity, and $\langle\cdot\rangle_L$ indicates Lagrangian averaging, that is, averaging over an ensemble of particles at a certain time lag t after their release at t_0.

The Taylor approach was formulated in the idealized context of statistically homogeneous, stationary, and isotropic flows. Davis (1991b) extended the Taylor framework for single-particle diffusivity estimation over inhomogeneous and anisotropic flows by introducing the eddy diffusivity tensor. The diffusivity is then calculated for an ensemble of particles originating at a certain location, or within a specified geographical region where the flow can be assumed as locally homogenous, for each tensor component $k_{jk}(\mathbf{x}, t)$ individually [j, k are the indices for the horizontal dimensions in Cartesian space with $j, k \in (1, 2)$]. Instead of the absolute, only the residual velocities $\mathbf{v}'_L(t|\mathbf{x}, t_o)$ and displacements $\mathbf{d}'(t|\mathbf{x}, t_o)$ for each particle (passing through $\mathbf{x}$ at time t_0) are considered. The residual velocity is defined as the departure from the local Eulerian mean velocity; the residual displacement is defined as the total displacements minus that due to the Eulerian mean velocity. This is why, strictly speaking, the eddy diffusivity is not a pure Lagrangian, but a mixed Eulerian–Lagrangian statistic (LaCasce 2008).

Single-particle eddy diffusivity estimation thus involves the following steps: 1) binning of particle trajectories on a longitudinal–latitudinal grid, 2) estimation of the mean flow and subsequent calculation of residual Lagrangian velocities and/or displacements, and 3) estimation of the ensemble-mean eddy diffusivity tensor components for each bin (either in fixed coordinate or along- and across-flow directions).

There are various approaches to estimate the components of the single-particle eddy diffusivity tensor $k_{jk}(\mathbf{x}, t)$, all deriving from Taylor's and Davis's diffusivity concepts but using different procedures to reduce potential biases caused by the inhomogeneity and nonstationarity of flows, that is, different binning techniques, mean flow definitions, and diffusivity estimators. Lagrangian averaging is performed using geographical bins (e.g., Swenson and Niiler 1996; Sallée et al. 2008), which may additionally overlap and/or be rotated with respect to the velocity variance axis (e.g., Lumpkin and Garzoli 2005; Peng et al. 2015). Alternatively, trajectories may be clustered according to the nearest neighbor distance (Koszalka and LaCasce 2010). The mean flow is estimated either by simple averaging or using advanced techniques such as spline fitting or Gauss–Markov decomposition (e.g., Bauer et al. 2002; Laurindo et al. 2017). Finally, diffusivity is estimated via the half-growth rate of the residual dispersion tensor (e.g., de Verdiere 1983; Oh et al. 2000; Rypina et al. 2012, 2016), the integral of the residual velocity autocorrelation (e.g., Koszalka et al. 2011; Peng et al. 2015), or the residual velocity displacement tensor (e.g., Davis 1991b; Swenson and Niiler 1996; Oh et al. 2000).

2) Single-particle eddy diffusivity estimation following Zhurbas et al. (2014)

In this study, we follow the approach for diffusivity estimation used by Zhurbas et al. (2014). This approach was first introduced and thoroughly tested by random-flight simulations of Lagrangian trajectories in a sheared flow (Oh et al. 2000) and was later employed in an improved version accounting for the mean flow suppression of eddy diffusivities by Zhurbas et al. (2014). Assuming isotropy in diffusivities/eddy statistics, the approach yields one time lag– and coordinate-dependent scalar lateral eddy diffusivity $K(\mathbf{x}, t)$, which is defined as the semisum of the minor principal component of the symmetric part of the Davis diffusivity tensor $k_{p2}^{\text{davis}}(\mathbf{x}, t)$ and the half-growth rate of the minor principal component of the single-particle dispersion tensor $k_{p2}^{\text{disp}}(\mathbf{x}, t)$, thus combining two frequently used approaches for diffusivity estimation:

$$K(\mathbf{x}, t) = [k_{p2}^{\text{davis}}(\mathbf{x}, t) + k_{p2}^{\text{disp}}(\mathbf{x}, t)]/2. \tag{3}$$

The Davis diffusivity tensor $k_{jk}(\mathbf{x}, t)$ is defined as

$$k_{jk}(\mathbf{x}, t) = -\langle v'_{Lj}(t_0|\mathbf{x}, t_0) \cdot d'_k(t_0 - t|\mathbf{x}, t_0)\rangle_L, \tag{4}$$

whereby the notation $d'_k(t_0 - t|\mathbf{x}, t_0)$ represents the kth component of the residual displacement for a particle passing through $\mathbf{x}$ at time t_0, obtained from following its trajectory backward in time for the period $[t_0 - t, t_0]$; and $v'_{Lj}(t_0|\mathbf{x}, t_0)$ is the residual velocity of that particle at time t_0. To avoid rotational eddy fluxes, which are nondiffusive, only the symmetric part of $k_{jk}(\mathbf{x}, t)$ is considered, which is here referred to as $k_{jk}^{\text{davis}}(\mathbf{x}, t)$:

$$k_{jk}^{\text{davis}}(\mathbf{x}, t) = [k_{jk}(\mathbf{x}, t) + k_{kj}(\mathbf{x}, t)]/2. \tag{5}$$

The half-growth rate of the single-particle dispersion tensor $k_{jk}^{\text{disp}}(\mathbf{x}, t)$ is defined as

$$k_{jk}^{\text{disp}}(\mathbf{x}, t) = 0.5\frac{\delta s_{jk}}{\delta t}, \quad \text{with} \tag{6}$$

$$s_{jk}(\mathbf{x}, t) = \langle d'_j(t_0 + t|\mathbf{x}, t_0) \cdot d'_k(t_0 + t|\mathbf{x}, t_0)\rangle_L, \tag{7}$$

whereby the notation $d'_k(t_0 + t|\mathbf{x}, t_0)$ represents the kth component of the residual displacement of a particle passing through $\mathbf{x}$ at time t_0, obtained from following its trajectory forward in time for the period $[t_0, t_0 + t]$. The dispersion tensor is symmetric by

construction and does not include rotational and advective eddy fluxes.

If diffusivities are estimated from ensembles of trajectories passing through a fixed position **x** at different times, $k_{jk}^{\mathrm{davis}}(\mathbf{x}, t)$ yields the true time lag–dependent diffusivity, whereas $k_{jk}^{\mathrm{disp}}(\mathbf{x}, t)$ can be biased by the shear effect. However, the limited spatial–temporal resolution of surface drifter data only allows for estimating diffusivities from ensembles of particles passing through a finite vicinity of **x,** in which case both measures can be positively biased by shear. Because Oh et al. (2000) showed that the minor principal components of $k_{jk}^{\mathrm{disp}}(\mathbf{x}, t)$ and $k_{jk}^{\mathrm{davis}}(\mathbf{x}, t)$, representing across-flow diffusivities (cf. Peng et al. 2015), are less biased by shear flow, these were chosen as (the only) representative estimates for lateral eddy diffusivities. They were obtained according to

$$k_{p2}(\mathbf{x},t) = k_{xx}(\mathbf{x},t)\sin^2\theta - k_{xy}(\mathbf{x},t)\sin 2\theta + k_{yy}(\mathbf{x},t)\cos^2\theta, \quad \text{and} \tag{8}$$

$$\tan 2\theta = 2k_{xy}(\mathbf{x},t)/[k_{xx}(\mathbf{x},t) - k_{yy}(\mathbf{x},t)]. \tag{9}$$

Consistently with Zhurbas et al. (2014), we used this approach to estimate lateral eddy diffusivities from all Lagrangian experiments and surface drifter data in overlapping 5° × 5° bins with a 2° offset in longitudinal and latitudinal direction. Residual velocities were calculated relative to climatological monthly mean currents. That means for each bin for each month of the year, all trajectories passing that bin in the respective month were selected. Then, all trajectory positions within the bin were considered as the origin of a pseudotrajectory (overlapping pseudotracks were removed), and individual backward and forward displacements $\mathbf{d}(t|\mathbf{x}, t_0)$, as well as the Lagrangian velocity at the pseudo-origin $\mathbf{v}_L(t_0|\mathbf{x}, t_0)$, were calculated (for the simulated trajectories, Lagrangian velocities were obtained by central time-differencing of the discrete displacements). Ensemble averaging yielded the mean displacement $\langle \mathbf{d}(t) \rangle_L$ and the climatological monthly mean velocity $\langle \mathbf{v}_L(t_0) \rangle_L$ that were used to derive the residual velocities and displacements as

$$\mathbf{v}'_L(t_0|\boldsymbol{x}, t_0) = \mathbf{v}_L(t_0|\mathbf{x}, t_0) - \langle \mathbf{v}_L(t_0) \rangle_L, \quad \text{and} \tag{10}$$

$$\mathbf{d}'(t|\boldsymbol{x}, t_0) = \mathbf{d}(t|\boldsymbol{x}, t_0) - \langle \mathbf{d}(t) \rangle_L. \tag{11}$$

From these, for each set of pseudotrajectories starting in the same month, $k_{jk}^{\mathrm{davis}}(\mathbf{x}, t)$, $k_{jk}^{\mathrm{disp}}(\mathbf{x}, t)$, and $K(\mathbf{x}, t)$ were estimated; the final diffusivity estimates were obtained as averages of the respective 12 individual estimates. Further details of the calculation, including smoothing details and small modifications with respect to the original Zhurbas et al. (2014) approach, are discussed in the appendix.

It is important to note the time-lag dependence of diffusivity estimates. Again, following Zhurbas et al. (2014), we distinguish the maximum diffusivity $K_{\max}(\mathbf{x})$, defined as the local maximum of $K(\mathbf{x}, t)$ within the time lag interval $1 \le t \le 20$ days, and the asymptotic diffusivity $K_{\inf}(\mathbf{x})$, defined as the local mean value of $K(\mathbf{x}, t)$ for the time lag interval $15 \le t \le 20$ days (Fig. 2). The usage of larger time lags was avoided because the sampling error and potential biases caused by spatial and/or temporal inhomogeneity of the residual velocity field increase with the time lag (Davis 1991b).

From a physical or parameterization point of view, $K_{\inf}$ is the sought-after estimate of diffusivity because at those large time lags, the mean residual distance traveled by a fluid parcel in a certain time interval is approximately proportional to the square root of that time interval, just as for a diffusive process in which fluid parcels undergo random walks (cf. discussion of the Lagrangian integral time scale below). Earlier studies used $K_{\max}$ (e.g., Oh et al. 2000; Lumpkin and Flament 2001; Sallée et al. 2008), but recently it has been shown that $K_{\max}$ can largely overestimate the "true" diffusivity due to a suppression of mixing in areas where eddies and mean flow propagate at different speeds (Griesel et al. 2010; Klocker et al. 2012a,b; Wolfram and Ringler 2017a).

In this work, we purposefully assess both $K_{\inf}$ and $K_{\max}$ because the relation of the two quantifies the strength of diffusivity suppression by mean flow (Klocker et al. 2012a) and thus can be used to diagnose how well the ocean models represent these effects (i.e., the relationship between the mean flow and the eddy propagation speed along the mean flow).

d. Pseudo-Eulerian EKE, Lagrangian eddy time, and length scales

In addition to Lagrangian eddy diffusivities, the pseudo-Eulerian mean eddy kinetic energy (EKE) and Lagrangian eddy integral time T_L and length L_L scales were calculated in overlapping 5° × 5° bins.

To be consistent with the definition of the eddy diffusivity, for which we only considered the minor principal component (i.e., the across-flow component), the pseudo-Eulerian mean EKE is defined as the minor principal component of the Lagrangian mean residual velocity covariance matrix at zero time lag $\langle \upsilon'_{Lj}(t_0|\mathbf{x}, t_0) \cdot \upsilon'_{Lk}(t_0|\mathbf{x}, t_0) \rangle_L$.

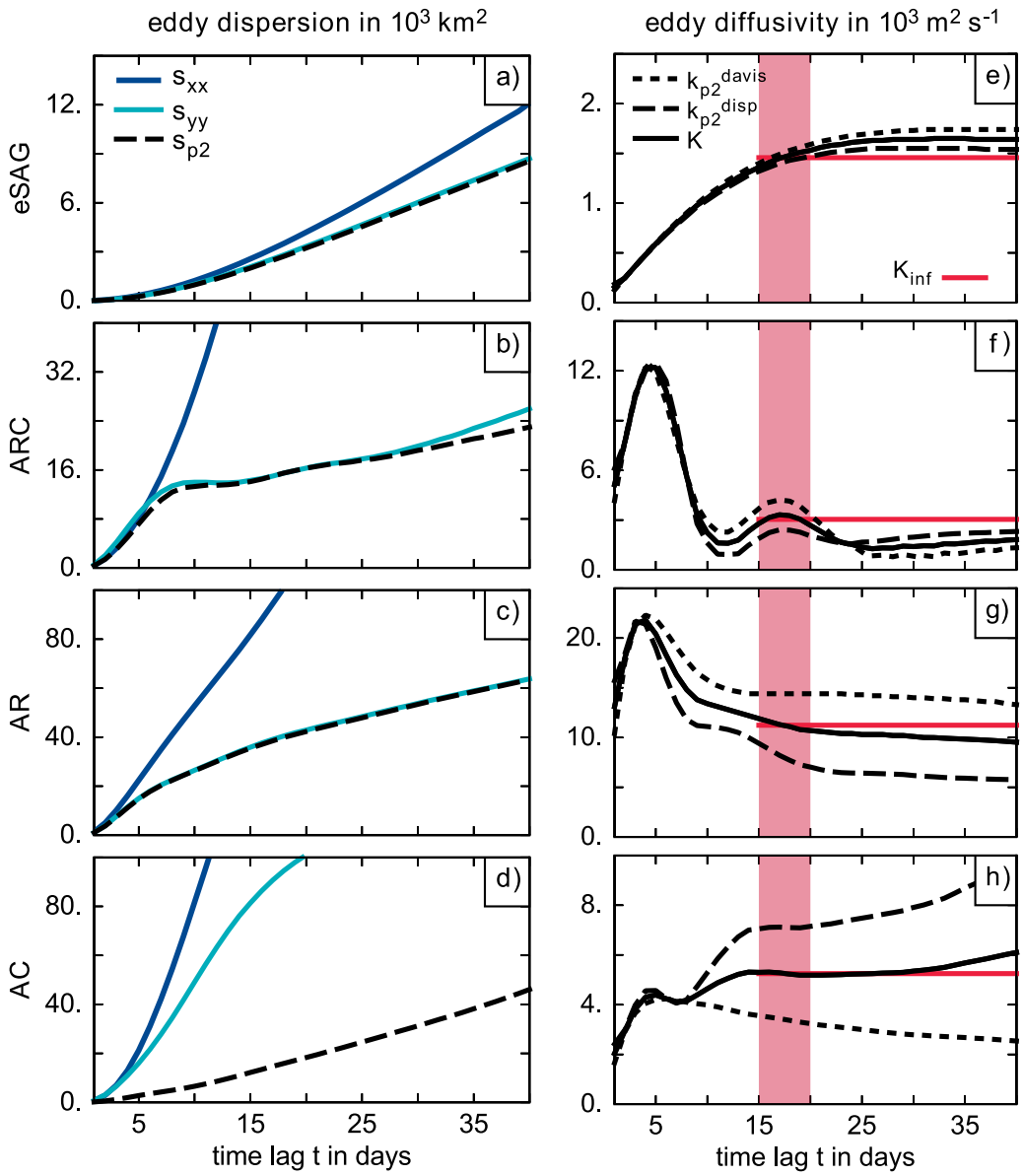

FIG. 2. Time lag–dependent near-surface eddy dispersion and diffusivity estimates for the four regions marked in Fig. 1, obtained from Lagrangian experiment SIMeddy-5d. (a)–(d) Zonal s_{xx} (dark blue line), meridional s_{yy} (light blue line), and minor principal component s_{p2} (black dashed line) of the ensemble-mean single-particle dispersion tensor. (e)–(h) Half-growth rate of the minor principal component of the single-particle dispersion tensor k_{p2}^{disp} (black dashed lines), minor principal component of the symmetric part of the Davis diffusivity tensor k_{p2}^{davis} (black dotted lines), and combined lateral eddy diffusivity estimate defined as the semisum of the two diffusivity measures K (black solid lines). Red horizontal lines indicate the asymptotic lateral eddy diffusivity estimate K_{inf} inferred as the average of K in the red shaded time lag interval $15 \leq t \leq 20$ days. Please note the different scaling of the y axis in all subplots.

Mixing, and thus, K_{inf}, can generally be represented as scaling with EKE and the time scale T_L over which mixing occurs, or equivalently, as scaling with the distance L_L a particle would travel with the characteristic root-mean-square eddy velocity v' (which equals $\sqrt{\text{EKE}}$) before it mixes with its surroundings: $K = \text{EKE}T_L = \sqrt{\text{EKE}}L_L$ (cf. LaCasce 2008). Analogously, we estimated T_L and L_L using our asymptotic diffusivity estimate K_{inf} and pseudo-Eulerian mean EKE as

TABLE 2. Statistics for four selected 5° × 5° bins centered on the listed coordinates: pseudo-Eulerian mean speed and mean EKE, as well as asymptotic K_{inf} and maximum K_{max} near-surface lateral eddy diffusivity estimates, and Lagrangian integral time T_L and length L_L scales obtained from OBS and Lagrangian experiment SIMeddy-5d.

Region	Lagrangian experiment	Speed ($cm\,s^{-1}$)	EKE ($cm^2\,s^{-2}$)	Diffusivity estimates ($10^3\,m^2\,s^{-1}$)						T_L (days)	L_L (km)
				K_{inf}	K_{inf}^{davis}	K_{inf}^{disp}	K_{max}	K_{max}^{davis}	K_{max}^{disp}		
eSAG; 24°S, 5°W	SIMeddy-5d	4	15	1.46	1.51	1.41	1.53	1.59	1.47	11.6	38.2
	OBS	5	42	1.95	2.02	1.89	1.96	2.03	1.91	5.4	30.2
ARC; 40°S, 35°E	SIMeddy-5d	17	482	3.04	3.88	2.20	12.20	12.30	12.50	0.7	13.9
	OBS	15	607	4.12	4.58	3.67	8.87	8.99	8.75	0.8	16.7
AR; 40°S, 17°E	SIMeddy-5d	6	1218	11.20	14.40	8.07	21.80	22.30	21.70	1.1	32.0
	OBS	12	1266	9.81	7.75	11.90	19.20	18.30	20.10	0.9	27.6
AC; 32°S, 31°E	SIMeddy-5d	16	193	5.25	3.40	7.10	5.31	4.23	7.15	3.2	38.2
	OBS	24	458	4.43	3.70	5.17	8.07	9.54	8.34	1.1	20.7

$$T_L = K_{inf}/\mathrm{EKE}, \quad \text{and} \tag{12}$$

$$L_L = K_{inf}/\sqrt{\mathrm{EKE}}. \tag{13}$$

Quantities T_L and L_L represent "memory" scales over which Lagrangian residual velocities stay strongly correlated; at time and space scales much larger than T_L and L_L, respectively, residual single-particle dispersion resembles diffusive spreading.

3. Results and discussion

a. *Eddy diffusivity estimates derived from trajectories simulated with an eddying ocean model*

In this section, we present and discuss near-surface lateral eddy diffusivity estimates obtained from residual velocities and displacements of Lagrangian trajectories simulated with the 5-day mean velocity output of the eddy resolving INALT01 hindcast experiment (Lagrangian experiment SIMeddy-5d).

1) TIME LAG DEPENDENCE OF EDDY DIFFUSIVITY ESTIMATES

Figure 2 shows time lag–dependent, ensemble-mean single-particle residual dispersion and eddy diffusivity estimates for four selected 5° × 5° bins representing different dynamic regimes (Fig. 1). Table 2 lists the respective pseudo-Eulerian and Lagrangian statistics. The bins are located in the eSAG, the ARC, the AR, and the AC.

The eSAG is an open ocean region characterized by weak mean flow and low EKE. Its dispersion and diffusivity curves (Figs. 2a,e) show the characteristic asymptotic behavior described in classical turbulence theory (LaCasce 2008): at time lags larger than ~20 days, $s_{p2}(t)$ grows approximately linear with time (meaning the mean residual displacement of a fluid parcel in a certain time interval is approximately proportional to the square root of that time interval), typical for the diffusive regime. Consequently, across-flow eddy diffusivities asymptotically approach a nearly constant value at those time lags, and $K_{max} \approx K_{inf} \approx 1.5 \times 10^3\,m^2 s^{-1}$. Because the curves for $s_{yy}(t)$ and $s_{p2}(t)$ are hardly distinguishable, and even $s_{xx}(t)$ shows a similar behavior, we conclude that the spreading is approximately isotropic. In this particular case, with weak influence of mean flow and nearly isotropic particle spreading, the diffusivity estimates $k_{p2}^{disp}(t)$, $k_{p2}^{davis}(t)$, and $K(t)$ yield nearly the same results, with only a small spread toward larger time lags.

The ARC is a strong alongfront current with pronounced meridional excursions, supposedly related to changes in bottom topography, and vigorous mesoscale variability (Lutjeharms and Ansorge 2001). In the ARC region, dispersion and diffusivity curves (Figs. 2b,f) differ substantially from those described for the eSAG. They can be considered typical of a region where eddies propagate westward relative to an eastward mean flow (Boebel et al. 2003; Chelton et al. 2011). On one hand, the instability of the ARC introduces high EKE, leading to an overall increased across-flow eddy diffusivity. On the other hand, the across-flow eddy diffusivity is suppressed by the mean flow, as shown conceptually for the ACC by Klocker et al. (2012a). The obtained across-flow eddy dispersion estimate $s_{p2}(t)$, which is nearly identical to $s_{yy}(t)$, increases quickly at short time lags but then levels off before finally increasing again approximately linearly with time. This yields across-flow eddy diffusivity curves to peak (and slightly oscillate) at short time lags before reaching their asymptotic values; the maximum diffusivity strongly overestimates the asymptotic diffusivity, $K_{max} \approx 12.2 \times 10^3$ and $K_{inf} \approx 3.0 \times 10^3\,m^2\,s^{-1}$. Still, the diffusivity estimates $k_{p2}^{disp}(t)$ and $k_{p2}^{davis}(t)$ yield nearly the same results, introducing only a small spread around $K(t)$ toward larger time lags.

The dispersion and diffusivity curves for the AR (Figs. 2c,g) show a very similar behavior to that described for the ARC, but with even higher diffusivity

values, related to a regional maximum in EKE (cf. Fig. 1d). The across-flow eddy diffusivity curves peak at short time lags before reaching their asymptotic values. Thus, as for the ARC, the maximum diffusivity overestimates the asymptotic diffusivity, $K_{max} \approx 21.8 \times 10^3$ and $K_{inf} \approx 11.2 \times 10^3\,m^2\,s^{-1}$. However, the result for K_{inf} should be interpreted with caution, because even though $k_{p2}^{disp}(t)$ and $k_{p2}^{davis}(t)$ show a similar temporal evolution, their spread around the combined estimate $K(t)$ increases after they reach their maximum value. Their respective asymptotic diffusivity estimates K_{inf}^{disp} and K_{inf}^{davis} are 8.1×10^3 and $14.4 \times 10^3\,m^2\,s^{-1}$, respectively.

The AC, heading southwestward, is one of the strongest western boundary currents of the World Ocean. However, in contrast to other western boundary currents, such as the Kuroshio or the Gulf Stream, it is remarkably stable (Lutjeharms 2006, 2007) and has lower EKE. The dispersion and diffusivity curves obtained for the AC (Figs. 2d,h) most resemble those of the eSAG, without strong suppression of eddy mixing by mean flow. This indicates that local eddies propagate at approximately the same speed and in the same direction of the mean flow, which is indeed the case for Natal pulses and Mozambique eddies traveling within and at the border of the AC (Schouten et al. 2002). In contrast to open ocean currents like the AR/ARC, where eddies can propagate westward separately from the mean flow, westward drift is impossible in the AC due to topographic constraints. However, at larger time lags, $s_{p2}(t)$ does not increase linearly. Consequently, $k_{p2}^{disp}(t)$ does not show an asymptotic behavior but steadily increases with increasing time lag, suggesting that the mean flow was not successfully removed. Moreover, $k_{p2}^{davis}(t)$ shows a different behavior: it reaches its maximum at a time lag of ~5 days and afterward slowly decreases with increasing time lag. Neither the asymptotic nor the maximum diffusivity can be determined unambiguously.

In general, the results for the eSAG and ARC (and, with some limitations, also those for the AR) suggest that even in a complex eddying flow system, as represented by the greater Agulhas system, with strong eddy–mean flow interaction, asymptotic diffusive regimes can be found. However, the results for the AC also highlight the limitations of a generalized binning method to quantify lateral eddy dispersion and diffusivity. Because of the spatial and probably also the temporal inhomogeneity of the residual velocity field, the eddy dispersion does not reach a diffusive regime everywhere, and the derived eddy diffusivity estimates are sensitive to the applied method.

We note that the time lag interval chosen for the calculation of asymptotic diffusivity estimates adopted from Zhurbas et al. (2014) for their global analysis of surface drifters is not perfectly suited for the simulated trajectories in the greater Agulhas system because the diffusivities do not yet converge in all cases. In particular, for the eSAG bin, the Lagrangian integral time scale is ~11.6 days (Table 2), indicating that the diffusive regime is only reached at substantially larger time lags (section 2d; LaCasce 2008). Indeed, convergence seems to be reached at time lags between 25 and 30 days. Yet, as changing the averaging interval does not impact the estimates substantially, we keep them as in Zhurbas et al. (2014) for the sake of comparison.

2) Spatial pattern of eddy diffusivity estimates

Figures 3a, 3d, and 3g show the spatial pattern of asymptotic eddy diffusivity estimates for the whole greater Agulhas system. The individual estimates K_{inf}^{davis} and K_{inf}^{disp} show the same general pattern and magnitude as the combined estimate K_{inf}: the highest eddy diffusivities are found around the AR region (cf. Fig. 2g), an area with strong unstable mean flow and high EKE (Figs. 1c, 5c). Relatively high eddy diffusivities also occur in regions with weaker background flow but still high EKE, such as in the Cape Basin around the major pathway for Agulhas rings (Schouten et al. 2000; Dencausse et al. 2010), and in the region west and south of Madagascar, where Mozambique Channel eddies and southeast Madagascar eddies propagate (Schouten et al. 2002). In the strong but relatively stable Agulhas Current, eddy diffusivities are lower due to high mean kinetic energy but comparatively low EKE. In the vicinity of the ARC (cf. Fig. 2f), diffusivities are further decreased despite locally high EKE (Figs. 1c, 5c). Lowest diffusivities occur around the low-energy eSAG region.

The spatial pattern of the maximum diffusivity estimates, as exemplarily shown for the combined estimate K_{max} in Fig. 4a, is similar to that of the asymptotic diffusivity estimates. However, despite a general increase in magnitude, the spatial pattern of K_{max} better resembles that of EKE. In particular, the region around the ARC shows strongly elevated diffusivities. The pronounced differences between K_{max} and K_{inf} in this region can be interpreted as the imprint of eddy mixing suppression by mean flow, as already discussed exemplarily for the ARC bin (section 2a). The relation K_{max}/K_{inf} displayed in Fig. 4d highlights all areas where K_{max} greatly overestimates K_{inf} and, thus, where eddy mixing suppression is strong. The region around the ARC clearly stands out, but eddy mixing suppression is also apparent in the northern part of the Antarctic Circumpolar Current (ACC). This fits well to the theory of eddy mixing because both regions feature an eastward mean flow and the possibility for westward propagation of eddies.

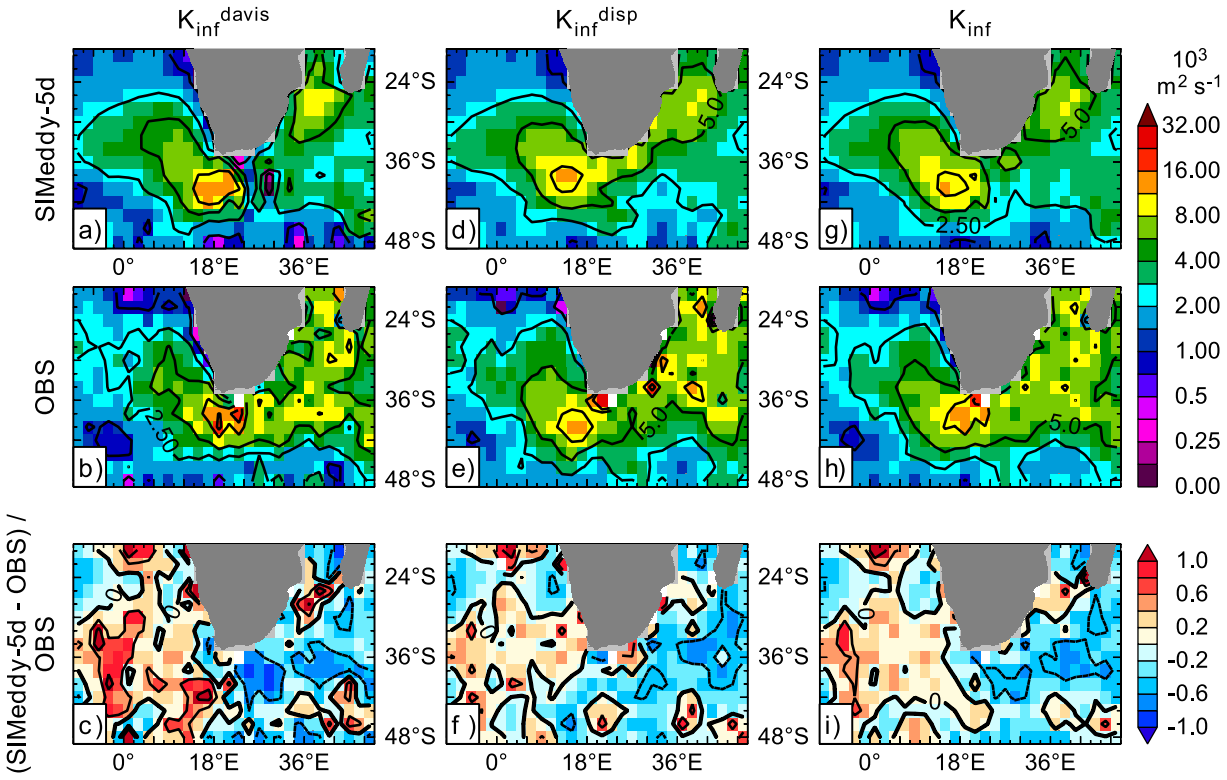

FIG. 3. Spatial pattern of asymptotic near-surface eddy diffusivity estimates. Shown are results obtained from Lagrangian experiment SIMeddy-5d (top panels) and OBS (middle panels), as well as the relative difference between simulations and observations (bottom panels). Asymptotic eddy diffusivity estimates from (left) the half-growth rate of the minor principal component of the single-particle dispersion tensor $K_{\mathrm{inf}}^{\mathrm{disp}}$; (center) the minor principal component of the symmetric part of the Davis diffusivity tensor $K_{\mathrm{inf}}^{\mathrm{davis}}$; and (right) the combined lateral eddy diffusivity estimate K_{inf}. The relative difference is defined as (SIMeddy-5d − OBS)/OBS; respective contours are displayed at a distance of 0.5.

Averaging over all spatial bins yields diffusivities of $\sim 3.3 \times 10^3$, $\sim 3.5 \times 10^3$, and $\sim 3.4 \times 10^3\,\mathrm{m^2\,s^{-1}}$ for $K_{\mathrm{inf}}^{\mathrm{davis}}$, $K_{\mathrm{inf}}^{\mathrm{disp}}$, and K_{inf}, respectively. Even though the spatially averaged $K_{\mathrm{inf}}^{\mathrm{disp}}$ constitutes a slightly higher estimate than the spatially averaged $K_{\mathrm{inf}}^{\mathrm{davis}}$, local differences between $K_{\mathrm{inf}}^{\mathrm{davis}}$ and $K_{\mathrm{inf}}^{\mathrm{disp}}$ vary in sign and magnitude. The largest discrepancies are found in the AR and AC regions, where diffusivities differ by up to more than $5.0 \times 10^3\,\mathrm{m^2\,s^{-1}}$ (Table 2). Furthermore, local discrepancies in K_{inf} are higher than those in K_{max} (not shown), highlighting the difficulty in capturing the convergence of the diffusivity estimates. Even though the approach introduced by Oh et al. (2000) and formulated in its refined form by Zhurbas et al. (2014) seems to be applicable in most regions, the combined diffusivity estimate $K(\mathbf{x}, t)$ should be interpreted with caution for areas with big discrepancies between the two individual diffusivity estimates.

b. *Comparison of eddy diffusivity estimates derived from simulated trajectories and drifter data*

In this section, we compare diffusivity estimates obtained from Lagrangian experiment SIMeddy-5d with those obtained from drifter data (OBS). A comparison with other observation-based eddy diffusivity estimates calculated with alternative techniques is given in section 4.

Estimates of K_{inf} and K_{max} obtained from OBS and SIMeddy-5d show a good agreement in their spatial pattern (Figs. 3, 4); averaging over all spatial bins yields values for K_{inf} (K_{max}) of $\sim 3.4 \times 10^3$ ($\sim 5.2 \times 10^3$) and $\sim 4.1 \times 10^3$ ($\sim 6.0 \times 10^3$) $\mathrm{m^2\,s^{-1}}$, for SIMeddy-5d and OBS, respectively.

For nearly the whole greater Agulhas system, pseudo-Eulerian mean EKE (Figs. 5c,d,f and Tables 2, 3) is lower in SIMeddy-5d than in OBS, indicating that the on-average slightly lower diffusivity values in SIMeddy-5d are mainly related to a weaker mesoscale variability. Averaging over all spatial bins yields 197 and 307 $\mathrm{cm^2\,s^{-2}}$ for SIMeddy-5d and OBS, respectively. Possible reasons for this discrepancy are the following: First, there are known weaknesses of the model configuration. The EKE in the open ocean is too low in most model simulations due to unresolved or underresolved processes, and it is further decreased in ocean model simulations forced with

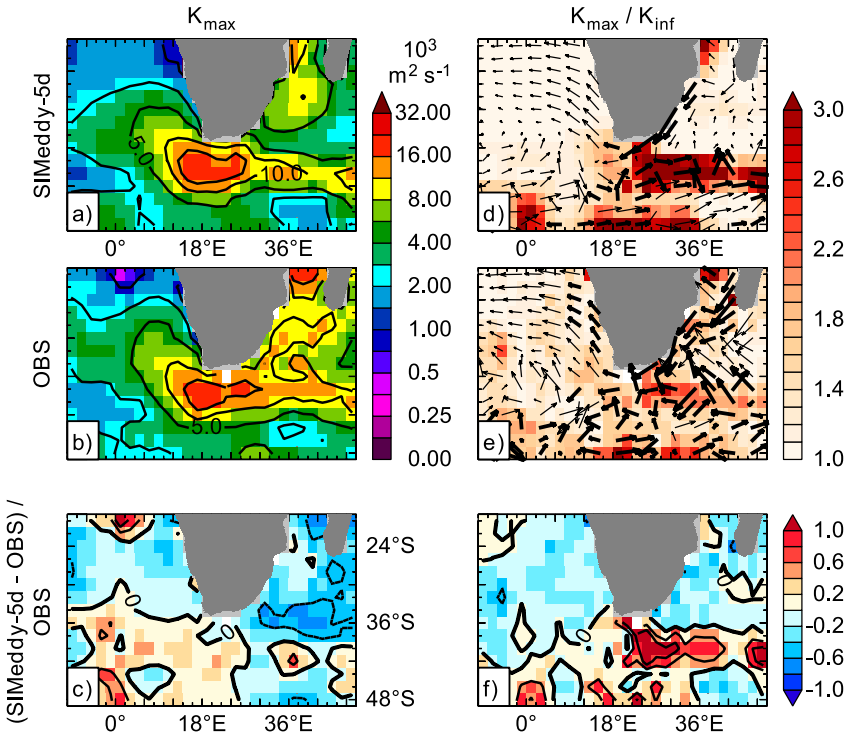

FIG. 4. Spatial pattern of maximum eddy diffusivity estimates and the relation of maximum to asymptotic eddy diffusivity estimates. Shown are results for the combined lateral eddy diffusivity estimates obtained from Lagrangian experiment SIMeddy-5d (top panels), and OBS (middle panels), as well as the relative difference between simulations and observations (bottom panels). (left) Maximum eddy diffusivity estimate K_{max}, included here as an approximate measure for the unsuppressed diffusivities. (right) Relation of K_{max} to the sought-after asymptotic diffusivity estimate K_{inf}, quantifying the strength of eddy diffusivity suppression (color shading) and pseudo-Eulerian mean velocity (vectors; cf. Fig. 6). The relative difference is defined as (SIMeddy-5d − OBS)/OBS, respective contours are displayed at a distance of 0.5.

relative winds, such as those employed in this study, due to enhanced surface drag (Eden and Dietze 2009). A limited representation of the depth-dependent Ekman drift in view of a too-scarce vertical grid spacing (6 m at the surface) of the model may have further contributed to lowered EKE values (this follows from the fact that the kinetic energy of a layer with velocity shear always exceeds the kinetic energy of a layer of the same thickness and momentum, but with uniform velocity). Second, the discrepancy between OBS and SIM could be partially related to the nature of surface drifters, which, despite being drogued at 15-m depth, do not perfectly follow the local current, but experience some additional wind-induced drift (Lumpkin and Pazos 2007; Poulain et al. 2009). Finally, the different spatiotemporal coverage of drifter data and simulated trajectories matters (see online supplementary material). However, keeping in mind that one-to-one comparisons of drifters and simulated trajectories are of limited use for non-assimilative models (cf. van Sebille et al. 2009), a much better agreement between SIMeddy-5d and OBS seems unlikely, even if the sampling of simulated trajectories would be adjusted to fit the one of drifter data. The choice of the overall time period also seems to be of minor importance because diffusivity estimates obtained from Lagrangian experiment SIMeddy5d hardly differ from Lagrangian experiment SIMeddy-5d-clim (Figs. 6a, 7 and Table 3), which is identical to SIMeddy-5d, except for the fact that the OGCM was forced with climatological atmospheric fields instead of interannually varying ones. This indicates only a minor impact of interannual-to-decadal variability on the diffusivity estimates—at least in the region of interest.

Despite lower mean diffusivities in SIMeddy-5d compared to OBS, we cannot conclude that trajectories simulated with SIMeddy-5d are generally not sufficiently diffusive because locally, the difference between SIMeddy-5d and OBS strongly varies in magnitude and sign.

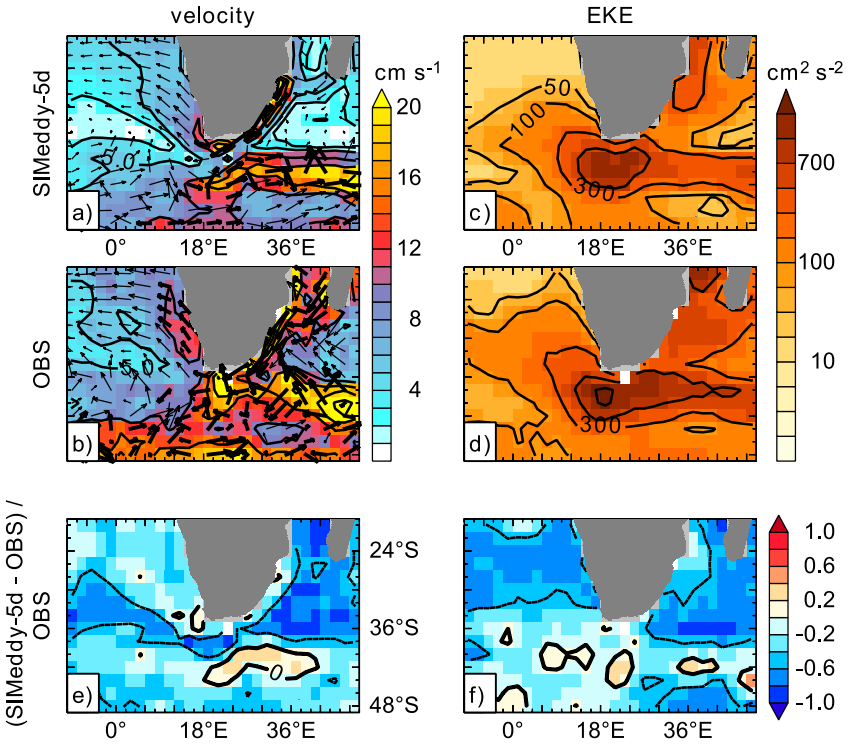

FIG. 5. Near-surface pseudo-Eulerian mean velocity and EKE. Shown are results obtained from experiment SIMeddy-5d (top panels) and OBS (middle panels). (a),(b) Mean speed (contours and color shading), and direction (vectors) of the pseudo-Eulerian mean velocity. Contours are displayed every 5 cm s^{-1}; velocity vectors for speeds >10 cm s^{-1} are displayed thick and at half-length compared to vectors for speeds <10 cm s^{-1}. (c),(d) Pseudo-Eulerian EKE. Contours are displayed for 50, 100, 300, 700, and 1300 cm^2 s^{-2}. (e),(f) Relative difference defined as (SIMeddy-5d − OBS)/OBS; contours are displayed at a distance of 0.5.

Because the general pattern of the difference between SIMeddy-5d and OBS is robust with respect to the method employed for diffusivity estimation (Figs. 3c,f,i), a closer investigation of this pattern is justified. One can distinguish regions where 1) K_{max} and K_{inf} are lower in SIMeddy-5d than in OBS, such as in the eSAG (Table 2) or south of Madagascar; 2) K_{max} and K_{inf} are higher in SIMeddy-5d than in OBS, such as in a broad region west of the retroflection; 3) K_{max} is lower but K_{inf} is higher in SIMeddy-5d than in OBS, such as northwest of the retroflection; and 4) K_{inf} is lower but K_{max} is higher in SIMeddy-5d than in OBS, such as in parts of the ARC (Table 2) and at the southern boundary of the study region. In the third and fourth cases, the local relation K_{max}/K_{inf} is substantially altered (Figs. 4d–f), implying that the local representation of eddy mixing suppression

TABLE 3. Summary of spatial mean pseudo-Eulerian and Lagrangian statistics for the greater Agulhas system obtained from OBS and the six Lagrangian experiments performed in this study: near-surface pseudo-Eulerian mean speed and EKE, as well as asymptotic K_{inf} and maximum K_{max} near-surface lateral eddy diffusivity, and Lagrangian integral time T_L and length L_L scales. The spatial mean has been calculated by averaging over all 416 spatial bins.

			Diffusivity estimates (10^3 m^2 s^{-1})							
Lagrangian experiment	Speed (cm s^{-1})	EKE (cm^2 s^{-2})	K_{inf}	K_{inf}^{davis}	K_{inf}^{disp}	K_{max}	K_{max}^{davis}	K_{max}^{disp}	T_L (days)	L_L (km)
OBS	11	307	4.09	3.87	4.33	6.03	5.94	6.58	2.1	24.6
SIMeddy-1d	7	200	3.42	3.29	3.56	5.10	5.04	5.28	3.8	29.0
SIMeddy-5d	7	197	3.41	3.27	3.54	5.15	5.08	5.34	3.9	29.3
SIMeddy-5d-clim	7	201	3.28	3.17	3.40	5.15	5.09	5.36	4.0	28.6
SIMeddy-1m	7	145	2.99	2.86	3.10	4.35	4.26	4.55	4.4	29.6
SIMnoeddy-5d	7	53	1.39	1.32	1.46	2.08	2.00	2.08	6.4	23.7
SIMpareddy-5d	6	6	0.28	0.27	0.29	0.31	0.31	0.33	6.2	10.3

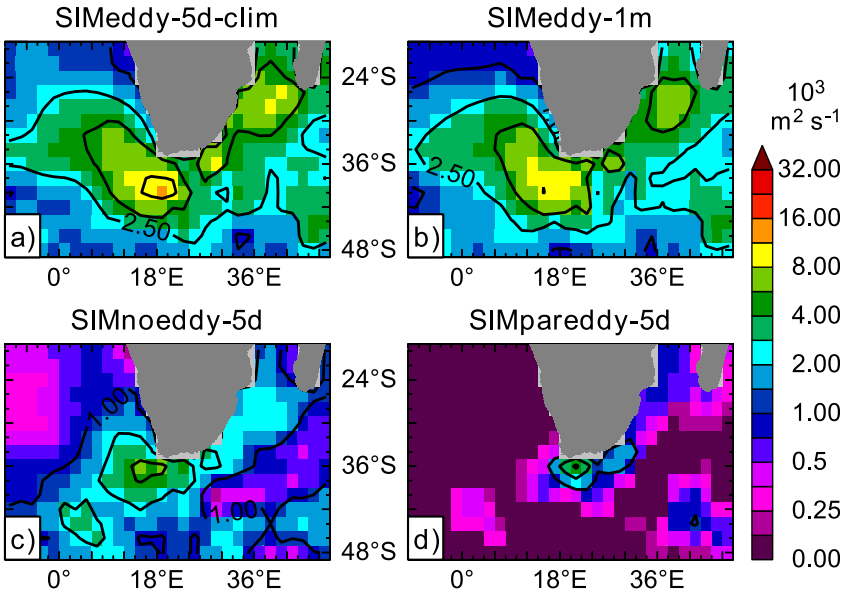

FIG. 6. Sensitivity of the asymptotic eddy diffusivity estimates K_{inf} to OGCM choices. Shown are results for the combined lateral eddy diffusivity estimates obtained from the Lagrangian experiments performed with the eddy-resolving OGCM configuration INALT01 (a) forced with climatological atmospheric fields (SIMeddy-5d-clim), and (b) forced with interannually varying atmospheric fields, but using monthly mean velocities (SIMeddy-1m). Also shown are the results from the Lagrangian experiments performed with the noneddying OGCM configuration ORCA05 (c) without (SIMnoeddy-5d), and (d) with GM parameterization of baroclinic eddies (SIMpareddy-5d).

differs (e.g., in the region around the ARC, eddy mixing suppression is higher in SIMeddy-5d than in OBS). This is most likely related to the fact that the local pseudo-Eulerian mean flow sampled by SIMeddy-5d clearly features a coherent eastward current, whereas in OBS, the mean flow pattern is less clear (Figs. 5a,b).

We conclude that differences in the near-surface lateral eddy diffusivity estimates between SIMeddy-5d and OBS cannot be directly linked to differences in EKE, but they are also influenced by differences in Lagrangian eddy length and time scales related to the suppression of eddy mixing. Even though local differences between the diffusivity estimates from SIMeddy-5d and OBS are strongly nonuniform and can be relatively high, the frequency distributions of K_{inf} are remarkably similar (Fig. 7; Table 3). Moreover, differences between SIMeddy-5d and OBS seem to fall in the uncertainty range. Differences between the two methods to estimate lateral diffusivities in SIMeddy-5d are of the same magnitude as differences between SIM and OBS (cf. section 3a; Table 2); differences between various observational approaches estimating near-surface lateral eddy diffusivity—for example, in the ACC region—are of comparable magnitude or even bigger (Klocker et al. 2012b and references therein). Thus, we conclude that the Lagrangian trajectories simulated with the 5-day mean output of the high-resolution ocean model INALT01 (SIMeddy-5d) capture Lagrangian eddy diffusivity characteristics of real drifter data fairly well, without the need for additional random-walk diffusion.

c. *Sensitivity of eddy diffusivity estimates derived from simulated trajectories to lateral and temporal resolution*

The spatial OGCM resolution determines to which degree eddies are explicitly resolved during the model simulation. The temporal model output resolution further restricts the scale of processes captured by offline simulated advective Lagrangian trajectories. In this section, we quantify the sensitivity of the Lagrangian eddy diffusivity estimates to the temporal (5-day mean vs daily and monthly mean) model output resolution and spatial (1/10° vs 1/2°) OGCM resolution, whereby we focus on K_{inf}.

1) SENSITIVITY TO TEMPORAL MODEL OUTPUT RESOLUTION

In general, studies of oceanic features from the mesoscale to basin scales require a temporal model output

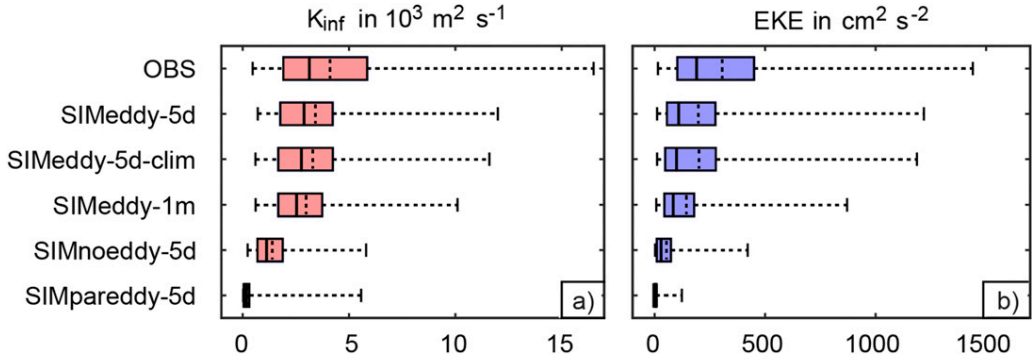

FIG. 7. Box plots of the spatial distributions of (a) the asymptotic eddy diffusivity estimates K_{inf} and (b) pseudo-Eulerian mean EKE. Shown are results for the main Lagrangian experiments employed in this study, whereby K_{inf} was inferred from the combined lateral eddy diffusivity estimate. On each box, the central mark indicates the median calculated out of the 416 overlapping 5° × 5° spatial ocean bins for the greater Agulhas system; the left and right edges of the box indicate the 25th and 75th percentiles, respectively; and the whiskers extend to the minimum and maximum values. The dashed vertical lines indicate the mean values (cf. Table 3).

resolution no longer than a few days. Using offline Lagrangian analyses within a high-resolution ocean model (1/10°), Qin et al. (2014) showed that the connectivity along six major currents does not significantly change for temporal resolutions between 3- and 9-day means. However, degradation in flow characteristics occurs at lower temporal resolutions, resulting in changed transit times and transports between selected upstream and downstream sections.

The comparison of our diffusivity estimates from SIMeddy-5d and SIMeddy-1d shows that 5-day mean output is sufficient to capture the cumulative effect of eddies on particle trajectories in the greater Agulhas system; using daily mean output does not substantially change the spatial distribution (not shown) and magnitude of K_{inf} and the Lagrangian integral time and length scales (Table 3).

SIMeddy-1m yields the same spatial pattern of K_{inf} as SIMeddy-5d (Fig. 6b), but with a generally reduced magnitude (exception: eddy diffusivities in the northern part of the ACC and in near-coastal parts of the AR are increased compared to SIMeddy-5d), resulting in lower spatial mean values and a slightly smaller spatial variability (Fig. 7; Table 3). Even though eddy diffusivities are reduced, the spatial mean K_{inf} still reaches $\sim 3.0 \times 10^3\,m^2\,s^{-1}$ (compared to $\sim 3.4 \times 10^3\,m^2\,s^{-1}$ in SIMeddy-5d). This suggests that monthly mean velocity fields do capture a substantial amount of eddy variability—at least in the greater Agulhas system. Yet, EKE is reduced by 26% (spatial average of $145\,cm^2\,s^{-2}$ in SIMeddy-1m compared to $197\,cm^2\,s^{-2}$ in SIMeddy-5d), and average T_L and L_L are increased (Table 3). The disproportional reduction of K_{inf} by only 12% again highlights that variability and changes in K_{inf} cannot be directly explained by changes in EKE. The results further support the idea that larger and more persistent eddy features are the dominant factors determining eddy diffusivities (Wolfram et al. 2015).

These results agree with Qin et al. (2014), who showed that the connectivity transports in the AC and AR revealed no significant changes for monthly mean fields compared to 3-day mean fields (in contrast to other investigated regions). Likewise, Biastoch et al. (2015) and Cheng et al. (2016) reported interannual-to-decadal variability in Agulhas leakage transport to be captured by monthly mean data. Qin et al. (2014) also noted that the mean transit time for the AC does change significantly for monthly mean fields compared to 3-day mean fields. This can be explained by the fact that in the greater Agulhas system, connectivity transports, as well as eddy diffusivities, are dominated by the largest and most persistent mesoscale features, which are associated with the largest transports (and constitute some of the largest eddies of the World Ocean), while transit time distributions are prone to be influenced by eddy variability at all scales.

2) SENSITIVITY TO LATERAL OGCM RESOLUTION

By the criteria of Hallberg (2013), the ORCA05 model configuration is noneddying in the extended Agulhas Current system, whereas INALT01 is eddy resolving (cf. section 2a). We already showed that SIMeddy-5d (as well as SIMeddy-1d and, with slight restrictions, SIMeddy-1m) captures the general features of observed eddy diffusivities. In principle, eddy diffusivities (as well as EKEs) obtained from noneddying simulations should approach zero. In reality, the scale separation between eddies and mean flow is imperfect. Depending over which time and space scales the mean is defined, some lower-frequency variance remains in the

residual velocities and may lead to nonzero eddy diffusivity estimates, even in so-called noneddying ocean models. Furthermore, numerical noise introduces artificial high-frequency variability. Our analysis for SIMnoeddy-5d yields a spatial mean pseudo-Eulerian EKE of $53\,\mathrm{cm^2\,s^{-2}}$ and corresponding K_{inf} of $\sim 1.4 \times 10^3\,\mathrm{m^2\,s^{-1}}$ (Table 3). Hence, K_{inf} in SIMnoeddy-5d (Fig. 6c) is, on average, $2.0 \times 10^3\,\mathrm{m^2\,s^{-1}}$ weaker than in SIMeddy-5d (cf. section 3a) but still shows the rough spatial pattern from SIMeddy-5d and does not reach values close to zero. Again, the reduction in EKE (~73%) is larger than that in K_{inf} (~58%). The reduction of estimated lateral eddy diffusivities is consistent with the reduction of estimated isopycnal eddy diffusivities of ~50%–60% reported by Wolfram et al. (2015), based on simulations with an idealized ocean model at 32-km resolution compared to simulations at 8-km resolution (their Table 2).

Using the noneddying OGCM configuration with online GM parameterization (SIMpareddy-5d) yields spatial mean pseudo-Eulerian EKE and eddy diffusivity estimates close to zero (Fig. 6d). This is because while parameterizing the advective effect of mesoscale eddies where they are not resolved by the model, GM also suppresses the explicit generation of physical as well as numerical mesoscale variability (Hallberg 2013; cf. section 2b).

In summary, Lagrangian trajectories simulated with the output from our coarse-resolution OGCM configuration do not sufficiently capture the effect of mesoscale eddies on particle dispersal, which results in too-low eddy diffusivity values compared to estimates based on observations and eddy-resolving model simulations. Lagrangian eddy diffusivity estimates are further reduced by the employed GM parameterization. Nevertheless, for Lagrangian particle simulations, the combined Eulerian and eddy-induced velocities from a model simulation with GM may be favored over velocities from coarse-resolution model simulations without GM because they are supposed to represent large-scale circulation patterns and the advective part of particle dispersal more realistically (cf. section 2b). To capture the effect of mesoscale turbulence, one could fill the gap between coarse-resolution simulations and observations/high-resolution simulations by stochastic Lagrangian parameterizations (cf. section 4).

4. Comparison with other eddy diffusivity estimates and implications for eddy parameterizations

a. *Comparison with other eddy diffusivity estimates for the greater Agulhas system*

Peng et al. (2015) estimated Lagrangian eddy diffusivity for the Indian Ocean from surface drifter data by using a binning technique similar to Zhurbas et al. (2014) but deriving diffusivities from the autocorrelation of residual velocities, which were calculated using the Gauss–Markov method (Lumpkin and Johnson 2013). They concluded that their diffusivity estimates (with seasonal effects removed) generally agree with the asymptotic estimates of Zhurbas et al. (2014), which can be confirmed by a closer inspection of Fig. 7 in Peng et al. (2015) and our Figs. 3g and 3h. In the region south of Madagascar, our estimates for K_{inf} between 2.0×10^3 and $12.0 \times 10^3\,\mathrm{m^2\,s^{-1}}$ correspond well to their asymptotic minor principal component diffusivity estimate κ_2 of $11.5 \times 10^3\,\mathrm{m^2\,s^{-1}}$ for region D7 (their Table 2).

Our results also match the Osborn–Cox diffusivity calculated from the evolution of passive tracers (simulated with surface velocities derived from AVISO sea surface height data) by Abernathey and Marshall (2013), who reported diffusivity values between 1.0 and $10.0 \times 10^3\,\mathrm{m^2\,s^{-1}}$ for the greater Agulhas system (their Fig. 2). The overall agreement in magnitude and spatial pattern of our particle-based and their tracer-based diffusivity estimates is encouraging. It supports the applicability of the results of Klocker et al. (2012b) and Wolfram and Ringler (2017b), showing that particle- and tracer-based diffusivities are similar in a simple zonal channel flow, to the complex real oceanic circulation of the greater Agulhas system.

b. *Implications for stochastic parameterizations in offline trajectory calculations*

To derive more diffusive pathways capturing the effect of unresolved turbulence even from coarse-resolution OGCMs, stochastic Lagrangian parameterizations can be employed in offline trajectory calculations (cf. section 1). However, it is still an open question how to robustly specify an appropriate stochastic model and how to fit the associated parameters with respect to the spatial and temporal resolutions of any given Eulerian ocean model output.

Though we did not implement a stochastic parameterization here, our study reveals important aspects to be considered: 1) because asymptotic diffusive regimes could be identified for different dynamic regimes in the greater Agulhas system, stochastic Lagrangian parameterizations, as described in Griffa et al. (1995), may indeed be appropriate to mimic the effect of mesoscale turbulence in this region; 2) stochastic Lagrangian parameterizations should account for the spatial variability of the diffusivity parameter, which does not necessarily scale with variability in EKE; and 3) the choice of parameters in the stochastic Lagrangian parameterizations should not only account for the horizontal (and

temporal) resolution of the underlying OGCM, but should also consider possible subgrid-scale parameterizations, such as GM.

Based on these considerations, we would like to emphasize that the application of a stochastic Lagrangian parameterization implies changing from a pure Lagrangian analysis of the Eulerian OGCM model output to a Lagrangian modeling approach of particle dispersion, which may break consistency with the underlying OGCM physics and thus—depending on the scientific question—may not always be desired.

c. *Relation between Lagrangian eddy diffusivity estimates and diffusivity coefficients of OGCM diffusion parameterizations*

The Lagrangian eddy diffusivity is a quantitative diagnostic for the cumulative effect of eddies on the Lagrangian dispersal, and, as such, it is used in this paper to assess simulated particle dispersal. However, other studies estimating Lagrangian eddy diffusivities from high-resolution OGCM output or drifter data are partially motivated by the desire to determine more realistic parameter values for Eulerian diffusion parameterizations in coarse-resolution OGCMs. It is, therefore, worthwhile to compare our Lagrangian diffusivity estimates with the diffusivity coefficients used in those parameterizations, such as the Redi coefficient A_{ht} (Redi 1982). The coefficient A_{ht} should quantify the effect of scales not resolved in the OGCM (i.e., variability occurring below 0.1° and 0.5° for INALT01 and ORCA05 experiments, respectively) on tracer mixing rates. Important for this context, Lagrangian eddy diffusivities derived from the respective OGCM represent the effect of the (fully or partially) resolved mesoscale on tracer mixing rates.

Following this reasoning, one would expect the difference in the Lagrangian eddy diffusivity estimates derived from a high-resolution OGCM experiment (e.g., SIMeddy-5d) and a coarse-resolution OGCM experiment (e.g., SIMnoeddy-5d) to be comparable in magnitude to the respective difference in the employed diffusivity coefficients. Both should be representative for the diffusive effect of mesoscale variability at horizontal scales between 0.1° and 0.5°. This is, however, not the case: the difference in the Lagrangian eddy diffusivities exhibit a pronounced spatial variability at magnitudes $O(10^3)$ $m^2 s^{-1}$. Because A_{ht} does not include spatial variability apart from its adaptation to the changing grid sizes, the difference in A_{ht} also does not feature spatial variability. Even more strikingly, the difference in A_{ht} only reaches magnitudes $O(10^2)$ $m^2 s^{-1}$.

This indicates that either the model coefficients are not chosen optimally, or Eulerian diffusivity coefficients and Lagrangian eddy diffusivity estimates are two measures that cannot be easily compared.

One could argue that Lagrangian eddy diffusivity estimates derived from drifter data quantify the rate of lateral dispersal in the surface mixed layer, whereas most modern ocean models, as those employed here, use isopycnal diffusivities for their subgrid-scale parameterizations. Yet, mesoscale eddies mix tracers along isopycnals and horizontally at the sea surface (Treguier et al. 1997; Abernathey et al. 2013), so the lateral eddy diffusivities estimated from GDP data and our simulated drifter trajectories can be treated as eddy diffusivity in the surface mixed layer. However, model diffusivities have to be tuned not only with respect to physical, but also to numerical considerations. Profound simplifications in the OGCM diffusion parameterization may further inhibit a direct relation between Eulerian diffusivity coefficients and Lagrangian eddy diffusivity estimates. Also to consider, as already stated by Rypina et al. (2016), Lagrangian diffusivity estimates constitute nonlocal measures, while the diffusivity coefficient for the subgrid-scale parameterization should represent the local effect of eddies. Finally, keeping in mind the challenges of Lagrangian eddy diffusivity estimation, such as removing the mean flow effect and capturing truly asymptotic regimes, Lagrangian eddy diffusivity estimates may not exclusively quantify the impact of mesoscale eddies but may be additionally influenced by methodological choices. Therefore, tuning coarse-resolution OGCM Eulerian eddy diffusivity coefficients based on Lagrangian eddy diffusivities estimated from high-resolution models or observations remains an outstanding issue that needs to be further addressed in more dedicated studies.

5. Conclusions

In this study, we assessed spatially variable near-surface lateral (mesoscale) eddy diffusivity estimates obtained from both simulated Lagrangian trajectories and real drifter data for the greater Agulhas system following the approach of Zhurbas et al. (2014). Answering the three questions outlined in section 1, we showed that in this region,

1) Using 5-day mean velocity fields from the eddy-resolving ocean model configuration INALT01, asymptotic diffusive regimes could be identified for dynamically different sites, some of which exhibit strong suppression of eddy mixing by mean flow.
2) The Lagrangian model-based eddy diffusivity estimates agree in pattern and magnitude with the observation-based estimates from Zhurbas et al. (2014)

and are also comparable to the tracer-based eddy diffusivity estimates provided by Abernathey and Marshall (2013).

3a) Using monthly mean velocity output decreases the EKE but decreases eddy diffusivity estimates disproportionally less, supporting the idea that larger and more persistent eddy features are the dominant factors determining eddy diffusivities (cf. Wolfram et al. 2015).

3b) Using 5-day mean velocity fields from the non-eddying ocean model configuration ORCA05 greatly reduces Lagrangian lateral eddy diffusivities; if a GM parameterization is employed, diffusivities further reduce to values close to zero.

These results suggest that when employing a stochastic Lagrangian parameterization to derive more diffusive trajectories from coarse-resolution model output—particularly for large-scale applications—one should consider the spatial variability of the diffusivity parameter, which does not necessarily scale with variability in EKE, as well as possible subgrid-scale parameterizations, such as GM.

Acknowledgments. OGCM experiments and trajectory simulations were performed at High Performance Computing Centers in Stuttgart (HLRS), Hannover (HLRN) and at the Christian-Albrechts-Universität zu Kiel. OGCM code and data are available upon request from the corresponding author. For reproducibility of the main result figures in this study, respective data and scripts are available at http://data.geomar.de. The project received funding by the Cluster of Excellence 80 "The Future Ocean" within the framework of the Excellence Initiative by the Deutsche Forschungsgemeinschaft (DFG) on behalf of the German federal and state governments (Siren Rühs, Grant CP1412), by the German Federal Ministry of Education and Research (BMBF) (Arne Biastoch, Grant 03F0750A of the SPACES-AGULHAS project), and by the Helmholtz Association and the GEOMAR Helmholtz Centre for Ocean Research Kiel (Jonathan V. Durgadoo, Grants IV014 and GH018). Victor Zhurbas was supported by the Russian Science Foundation (Grant 14-50-00095) and the Russian Foundation for Basic Research (Grant 18-05-00278). The authors further wish to acknowledge the DRAKKAR group for support in model development and two anonymous reviewers for their insightful comments that helped to improve this manuscript.

APPENDIX

Details of the Eddy Diffusivity Estimation—Smoothing Choices and Deviation from the Original Zhurbas et al. (2014) Approach

We followed the approach by Zhurbas et al. (2014) in all fundamental steps summarized in Fig. A1, which were already introduced by Oh et al. (2000), including the smoothing approaches adjusted to the spatiotemporal coverage of drifter data. Because of the increase of the sampling error with increasing time lag (Davis 1991b), a time-dependent finite differencing was applied to obtain $k_{jk}^{\mathrm{disp}}(\mathbf{x}, t)$, and the tensor components $k_{jk}(\mathbf{x}, t)$ and $s_{jk}(\mathbf{x}, t)$ were low-pass filtered with a cosine filter and time-dependent filter window length. The time increment δt was chosen to equal the filter window $[t - 0.2t,\ t + 0.2t]$. Further details can be found in Oh et al. (2000), Zhurbas and Oh (2004), and Zhurbas et al. (2014). Note that simulated drifter trajectories were processed identically to the drifter data for comparability reasons. For a pure model study with a very large number of

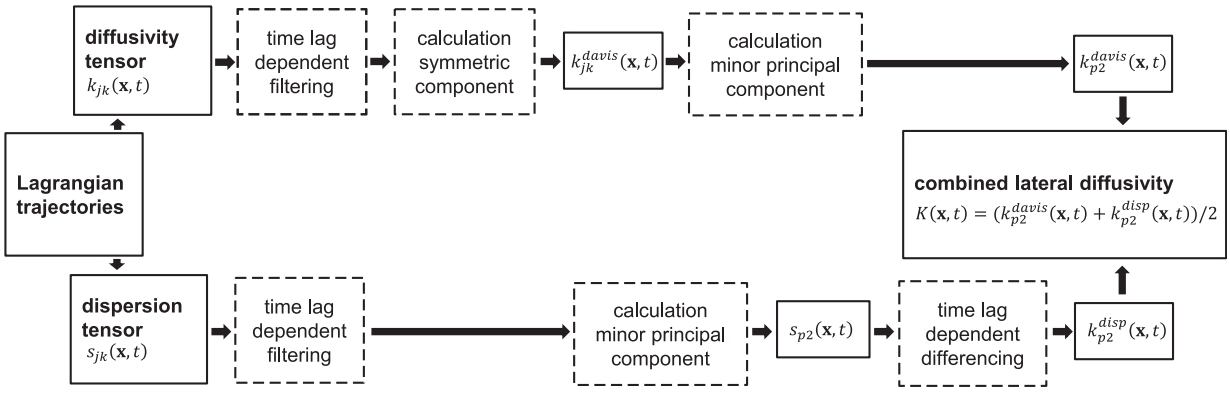

FIG. A1. Lateral eddy diffusivity estimation following Oh et al. (2000).

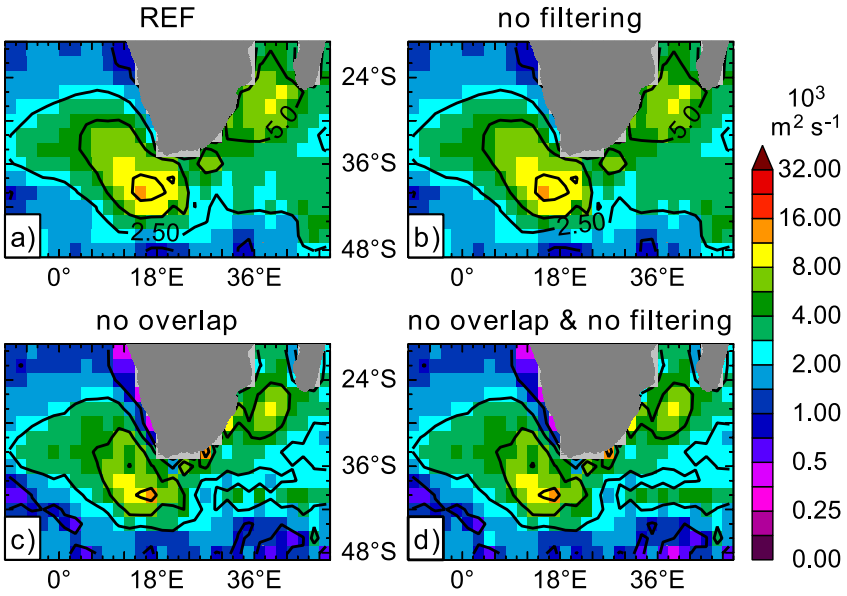

FIG. A2. Robustness of the asymptotic eddy diffusivity estimates K_{inf} with respect to smoothing choices. Shown are the results for the combined lateral eddy diffusivity estimates obtained from Lagrangian experiment SIMeddy-5d with different bin sizes and filters employed: (a) overlapping 5° × 5° bins and time-dependent filtering of the diffusivity and dispersion tensors, as well as time-dependent finite differencing as described in the method section (same as Fig. 2g); (b) overlapping 5° × 5° bins, but no filtering and no time-dependent finite differencing; (c) time-dependent filtering of the diffusivity and dispersion tensors, as well as time-dependent finite differencing as described in the method section, but nonoverlapping 2° × 2° bins; and (d) nonoverlapping 2° × 2° bins, as well as no filtering and no time-dependent finite differencing.

trajectories, less smoothing and nonoverlapping bins may be sufficient and preferred, as indicated by Fig. A2; the asymptotic diffusivity estimates inferred from SIMeddy-5d hardly change when removing the time-dependent filtering and differencing and also show only small changes when changing to nonoverlapping 2° × 2° bins.

We deviated from the original Zhurbas et al. (2014) approach by slightly altering the quality control of drifter data to allow for speeds until 3 m s^{-1} (instead of removing data with speeds >2 m s^{-1}) because in the region of interest, velocities reaching (exceeding) 2 m s^{-1} were reported from observations (and are apparent in the modeled velocity fields). We were further able to increase the number of considered pseudotracks for large time lags by extending the area over which trajectories were sampled for a certain bin (also necessary due to the very high local current velocities and, thus, large dispersion due to mean currents). Finally, we fixed a slight inconsistency in the estimation of K_{max} that previously only considered time lags until 10 days (occasionally leading to $K_{inf} > K_{max}$).

REFERENCES

Abernathey, R. P., and J. Marshall, 2013: Global surface eddy diffusivities derived from satellite altimetry. *J. Geophys. Res. Oceans*, **118**, 901–916, https://doi.org/10.1002/jgrc.20066.

——, D. Ferreira, and A. Klocker, 2013: Diagnostics of isopycnal mixing in a circumpolar channel. *Ocean Modell.*, **72**, 1–16, https://doi.org/10.1016/j.ocemod.2013.07.004.

Arakawa, A., and Y.-J. G. Hsu, 1990: Energy conserving and potential-enstrophy dissipating schemes for the shallow water equations. *Mon. Wea. Rev.*, **118**, 1960–1969, https://doi.org/10.1175/1520-0493(1990)118<1960:ECAPED>2.0.CO;2.

Barnier, B., and Coauthors, 2007: Eddy-permitting ocean circulation hindcasts of past decades. *CLIVAR Exchanges*, No. 3, International CLIVAR Project Office, Southampton, United Kingdom, 8–11.

——, and Coauthors, 2014: DRAKKAR: Developing high resolution ocean components for European Earth system models. *CLIVAR Exchanges*, No. 65, International CLIVAR Project Office, Southampton, United Kingdom, 18–21.

Bauer, S., M. S. Swenson, and A. Griffa, 2002: Eddy mean flow decomposition and eddy diffusivity estimates in the tropical Pacific Ocean: 2. Results. *J. Geophys. Res.*, **107**, 3154, https://doi.org/10.1029/2000JC000613.

Beal, L. M., and Coauthors, 2011: On the role of the Agulhas system in ocean circulation and climate. *Nature*, **472**, 429–436, https://doi.org/10.1038/nature09983.

Berloff, P. S., and J. C. McWilliams, 2002: Material transport in oceanic gyres. Part II: Hierarchy of stochastic models. *J. Phys. Oceanogr.*, **32**, 797–830, https://doi.org/10.1175/1520-0485(2002)032<0797:MTIOGP>2.0.CO;2.

Biastoch, A., C. W. Böning, and J. R. E. Lutjeharms, 2008a: Agulhas leakage dynamics affects decadal variability in Atlantic overturning circulation. *Nature*, **456**, 489–492, https://doi.org/10.1038/nature07426.

——, J. R. E. Lutjeharms, C. W. Böning, and M. Scheinert, 2008b: Mesoscale perturbations control inter-ocean exchange south of Africa. *Geophys. Res. Lett.*, **35**, L20602, https://doi.org/10.1029/2008GL035132.

——, J. V. Durgadoo, A. K. Morrison, E. van Sebille, W. Weijer, and S. M. Griffies, 2015: Atlantic multi-decadal oscillation covaries with Agulhas leakage. *Nat. Commun.*, **6**, 10082, https://doi.org/10.1038/ncomms10082.

Blanke, B., and S. Raynaud, 1997: Kinematics of the Pacific Equatorial Undercurrent: An Eulerian and Lagrangian approach from GCM results. *J. Phys. Oceanogr.*, **27**, 1038–1053, https://doi.org/10.1175/1520-0485(1997)027<1038:KOTPEU>2.0.CO;2.

——, S. Speich, G. Madec, and K. Döös, 2001: A global diagnostic of interocean mass transfers. *J. Phys. Oceanogr.*, **31**, 1623–1632, https://doi.org/10.1175/1520-0485(2001)031<1623:AGDOIM>2.0.CO;2.

——, ——, ——, and R. Maugé, 2002: A global diagnostic of interior ocean ventilation. *Geophys. Res. Lett.*, **29**, 1267, https://doi.org/10.1029/2001GL013727.

Boebel, O., T. Rossby, J. Lutjeharms, W. Zenk, and C. Barron, 2003: Path and variability of the Agulhas Return Current. *Deep-Sea Res. II*, **50**, 35–56, https://doi.org/10.1016/S0967-0645(02)00377-6.

Chelton, D. B., M. G. Schlax, and R. M. Samelson, 2011: Global observations of nonlinear mesoscale eddies. *Prog. Oceanogr.*, **91**, 167–216, https://doi.org/10.1016/j.pocean.2011.01.002.

Chen, R., J. L. McClean, S. T. Gille, and A. Griesel, 2014: Isopycnal eddy diffusivities and critical layers in the Kuroshio Extension from an eddying ocean model. *J. Phys. Oceanogr.*, **44**, 2191–2211, https://doi.org/10.1175/JPO-D-13-0258.1.

Cheng, Y., D. Putrasahan, L. Beal, and B. Kirtman, 2016: Quantifying Agulhas leakage in a high-resolution climate model. *J. Climate*, **29**, 6881–6892, https://doi.org/10.1175/JCLI-D-15-0568.1.

Cronin, M. F., T. Tozuka, A. Biastoch, J. V. Durgadoo, and L. M. Beal, 2013: Prevalence of strong bottom currents in the greater Agulhas system. *Geophys. Res. Lett.*, **40**, 1772–1776, https://doi.org/10.1002/grl.50400.

Danabasoglu, G., and Coauthors, 2014: North Atlantic simulations in Coordinated Ocean-Ice Reference Experiments phase II (CORE-II). Part I: Mean states. *Ocean Modell.*, **73**, 76–107, https://doi.org/10.1016/j.ocemod.2013.10.005.

Davis, R. E., 1991a: Lagrangian ocean studies. *Annu. Rev. Fluid Mech.*, **23**, 43–64, https://doi.org/10.1146/annurev.fl.23.010191.000355.

——, 1991b: Observing the general circulation with floats. *Deep-Sea Res.*, **38A** (Suppl.), S531–S571, https://doi.org/10.1016/S0198-0149(12)80023-9.

De Dominicis, M., G. Leuzzi, P. Monti, N. Pinardi, and P. M. Poulain, 2012: Eddy diffusivity derived from drifter data for dispersion model applications. *Ocean Dyn.*, **62**, 1381–1398, https://doi.org/10.1007/s10236-012-0564-2.

Dencausse, G., M. Arhan, and S. Speich, 2010: Routes of Agulhas rings in the southeastern Cape Basin. *Deep-Sea Res. I*, **57**, 1406–1421, https://doi.org/10.1016/j.dsr.2010.07.008.

de Verdiere, A. C., 1983: Lagrangian eddy statistics from surface drifters in the eastern North Atlantic. *J. Mar. Res.*, **41**, 375–398, https://doi.org/10.1357/002224083788519713.

Döös, K., V. Rupolo, and L. Brodeau, 2011: Dispersion of surface drifters and model-simulated trajectories. *Ocean Modell.*, **39**, 301–310, https://doi.org/10.1016/j.ocemod.2011.05.005.

——, J. Nilsson, J. Nycander, L. Brodeau, and M. Ballarotta, 2012: The World Ocean thermohaline circulation. *J. Phys. Oceanogr.*, **42**, 1445–1460, https://doi.org/10.1175/JPO-D-11-0163.1.

Drijfhout, S. S., P. de Vries, K. Döös, and A. C. Coward, 2003: Impact of eddy-induced transport on the Lagrangian structure of the upper branch of the thermohaline circulation. *J. Phys. Oceanogr.*, **33**, 2141–2155, https://doi.org/10.1175/1520-0485(2003)033<2141:IOETOT>2.0.CO;2.

Durgadoo, J. V., B. R. Loveday, C. J. C. Reason, P. Penven, and A. Biastoch, 2013: Agulhas leakage predominantly responds to the Southern Hemisphere westerlies. *J. Phys. Oceanogr.*, **43**, 2113–2131, https://doi.org/10.1175/JPO-D-13-047.1.

——, S. Rühs, A. Biastoch, and C. W. B. Böning, 2017: Indian Ocean sources of Agulhas leakage. *J. Geophys. Res. Oceans*, **122**, 3481–3499, https://doi.org/10.1002/2016JC012676.

Eden, C., and H. Dietze, 2009: Effects of mesoscale eddy/wind interactions on biological new production and eddy kinetic energy. *J. Geophys. Res.*, **114**, C05023, https://doi.org/10.1029/2008JC005129.

Gary, S. F., M. S. Lozier, Y.-O. Kwon, and J. J. Park, 2014: The fate of North Atlantic Subtropical Mode Water in the FLAME model. *J. Phys. Oceanogr.*, **44**, 1354–1371, https://doi.org/10.1175/JPO-D-13-0202.1.

Gent, P. R., 2011: The Gent–McWilliams parameterization: 20/20 hindsight. *Ocean Modell.*, **39**, 2–9, https://doi.org/10.1016/j.ocemod.2010.08.002.

——, and J. C. McWilliams, 1990: Isopycnal mixing in ocean circulation models. *J. Phys. Oceanogr.*, **20**, 150–155, https://doi.org/10.1175/1520-0485(1990)020<0150:IMIOCM>2.0.CO;2.

——, J. Willebrand, T. J. McDougall, and J. C. McWilliams, 1995: Parameterizing eddy-induced tracer transports in ocean circulation models. *J. Phys. Oceanogr.*, **25**, 463–474, https://doi.org/10.1175/1520-0485(1995)025<0463:PEITTI>2.0.CO;2.

Griesel, A., S. T. Gille, J. Sprintall, J. L. McClean, J. H. LaCasce, and M. E. Maltrud, 2010: Isopycnal diffusivities in the Antarctic Circumpolar Current inferred from Lagrangian floats in an eddying model. *J. Geophys. Res.*, **115**, C06006, https://doi.org/10.1029/2009JC005821.

——, J. L. McClean, S. T. Gille, J. Sprintall, and C. Eden, 2014: Eulerian and Lagrangian isopycnal eddy diffusivities in the Southern Ocean of an eddying model. *J. Phys. Oceanogr.*, **44**, 644–661, https://doi.org/10.1175/JPO-D-13-039.1.

Griffa, A., 1996: Applications of stochastic particle models to oceanographic problems. *Stochastic Modelling in Physical Oceanography*, R. J. Adler, P. Müller, and B. L. Rozovskii, Eds., Progress in Probability Series, Vol. 39, Birkhäuser, 113–140.

——, K. Owens, L. Piterbarg, and B. Rozovskii, 1995: Estimates of turbulence parameters from Lagrangian data using a stochastic particle model. *J. Mar. Res.*, **53**, 371–401, https://doi.org/10.1357/0022240953213151.

Griffies, S., and Coauthors, 2009: Coordinated Ocean-Ice Reference Experiments (COREs). *Ocean Modell.*, **26**, 1–46, https://doi.org/10.1016/j.ocemod.2008.08.007.

Hallberg, R., 2013: Using a resolution function to regulate parameterizations of oceanic mesoscale eddy effects. *Ocean Modell.*, **72**, 92–103, https://doi.org/10.1016/j.ocemod.2013.08.007.

Hansen, D. V., and P.-M. Poulain, 1996: Quality control and interpolations of WOCE-TOGA drifter data. *J. Atmos.*

Oceanic Technol., **13**, 900–909, https://doi.org/10.1175/1520-0426(1996)013<0900:QCAIOW>2.0.CO;2.

Keating, S. R., K. S. Smith, and P. R. Kramer, 2011: Diagnosing lateral mixing in the upper ocean with virtual tracers: Spatial and temporal resolution dependence. *J. Phys. Oceanogr.*, **41**, 1512–1534, https://doi.org/10.1175/2011JPO4580.1.

Klocker, A., R. Ferrari, and J. H. LaCasce, 2012a: Estimating suppression of eddy mixing by mean flows. *J. Phys. Oceanogr.*, **42**, 1566–1576, https://doi.org/10.1175/JPO-D-11-0205.1.

——, ——, ——, and S. T. Merrifield, 2012b: Reconciling float-based and tracer-based estimates of lateral diffusivities. *J. Mar. Res.*, **70**, 569–602, https://doi.org/10.1357/002224012805262743.

Koszalka, I. M., and J. H. LaCasce, 2010: Lagrangian analysis by clustering. *Ocean Dyn.*, **60**, 957–972, https://doi.org/10.1007/s10236-010-0306-2.

——, ——, M. Andersson, K. A. Orvik, and C. Mauritzen, 2011: Surface circulation in the Nordic Seas from clustered drifters. *Deep-Sea Res. I*, **58**, 468–485, https://doi.org/10.1016/j.dsr.2011.01.007.

——, T. W. N. Haine, and M. G. Magaldi, 2013a: Fates and travel times of Denmark Strait Overflow water in the Irminger Basin. *J. Phys. Oceanogr.*, **43**, 2611–2628, https://doi.org/10.1175/JPO-D-13-023.1.

——, J. H. LaCasce, and C. Mauritzen, 2013b: In pursuit of anomalies—Analyzing the poleward transport of Atlantic water with surface drifters. *Deep-Sea Res. II*, **85**, 96–108, https://doi.org/10.1016/j.dsr2.2012.07.035.

Krauss, W., and C. W. Böning, 1987: Lagrangian properties of eddy fields in the northern North Atlantic as deduced from satellite-tracked buoys. *J. Mar. Res.*, **45**, 259–291, https://doi.org/10.1357/002224087788401142.

LaCasce, J. H., 2008: Statistics from Lagrangian observations. *Prog. Oceanogr.*, **77**, 1–29, https://doi.org/10.1016/j.pocean.2008.02.002.

Large, W. G., and S. G. Yeager, 2009: The global climatology of an interannually varying air–sea flux data set. *Climate Dyn.*, **33**, 341–364, https://doi.org/10.1007/s00382-008-0441-3.

Laurindo, L. C., A. J. Mariano, and R. Lumpkin, 2017: An improved near-surface velocity climatology for the global ocean from drifter observations. *Deep-Sea Res. I*, **124**, 73–92, https://doi.org/10.1016/j.dsr.2017.04.009.

Lique, C., A. M. Treguier, B. Blanke, and N. Grima, 2010: On the origins of water masses exported along both sides of Greenland: A Lagrangian model analysis. *J. Geophys. Res.*, **115**, C05019, https://doi.org/10.1029/2009JC005316.

Loveday, B. R., J. V. Durgadoo, C. J. C. Reason, A. Biastoch, and P. Penven, 2014: Decoupling of the Agulhas leakage from the Agulhas Current. *J. Phys. Oceanogr.*, **44**, 1776–1797, https://doi.org/10.1175/JPO-D-13-093.1.

Lübbecke, J. F., J. V. Durgadoo, and A. Biastoch, 2015: Contribution of increased Agulhas leakage to tropical Atlantic warming. *J. Climate*, **28**, 9697–9706, https://doi.org/10.1175/JCLI-D-15-0258.1.

Lumpkin, R., and P. Flament, 2001: Lagrangian statistics in the central North Pacific. *J. Mar. Syst.*, **29**, 141–155, https://doi.org/10.1016/S0924-7963(01)00014-8.

——, and S. L. Garzoli, 2005: Near-surface circulation in the tropical Atlantic Ocean. *Deep-Sea Res. I*, **52**, 495–518, https://doi.org/10.1016/j.dsr.2004.09.001.

——, and M. Pazos, 2007: Measuring surface currents with Surface Velocity Program drifters: The instrument, its data, and some recent results. *Lagrangian Analysis and Prediction of Coastal and Ocean Dynamics*, A. Griffa et al., Eds., Cambridge University Press, 39–67.

——, and G. C. Johnson, 2013: Global ocean surface velocities from drifters: Mean, variance, El Niño–Southern Oscillation response, and seasonal cycle. *J. Geophys. Res. Oceans*, **118**, 2992–3006, https://doi.org/10.1002/jgrc.20210.

——, S. A. Grodsky, L. Centurioni, M. H. Rio, J. A. Carton, and D. Lee, 2013: Removing spurious low-frequency variability in drifter velocities. *J. Atmos. Oceanic Technol.*, **30**, 353–360, https://doi.org/10.1175/JTECH-D-12-00139.1.

——, T. Özgökmen, and L. Centurioni, 2017: Advances in the application of surface drifters. *Annu. Rev. Mar. Sci.*, **9**, 59–81, https://doi.org/10.1146/annurev-marine-010816-060641.

Lutjeharms, J. R. E., 2006: *The Agulhas Current.* Springer, 329 pp.

——, 2007: Three decades of research on the greater Agulhas Current. *Ocean Sci.*, **3**, 129–147, https://doi.org/10.5194/os-3-129-2007.

——, and I. J. Ansorge, 2001: The Agulhas Return Current. *J. Mar. Syst.*, **30**, 115–138, https://doi.org/10.1016/S0924-7963(01)00041-0.

Madec, G., 2008: NEMO ocean engine. IPSL Note du Pôle de modélisation 27, 396 pp., https://www.nemo-ocean.eu/wp-content/uploads/NEMO_book.pdf.

McClean, J. L., P. M. Poulain, J. W. Pelton, and M. E. Maltrud, 2002: Eulerian and Lagrangian statistics from surface drifters and a high-resolution POP simulation in the North Atlantic. *J. Phys. Oceanogr.*, **32**, 2472–2491, https://doi.org/10.1175/1520-0485-32.9.2472.

Mesinger, F., and A. Arakawa, 1976: Numerical methods used in atmospheric models. WMO Tech. Rep. GARP 17, 70 pp., http://weather.ou.edu/~scavallo/classes/metr_5004/f2013/lectures/Mesinger_ArakawaGARP.pdf.

Monti, P., and G. Leuzzi, 2010: Lagrangian models of dispersion in marine environment. *Environ. Fluid Mech.*, **10**, 637–656, https://doi.org/10.1007/s10652-010-9184-x.

Oh, I. S., V. Zhurbas, and W. Park, 2000: Estimating horizontal diffusivity in the East Sea (Sea of Japan) and the northwest Pacific from satellite-tracked drifter data. *J. Geophys. Res.*, **105**, 6483–6492, https://doi.org/10.1029/2000JC900002.

Peng, S., Y.-K. Qian, R. Lumpkin, P. Li, D. Wang, and Y. Du, 2015: Characteristics of the near-surface currents in the Indian Ocean as deduced from satellite-tracked surface drifters. Part II: Lagrangian statistics. *J. Phys. Oceanogr.*, **45**, 459–477, https://doi.org/10.1175/JPO-D-14-0049.1.

Poulain, P.-M., 2001: Adriatic Sea surface circulation as derived from drifter data between 1990 and 1999. *J. Mar. Syst.*, **29**, 3–32, https://doi.org/10.1016/S0924-7963(01)00007-0.

——, R. Gerin, E. Mauri, and R. Pennel, 2009: Wind effects on drogued and undrogued drifters in the eastern Mediterranean. *J. Atmos. Oceanic Technol.*, **26**, 1144–1156, https://doi.org/10.1175/2008JTECHO618.1.

Qin, X., E. van Sebille, and A. Sen Gupta, 2014: Quantification of errors induced by temporal resolution on Lagrangian particles in an eddy-resolving model. *Ocean Modell.*, **76**, 20–30, https://doi.org/10.1016/j.ocemod.2014.02.002.

Redi, M. H., 1982: Oceanic isopycnal mixing by coordinate rotation. *J. Phys. Oceanogr.*, **12**, 1154–1158, https://doi.org/10.1175/1520-0485(1982)012<1154:OIMBCR>2.0.CO;2.

Rieck, J. K., C. W. Böning, R. J. Greatbatch, and M. Scheinert, 2015: Seasonal variability of eddy kinetic energy in a global high-resolution ocean model. *Geophys. Res. Lett.*, **42**, 9379–9386, https://doi.org/10.1002/2015GL066152.

Rühs, S., J. V. Durgadoo, E. Behrens, and A. Biastoch, 2013: Advective timescales and pathways of Agulhas leakage. *Geophys. Res. Lett.*, **40**, 3997–4000, https://doi.org/10.1002/grl.50782.

Rypina, I. I., I. Kamenkovich, P. Berloff, and L. J. Pratt, 2012: Eddy-induced particle dispersion in the near-surface North

Atlantic. *J. Phys. Oceanogr.*, **42**, 2206–2228, https://doi.org/10.1175/JPO-D-11-0191.1.

——, A. Kirincich, S. Lentz, and M. Sundermeyer, 2016: Investigating the eddy diffusivity concept in the coastal ocean. *J. Phys. Oceanogr.*, **46**, 2201–2218, https://doi.org/10.1175/JPO-D-16-0020.1.

Sallée, J. B., K. Speer, R. Morrow, and R. Lumpkin, 2008: An estimate of Lagrangian eddy statistics and diffusion in the mixed layer of the Southern Ocean. *J. Mar. Res.*, **66**, 441–463, https://doi.org/10.1357/002224008787157458.

Schouten, M. W., W. P. M. de Ruijter, P. J. van Leeuwen, and J. R. E. Lutjeharms, 2000: Translation, decay and splitting of Agulhas rings in the southeastern Atlantic Ocean. *J. Geophys. Res.*, **105**, 21 913–21 925, https://doi.org/10.1029/1999JC000046.

——, ——, and ——, 2002: Upstream control of Agulhas ring shedding. *J. Geophys. Res.*, **107**, 3109, https://doi.org/10.1029/2001JC000804.

Speich, S., B. Blanke, and G. Madec, 2001: Warm and cold water routes of an O.G.C.M. thermohaline conveyor belt. *Geophys. Res. Lett.*, **28**, 311–314, https://doi.org/10.1029/2000GL011748.

Swenson, M. S., and P. P. Niiler, 1996: Statistical analysis of the surface circulation of the California Current. *J. Geophys. Res.*, **101**, 22 631–22 645, https://doi.org/10.1029/96JC02008.

Taylor, G. I., 1922: Diffusion by continuous movements. *Proc. London Math. Soc.*, **s2-20**, 196–212, https://doi.org/10.1112/plms/s2-20.1.196.

Treguier, A. M., I. M. Held, and V. D. Larichev, 1997: Parameterization of quasigeostrophic eddies in primitive equation ocean models. *J. Phys. Oceanogr.*, **27**, 567–580, https://doi.org/10.1175/1520-0485(1997)027<0567:POQEIP>2.0.CO;2.

Uchida, T., R. Abernathey, and S. Smith, 2017: Seasonality of eddy kinetic energy in an eddy permitting global climate model. *Ocean Modell.*, **118**, 41–58, https://doi.org/10.1016/j.ocemod.2017.08.006.

van Sebille, E., P. J. van Leeuwen, A. Biastoch, C. N. Barron, and W. P. M. de Ruijter, 2009: Lagrangian validation of numerical drifter trajectories using drifting buoys: Application to the Agulhas system. *Ocean Modell.*, **29**, 269–276, https://doi.org/10.1016/j.ocemod.2009.05.005.

——, L. M. Beal, and W. E. Johns, 2011: Advective time scales of Agulhas leakage to the North Atlantic in surface drifter observations and the 3D OFES model. *J. Phys. Oceanogr.*, **41**, 1026–1034, https://doi.org/10.1175/2010JPO4602.1.

——, P. Spence, M. R. Mazloff, M. H. England, S. R. Rintoul, and O. A. Saenko, 2013: Abyssal connections of Antarctic Bottom Water in a Southern Ocean State Estimate. *Geophys. Res. Lett.*, **40**, 2177–2182, https://doi.org/10.1002/grl.50483.

——, J. Sprintall, F. U. Schwarzkopf, A. Sen Gupta, A. Santoso, M. H. England, A. Biastoch, and C. W. Böning, 2014: Pacific-to-Indian Ocean connectivity: Tasman leakage, Indonesian Throughflow, and the role of ENSO. *J. Geophys. Res. Oceans*, **119**, 1365–1382, https://doi.org/10.1002/2013JC009525.

——, and Coauthors, 2018: Lagrangian ocean analysis: Fundamentals and practices. *Ocean Modell.*, **121**, 49–75, https://doi.org/10.1016/j.ocemod.2017.11.008.

Wolfram, P. J., and T. D. Ringler, 2017a: Quantifying residual, eddy, and mean flow effects on mixing in an idealized circumpolar current. *J. Phys. Oceanogr.*, **47**, 1897–1920, https://doi.org/10.1175/JPO-D-16-0101.1.

——, and ——, 2017b: Computing eddy-driven effective diffusivity using Lagrangian particles. *Ocean Modell.*, **118**, 94–106, https://doi.org/10.1016/j.ocemod.2017.08.008.

——, ——, M. E. Maltrud, D. W. Jacobsen, and M. R. Petersen, 2015: Diagnosing isopycnal diffusivity in an eddying, idealized midlatitude ocean basin via Lagrangian, in Situ, Global, High-Performance Particle Tracking (LIGHT). *J. Phys. Oceanogr.*, **45**, 2114–2133, https://doi.org/10.1175/JPO-D-14-0260.1.

Zalesak, S. T., 1979: Fully multidimensional flux-corrected transport algorithms for fluids. *J. Comput. Phys.*, **31**, 335–362, https://doi.org/10.1016/0021-9991(79)90051-2.

Zhurbas, V., and I. S. Oh, 2004: Drifter-derived maps of lateral diffusivity in the Pacific and Atlantic Oceans in relation to surface circulation patterns. *J. Geophys. Res.*, **109**, C05015, https://doi.org/10.1029/2003JC002241.

——, D. Lyzhkov, and N. Kuzmina, 2014: Drifter-derived estimates of lateral eddy diffusivity in the World Ocean with emphasis on the Indian Ocean and problems of parameterisation. *Deep-Sea Res. I*, **83**, 1–11, https://doi.org/10.1016/j.dsr.2013.09.001.

6 Synthesis

In this thesis I addressed different facets of the question: *How can Lagrangian connectivity studies with high-resolution ocean models help improving our understanding of the spreading of water masses associated with the global overturning circulation?* To do so, I reviewed the theoretical background of Lagrangian connectivity studies with ocean models (chapter 2), thereby contrasting the interpretation of Lagrangian trajectories as volume, tracer, or object pathways and highlighting the importance of distinguishing Lagrangian analyzes of a simulated flow (purely advective trajectories) from Lagrangian modeling approaches (including Lagrangian sub-grid scale parameterizations). I subsequently focused on Lagrangian analyzes of high-resolution ocean general circulation models (OGCMs). I made use of them to investigate volume transport pathways and along-track property transformations associated with the upper limb of the global overturning circulation (GOC) in the South Atlantic (chapter 3) and Indian Ocean (chapter 4). In addition, I assessed their performance in the extended Agulhas region by comparing lateral eddy diffusivity estimates derived from simulated particle dispersal and observed drifter trajectories (chapter 5). Overall, these studies contributed to a revised picture of the large-scale connectivity associated with the GOC and yielded new insights on the suitability of Lagrangian model analyzes of volume transport pathways for assessing large-scale spreading pathways and transformation of water masses, as summarized and discussed below in section 6.1 and section 6.2, respectively. Both sections further include an outlook in terms of unresolved questions and newly emerged issues, which need to be addressed in future studies. Finally, section 6.3 provides brief conclusive remarks.

6.1 Revision of large-scale connectivity associated with the upper limb of the GOC under consideration of small-scale flow variability

Acknowledging the important role of small-scale processes for the large-scale GOC has required a revision of the pathways, as well as associated timescales, transports, and water property modifications related to the lower and upper limb of the GOC. Despite an increasing number of studies addressing individual aspects of this issue by means of Lagrangian analyzes with high-resolution ocean models, comprehensive

studies of the upper limb of the GOC in the Indian and South Atlantic Oceans have been scarce. The studies presented in chapter 3 and chapter 4 of this thesis targeted this gap and their results challenge some of the current views of these circulation pattern. The most important findings of this thesis in terms of estimated Lagrangian connectivity measures are:

- **Volumetric decomposition**: The strength of the upper cell of the GOC amounts to ∼13 Sv in the tropical South Atlantic, from which ∼7 Sv are supplied by the so-called warm water route via the Agulhas Current system and ∼6 Sv by the direct cold water route through Drake Passage. This is in contrast to previous Lagrangian analyzes with coarser resolution models which suggested an only minor Drake Passage contribution.

- **Transit times**: The dominant timescale with that the GOC's upper limb water volumes are advected through the Indian and South Atlantic Ocean is in the order of a few decades. Thus, the Pacific-Indo-Atlantic return flow constitutes a very fast branch of the GOC for which total turnover timescales have been estimated in the centennial to millennial range [Döös et al., 2012]. The transit time distributions show a broad tail and less distinct peaks than suggested by coarser resolution models, reflecting very diverse pathways resulting from small-scale flow variability.

- **Along-track property changes**: The Indian and South Atlantic Oceans by no means can be regarded as passive connectors of upper ocean waters between upwelling and convection regions, but largely modify waters during their transit. Most importantly, net evaporation regions along major spreading pathways in both basins cause a substantial salinification of a large fraction of upper limb waters.

These results highlight the benefits of Lagrangian analyzes to investigate the simulated flow field of ocean models in terms of advective volume transport pathways and timescales, as well as net water mass transformations inferred from along-track property changes. However, in light of the substantial along-track property changes, the interpretation of advective pathways and timescales inferred from Lagrangian analyzes as the propagation pathways and timescales of upper ocean temperature and salinity anomalies becomes questionable. Upper limb property changes in distinct regions in the Indian Ocean and South Atlantic, such as warming signals in the Agulhas Current system [Rouault et al., 2009; Loveday et al., 2015] or the Indonesian Throughflow [Lee et al., 2015], are most likely not — or at least not only — directly transmitted along the derived advective pathways and with the advective timescales towards the equatorial Atlantic and beyond. Overall, the results are in line with the argumentation of Lozier [2010] who revisited the Atlantic part of the

GOC (with particular focus on the Northern Hemisphere) and stated that the view of the GOC as a coherent conveyer belt transporting heat and dissolved substances through the world ocean is on its way to deconstruction. It is noteworthy though that the deeper parts of the upper limb, such as the intermediate waters originating south of Australia and those entering through Drake passage and transiting the South Atlantic without mixed layer contact, indeed may keep their characteristic properties along their transit. This suggests that for these water types simulated advective timescales and pathways may be of larger relevance for the propagation of potential temperature and salinity anomalies. To better understand how property anomalies in distinct regions of the GOC's upper limb may be communicated across the Indian Ocean and South Atlantic basins, additional sensitivity model experiments as employed by Lübbecke et al. [2015] could be performed [Durgadoo et al., 2017]. Some of the novel features listed above have been attributed to an increased horizontal and temporal resolution of the OGCM output employed for the Lagrangian analyzes, that is, to the so far often neglected impact of small-scale processes on the large-scale circulation (cf. chapter 3 and chapter 4). Yet, a limitation of these new studies is that their results reflect features of the circulation simulated with only two specific OGCMs. Even though the OGCMs have been carefully validated and show particular good skill in the representation of the upper ocean circulation, it can not be completely excluded that the results are partially affected by details in the model configurations and forcings. Unfortunately, even though Lagrangian model analyzes are less costly than the original OGCM integrations, vast and thorough Lagrangian analyzes based on high-resolution OGCM data as those presented here are still associated with very high computational efforts. Thus, a repetition of the Lagrangian analyzes with different OGCM configurations to specifically test certain sensitivities with respect to model configuration details and employed forcing data sets is beyond the scope of this thesis, but is worth being investigated in future studies.

Another question that needs future studies is: What controls the strength of the direct Drake Passage contribution to the upper limb of the GOC in the Atlantic and how is it related to the Agulhas contribution? In chapter 3 it has been shown that the relative contributions of the two routes to the upper limb flow in the tropical Atlantic may experience multi-decadal changes. In particular, it is indicated that the Agulhas contribution to the upper limb of the AMOC is increasing, while the Drake Passage contribution decreases. However, more research is needed to explain the mechanisms of potential temporal variability in the ratio of the two sources. The ultimate goal would then be to use high-resolution OGCMs or even coupled ocean-atmosphere models to link the variability in the two upper limb routes to the variability in the lower limb of the GOC.

6.2 Suitability of Lagrangian model analyzes for assessing large-scale spreading and transformation of water masses

The conclusions presented above highlight the benefits of Lagrangian particle analyzes to study the simulated flow field of ocean models in terms of volume transport pathways and along-track water property modifications. But how well do volume transport pathways inferred from Lagrangian analyzes actually describe *real* large-scale water mass spreading pathways and transformation?

To answer this question, we first have to recap the definitions of a water mass, as well as volume and tracer transport pathways. In observational oceanography, a water mass is defined as a body of water with common formation history and distinct conservative properties, that are, properties that only change at the sea surface [e.g., Talley et al., 2011]. In the continuous real ocean, the spreading of a certain water mass can be described by a set of trajectories of infinitesimal water volumes with a specific temperature and salinity or other tracer content. Ignoring molecular diffusion, water mass transformation through mixing processes can then be regarded as a spatial reorganization of infinitesimal water volumes with different properties. However, in the discretized simulated ocean (advective-diffusive) tracer spreading and (purely advective) Lagrangian particle trajectories representing volume transport pathways are distinct (cf. section 1.1 and section 2.1) and neither of those fully describe the spreading of a certain water mass as defined in observational oceanography. Simulated Lagrangian volume transport pathways describe the net spreading of selected small volumes of ocean water, but these may experience along-track tracer changes. Simulated tracer spreading can be interpreted as the net pathways of individual particles with distinct constant characteristics, but can not be directly associated with a volume transport. However, these discrepancies become smaller with increasing model resolution which results in more explicitly resolved small-scale mixing processes and hence weaker diffusion parameterizations.

Following this reasoning the suitability of Lagrangian model analyzes for assessing water mass pathways can be assessed in two ways. On the one hand one can compare the simulated Lagrangian volume transport pathways with simulated tracer spreading to judge the suitability of Lagrangian model analyzes to estimate the pathways of a distinct water mass within the underlying OGCM simulation. On the other hand, one can compare the simulated Lagrangian volume transport trajectories with observed water mass spreading as inferred from observed particle trajectories or tracer spreading. It is important to distinguish model reality from observed reality, since even if Lagrangian volume transport trajectories may appear not sufficiently diffusive compared to directly simulated tracer spreading, they still may adequately represent observed tracer and particle spreading (this is due to the potential impact

of numerical diffusion which could yield a simulated tracer spreading that is too diffusive compared to observed tracer spreading). In this dissertation I addressed this issue by investigating the question of how well the simulated particle spreading compares with observed particle spreading in terms of estimated Lagrangian lateral eddy diffusivities, which quantify the rate of particle dispersal due to mesoscale eddies[1]. The main finding was that:

- Near-surface lateral eddy diffusivity estimates inferred from Lagrangian analyzes with daily and 5-day mean output of a fully mesoscale resolving OGCM show similar spatial pattern and magnitude to eddy diffusivity estimates inferred from drifter observations.

Thus, at least for the chosen model configuration and in the region considered, the lateral near-surface dispersal of simulated purely advective particle trajectories seems to be sufficiently "diffusive" compared to observed particle dispersal in the real ocean. Within this dissertation I did not address the question of how well the dispersal of the simulated advective particle trajectories compares to simulated tracer spreading. Yet, in an accompanying study [Wagner et al., in preparation], we do compare the spreading of a passive tracer (integrated online in a successive version of the fully mesoscale resolving OGCM configuration) to the dispersal of Lagrangian particles (advected with the stored daily mean velocities of the same OGCM). A sub-surface region of the greater Agulhas system which is characterized by intense mesoscale eddy variability and weak mean flow serves as a test domain. The comparison in terms of mean pathways, horizontal and vertical distributions, as well as eddy diffusivity estimates is generally favorable and does not yield substantial differences between tracer spreading and particle dispersal (Fig. 6.1). Together, these studies indicate that:

- Water mass pathways can be reasonably well represented by a set of simulated purely advective (volume transport) trajectories, provided that the employed model output resolves the turbulent processes that dominate the local mixing.

These are generally very encouraging results. However, a generalization in terms of a certain model resolution required for offline calculated purely advective (volume transport) pathways being able to represent observed tracer and particle or simulated tracer spreading is yet not possible. The here discussed studies assessed particle dispersal in a relatively confined region with specific OGCMs for relatively short time periods. Results again may be sensitive to details of the OGCM configurations and may as well depend on the region and timescales of interest.
In any case, discrepancies between the dispersal of the simulated advective particle

[1] The term eddy diffusivity has been established with respect to its usage as a quantity that specifies the strength of turbulent mixing expressed via a diffusive process.

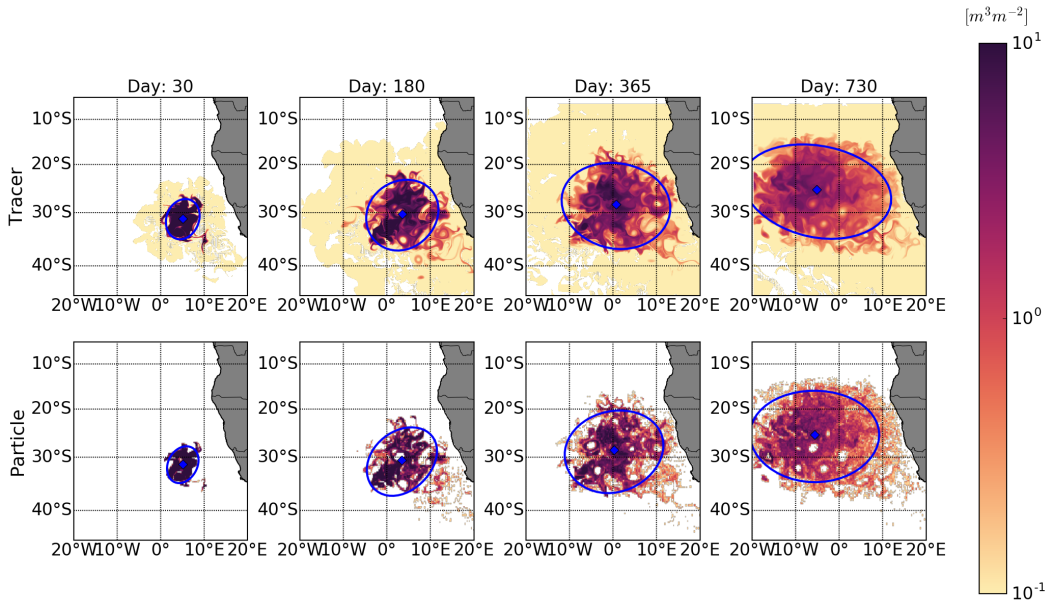

Fig. 6.1 *Vertical integral of tracer (top) and particle (bottom) concentration ($m^3\,m^{-2}$, logarithmic scale) at different time steps (daily averages) after release. Variance ellipses with radii of two standard deviations are shown and blue diamonds indicate center of mass. Adopted from Wagner et al. [in preparation].*

trajectories and observed drifter trajectories increase with decreasing horizontal and temporal resolution as shown in chapter 5. Likewise, the suitability of simulated advective particle trajectories to represent simulated tracer spreading is expected to decrease with coarsening resolution. Even though I did not directly tested the implementation of Lagrangian diffusion parameterizations for reducing these discrepancies, I highlighted that:

- Stochastic Lagrangian parameterizations in diffusion form may indeed be appropriate to mimic the effect of turbulent processes not resolved in OGCM output fields on simulated particle trajectories. However, for such parameterizations not only the model resolution but also the spatial variability of the diffusivity parameter should be considered, which does not necessarily scale with eddy kinetic energy.

Even though Lagrangian diffusion parameterizations lead to more diverse trajectories, it is to emphasize that they break the consistency with the underlying model output. Consequently, they do no longer represent volume transport pathways but have to be interpreted as offline simulated tracer particle trajectories.

6.3 Conclusions

Lagrangian studies with ocean models constitute a unique tool to coherently study seawater pathways associated with the global overturning circulation (GOC) and they substantially contributed to our current knowledge of its spatio-temporal characteristics. Acknowledging one of the most fundamental alterations in the conceptual view of the GOC, which is the substantial impact of small-scale flow variability on the large-scale overturning, Lagrangian connectivity studies with high-resolution models are of particular value to further improve our knowledge of the GOC.
However, with respect to the question how well the derived pathways and associated connectivity measures represent real water mass spreading, it is important to carefully distinguish Lagrangian analyzes of simulated volume transport pathways (purely advective trajectories) from Lagrangian modeling approaches to estimate tracer pathways (including sub-grid scale parameterizations). Neither of these approaches is able to fully describe water mass spreading as defined in observational oceanography, but both are useful means to study individual aspects of it. In the end it depends on the exact research question, which approach is to be preferred.

Acknowledgments

I would like to thank all those who accompanied and supported me during this very exciting and inspiring, but sometimes also exhausting and tedious last years as a PhD candidate.

Without the encouragement and guidance from my supervisor Arne Biastoch this thesis would not have been possible. I have been greatly appreciating his trust in my scientific skills and his willingness to let me follow my own ideas while at the same time helping me to stay focused and not to get too absorbed by the many evolving interesting side stories. A great help with keeping track also came from regular ISOS committee meetings with Richard Greatbach and Steffen Börm.
During my whole time as a member of the theory and modeling department at GEOMAR I always enjoyed the fruitful scientific discussions and funny to weird lunch breaks in the coffee room. Particular thanks go to Willi Rath, who more than once saved me from sleepless nights with his technical skills, as well as to those colleagues with whom I collaborated for scientific publications, namely, Jonathan Durgadoo, Franziska Schwarzkopf, Inga Koszalka, Patrick Wagner, Nele Tim, and Claus Böning.
I am also very thankful for the great experiences and support I have been offered by the external researchers Erik van Sebille and Susan Lozier in form of invitations to workshops, research visits, and helpful advise in terms of career planning, as well as by Victor Zhurbas, who agreed to co-author a paper of mine without ever having met me in person. I am further aware that my scientific as well as personal development largely benefited from the very diverse ISOS courses I have been able to attend over the last years.
And without the regular meetings with ”my girls”, everything would have been less fun. But also in difficult times, I could rely on the help of Katha, Fine, and Annika — be it for test talks, proofreading, or just time to relax and talk. Also Theo always has had an open ear for me and continuously provided suggestions how to improve the graphical design of my research output.
Moreover, I will always be grateful for the unique and truly moving experiences with the Ice Climate Education project, initiated by Arved Fuchs and supported by Dirk

Notz, which sensitized me for questions of sustainability and climate justice, that later lead me on my way to study climate physics.

Besides, I am just happy to have such great friends as Katti and Björn, and my chilled brother Basti, who every now and then help me to remember that yes — even though the PhD is a very important thing to pursue — there are other things in live that matter.
Finally, I owe my deepest gratitude to Farina and my parents, who have always been there supporting me following my own path, and last but not least to Damian, who simply has been sharing live with me for nearly five years now, including all its highs and lows.

References

This bibliography contains references for chapters 1-3 and chapter 6. Chapters 4-5 contain their own list of references included in the inserted print version of the respective manuscripts.

Ådlandsvik, B., J. Bartsch, D. Brickman, H. I. Browman, K. Edwards, Ø. Fiksen, A. Gallego, A. J. Hermann, S. Hinckley, E. Houde, M. Huret, J.-O. Irisson, G. Lacroix, J. M. Leis, P. McCloghrie, B. A. Megrey, T. Miller, J. van der Molen, C. Mullon, E. W. North, C. Parada, C. B. Paris, P. Pepin, P. Petitgas, K. Rose, U. H. Thygesen, and C. Werner (1992). *Manual of recommended practices for modelling physical-biological interactions during fish early life*. Ed. by E. W. North, A. Gallego, and P. Petitgas. 295. International Council for the Exploration of the Sea (cit. on p. 14).

Appen, W.-J. von, I. M. Koszalka, R. S. Pickart, T. W. Haine, D. Mastropole, M. G. Magaldi, H. Valdimarsson, J. Girton, K. Jochumsen, and G. Krahmann (2014). „The East Greenland Spill Jet as an important component of the Atlantic Meridional Overturning Circulation“. In: *Deep Sea Res. Part I Oceanogr. Res. Pap.* 92, pp. 75–84. DOI: 10.1016/J.DSR.2014.06.002 (cit. on p. 17).

Arakawa, A and Y.-J. G Hsu (1990). „Energy Conserving and Potential-Enstrophy Dissipating Schemes for the Shallow Water Equations“. In: *Mon. Weather Rev.* 118, pp. 1960–1969 (cit. on p. 30).

Backeberg, B. C., P. Penven, and M. Rouault (2012). „Impact of intensified Indian Ocean winds on mesoscale variability in the Agulhas system“. In: *Nat. Clim. Chang.* 2.8, pp. 608–612. DOI: 10.1038/nclimate1587 (cit. on p. 28).

Baltazar-Soares, M., A. Biastoch, C. Harrod, R. Hanel, L. Marohn, E. Prigge, D. Evans, K. Bodles, E. Behrens, C. W. Böning, and C. Eizaguirre (2014). „Recruitment collapse and population structure of the European eel shaped by local ocean current dynamics.“ In: *Curr. Biol.* 24.1, pp. 104–8. DOI: 10.1016/j.cub.2013.11.031 (cit. on pp. 2, 14).

Barnier, B., A. Blaker, A. Biastoch, C. Böning, A. Coward, J. Deshayes, J. Hirshi, J. Le Sommer, G. Madec, G. Maze, J. Molines, A. New, T. Penduff, M. Scheinert, C. Talandier, and A.-M. Treguier (2014). „DRAKKAR: developing high resolution ocean components for European Earth system models“. In: *CLIVAR Exch. No. 65* 19.2, pp. 18–21 (cit. on p. 29).

Batchelor, G. K. (1967). *An Introduction to Fluid Dynamics*. Cambridge, England: Cambridge University Press (cit. on p. 10).

Beal, L. M., W. P. M. de Ruijter, A. Biastoch, R. Zahn, and SCOR/WCRP/IAPSO working group 136 (2011). „On the role of the Agulhas system in ocean circulation and climate“. In: *Nature* 472.7344, pp. 429–436. DOI: 10.1038/nature09983 (cit. on pp. 5, 28).

Beal, L. M., T. K. Chereskin, Y. D. Lenn, and S. Elipot (2006). „The Sources and Mixing Characteristics of the Agulhas Current“. In: *J. Phys. Oceanogr.* 36.11, pp. 2060–2074. DOI: 10.1175/JPO2964.1 (cit. on p. 42).

Beal, L. M., S. Elipot, A. Houk, and G. M. Leber (2015). „Capturing the Transport Variability of a Western Boundary Jet: Results from the Agulhas Current Time-Series Experiment (ACT)“. In: *J. Phys. Oceanogr.* 45.5, pp. 1302–1324. DOI: 10.1175/JPO-D-14-0119.1 (cit. on p. 32).

Berglund, S., K. Döös, and J. Nycander (2017). „Lagrangian tracing of the water-mass transformations in the Atlantic Ocean“. In: *Tellus, Ser. A Dyn. Meteorol. Oceanogr.* 69.1, pp. 1–15. DOI: 10.1080/16000870.2017.1306311 (cit. on pp. 2, 12, 21, 22, 33).

Berloff, P. S. and J. C. McWilliams (2002). „Material Transport in Oceanic Gyres. Part II: Hierarchy of Stochastic Models“. In: *J. Phys. Oceanogr.* 32.3, pp. 797–830. DOI: 10.1175/1520-0485(2002)032<0764:MTIOGP>2.0.CO;2 (cit. on pp. 6, 11).

Biastoch, A., C. W. Böning, and J. R. E. Lutjeharms (2008a). „Agulhas leakage dynamics affects decadal variability in Atlantic overturning circulation“. In: *Nature* 456, pp. 489–492 (cit. on pp. 19, 28).

Biastoch, A., C. W. Böning, F. U. Schwarzkopf, and J. R. E. Lutjeharms (2009). „Increase in Agulhas leakage due to poleward shift of the Southern Hemisphere westerlies“. In: *Nature* 462, pp. 495–498 (cit. on pp. 5, 28).

Biastoch, A. and C. W. Böning (2013). „Anthropogenic impact on Agulhas leakage“. In: *Geophys. Res. Lett.* 40, pp. 1138–1143. DOI: 10.1002/grl.50243 (cit. on pp. 28, 42).

Biastoch, A., C. W. Böning, J. Getzlaff, J.-M. Molines, and G. Madec (2008b). „Causes of Interannual–Decadal Variability in the Meridional Overturning Circulation of the Midlatitude North Atlantic Ocean“. In: *J. Clim.* 21.24, pp. 6599–6615. DOI: 10.1175/2008JCLI2404.1 (cit. on p. 26).

Biastoch, A., J. R. E. Lutjeharms, C. W. Böning, and M. Scheinert (2008c). „Mesoscale perturbations control inter-ocean exchange south of Africa“. In: *Geophys. Res. Lett.* 35.20, p. L20602. DOI: 10.1029/2008GL035132 (cit. on pp. 2, 3, 5, 20, 27).

Biastoch, A., J. V. Durgadoo, A. K. Morrison, E. van Sebille, W. Weijer, and S. M. Griffies (2015). „Atlantic multi-decadal oscillation covaries with Agulhas leakage“. In: *Nat. Commun.* 6.1, p. 10082. DOI: 10.1038/ncomms10082 (cit. on p. 28).

Blanke, B. and S. Raynaud (1997). „Kinematics of the Pacific Equatorial Undercurrent: An Eulerian and Lagrangian approach from GCM results“. In: *J. Phys. Oceanogr.* 27.6, pp. 1038–1053. DOI: 10.1175/1520-0485(1997)027<1038:KOTPEU>2.0.CO;2 (cit. on pp. 13, 20, 32).

Blanke, B., M. Arhan, G. Madec, and S. Roche (1999). „Warm Water Paths in the Equatorial Atlantic as Diagnosed with a General Circulation Model“. In: *J. Phys. Ocean.* 29, pp. 2753–2768 (cit. on pp. 13, 20, 32, 34).

Blanke, B., S. Speich, G. Madec, and R. Maugé (2002). „A global diagnostic of interior ocean ventilation“. In: *Geophys. Res. Lett.* 29.8, p. 1267. DOI: 10.1029/2001GL013727 (cit. on p. 19).

Blanke, B., S. Bonhommeau, N. Grima, and Y. Drillet (2012). „Sensitivity of advective transfer times across the North Atlantic Ocean to the temporal and spatial resolution of model velocity data: Implication for European eel larval transport“. In: *Dyn. Atmos. Ocean.* 55-56, pp. 22–44. DOI: 10.1016/j.dynatmoce.2012.04.003 (cit. on p. 12).

Bower, A. S., M. S. Lozier, S. F. Gary, and C. W. Böning (2009). „Interior pathways of the North Atlantic meridional overturning circulation“. In: *Nature* 459, pp. 243–248. DOI: 10.1038/nature07979 (cit. on pp. 1, 3).

Breusing, C., A. Biastoch, A. Drews, A. Metaxas, D. Jollivet, R. C. Vrijenhoek, T. Bayer, F. Melzner, L. Sayavedra, J. M. Petersen, N. Dubilier, M. B. Schilhabel, P. Rosenstiel, and T. B. Reusch (2016). „Biophysical and Population Genetic Models Predict the Presence of “Phantom” Stepping Stones Connecting Mid-Atlantic Ridge Vent Ecosystems“. In: *Curr. Biol.* 26.17, pp. 2257–2267. DOI: 10.1016/j.cub.2016.06.062 (cit. on p. 2).

Broecker, W. S. (1991). „The Great Ocean Conveyor“. In: *Oceanogr.* 4, pp. 79–89 (cit. on pp. 1, 3, 26).

Broeker, W. S. and T.-H. Peng (1982). *Tracers in the sea*. Palisades, N.Y., USA: Eldigio Press, p. 690 (cit. on p. 3).

Bryden, H. L., L. M. Beal, and L. M. Duncan (2005). „Structure and transport of the Agulhas current and its temporal variability“. In: *J. Oceanogr.* 61.3, pp. 479–492. DOI: 10.1007/s10872-005-0057-8 (cit. on p. 32).

Buckley, M. W. and J. Marshall (2016). „Observations, inferences, and mechanisms of the Atlantic Meridional Overturning Circulation: A review“. In: *Rev. Geophys.* 54. DOI: 10.1002/2015RG000493. (cit. on pp. 1, 5, 26).

Burkholder, K. C. and M. S. Lozier (2011). „Subtropical to subpolar pathways in the North Atlantic: Deductions from Lagrangian trajectories“. In: *J. Geophys. Res.* 116.C7, p. C07017. DOI: 10.1029/2010JC006697 (cit. on p. 2).

Burkholder, K. C. and M. S. Lozier (2014). „Tracing the pathways of the upper limb of the North Atlantic Meridional Overturning Circulation“. In: *Geophys. Res. Lett.* 41, pp. 4254–4260. DOI: 10.1002/2014GL060226 (cit. on pp. 2, 3).

Butcher, J. C. (2016). *Numerical methods for ordinary differential equations*. John Wiley and Sons. DOI: 10.1002/9781119121534 (cit. on p. 12).

Castellanos, P., E. J. D. Campos, J. Piera, O. T. Sato, and M. A. F. Silva Dias (2017). „Impacts of Agulhas leakage on the tropical Atlantic western boundary systems“. In: *J. Clim.* 30.17, pp. 6645–6659. DOI: 10.1175/JCLI-D-15-0878.1 (cit. on p. 50).

Cetina-Heredia, P., M. Roughan, E. van Sebille, M. Feng, and M. A. Coleman (2015). „Strengthened currents override the effect of warming on lobster larval dispersal and survival“. In: *Glob. Chang. Biol.* 21.12, pp. 4377–4386. DOI: 10.1111/gcb.13063 (cit. on p. 2).

Cheng, Y. (2018). „Agulhas Leakage Variability and Its Climate Implications in a Coupled System“. PhD thesis (cit. on pp. 5, 28).

Chenillat, F., B. Blanke, N. Grima, P. J. S. Franks, X. Capet, and P. Rivière (2015). „Quantifying tracer dynamics in moving fluids: a combined Eulerian-Lagrangian approach“. In: *Front. Environ. Sci.* 3, p. 43. DOI: 10.3389/fenvs.2015.00043 (cit. on pp. 12, 22).

Cimatoribus, A. A., S. S. Drijfhout, M. den Toom, and H. A. Dijkstra (2012). „Sensitivity of the Atlantic meridional overturning circulation to South Atlantic freshwater anomalies“. In: *Clim. Dyn.* 39, pp. 2291–2306. DOI: 10.1007/s00382-012-1292-5. arXiv: arXiv:1108.1340v4 (cit. on p. 26).

Cózar, A., E. Martí, C. M. Duarte, J. García-de Lomas, E. van Sebille, T. J. Ballatore, V. M. Eguíluz, J. I. González-Gordillo, M. L. Pedrotti, F. Echevarría, R. Troublè, and X. Irigoien (2017). „The Arctic Ocean as a dead end for floating plastics in the North Atlantic branch of the Thermohaline Circulation“. In: *Sci. Adv.* 3.4, e1600582. DOI: 10.1126/sciadv.1600582 (cit. on p. 2).

Cunningham, S. A., S. G. Alderson, B. A. King, and M. A. Brandon (2003). „Transport and variability of the Antarctic Circumpolar Current in Drake Passage“. In: *J. Geophys. Res.* 108.C5, p. 8084. DOI: 10.1029/2001JC001147 (cit. on pp. 32, 40).

de Dominicis, M., G. Leuzzi, P. Monti, N. Pinardi, and P. M. Poulain (2012). „Eddy diffusivity derived from drifter data for dispersion model applications“. In: *Ocean Dyn.* 62.9, pp. 1381–1398. DOI: 10.1007/s10236-012-0564-2 (cit. on p. 6).

de Groot, S. R. and P. Mazur (1984). *Non-equilibrium thermodynamics*. Dover Publications, p. 510 (cit. on p. 9).

de Ruijter, W. P. M., A. Biastoch, S. S. Drijfhout, J. R. E. Lutjeharms, R. P. Matano, T. Pichevin, P. J. van Leeuwen, and W. Weijer (1999). „Indian-Atlantic interocean exchange: Dynamics, estimation and impact“. In: *J. Geophys. Res. Ocean.* 104.C9, pp. 20885–20910. DOI: 10.1029/1998JC900099 (cit. on p. 26).

de Vries, P. and K. Döös (2001). „Calculating Lagrangian trajectories using time-dependent velocity fields“. In: *J. Atmos. Ocean. Technol.* 18.6, pp. 1092–1101. DOI: 10.1175/1520-0426(2001)018<1092:CLTUTD>2.0.CO;2 (cit. on p. 13).

Debreu, L. and E. Blayo (2008). „Two-way embedding algorithms: a review“. In: *Ocean Dyn.* 58, pp. 415–428. DOI: 10.1007/s10236-008-0150-9 (cit. on p. 30).

Deleersnijder, E., J. M. Campin, and E. J. M. Delhez (2001). „The concept of age in marine modelling I. Theory and preliminary model results“. In: *J. Mar. Syst.* 28, pp. 229–267. DOI: 10.1016/S0924-7963(01)00026-4 (cit. on p. 18).

Dong, S., S. Garzoli, and M. Baringer (2011). „The Role of Interocean Exchanges on Decadal Variations of the Meridional Heat Transport in the South Atlantic“. In: *J. Phys. Oceanogr.* 41, pp. 1498–1511. DOI: 10.1175/2011JPO4549.1 (cit. on p. 27).

Donners, J. and S. S. Drijfhout (2004). „The Lagrangian View of South Atlantic Interocean Exchange in a Global Ocean Model Compared with Inverse Model Results“. In: *J. Phys. Oceanogr.* 34, pp. 1019–1035. DOI: 10.1175/JPO2782.1 (cit. on pp. 2, 5, 27, 36).

Döös, K., J. Nycander, and A. C. Coward (2008). „Lagrangian decomposition of the Deacon Cell“. In: *J. Geophys. Res.* 113.C7, p. C07028. DOI: 10.1029/2007JC004351 (cit. on pp. 2, 12, 21, 33).

Döös, K., V. Rupolo, and L. Brodeau (2011). „Dispersion of surface drifters and model-simulated trajectories“. In: *Ocean Model.* 39.3-4, pp. 301–310. DOI: 10.1016/j.ocemod.2011.05.005 (cit. on pp. 6, 11, 23).

Döös, K., J. Nilsson, J. Nycander, L. Brodeau, and M. Ballarotta (2012). „The World Ocean Thermohaline Circulation“. In: *J. Phys. Oceanogr.* 42.9, pp. 1445–1460. DOI: 10.1175/JPO-D-11-0163.1 (cit. on p. 98).

Döös, K., B. Jönsson, and J. Kjellsson (2017). „Evaluation of oceanic and atmospheric trajectory schemes in the TRACMASS trajectory model v6.0“. In: *Geosci. Model Dev.* 10.4, pp. 1733–1749. DOI: 10.5194/gmd-10-1733-2017 (cit. on p. 13).

Döös, K., J. Kjellsson, and B. Jönsson (2013). „TRACMASS - A Lagrangian Trajectory Model“. In: *Prev. Methods Coast. Prot.* Heidelberg: Springer International Publishing, pp. 225–249 (cit. on p. 13).

Drake, H. F., A. K. Morrison, S. M. Griffies, J. L. Sarmiento, W. Weijer, and A. R. Gray (2018). „Lagrangian Timescales of Southern Ocean Upwelling in a Hierarchy of Model Resolutions“. In: *Geophys. Res. Lett.* 45.2, pp. 891–898. DOI: 10.1002/2017GL076045 (cit. on pp. 2, 12, 33).

Drijfhout, S. S., P. de Vries, K. Döös, and A. C. Coward (2003). „Impact of Eddy-Induced Transport on the Lagrangian Structure of the Upper Branch of the Thermohaline Circulation“. In: *J. Phys. Ocean.* 33, pp. 2141–2155. DOI: 10.1175/1520-0485(2003)033<2141:IOETOT>2.0.CO;2 (cit. on p. 21).

Durbin, P. A. (2018). „Some Recent Developments in Turbulence Closure Modeling“. In: *Annu. Rev. Fluid Mech.* 50.1, pp. 77–103. DOI: 10.1146/annurev-fluid-122316-045020 (cit. on p. 6).

Durgadoo, J. V. (2013). „Controls and impact of Agulhas leakage“. PhD thesis. Faculty of Mathematics and Natural Sciences, Christian-Albrechts-Universität zu Kiel (cit. on p. 49).

Durgadoo, J. V., B. R. Loveday, C. J. C. Reason, P. Penven, and A. Biastoch (2013). „Agulhas Leakage Predominantly Responds to the Southern Hemisphere Westerlies“. In: *J. Phys. Oceanogr.* 43.10, pp. 2113–2131. DOI: 10.1175/JPO-D-13-047.1 (cit. on pp. 2, 5, 16, 20, 27–29, 34).

Durgadoo, J. V., S. Rühs, A. Biastoch, and C. W. Böning (2017). „Indian Ocean sources of Agulhas leakage“. In: *J. Geophys. Res. Ocean.* 122.4, pp. 3481–3499. DOI: 10.1002/2016JC012676 (cit. on pp. 7, 21, 26, 99).

England, M. H. and E. Maier-Reimer (2001). „Using Chemical Tracers to Assess Ocean Models“. In: *Rev. Geophys.* 39.1, pp. 29–70. DOI: 10.1029/1998RG000043 (cit. on p. 1).

Fichefet, T. and M. A. Maqueda (1997). „Sensitivity of a global sea ice model to the treatment of ice thermodynamics and dynamics“. In: *J. Geophys. Res. Ocean.* 102.C6, pp. 12609–12646. DOI: 10.1029/97JC00480 (cit. on p. 29).

Fine, R. A. (2011). „Observations of CFCs and SF6 as Ocean Tracers“. In: *Ann. Rev. Mar. Sci.* 3.1, pp. 173–195. DOI: 10.1146/annurev.marine.010908.163933 (cit. on p. 1).

Firing, Y. L., T. K. Chereskin, and M. R. Mazloff (2011). „Vertical structure and transport of the Antarctic Circumpolar Current in Drake Passage from direct velocity observations“. In: *J. Geophys. Res.* 116.C8, p. C08015. DOI: 10.1029/2011JC006999 (cit. on p. 40).

Foukal, N. P. and M. S. Lozier (2016). „No inter-gyre pathway for sea-surface temperature anomalies in the North Atlantic“. In: *Nat. Commun.* 7, p. 11333. DOI: 10.1038/ncomms11333 (cit. on pp. 2, 5).

Gary, S. F., M. S. Lozier, A. Biastoch, and C. W. Böning (2012). „Reconciling tracer and float observations of the export pathways of Labrador Sea Water“. In: *Geophys. Res. Lett.* 39, p. L24606. DOI: 10.1029/2012GL053978 (cit. on pp. 2, 19, 23).

Gary, S. F., M. S. Lozier, C. W. Böning, and A. Biastoch (2011). „Deciphering the pathways for the deep limb of the Meridional Overturning Circulation“. In: *Deep Sea Res. Part II Top. Stud. Oceanogr.* 58.17-18, pp. 1781–1797. DOI: 10.1016/j.dsr2.2010.10.059 (cit. on pp. 2, 3, 17).

Garzoli, S. L. and R. Matano (2011). „The South Atlantic and the Atlantic Meridional Overturning Circulation“. In: *Deep Sea Res. Part II Top. Stud. Oceanogr.* 58, pp. 1837–1847. DOI: 10.1016/j.dsr2.2010.10.063 (cit. on pp. 26, 27).

Garzoli, S. L., M. O. Baringer, S. Dong, R. C. Perez, and Q. Yao (2013). „South Atlantic meridional fluxes“. In: *Deep Sea Res. Part I Oceanogr. Res. Pap.* 71, pp. 21–32. DOI: 10.1016/J.DSR.2012.09.003 (cit. on p. 26).

Gaspar, P., Y. Grégoris, and J.-M. Lefevre (1990). „A simple eddy kinetic energy model for simulations of the oceanic vertical mixing: Tests at station Papa and long-term upper ocean study site“. In: *J. Geophys. Res.* 95.C9, p. 16179. DOI: 10.1029/JC095iC09p16179 (cit. on p. 30).

Gent, P. R. and J. C. McWilliams (1990). „Isopycnal Mixing in Ocean Circulation Models“. In: *J. Phys. Oceanogr.* 20.1, pp. 150–155. DOI: 10.1175/1520-0485(1990)020<0150:IMIOCM>2.0.CO;2 (cit. on p. 30).

Gordon, A. L. (1986). „Interocean exchange of thermocline water“. In: *J. Geophys. Res.* 91.C4, pp. 5037–5046 (cit. on pp. 26, 27).

– (1991). „The Role of Thermohaline Circulation in Global Climate Change“. In: *Lamont-Doherty Geol. Obs. Bienn. Rep.* Columbia University Academic Commons. DOI: 10.7916/D8M04G8H (cit. on p. 3).

Gordon, A. L., R. F. Weiss, W. M. Smethie, and M. J. Warner (1992). „Thermocline and intermediate water communication between the south Atlantic and Indian oceans“. In: *J. Geophys. Res.* 97.C5, p. 7223. DOI: 10.1029/92JC00485 (cit. on p. 26).

Griffa, A. (1996). „Applications of stochastic particle models to oceanographic problems“. In: *Stoch. Model. Phys. Oceanogr.* Ed. by R. J. Adler, P. Müller, and B. L. Rozowskii. Boston: Springer, pp. 113–140. DOI: 10.1007/978-1-4612-2430-3_5 (cit. on pp. 6, 11).

Griffies, S. M., A. Biastoch, C. W. Böning, F. Bryan, G. Danabasoglu, E Chassignet, M. England, R. Gerdes, H. Haak, R. W. Hallberg, W. Hazeleger, J. Jungclaus, W. G. Large, G. Madec, A. Pirani, B. L. Samuels, M. Scheinert, A. S. Gupta, C. A. Severijns, H. L. Simons, A. M. Treguier, M. Winton, S. Yeager, and J. Yin (2009). „Coordinated Ocean-ice Reference Experiments (COREs)“. In: *Ocean Model.* 26, pp. 1–46. DOI: 10.1016/j.ocemod.2008.08.007 (cit. on p. 30).

Griffies, S. M., C. W. Böning, F. O. Bryan, E. P. Chassignet, R. Gerdes, H. Hasumi, A. C. Hirst, A.-M. Treguier, and D. J. Webb (2000). „Developments in ocean climate modelling“. In: *Ocean Model.* 2.3-4, pp. 123–192. DOI: 10.1016/S1463-5003(00)00014-7 (cit. on p. 13).

Haarsma, R. J., E. J. D. Campos, S. Drijfhout, W. Hazeleger, and C. Severijns (2011). „Impacts of interruption of the Agulhas leakage on the tropical Atlantic in coupled ocean–atmosphere simulations“. In: *Clim. Dyn.* 36.5-6, pp. 989–1003. DOI: 10.1007/s00382-009-0692-7 (cit. on p. 26).

Hallberg, R. (2013). „Using a resolution function to regulate parameterizations of oceanic mesoscale eddy effects“. In: *Ocean Model.* 72, pp. 92–103. DOI: 10.1016/j.ocemod.2013.08.007 (cit. on p. 30).

Hanawa, K. and L. D. Talley (2001). „Chapter 5.4 Mode waters“. In: *Int. Geophys. Ser. Vol. 77: Ocean Circulation and Climate - Observing and Modelling the Global Ocean*. Ed. by G. Siedler, J. Church, and J. Gould. Academic Press, pp. 373–386. DOI: 10.1016/S0074-6142(01)80129-7 (cit. on p. 45).

Hardesty, B. D., J. Harari, A. Isobe, L. Lebreton, N. Maximenko, J. Potemra, E. van Sebille, A. D. Vethaak, and C. Wilcox (2017). „Using Numerical Model Simulations to Improve the Understanding of Micro-plastic Distribution and Pathways in the Marine Environment“. In: *Front. Mar. Sci.* 4, p. 30. DOI: 10.3389/fmars.2017.00030 (cit. on p. 2).

Hazeleger, W. and S. Drijfhout (2006). „Subtropical cells and meridional overturning circulation pathways in the tropical Atlantic“. In: *J. Geophys. Res.* 111.C3, p. C03013. DOI: 10.1029/2005JC002942 (cit. on p. 45).

Holfort, J. and G. Siedler (2001). „The Meridional Oceanic Transports of Heat and Nutrients in the South Atlantic“. In: *J. Phys. Oceanogr.* 31.1, pp. 5–29. DOI: 10.1175/1520-0485(2001)031<0005:TMOTOH>2.0.CO;2 (cit. on pp. 27, 43).

Holzer, M. and T. M. Hall (2000). „Transit-Time and Tracer-Age Distributions in Geophysical Flows“. In: *J. Atmos. Sci.* 57.21, pp. 3539–3558. DOI: 10.1175/1520-0469(2000)057<3539:TTATAD>2.0.CO;2 (cit. on p. 18).

Hüttl-Kabus, S. and C. W. Böning (2008). „Pathways and variability of the off-equatorial undercurrents in the Atlantic Ocean“. In: *J. Geophys. Res.* 113.C10, p. C10018. DOI: 10.1029/2007JC004700. (cit. on p. 16).

Jönsson, B. F., P. A. Lundberg, and K. Döös (2004). „Baltic sub-basin turnover times examined using the Rossby Centre Ocean model.“ In: *Ambio* 33.4-5, pp. 257–260. DOI: 10.1579/0044-7447-33.4.257 (cit. on p. 19).

Keating, S. R., K. S. Smith, and P. R. Kramer (2011). „Diagnosing Lateral Mixing in the Upper Ocean with Virtual Tracers: Spatial and Temporal Resolution Dependence“. In: *J. Phys. Oceanogr.* 41.8, pp. 1512–1534. DOI: 10.1175/2011JPO4580.1 (cit. on p. 14).

Kelly, K. A., L. Thompson, and J. Lyman (2014). „The coherence and impact of meridional heat transport anomalies in the atlantic ocean inferred from observations“. In: *J. Clim.* 27, pp. 1469–1487. DOI: 10.1175/JCLI-D-12-00131.1 (cit. on p. 26).

Klocker, A., R. Ferrari, J. H. LaCasce, and S. T. Merrifield (2012). „Reconciling float-based and tracer-based estimates of lateral diffusivities“. In: *J. Mar. Res.* 70.4, pp. 569–602. DOI: 10.1357/002224012805262743 (cit. on p. 6).

Knorr, G. and G. Lohmann (2003). „Southern ocean origin for the resumption of Atlantic thermohaline circulation during deglaciation“. In: *Nature* 424, pp. 532–536. DOI: 10.1038/nature01855 (cit. on p. 28).

Koch-Larrouy, A., R. Morrow, T. Penduff, and M. Juza (2010). „Origin and mechanism of Subantarctic Mode Water formation and transformation in the Southern Indian Ocean“. In: *Ocean Dyn.* 60.3, pp. 563–583. DOI: 10.1007/s10236-010-0276-4 (cit. on p. 19).

Kool, J. T., A. Moilanen, and E. A. Treml (2013). „Population connectivity: recent advances and new perspectives“. In: *Landsc. Ecol.* 28.2, pp. 165–185. DOI: 10.1007/s10980-012-9819-z (cit. on p. 2).

Koszalka, I. M., T. W. N. Haine, and M. G. Magaldi (2013). „Fates and Travel Times of Denmark Strait Overflow Water in the Irminger Basin“. In: *J. Phys. Oceanogr.* 43.12, pp. 2611–2628. DOI: 10.1175/JPO-D-13-023.1 (cit. on pp. 2, 6).

LaCasce, J. H. (2008). „Statistics from Lagrangian observations“. In: *Prog. Oceanogr.* 77.1, pp. 1–29. DOI: 10.1016/j.pocean.2008.02.002 (cit. on p. 5).

Lange, M. and E. van Sebille (2017). „Parcels v0.9: prototyping a Lagrangian ocean analysis framework for the petascale age“. In: *Geosci. Model Dev.* 10, pp. 4175–4186. DOI: 10.5194/gmd-10-4175-2017 (cit. on pp. 14, 23).

Large, W. G. and S. G. Yeager (2009). „The global climatology of an interannually varying air–sea flux data set“. In: *Clim. Dyn.* 33, pp. 341–364. DOI: 10.1007/s00382-008-0441-3 (cit. on p. 30).

Le Bars, D., H. A. Dijkstra, and W. P. M. de Ruijter (2013). „Impact of the Indonesian throughflow on Agulhas leakage“. In: *Ocean Sci. Discuss.* 10.1, pp. 353–391. DOI: 10.5194/osd-10-353-2013 (cit. on p. 26).

Le Bars, D., J. V. Durgadoo, H. A. Dijkstra, A. Biastoch, and W. P. M. de Ruijter (2014). „An observed 20-year time series of Agulhas leakage“. In: *Ocean Sci.* 10.4, pp. 601–609. DOI: 10.5194/os-10-601-2014 (cit. on p. 28).

Lee, S. K., W. Park, M. O. Baringer, A. L. Gordon, B. Huber, and Y. Liu (2015). „Pacific origin of the abrupt increase in Indian Ocean heat content during the warming hiatus“. In: *Nat. Geosci.* 8.6, pp. 445–449. DOI: 10.1038/NGEO2438 (cit. on p. 98).

Lenz, E. (1845). „Bermerkunge über die Temperatur des Weltmeeres in verschiedenen Tiefen“. In: *Bulletin de la Classe Physico-Mathématique de l'Académie Impériale des Sciences de Saint-Pétersbourg* 5.S4, pp. 67–74. DOI: 10.1002/andp.18481490406 (cit. on p. 1).

Lester, S. E. and B. I. Ruttenberg (2005). „The relationship between pelagic larval duration and range size in tropical reef fishes: a synthetic analysis.“ In: *Proc. Biol. Sci.* 272.1563, pp. 585–91. DOI: 10.1098/rspb.2004.2985 (cit. on p. 19).

Levitus, S., T. P. Boyer, M. E. Conkright, T. O'Brien, J. Antonov, C. Stephens, L. Stathoplos, D. Johnson, and R. Gelfeld (1998). *NOAA Atlas NESDIS 18, World Ocean Database 1998: Volume 1: Introduction*. Washington, D.C.: U.S. Gov. Printing Office, p. 346 (cit. on p. 30).

Lique, C., A. M. Treguier, B. Blanke, and N. Grima (2010). „On the origins of water masses exported along both sides of Greenland: A Lagrangian model analysis“. In: *J. Geophys. Res.* 115.C5, p. C05019. DOI: 10.1029/2009JC005316 (cit. on pp. 19, 22).

Loveday, B. R., P. Penven, and C. J. C. Reason (2015). „Southern Annular Mode and westerly-wind-driven changes in Indian-Atlantic exchange mechanisms“. In: *Geophys. Res. Lett.* 42.12, pp. 4912–4921. DOI: 10.1002/2015GL064256 (cit. on p. 98).

Lozier, M. S. (2010). „Deconstructing the Conveyor Belt“. In: *Science (80-.).* 328.5985, pp. 1507–1511. DOI: 10.1126/science.1189250 (cit. on pp. 3, 98).

Lozier, M. S., S. F. Gary, and A. S. Bower (2013). „Simulated pathways of the overflow waters in the North Atlantic: Subpolar to subtropical export“. In: *Deep Sea Res. Part II Top. Stud. Oceanogr.* 85, pp. 147–153. DOI: 10.1016/j.dsr2.2012.07.037 (cit. on pp. 2, 3).

Lübbecke, J. F., J. V. Durgadoo, and A. Biastoch (2015). „Contribution of Increased Agulhas Leakage to Tropical Atlantic Warming“. In: *J. Clim.* 28.24, pp. 9697–9706. DOI: 10.1175/JCLI-D-15-0258.1 (cit. on pp. 50, 99).

Lumpkin, R. and K. Speer (2007). „Global Ocean Meridional Overturning“. In: *J. Phys. Oceanogr.* 37.10, pp. 2550–2562. DOI: 10.1175/JPO3130.1 (cit. on p. 3).

Lumpkin, R., T. Özgökmen, and L. Centurioni (2017). „Advances in the Application of Surface Drifters“. In: *Ann. Rev. Mar. Sci.* 9.1, pp. 59–81. DOI: 10.1146/annurev-marine-010816-060641 (cit. on p. 1).

Lutjeharms, J. R. E. (2006). *The Agulhas Current*. Berlin: Springer, p. 329 (cit. on p. 26).

Lynch-Stieglitz, J. (2017). „The Atlantic Meridional Overturning Circulation and Abrupt Climate Change“. In: *Ann. Rev. Mar. Sci.* 9, pp. 83–104. DOI: 10.1146/annurev-marine-010816-060415 (cit. on p. 26).

Macdonald, A. M. (1993). „Property fluxes at 30°S and their implications for the Pacific-Indian throughflow and the global heat budget“. In: *J. Geophys. Res. Ocean.* 98.C4, pp. 6851–6868. DOI: 10.1029/92JC02964 (cit. on p. 43).

– (1998). „The global ocean circulation: a hydrographic estimate and regional analysis“. In: *Prog. Oceanogr.* 41.3, pp. 281–382. DOI: 10.1016/S0079-6611(98)00020-2 (cit. on p. 27).

Madec, G., P. Delecluse, M. Imbard, and C. Levy (1998). *OPA 8 Ocean General Circulation Model - Reference Manual*. Tech. rep. LODYC/IPSL Note 11 (cit. on p. 30).

Madec, G. and NEMO-team (2016). *NEMO Ocean Engine*. Tech. rep. Institut Pierre-Simon Laplace (IPSL) (cit. on pp. 6, 29).

Meinen, C. S., S. Speich, A. R. Piola, I. Ansorge, E. Campos, M. Kersalé, T. Terre, M. P. Chidichimo, T. Lamont, O. T. Sato, R. C. Perez, D. Valla, M. van den Berg, M. Le Hénaff, S. Dong, and S. L. Garzoli (2018). „Meridional Overturning Circulation Transport Variability at 34.5°S During 2009-2017: Baroclinic and Barotropic Flows and the Dueling Influence of the Boundaries“. In: *Geophys. Res. Lett.* 45.9, pp. 4180–4188. DOI: 10.1029/2018GL077408 (cit. on p. 32).

Merz, A. and G Wüst (1922). „Die atlantische Vertikalzirkulation“. In: *Zeitschrift der Gesellschaft fuer Erdkd. Berlin* Jahrgang 1, pp. 1–35 (cit. on p. 1).

Mesinger, F. and A. Arakawa (1976). „Numerical methods used in atmospheric models“. In: *Glob. Atmos. Res. Progr. World Meteorol. Organ.* 1.17, pp. 1–66 (cit. on p. 30).

Moffa-Sánchez, P. and I. R. Hall (2017). „North Atlantic variability and its links to European climate over the last 3000 years“. In: *Nat. Commun.* 8, p. 1726. DOI: 10.1038/s41467-017-01884-8 (cit. on p. 26).

Monti, P. and G. Leuzzi (2010). „Lagrangian models of dispersion in marine environment“. In: *Environ. Fluid Mech.* 10.6, pp. 637–656. DOI: 10.1007/s10652-010-9184-x (cit. on p. 6).

Olbers, D., J. Willebrand, and C. Eden (2012). *Ocean Dynamics*. Heidelberg: Springer, Berlin, Heidelberg, p. 704. DOI: https://doi.org/10.1007/978-3-642-23450-7 (cit. on p. 9).

Palter, J. B. (2015). „The Role of the Gulf Stream in European Climate“. In: *Ann. Rev. Mar. Sci.* 7, pp. 113–137. DOI: 10.1146/annurev-marine-010814-015656 (cit. on p. 26).

Paris, C. B., R. K. Cowen, R Claro, and K Lindeman (2005). „Larval transport pathways from Cuban spawning aggregattions (Snappers; Lutjanidae) based on biophysical modeling“. In: *Mar. Ecol. Prog. Ser.* 296.93-106, pp. 93–106. DOI: 10.3354/meps296093 (cit. on p. 2).

Paris, C. B., J. Helgers, E. van Sebille, and A. Srinivasan (2013). „Connectivity Modeling System: A probabilistic modeling tool for the multi-scale tracking of biotic and abiotic variability in the ocean“. In: *Environ. Model. Softw.* 42, pp. 47–54. DOI: 10.1016/j.envsoft.2012.12.006 (cit. on p. 14).

Phelps, J. J. C., J. A. Polton, A. J. Souza, and L. A. Robinson (2015). „Behaviour influences larval dispersal in shelf sea gyres: Nephrops norvegicus in the Irish Sea“. In: *Mar. Ecol. Prog. Ser.* 518, pp. 177–191. DOI: 10.3354/meps11040 (cit. on p. 14).

Pineda, J., J. A. Hare, and S. Sponaungle (2007). „Larval transport and dispersal in the coastal ocean and consequences for population connectivity“. In: *Oceanography* 20.3, pp. 22–39. DOI: 10.5670/oceanog.2007.27 (cit. on p. 2).

Poje, A. C., A. C. Haza, T. M. Özgökmen, M. G. Magaldi, and Z. D. Garraffo (2010). „Resolution dependent relative dispersion statistics in a hierarchy of ocean models“. In: *Ocean Model.* 31.1-2, pp. 36–50. DOI: 10.1016/j.ocemod.2009.09.002 (cit. on p. 12).

Qin, X., E. van Sebille, and A. Sen Gupta (2014). „Quantification of errors induced by temporal resolution on Lagrangian particles in an eddy-resolving model“. In: *Ocean Model.* 76, pp. 20–30. DOI: 10.1016/j.ocemod.2014.02.002 (cit. on pp. 12, 13).

Richardson, P. L. (2007). „Agulhas leakage into the Atlantic estimated with subsurface floats and surface drifters“. In: *Deep Sea Res. Part I Oceanogr. Res. Pap.* 54.8, pp. 1361–1389. DOI: 10.1016/J.DSR.2007.04.010 (cit. on pp. 26, 27).

– (2008). „On the history of meridional overturning circulation schematic diagrams“. In: *Prog. Oceanogr.* 76, pp. 466–486. DOI: 10.1016/j.pocean.2008.01.005 (cit. on pp. 1, 3–5, 26).

Rimaud, J., S. Speich, B. Blanke, and N. Grima (2012). „The exchange of Intermediate Water in the southeast Atlantic: Water mass transformations diagnosed from the Lagrangian analysis of a regional ocean model“. In: *J. Geophys. Res.* 117, p. C08034. DOI: 10.1029/2012JC008059 (cit. on pp. 2, 22, 47).

Rintoul, S. R. (1991). „South Atlantic Interbasin Exchange“. In: *J. Geophys. Res.* 96.C2, pp. 2675–2692 (cit. on pp. 26, 27).

Roemmich, D. (1983). „The Balance of Geostrophic and Ekman Transports in the Tropical Atlantic Ocean“. In: *J. Phys. Oceanogr.* 13.8, pp. 1534–1539. DOI: 10.1175/1520-0485(1983)013<1534:TBOGAE>2.0.CO;2 (cit. on p. 43).

Rouault, M, P Penven, and B Pohl (2009). „Warming in the Agulhas Current system since the 1980's“. In: *Geophys. Res. Lett.* 36, p. L12602 (cit. on p. 98).

Rühs, S., J. V. Durgadoo, E. Behrens, and A. Biastoch (2013). „Advective timescales and pathways of Agulhas leakage“. In: *Geophys. Res. Lett.* 40.15, pp. 3997–4000. DOI: 10.1002/grl.50782 (cit. on pp. 2, 12, 16, 18, 19, 28, 33, 38, 40).

Rühs, S., K. Getzlaff, J. V. Durgadoo, A. Biastoch, and C. W. Böning (2015). „On the suitability of North Brazil Current transport estimates for monitoring basin-scale AMOC changes“. In: *Geophys. Res. Lett.* 42.19, pp. 8072–8080. DOI: 10.1002/2015GL065695 (cit. on pp. 28, 31, 32, 36).

Rühs, S., V. Zhurbas, I. M. Koszalka, J. V. Durgadoo, and A. Biastoch (2018). „Eddy diffusivity estimates from Lagrangian trajectories simulated with ocean models and surface drifter data - a case study for the greater Agulhas system“. In: *J. Phys. Oceanogr.* 48.1, pp. 175–196. DOI: 10.1175/JPO-D-17-0048.1 (cit. on pp. 6, 7, 13, 23).

Rypina, I. I., A Kirincich, S. Lentz, and M Sundermeyer (2016). „Investigating the Eddy Diffusivity Concept in the Coastal Ocean“. In: *J. Phys. Oceanogr.* 46.7, pp. 2201–2218. DOI: 10.1175/JPO-D-16-0020.1 (cit. on p. 6).

Schmitz, W. J. (1995). „On the interbasin-scale thermohaline circulation“. In: *Rev. Geophys.* 33.2, p. 151. DOI: 10.1029/95RG00879 (cit. on pp. 3, 27).

– (1996). *On the World Ocean Circulation: Volume II, The Pacific and Indian Oceans/ A Global Update*. WHOI-96-08. Woods Hole, MA: Woods Hole Oceanographic Institution. DOI: 10.1575/1912/356 (cit. on p. 3).

Schott, F. A., J. P. McCreary, and G. C. Johnson (2004). „Shallow overturning circulations of the tropical-subtropical oceans“. In: *Geophys. Monogr. Ser.* Vol. 147. American Geophysical Union (AGU), pp. 261–304. DOI: 10.1029/147GM15 (cit. on p. 45).

Schott, F. A., M. Dengler, R. Zantopp, L. Stramma, J. Fischer, and P. Brandt (2005). „The shallow and deep western boundary circulation of the South Atlantic at 5°-11°S“. In: *J. Phys. Oceanogr.* 35, pp. 2031–2053 (cit. on p. 31).

Schott, G. (1902). „Oceanographie und maritime Meteorologie“. In: *Wissenschaftliche Ergebnisse der Dtsch. Tiefsee-Expedition auf dem Dampfer “Valdivia” 1898–1899* 1, p. 403 (cit. on p. 1).

Scott, R., R. Marsh, and G. C. Hays (2011). „A little movement orientated to the geomagnetic field makes a big difference in strong flows“. In: *Mar. Biol.* 159.3, pp. 481–488. DOI: 10.1007/s00227-011-1825-1 (cit. on p. 2).

Scott, R., A. Biastoch, P. D. Agamboue, T. Bayer, F. L. Boussamba, A. Formia, B. J. Godley, B. D. K. Mabert, J. C. Manfoumbi, F. U. Schwarzkopf, G.-P. Sounguet, P. Wagner, and M. J. Witt (2017). „Spatio-temporal variation in ocean current-driven hatchling dispersion: Implications for the world’s largest leatherback sea turtle nesting region“. In: *Divers. Distrib.* 23.6. Ed. by M. Beger, pp. 604–614. DOI: 10.1111/ddi.12554 (cit. on p. 2).

Simons, R. D., D. A. Siegel, and K. S. Brown (2013). „Model sensitivity and robustness in the estimation of larval transport: a study of particle tracking parameters“. In: *J. Mar. Syst.* 119 (cit. on p. 23).

Sloyan, B. M. and S. R. Rintoul (2001). „Circulation, Renewal, and Modification of Antarctic Mode and Intermediate Water“. In: *J. Phys. Oceanogr.* 31.4, pp. 1005–1030. DOI: 10.1175/1520-0485(2001)031<1005:CRAMOA>2.0.CO;2 (cit. on p. 27).

Speich, S., B. Blanke, and G. Madec (2001). „Warm and cold water routes of an O.G.C.M. thermohaline conveyor belt“. In: *Geophys. Res. Lett.* 28.2, pp. 311–314. DOI: 10.1029/2000GL011748 (cit. on pp. 2, 19, 21, 26–28, 36, 38–40).

Speich, S., B. Blanke, P. de Vries, S. Drijfhout, K. Döös, A. Ganachaud, and R. Marsh (2002). „Tasman leakage: A new route in the global ocean conveyor belt“. In: *Geophys. Res. Lett.* 29.10, p. 1416. DOI: 10.1029/2001GL014586, (cit. on pp. 2, 21, 26).

Speich, S., B. Blanke, and W. Cai (2007). „Atlantic meridional overturning circulation and the Southern Hemisphere supergyre“. In: *Geophys. Res. Lett.* 34, p. L23614. DOI: 10.1029/2007GL031583 (cit. on pp. 2, 3, 22, 27, 37).

Spiegel, E. A. and G. Veronis (1960). „On the Boussinesq approximation for a compressible fluid“. In: *Astrophys. J.* 131, pp. 442–447 (cit. on p. 10).

Srokosz, M., M. Baringer, H. Bryden, S. Cunningham, T. Delworth, S. Lozier, J. Marotzke, and R. Sutton (2012). „Past, Present, and Future Changes in the Atlantic Meridional Overturning Circulation“. In: *Bull. Am. Meteorol. Soc.* 93.11, pp. 1663–1676. DOI: 10.1175/BAMS-D-11-00151.1 (cit. on p. 26).

Staaterman, E. and C. B. Paris (2014). „Modelling larval fish navigation: the way forward“. In: *J. Mar. Sci.* 71.4, pp. 918–924. DOI: 10.1093/icesjms/fst103 (cit. on p. 14).

Stramma, L. and M. England (1999). „On the water masses and mean circulation of the South Atlantic Ocean“. In: *J. Geophys. Res.* 104.C9, pp. 20,863–20,883 (cit. on p. 32).

Talley, L. D., G. L. Pickard, W. J. Emery, and J. H. Swift (2011). „Typical Distributions of Water Characteristics“. In: *Descr. Phys. Oceanogr.* Chap. 4, pp. 67–110. DOI: 10.1016/B978-0-7506-4552-2.10016-2 (cit. on pp. 18, 19, 100).

Thomas, M. D., A.-M. Tréguier, B. Blanke, J. Deshayes, and A. Voldoire (2015). „A Lagrangian Method to Isolate the Impacts of Mixed Layer Subduction on the Meridional Overturning Circulation in a Numerical Model“. In: *J. Clim.* 28.19, pp. 7503–7517. DOI: 10.1175/JCLI-D-14-00631.1 (cit. on pp. 12, 21, 23, 33).

Tim, N., E. Zorita, F. U. Schwarzkopf, S. Rühs, K.-C. Emeis, and A. Biastoch (submitted to J. Geophys. Res. Ocean.). „The impact of Agulhas leakage on the central water masses in the Benguela upwelling system from a high-resolution ocean simulation“. In: (cit. on pp. 35, 44, 45, 50).

Torri, M., R. Corrado, F. Falcini, A. Cuttitta, L. Palatella, G. Lacorata, B. Patti, M. Arculeo, R. Mifsud, S. Mazzola, and R. Santoleri (2018). „Planktonic stages of small pelagic fishes (Sardinella aurita and Engraulis encrasicolus) in the central Mediterranean Sea: The key role of physical forcings and implications for fisheries management“. In: *Prog. Oceanogr.* 162, pp. 25–39. DOI: 10.1016/j.pocean.2018.02.009 (cit. on p. 2).

Tsubouchi, T., T. Suga, and K. Hanawa (2016). „Comparison Study of Subtropical Mode Waters in the World Ocean“. In: *Front. Mar. Sci.* 3.December, pp. 1–15. DOI: 10.3389/fmars.2016.00270 (cit. on p. 45).

Valdivieso Da Costa, M. and B. Blanke (2004). „Lagrangian methods for flow climatologies and trajectory error assessment“. In: *Ocean Model.* 6.3-4, pp. 335–358. DOI: 10.1016/S1463-5003(03)00023-4 (cit. on pp. 13, 20).

van Sebille, E. (2015). „The oceans' accumulating plastic garbage“. In: *Phys. Today* 68.2, pp. 60–61. DOI: 10.1063/PT.3.2697 (cit. on p. 2).

van Sebille, E., P. J. van Leeuwen, A. Biastoch, C. N. Barron, and W. P. M. de Ruijter (2009). „Lagrangian validation of numerical drifter trajectories using drifting buoys: Application to the Agulhas system“. In: *Ocean Model.* 29.4, pp. 269–276. DOI: 10.1016/j.ocemod.2009.05.005 (cit. on p. 23).

van Sebille, E., P. J. van Leeuwen, A. Biastoch, and W. P. M. de Ruijter (2010). „Flux comparison of Eulerian and Lagrangian estimates of Agulhas leakage: A case study using a numerical model“. In: *Deep Sea Res. Part I Oceanogr. Res. Pap.* 57.3, pp. 319–327. DOI: 10.1016/J.DSR.2009.12.006 (cit. on pp. 20, 27).

van Sebille, E., L. M. Beal, and W. E. Johns (2011). „Advective Time Scales of Agulhas Leakage to the North Atlantic in Surface Drifter Observations and the 3D OFES Model“. EN. In: *J. Phys. Oceanogr.* 41.1947, pp. 1026–1034. DOI: 10.1175/201 (cit. on pp. 2, 19, 20, 28, 38, 40).

van Sebille, E., P. Spence, M. R. Mazloff, M. H. England, S. R. Rintoul, and O. A. Saenko (2013). „Abyssal connections of Antarctic Bottom Water in a Southern Ocean State Estimate“. In: *Geophys. Res. Lett.* 40.10, pp. 2177–2182. DOI: 10.1002/grl.50483 (cit. on pp. 2, 17).

van Sebille, E., J. Sprintall, F. U. Schwarzkopf, A. Sen Gupta, A. Santoso, M. H. England, A. Biastoch, and C. W. Böning (2014). „Pacific-to-Indian Ocean connectivity: Tasman leakage, Indonesian Throughflow, and the role of ENSO“. In: *J. Geophys. Res. Ocean.* 119.2, pp. 1365–1382. DOI: 10.1002/2013JC009525.Received (cit. on pp. 2, 21).

van Sebille, E., S. M. Griffies, R. Abernathey, T. P. Adams, P. Berlof, A. Biastoc, B. Blanke, E. P. Chassignet, Y. Cheng, C. J. Cotter, E. Deleersnijder, K. Döös, H. Drake, S. Drijfhout, S. F. Gar, A. W. Heemink, J. Kjellsson, I. M. Koszalka, M. Lange, C. Lique, G. A. MacGilchrist, R. Marsh, G. C. M. Adame, R. McAdam, F. Nencioli, C. B. Paris, M. D. Piggott, J. A. Polton, S. Rühs, S. H. Shah, M. D. Thomas, J. Wang, P. J. Wolfram, L. Zanna, and J. D. Zika (2018). „Lagrangian ocean analysis : fundamentals and practices“. In: *Ocean Model.* 121, pp. 49–75. DOI: 10.1016/j.ocemod.2017.11.008 (cit. on pp. 1, 2, 7, 9, 13, 16, 17, 19, 21, 22).

Viglione, G. A. and A. F. Thompson (2016). „Lagrangian pathways of upwelling in the Southern Ocean“. In: *J. Geophys. Res. Ocean.* 121.8, pp. 6295–6309. DOI: 10.1002/2016JC011773 (cit. on p. 2).

Weijer, W., W. P. de Ruijter, A. Sterl, and S. S. Drijfhout (2002). „Response of the Atlantic overturning circulation to South Atlantic sources of buoyancy“. In: *Glob. Planet. Change* 34, pp. 293–311. DOI: 10.1016/S0921-8181(02)00121-2 (cit. on p. 28).

White, C., K. A. Selkoe, J. Watson, D. A. Siegel, D. C. Zacherl, and R. J. Toonen (2010). „Ocean currents help explain population genetic structure“. In: *Proc. R. Soc. B Biol. Sci.* 277.1688, pp. 1685–1694. DOI: 10.1098/rspb.2009.2214 (cit. on p. 2).

Wood, S., C. B. Paris, A. Ridgwell, and E. J. Hendy (2014). „Modelling dispersal and connectivity of broadcast spawning corals at the global scale“. In: *Glob. Ecol. Biogeogr.* 23.1, pp. 1–11. DOI: 10.1111/geb.12101 (cit. on p. 2).

Wüst, G. (1949). „Die Kreisläufe der atlantischen Wassermassen, ein neuer Versuch räumlicher Darstellung.“ In: *Forschungen und Fortschritte* 25, pp. 285–289 (cit. on p. 1).

Yeager, S. and G. Danabasoglu (2014). „The Origins of Late-Twentieth-Century Variations in the Large-Scale North Atlantic Circulation“. In: *J. Clim.* 27.9, pp. 3222–3247. DOI: 10.1175/JCLI-D-13-00125.1 (cit. on p. 26).

Youngs, M. K., A. F. Thompson, M. M. Flexas, and K. J. Heywood (2015). „Weddell Sea Export Pathways from Surface Drifters“. In: *J. Phys. Oceanogr.* 45.4, pp. 1068–1085. DOI: 10.1175/JPO-D-14-0103.1 (cit. on p. 1).

Zalesak, S. T. (1979). „Fully multidimensional flux-corrected transport algorithms for fluids“. In: *J. Comput. Phys.* 31.3, pp. 335–362. DOI: 10.1016/0021-9991(79)90051-2 (cit. on p. 30).

Zhang, D (2003). „Observational Evidence for Flow between the Subtropical and Tropical Atlantic: The Atlantic Subtropical Cells“. In: *J. Phys. Oceanogr.* 33, pp. 1783–1797 (cit. on p. 45).

Zou, S. and M. S. Lozier (2016). „Breaking the Linkage Between Labrador Sea Water Production and Its Advective Export to the Subtropical Gyre“. In: *J. Phys. Oceanogr.* 46.7, pp. 2169–2182. DOI: 10.1175/JPO-D-15-0210.1 (cit. on pp. 2, 5).